KEK Proceedings 2007-5
November 2007
R

Proceedings of the Fourteenth EGS Users' Meeting in Japan

August 7 - 9, 2007.

KEK, Tsukuba, Japan

Edited by

Y. Namito, H. Hirayama and S. Ban

High Energy Accelerator Research Organization

High Energy Accelerator Research Organization (KEK), 2007

KEK Reports are available from:

High Energy Accelerator Research Organization (KEK)
1-1 Oho, Tsukuba-shi
Ibaraki-ken, 305-0801
JAPAN

Phone: +81-29-864-5124
Fax: +81-29-864-4602
E-mail: irdpub@mail.kek.jp
Internet: http://www.kek.jp

FOREWARD

The Fourteenth EGS Users' Meeting in Japan was held at High Energy Accelerator Research Organization (KEK) from August 7 to 9. The meeting has been hosted by the Radiation Science Center. More than 100 participants attended the meeting.

The meeting was divided into two parts. Short course on EGS was held at the first half of the workshop using EGS5 code. In the later half, 22 talks related EGS were presented. The talk covered the wide fields, like the medical application and the calculation of various detector responses *etc.* These talks were very useful to exchange the information between the researchers in the different fields.

Finally, we would like to express our great appreciation to all authors who have prepared manuscript quickly for the publication of this proceedings.

Hideo Hirayama
Yoshihito Namito
Syuichi Ban
Radiation Science Center
KEK, High Energy Accelerator Research Organization

CONTENTS

BACKSCATTERING COEFFICIENTS OF ELECTRONS: A REVIEW

Tatsuo Tabata

Osaka Prefecture University
1-1 Gakuen-cho, Naka-ku, Sakai, Osaka 599-8531, Japan
and
Institute for Data Evaluation and Analysis
198-51 Kami, Nishi-ku, Sakai, Osaka 593-8311, Japan
Email: tttabata@pearl.ocn.ne.jp

Abstract

The experiment on the backscattering coefficient of electrons of energies from 3.2 to 14 MeV, published in 1967 by the present author, is reviewed to confirm the usefulness of its results as a benchmark for Monte Carlo calculations. The cause of large discrepancies between Dressel's and other results is described. Comparisons of compiled experimental data and results of Integrated TIGER Series Monte Carlo Code System are cited and discussed. In Appendix, experimental data of the present author's group on the charge deposition profile of electrons are mentioned as another useful benchmark.

1. Introduction

Experimental data on the backscattering coefficient of electrons are useful as a benchmark for Monte Carlo codes for electron–photon transport calculations. In this paper a review is first given of one of the best experiments in the MeV region, published by the present author [1] in 1967, mainly from the viewpoint of the experimental method and evaluation of errors. Secondly the cause of large discrepancies between Dressel's [2] and other authors' results, the latter including the present author's, is mentioned, because it has not been well documented yet. Thirdly graphical comparisons of compiled experimental data and results of Integrated TIGER Series (ITS) Monte Carlo Code System [3] are cited from a previous publication [4] and discussed. In Appendix another useful benchmark on the charge deposition profile of electrons [5, 6] and its comparison with the old version of ETRAN and ITS are reviewed.

2. Present Author's Experiment

2.1. Method

2.1.1. Electron Beam

The linear electron accelerator of the former Radiation Center of Osaka Prefecture (see[1] Fig. 1) produced the electron beams of energies from 3.2 to 14 MeV. An analyzing magnet deflected the beam by 70 deg. A pair of quadrupole magnets focused the beam on the entrance collimator of the scattering chamber placed 5.5 m away in an experimental room. The collimator was made of copper and was 160 mm in length, allowing self-absorption of bremsstrahlung generated near its entrance hole. The energy scale of the analyzing magnet was calibrated within an error of 1.1 % by measuring the conversion-electron line of Cs^{137} and the threshold of the Cu^{63} (γ, n) reaction.

[1] This and the other figures related to this experiment are those not used in the original paper [1].

2.1.2. Scattering Chamber

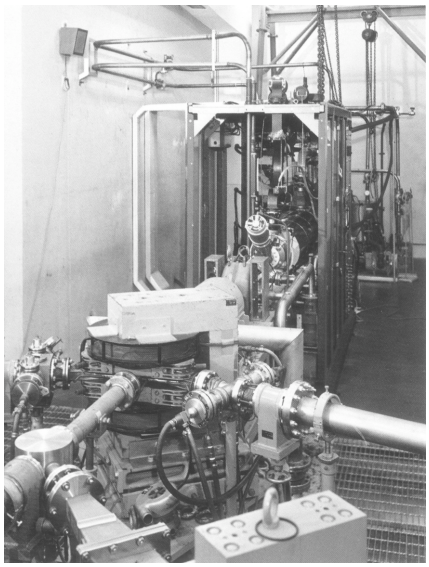

Figure 1. Linear electron accelerator (in the backward) and analyzing magnet (at the center). The analyzed electron beam goes into an experimental room through the pipe on the right. In the forward an energy-monitor system (not used in the experiment described here) is seen.

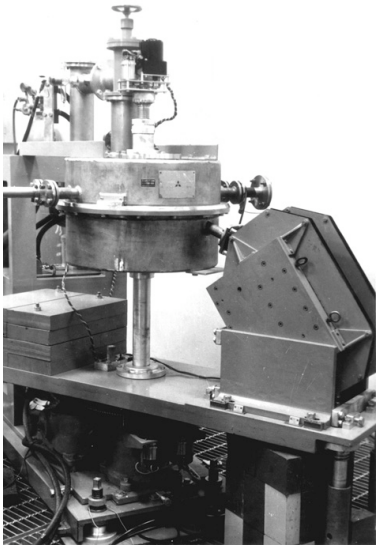

Figure 2. Scattering chamber. The electron beam comes into the chamber from left. The magnet on the right was not used in the experiment described here.

The scattering chamber consisted of a fixed lid and a cylindrical box, each 50 cm i.d. and 15 cm high and made of stainless steel. The measuring port is attached to the box with a dip of 20 deg from the horizontal plane. The box could be rotated by remote control of a drive motor under the preservation of the vacuum of the scattering chamber. The angular position θ_0 of the measuring port in the horizontal plane was indicated to 0.2 deg at the control panel. The scattering angle θ is given by:

$$\cos\theta = \cos(20\ \text{deg})\cos\theta_0 \qquad (1)$$

The vacuum in the scattering chamber was of the order of 10^{-3} Pa. After passing through a detector collimator and through a 3.5-mg/cm^2 Mylar window in the measuring port, the backscattered electrons entered an ionization chamber. The detector collimator was made of copper and had a conical taper matching the solid-angle cone subtended at the center of the target surface.

2.1.3. Targets and Target Assembly

The target was mounted on the supporting rod with a ring-shaped copper holder and a ceramic insulator, being placed perpendicular to the beam with the center of the incident surface at the center of the scattering chamber. When it was thinner than the maximum range of incident electrons (to measure the dependence of the backscattering coefficient on thickness), the target was backed with an aluminum Faraday cup having an entrance hole 11 mm in diameter and 35 mm in depth, as shown in Fig. 3. All the targets were of purity better than 99.5 %.

2.1.4. Ionization Chamber and Measurement

The ionization chamber was of the X-ray compensation type developed by Van de Graaff *et al*. [7]. The charge collector was an aluminum plate 60 mm in diameter and 30 mm thick, sandwiched between two sheets of aluminum foil 27 mg/cm^2 thick. The gap between the charge collector and each of the sheets was about 4 mm, being filled with air at atmospheric pressure. High voltages of opposite polarities applied to the foils reduced X-ray background.

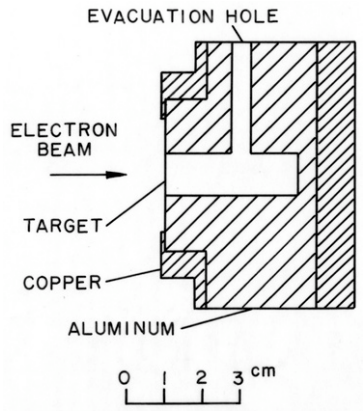

Figure 3. Target assembly for measuring dependence of backscattering coefficient on absorber thickness.

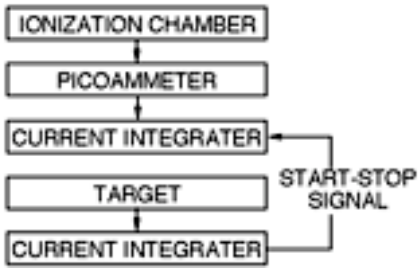

Figure 4. Block diagram of measurement.

A block diagram of measurement is given in Fig. 4. The current from the ionization chamber was amplified with a picoammeter and fed to a current integrator, while the target current was measured with another current integrator. The signal from the latter integrator controlled the simultaneous start and stop of measurement with the former integrator.

The multiplication factor f of the ionization chamber depends on the energy spectrum of backscattered electrons, but a simple assumption was made that it was determined as a function of average energy $E_{av}(E_0, Z)$ of backscattered electrons from the effectively semi-infinite target, where E_0 is the incident electron energy and Z is the atomic number of the target material. Values of $E_{av}(E_0, Z)$ were estimated by interpolation and extrapolation of the experimental results of Wright and Trump [8].

On the above assumption, the calibration of f was made from the ratio of fI_b obtained with the ionization chamber to I_b measured with a Faraday chamber for the absorber of a thick gold target. The Faraday chamber consisted of a brass chamber in which an aluminum collector of 60 mm in diameter and 30 mm thick was contained, and it was directly attached to the measuring port of the scattering chamber. A correction of Faraday chamber efficiency for backscattering and secondary emission from the collector was made, and ranged from 4.1 to 8.9 %.

2.1.5. Background

The X-ray background uncompensated in the ionization chamber was measured under each condition by closing a remotely controlled shutter in front of the ionization chamber, The shutter consisted of a copper plate 40 mm in diameter and 10 cm thick, and could prevent electrons from entering the ionization chamber. Smaller background of another type, mainly due to secondary electrons produced near the measuring port of the scattering chamber by bremsstrahlung X rays from the entrance collimator, was studied for each incident energy without the target. The total background was always highest at 160 deg where the ratio of background to signal was about 0.5–20 % depending on E_0 and Z.

When the Faraday chamber was used for calibration, the background was measured by inserting an aluminum plug 35 mm long in the detector collimator. The ratio of background to signal at 160 deg increased from 2 to 12 % with increasing energy.

2.1.6. Secondary Electrons

Values of the secondary emission coefficient δ were necessary for the correction of the target current I_t. These were measured with the aid of a ring-shaped electrode attached to the incident side of the target.

2.2. Errors

Possible sources of systematic errors and their values were as follows:

(1) The multiplication factor f of the ionization chamber, ± 2.9–8.1 % depending on E_0 and Z.

(2) The solid angle of detection, ± 1.8%.

(3) The secondary emission coefficient δ (due to the possible change of surface condition during bombardment with electron beams), ± 10%.

(4) The ionization chamber current $I_i(\theta)$ (due to a possible unmeasured background), ± 1%.

(5) The target current I_t (due to secondary emission from the target caused by bremsstrahlung, and re-backscattering of electrons from the walls of the scattering chamber to the target), ± 0.5%.

(6) The ratio $I_i(\theta)$ (due to the relative accuracy of the picoammeter and the current integrator), ± 1.5%.

Total errors in backscattering coefficients were 6.7–14 % depending on E_0 and Z, as shown in Tables I and II of the original paper [1]. The present review, made after forty years since the publication of the paper, has found no problems either in the experimental method or in the evaluation of errors. The backscattering coefficients obtained are shown in Figs. 5 and 6 by solid symbols.

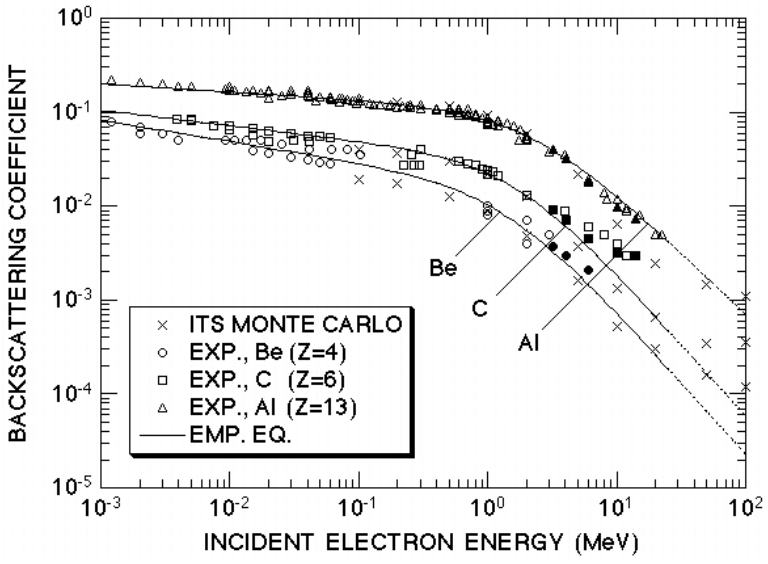

Figure 5. Comparison of compiled experimental back-scattering coefficients of electrons for Be, C and Al targets with ITS Monte Carlo results (cited from Ref. 4 with changes in symbols). Solid symbols show present author's experimental results [1].

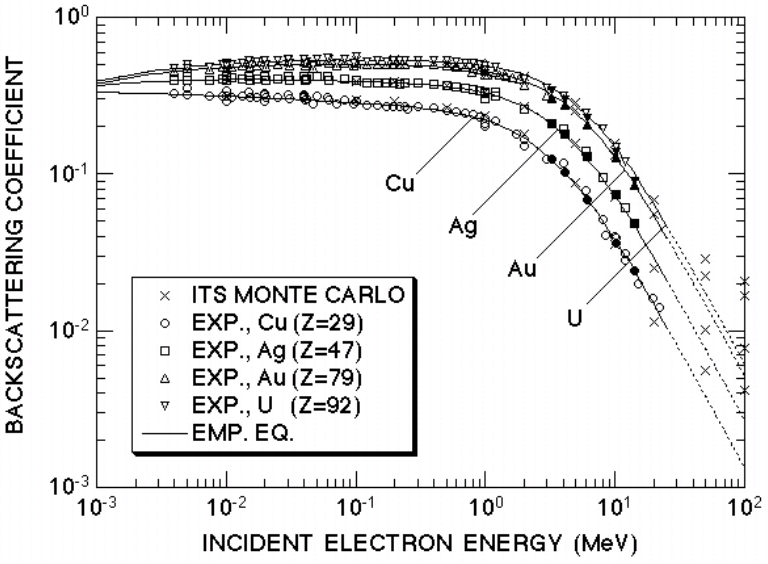

Figure 6. Comparison of compiled experimental back-scattering coefficients of electrons for Cu, Ag, Au and U targets with ITS Monte Carlo results (cited from Ref. 4 with changes in symbols). Solid symbols show present author's experimental results [1].

3. Cause of Discrepancies between Dressel's and Other Results

A little before the publication of the present author's experimental results, Dressel [2] reported the backscattering coefficients measured in the energy region from 0.5 to 10 MeV, and these were appreciably higher than previous authors' results. On the other hand, the present author's results were in agreement or consistent with the previous authors'. Therefore, the present author wrote in his paper [1] about possible causes of errors in Dressel's experiment. Among the four items written, the first one, i.e., the efficiency of the beam current monitor, had been rather close to the actual cause found later by Dressel [9], but had not been an entirely correct guess.

In Dressel's experiment, the electron beam was monitored by a pickup loop [10], which received an induced voltage pulse for each passage of an electron bunch. This monitor was placed at the upstream side of the last-stage collimator, which was located at the entrance of the scattering chamber. The diameter of the main beam was smaller than the hole of the collimator, but an unnoticed peripheral halo of electrons, which issued from collimators, was accompanying the main beam. While most of the halo electrons were incident on the target, the forward exit port of the scattering chamber, to which a Faraday cup was connected for calibrating the monitor, was too narrow to make all the halo electrons to pass through. Thus the number of electrons actually incident on the target was much larger than indicated by the monitor. Dressel did not notice the halo electrons earlier because of the following reason: These electrons had a broad distribution with a few percent of the current density of the main beam, and this density was below the background of his beam profile measurement, in which he used photographic film and Plexiglas.

4. Comparison of Experimental Data with ITS Monte Carlo Results

In 1971 the present author's group compiled experimental data on the backscattering coefficient of electrons, and made an empirical equation fitted to these [11]. Later they published a modified equation on the basis of an extended compilation [4, 12, 13], with which comparison was made of the Monte Carlo results (numerical data are given in Ref. 12) generated by ITS [3]. Figures 5 and 6, which show the comparison, have been taken from Ref. 4 with some changes in symbols. It can be seen that the ITS results agree rather well with experimental data except when the backscattering coefficient is considerably small, i.e., at 5 MeV for Be, at 10 MeV for C and at 10 and 20 MeV for Al (see Fig. 5). Another feature seen from these figures is this: Experimental data for Be, C and Al, as well as the ITS results for all absorbers studied, have the trend that the coefficient decreases slower than indicated by the empirical equation at high energies.

References

1) T. Tabata, Phys. Rev. **162**, 336 (1967).
2) R. W. Dressel, Phys. Rev. **144**, 332 (1966).
3) J. A. Halbleib, R. P. Kensek, T. A. Melhorn, G. Valdez, S. M. Seltzer and M. J. Berger, ITS Version 3.0: The Integrated TIGER Series of Coupled Electron/Photon Monte Carlo Transport Codes, Report SAND91-1634, Sandia Nat. Labs. (1992).
4) R. Ito, P. Andreo and T. Tabata, Radiat. Phys. Chem. **42**, 761 (1993).
5) T. Tabata, R. Ito, S. Okabe and Y. Fujita, Phys. Rev. B **3**, 572 (1971).
6) T. Tabata, P. Andreo, K. Shinoda and R. Ito, Nucl. Instr. Methods B **95**, 289 (1995).
7) R. J. Van de Graaff, W. W. Buechner and H. Feshbach, Phys. Rev. **69**, 452 (1955).
8) K. A. Wright and J. G. Trump, J. Appl. Phys. **33**, 687 (1962).
9) R. W. Dressel, Private communication (1968).
10) R. W. Dressel, Nucl. Instr. Methods **24**, 61 (1963).
11) T. Tabata, R. Ito and S. Okabe, Nucl. Instr. Methods **94**, 509 (1971).
12) R. Ito, P. Andreo, and T. Tabata, Bull. Univ. Osaka Pref. **41**, No. 2, 69 (1993).
13) T. Tabata, P. Andreo and K. Shinoda, Radiat. Phys. Chem. **54**, 11 (1999).
14) D. W. O. Rogers, Health Phys. **46**, 891 (1984).
15) P. Andreo and A. Brahme, Radiat. Res. **100**, 16 (1984).
16) D. W. O. Rogers and A. F. Bielajew, Trans. Am. Nucl. Soc. **52**, 380 (1986).
17) T. Tabata, P. Andreo and R. Ito, Nucl. Instr. Methods B **94**, 103 (1994).

Appendix

In this Appendix, the charge deposition profiles measured by the present author's group [5] are mentioned as another useful benchmark for Monte Carlo calculations. They used the same experimental system as described in Sec. 2 to measure the depth profiles of charge deposition in elemental materials produced by electrons of energies from 4.09 to 23.5 MeV (measurements at the highest energy were made with the linear accelerator of Kyoto University Research Reactor Institute). An absorber assembly was attached to the outside of the straight window of the scattering chamber, being insulated with Plexiglas plates. A thin collector, which was of the same material as the absorbers and put in an insulating sheath, was placed between the absorbers. Currents from the collector and the absorber assembly were respectively amplified with picoammeters, and then were fed to current integrators. Results obtained were given numerically in Ref. 5, in which comparisons were made with ETRAN Monte Carlo results of Berger and Seltzer obtained at slightly different energies. When the

comparisons were made in scaled coordinates of z/r_0 and $r_0 D_c$ (z denotes depth in the absorber; r_0, the continuous slowing-down approximation range of electrons; and D_c, charge deposition per unit depth[2]) agreement between the experimental data and the ETRAN results were good except for the absorber of Be. ETRAN showed deeper average penetration for Be than experimental results.

Rogers later found that ETRAN showed deeper penetration than EGS Monte Carlo results in the calculation for the depth–dose curves of 1- to 50-MeV electrons incident on a water phantom [14]. Using a mixed-procedure Monte-Carlo code, Andreo and Brahme [15] found a similar discrepancy between the depth–dose curves obtained by them and by ETRAN for the central-axis depth–dose curve for 20-MeVelectrons. Rogers and Bielajew [16] pointed out that the discrepancies were due to an error in the energy-loss straggling distribution used in ETRAN, i.e., the Landau distribution as modified by Blunck and Leisegang. Rogers and Bielajew wrote that because ETRAN had rightly been considered the definitive electron Monte Carlo transport code for over twenty years, their conclusions were somewhat surprising and demanded an answer to the question why this had not been *discovered* before. In fact, however, the present author's group had discovered the discrepancies 15 years before from the comparison of the charge deposition profiles for Be.

Then Berger and Seltzer corrected the error in the sampling of the energy-loss straggling distribution in ETRAN, and the corrected version of ETRAN was incorporated into ITS. The present author's group compared charge deposition profiles obtained by ITS as a byproduct of generating depth–dose curves with the earlier experimental results, and found that the discrepancies were removed [17]. To make better comparison, the present author's group accurately interpolated the experimental results and obtained benchmark data on the charge deposition profile as well as on the derived parameters of the extrapolated range, most probable depth of charge deposition and average depth of charge deposition [6]. Comparisons of the interpolated experimental data on charge deposition profile with the ITS results generally showed good agreement. However, very small but systematic discrepancies were observed for the Au absorber. These discrepancies are numerically clear in the comparison of the average depth of charge deposition as shown in Table 1. The reason for these discrepancies is yet to be found.

Table 1. Relative deviations of ITS results of average depth of charge deposition from experimental data (cited from Ref. 6).

Incident energy of electrons	Relative deviation of ITS results from experiment in %
5 MeV	−3.6
10 MeV	−1.8
20 MeV	−2.5
Error in experimental results	± 1.3

[2] These are the notations of our later paper [6]. In the original paper [5], x, L and y_0 were used.

Investigation of Electron Backscattering Experiments

Y. Kirihara, Y. Namito†, H. Hirayama†, M. Hagiwara†, H. Iwase†
The Graduate University for Advanced Studies, Oho1-1, Tsukuba, Ibaraki 305-0801, Japan
†*KEK High Energy Accelerator Research Organization, Oho1-1, Tsukuba, Ibaraki 305-0801, Japan*

Abstract

We have investigated eight typical experiments of electron backscattering, and have compared experimental data. Electron backscattering coefficients η were measured for a few keV to tens of MeV monoenergetic electrons on targets of Z=4 to 92 materials in the experiments. A Faraday cup, an ionization chamber, a silicon detector and an electron probe micro analyzer (EPMA) were used as a detector. In a few keV to hundreds keV, the experiment data had the difference within 22 %. The experiment data except Dressel's had the difference within 14 % for Al, Cu, Ag, Au and U target in a few to tens of MeV. In contrast, Dressel's data are significantly higher than other data.

1 Introduction

A lot of experiments of electron backscattering have been performed so far. We investigate eight experiments as shown in table 1. The purpose of this study is to compare the experimental data, and to obtain reliable data.

Table 1: Eight experiments of electron backscattering

No.	Auteur	Incident energy [MeV]	Target	Direction	Detector
1	Wright [1]	1.0∼3.0	Be,Mg,Al,Cu,Zn,Cd,Au,Pb,U	Whole backward	Calorimetry
2	Dressel [2]	0.68∼9.76	Be,C,Al,Cu,Sr,Mo,Ag,Ba,W, Pb,U	100∼180° (5 points)	Faraday cup
3	Tabata [3]	3.2∼14	Be,C,Al,Cu,Ag,Au,U	100∼160° (7 points)	Ionization chamber
4	Ebert [4]	4.0∼12.0	C,Al,Cu,Ag,Ta,U	Whole backward	Faraday cup
5	Rester [5]	1.0	Al,Fe,Sn,Au	102.5∼162.5° (8 points)	Silicon detector
6	Hunger [6]	0.004∼0.04	B,C,Mg,Si,Ti,V,Cr,Fe,Co,Ni, Cu,Zn,Ge,Zr,Ag,Cd,Sn,Sb, Te,Sm,Hf,Ta,W,Pt,Au,Bi,U	Whole backward	Electron probe micro analyzer (EPMA)
7	Neubert [7]	0.015∼0.06	Be,C,Al,Ti,Fe,Cu,Nb,Ag,Ta, Au,U	Whole backward	Faraday cup
8	Martin [8]	0.044∼0.124	Be,Si	Whole backward	Silicon detector

2 Experimental methods

2.1 Wright and Trump's experiment

Wright and Trump's experimental arrangement is shown in Fig. 1. Targets were irradiated by electron beams with the energy of 1∼3 MeV from a Vande de Graaff electrostatic accelerator. Nine materials (Be, Mg, Al, Cu, Zn, Cd, Au, Pb and U) were used for targets. Scattered electrons were obtained from measurements of collector currents which is covered over whole backward.

2.2 Dressel's experiment

Dressel's experimental arrangement is shown in Fig. 2. Targets in the cylindrical scattering chamber were irradiated by electron beams with the energy of 0.68∼9.76 MeV from LINAC. Eleven materials (Be, C, Al, Cu, Sr, Mo, Ag, Ba, W, Pb and U) were used for targets. Scattered electrons were measured using the faraday cup placed in backward (five points at $100 \sim 180°$).

2.3 Tabata's experiment

Tabata's experimental arrangement is shown in Fig. 3. Targets in the cylindrical scattering chamber were irradiated by electron beams with the energy of 3.2∼14 MeV from LINAC. Seven materials (Be, C, Al, Cu, Ag, Au and U) were used for targets. Background electrons from LINAC were well shielded by the wall between LINAC and the experiment room. Scattered electrons were measured using the ionization chamber placed in backward (seven points at $100 \sim 160°$). The accuracy of the measurement was improved by using the mean value measured on both sides.

2.4 Ebert, Lauzon and Lent's experiment

Ebert, Lauzon and Lent performed electron backscattering experiments using the target chamber as shown in Fig. 4. Targets were irradiated by electron beams with the energy of 4.0∼12.0 MeV from LINAC. Six materials (C, Al, Cu, Ag, Ta and U) were used for targets. Backscattered electrons were measured using the Faraday cup covered over whole backward.

2.5 Rester and Derrickson's experiment

Rester and Derrickson performed electron backscattering experiments using the Si(Li) detector placed in backward (eight points at $102.5 \sim 162.5°$). Targets were irradiated by electron beams with the energy of 1.0 MeV. Four materials (Al, Fe, Sn and Au) were used for targets.

2.6 Hunger and Küchler's experiment

Hunger and Küchler's experimental arrangement is shown in Fig. 5. Targets on copper holder were irradiated by electron beams with the energy of 4.0∼40 keV. Twenty-seven materials (B, C, Mg, Si, Ti, V, Cr, Fe, Co, Ni, Cu, Zn, Ge, Zr, Ag, Cd, Sn, Sb, Te, Sm, Hf, Ta, W, Pt, Au, Bi and U) were used for targets. Scattered electrons were pulled out by the positively biased nickel net, and electron absorbed by the graphite plate behind the net were measured.

2.7 Neubert and Ragaschewski's experiment

Neubert and Ragaschewski performed electron backscattering experiments using the faraday cup covered over whole backward. Targets were irradiated by electron beams with the energy of 15∼60 keV. Eleven materials (Be, C, Al, Ti, Fe, Cu, Nb, Ag, Ta, Au and U) were used for targets. Two targets of the same material were located at the center of a large target chamber. One target was under the incident beam and the other one was used to measure secondary electron and stray currents from the chamber walls.

2.8 Martin's experiment

Martin's experimental arrangement is shown in Fig. 6. Targets were irradiated by electron beams with the energy of 43.5∼124.0 keV from the electron gun. Two materials (Be and Si) were used for targets. Scattered electrons were measured using the silicon detector placed in backward (seven points at $100 \sim 160°$) In this experiments, two measurements of the integrate silicon detector and current integration were done. Of them, Integrate silicon detector values were shown in Fig. 7 (1).

2.9 Other experiment

Other experiment data were refered from Tabata (1971) [9], and numerical values in [10] [11] [12] [13] [14] [15] [16] were obtained in private communication with Tabata. We does not describe these experiment method in this paper. Details have the description in each literature.

3 Comparison of experiments and discussions

Electron backscattering coefficient η of experiments in Sec. 2 are shown in Fig. 7 (Be to Cu targets) and Fig. 8 (Ag to U targets). η increase with increasing an atomic number of the targets. In a few keV to hundreds of keV, the experiment data had the difference within 22 % (relative error). In hundreds of keV to tens of MeV, those data except Dressel's had the difference within 14 % for Al, Cu, Ag, Au and U target. In contrast, Dressel's data were about the twice as large as the other data. The cause of the disagreement was later explained by himself due to the halo of the beam, which was incident on the target but missed by the faraday cup to calibrate the beam monitor [17].

4 Conclusions

In this study, we investigated eight typical experiments of electron backscattering, and compared electron backscattering coefficient η including other experimental data. In a few keV $\sim$ 100 keV, the data had the difference of 22 %. In 1 MeV $\sim$ 14 MeV, the data except Dressel's had the difference of 14 % for Al, Cu, Ag, Au and U target.

References

[1] K. A. Wright and J. G. Trump, J. Appl. Phys. **31,** 1483 (1960).

[2] R. W. Dressel, Phys. Rev. **144,** 332 (1966).

[3] T. Tabata, Phys. Rev. **162,** 336 (1967).

[4] P. J. Ebert, A. F. Lauzon, and E. M. Lent, Phys. Rev. **183,** 422 (1969).

[5] D. H. Rester and J. H. Derrickson, Nucl. Inst. and Meth. **261,** 86 (1970).

[6] H. J. Hunger and L. Küchler, Phys. Stat. Sol. (a) **56,** K45 (1979).

[7] G. Neubert and S. Rogaschewski, Phys. Stat. Sol. (a) **59,** 35 (1980).

[8] J. W. Martin et al., Phys. Rev. C **68,** 055503 (1960).

[9] T. Tabata, R. Ito and S. Okabe, Nucl. Instr. Meth. **94,** 509-513 (1971).

[10] H. E. Bishop, Optique de Rayons X et Microanalyse, ed. R. Castaing, P. Deschamps and J. Philibert (Hermann, Paris, 1966) p. 153. (cited in [7]).

[11] I. M. Bronshtein and B. S. Fraiman, Soviet Phys. -Solid State **3,** 1188 (1961).

[12] I. M. Bronshtein and V. A. Dolinin, Soviet Phys. -Solid State **9,** 2133 (1968).

[13] V. E. Cosslett and R. N. Thomas, Brit. J. Appl. Phys. **16,** 779 (1965).

[14] D. Harder and G. Poschet, Phys. Letters **24B** 519 (1967).

[15] H. Kulenkampff and K. Rüttiger, Z. Physik **137** 426 (1954).

[16] H. Drescher, L. Reimer and H. Seidel, Z. Angew. Phys. **29,** (6) 331-6 (1970).

[17] T. Tabata, "Backscattering of Electrons from 3.2 to 14 MeV: Reflection of Experimental Method and Errors", In: *Proceedings of the Fourteenth EGS Users' Meeting in Japan*, KEK Proc. To be published.

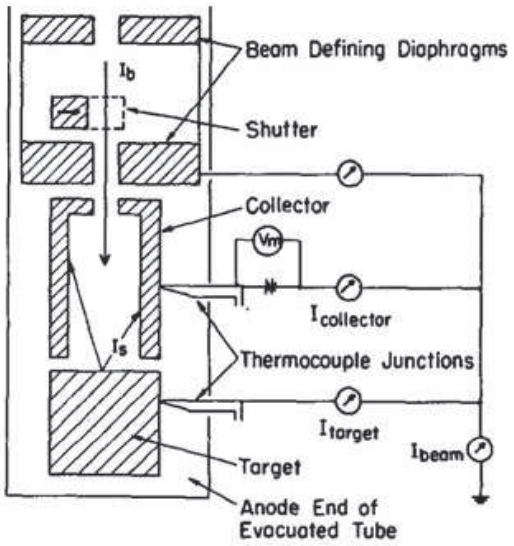

Figure 1: Wright and Trump's experimental arrangement [1]

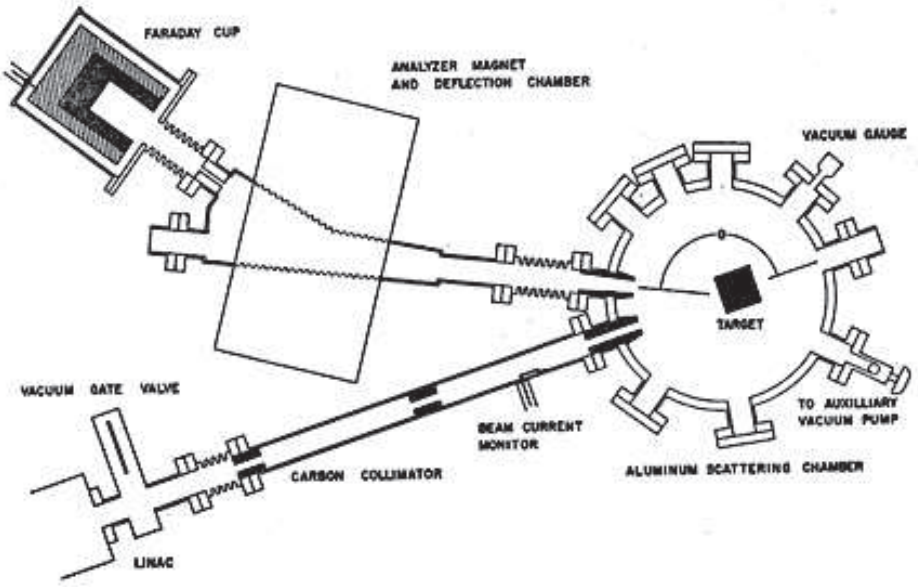

Figure 2: Dressel's experimental arrangement [2]

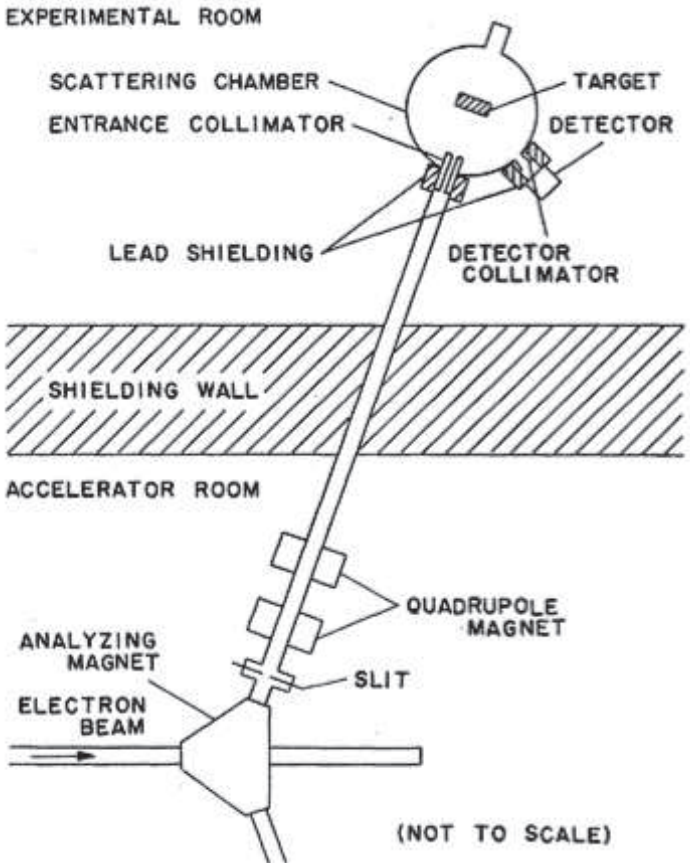

Figure 3: Tabata's experimental arrangement [3]

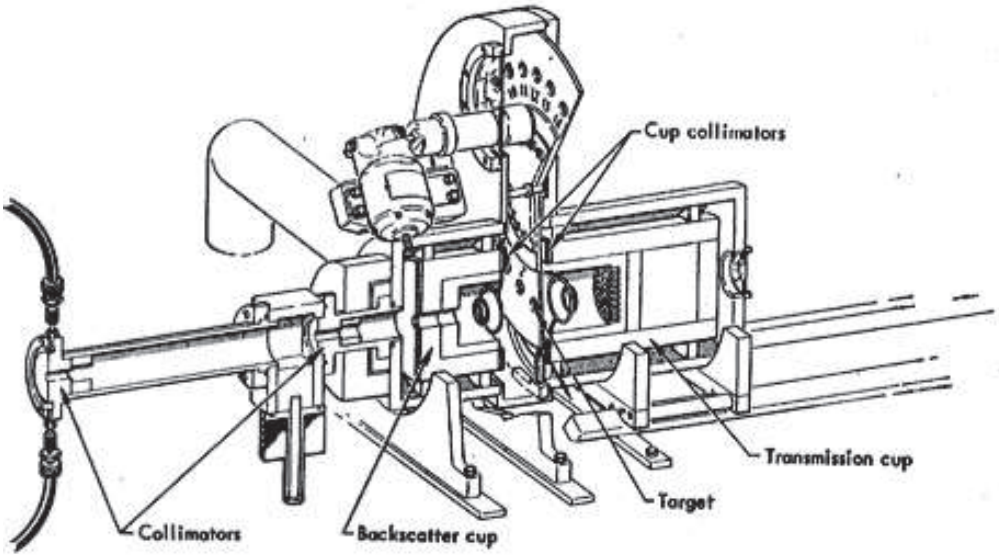

Figure 4: Ebert, Lauzon and Lent's experimental arrangement [4]

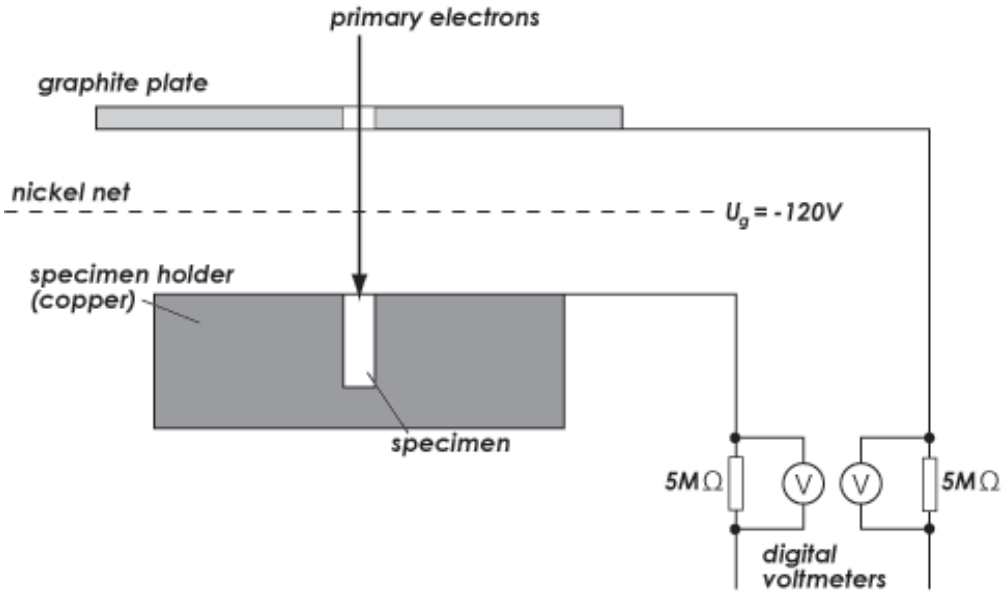

Figure 5: Hunger and Küchler's experimental arrangement [6]

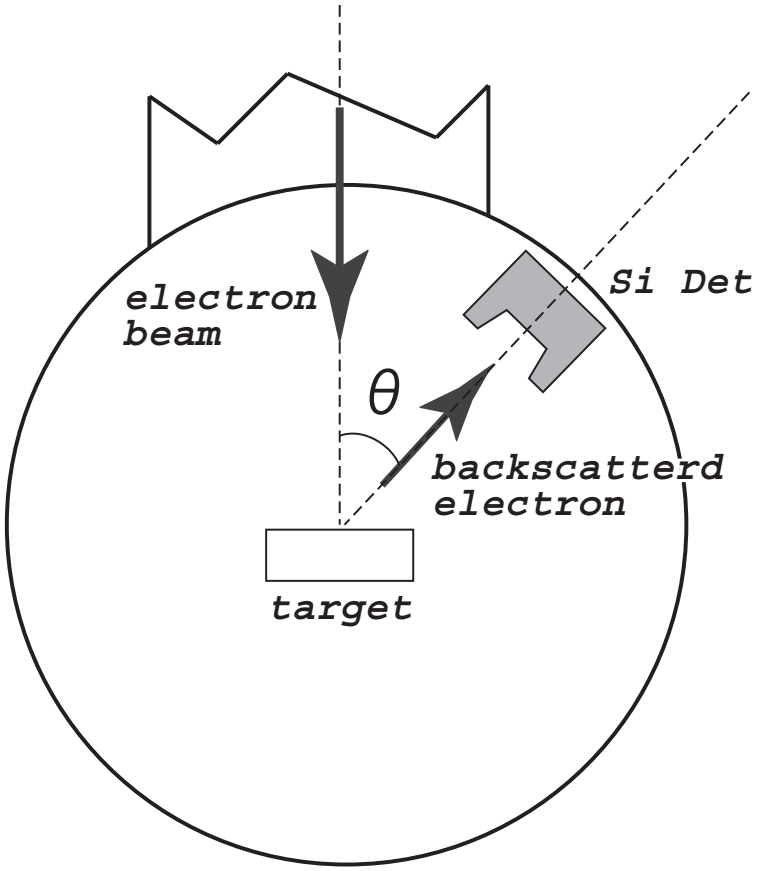

Figure 6: Martin's experimental arrangement [8]

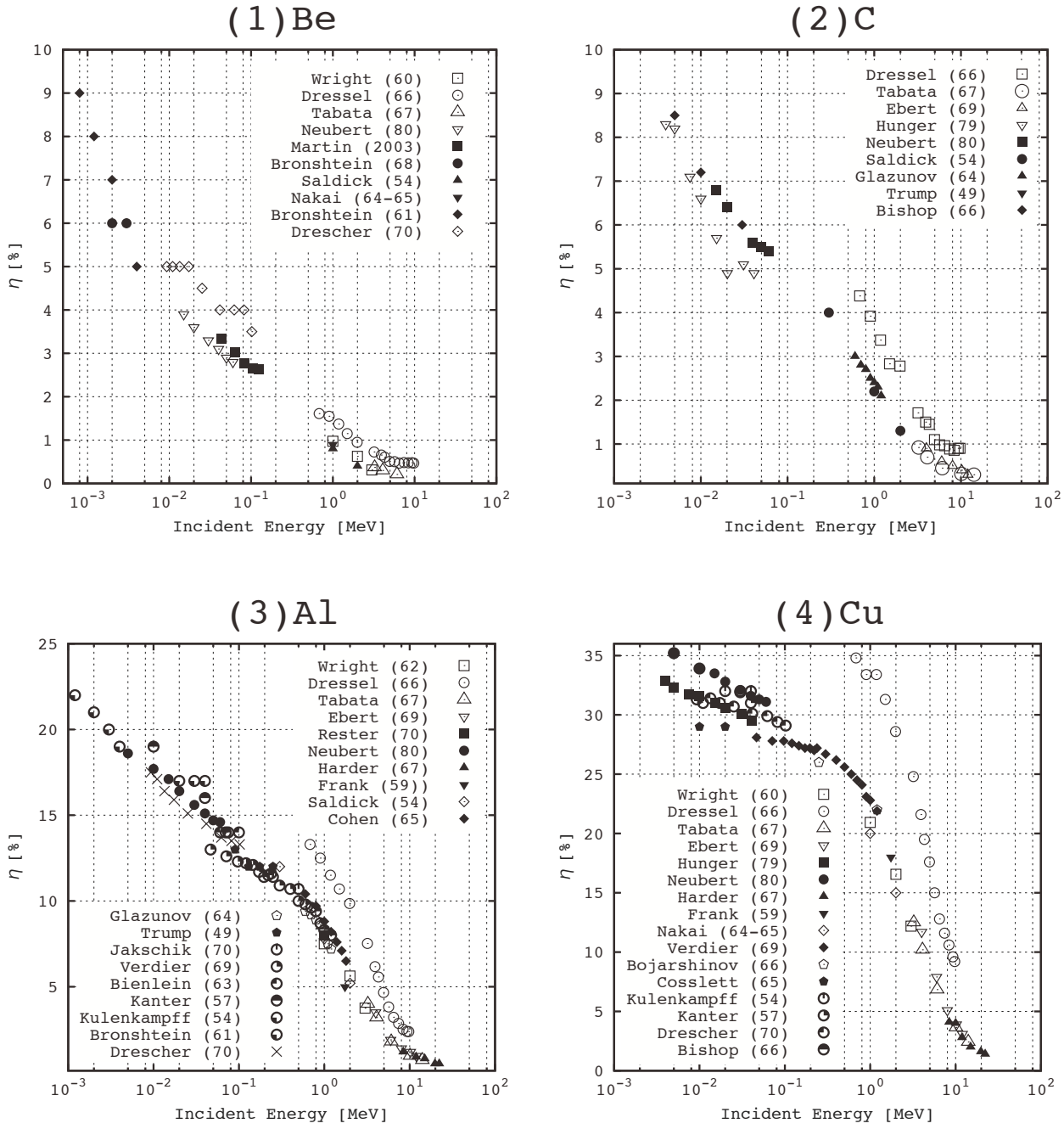

Figure 7: Electron backscattering coefficient η of (1) Be, (2) C, (3) Al and (4) Cu.

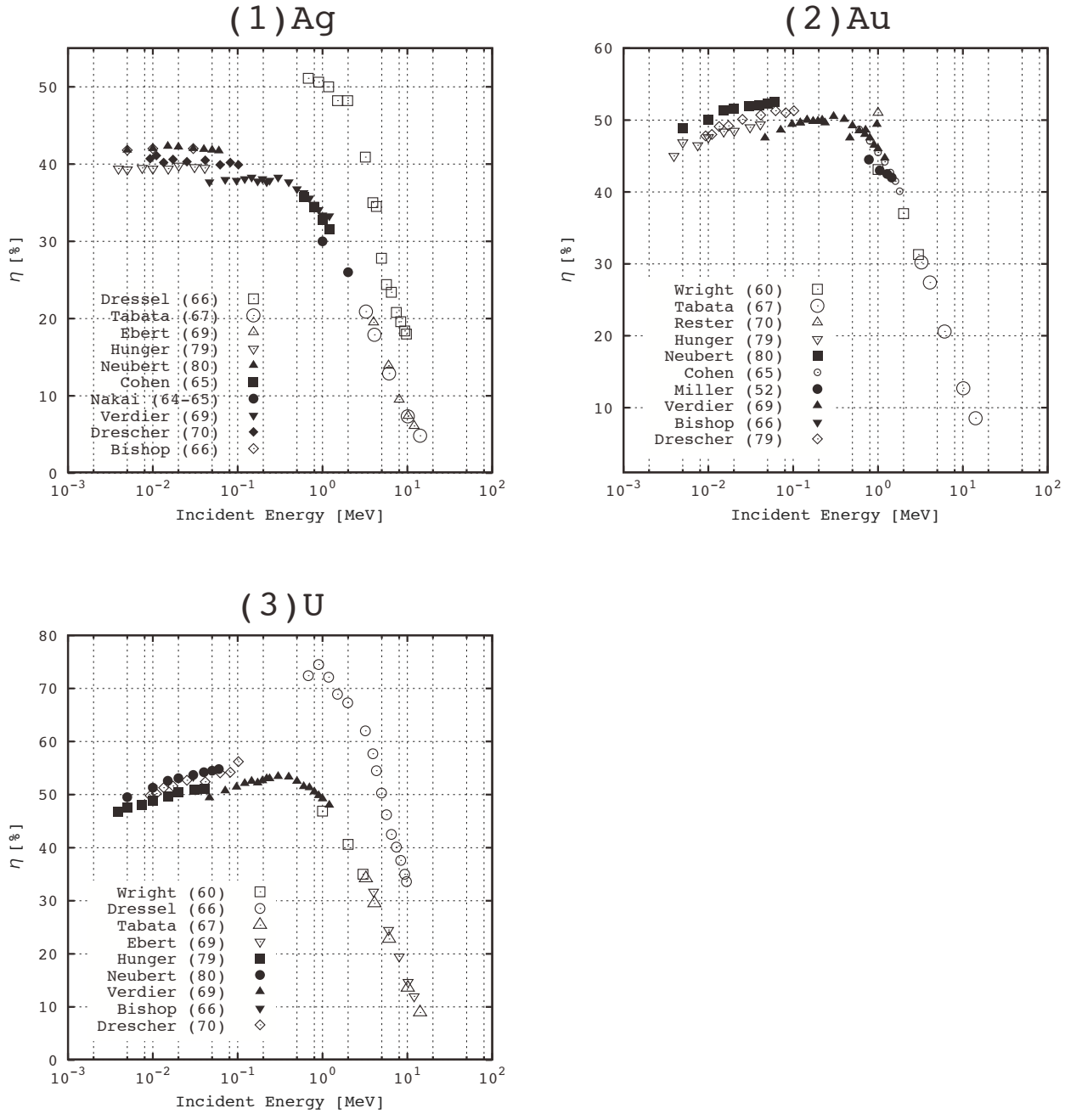

Figure 8: Electron backscattering coefficient η of (1) Ag, (2) Au and (3) U.

MOLIÈRE ANGULAR DISTRIBUTION EXPRESSED BY GOLDSTEIN SERIES AND ITS APPLICATIONS

T. Nakatsuka and K. Okei[†]

Okayama Shoka University, Okayama 700-8601, Japan

[†]*Dept. of Information Sciences, Kawasaki Medical School, Kurashiki 701-0192, Japan*

Abstract

Solution of Molière series function $f^{(n)}(\vartheta)$ of higher orders by Goldstein expansion is found for general n. Numerical results of $f^{(n)}(\vartheta)$ has become more reliable than ever, by Goldstein expansion than by numerical functional transforms or by analytical method using definite integrals, reducing ambiguities of convergence. Goldstein coefficients G_{ln} appearing in the expansion are tabulated. We reconfirm meaning and significance of Molière series functions of higher orders. Integral Molière angular distribution $F(\vartheta)$ is obtained using solution for Goldstein expansion, and applied on sampling of Molière angular distribution using Newton method.

1 Introduction

Molière theory of multiple Coulomb scattering [1, 2, 3] is accurate, reflecting the single scattering in the result, and efficient, showing very rapid convergence. So it is used widely in analyses of experiment concerning charged particles and tracing passage of charged particles in Monte Carlo simulations [4, 5, 6]. Usually the first three terms of Molière series $f^{(n)}(\vartheta)$ up to $n = 2$ are applied to derive the angular distribution [5]. Andreo et al. derived the Molière series functions of higher orders up to $n = 6$ for spatial angular distribution by numerical functional transforms [7], and we got the analytical solution of Molière series function of general higher orders for both the spatial and the projected angular distributions [8]. We investigate and clarify meanings and roles of the higher order terms of Molière series, quantitatively.

We compared our analytical results of Molière series function of higher orders up to $n = 6$ [8] with results from numerical functional transforms evaluated by ourselves. We confirmed good agreements between them. But we found some discrepancies in very rare times due to ill conditions of convergence. Numerical functional transforms has defects of integration of frequently oscillating function. On the other hand our analytical method has defects of difficult definite integration due to reduced accuracy by substitution of integrand of similar magnitude. To improve the reliability of numerical results of Molière series function, we examined the third method to derive the series functions of higher orders. Bethe reached to Goldstein solution of series expansion after examining various methods for reliable derivation [3]. Unfortunately Goldstein method was introduced only for $n = 2$ of $f^{(n)}(\vartheta)$, so we have attempted to obtain his solution for general n.

We can acquire the integrated Molière angular distribution, easily from Goldstein solution of series expansion. We applied the integrated Molière angular distribution on sampling of Molière angular distribution using Newton method. We could determine the objective angle in two or three recursions of correction.

2 Solution of Molière series function by Goldstein expansion

The probability densities of Molière spatial angular distribution $f(\vartheta)\vartheta d\vartheta$ and projected angular distribution $f_{\rm P}(\varphi)d\varphi$ are expressed as

$$f(\vartheta) = f^{(0)}(\vartheta) + B^{-1}f^{(1)}(\vartheta) + B^{-2}f^{(2)}(\vartheta) + \ldots, \tag{1}$$

$$f_{\rm P}(\varphi) = f_{\rm P}^{(0)}(\varphi) + B^{-1}f_{\rm P}^{(1)}(\varphi) + B^{-2}f_{\rm P}^{(2)}(\varphi) + \ldots, \tag{2}$$

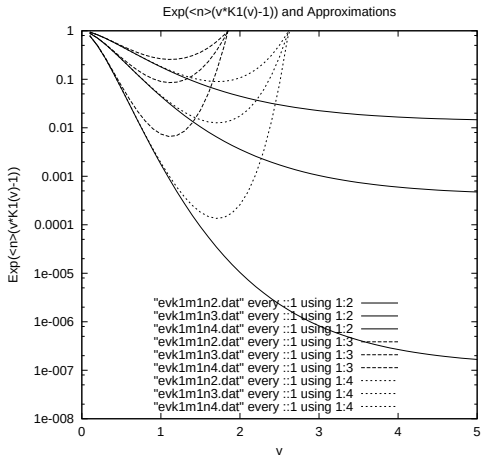

Figure 1: Frequency distributions at $B = 2, 3, 4$. Exact distribution (solid line) and approximated ones with the exponent expanded up to ζ^2 (dot line) and ζ^4 (thin dot line).

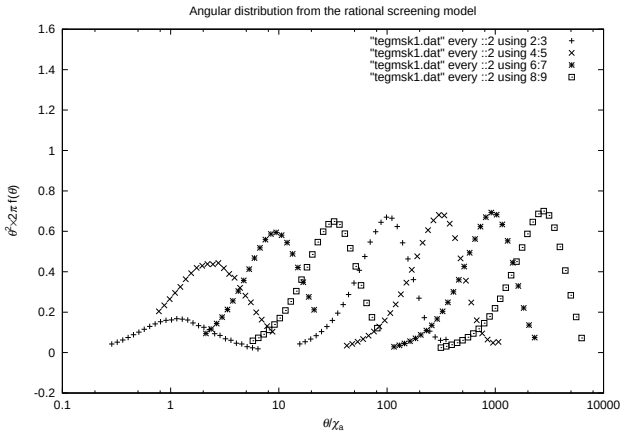

Figure 2: Variation of θ^2-weighted angular distribution at $t = e^{2j-2+2C}t_0$ with $j = 0, 1, 2, \cdots, 7$, from left to right.

where the angles ϑ and φ are spatial and projected angles measured by the scale angle $\theta_{\rm M}$, B denotes the expansion parameter [9], and

$$f^{(n)}(\vartheta) = \frac{1}{n!}\int_0^\infty y dy J_0(\vartheta y) e^{-\frac{y^2}{4}} \left(\frac{y^2}{4}\ln\frac{y^2}{4}\right)^n, \tag{3}$$

$$f_{\rm P}^{(n)}(\varphi) = \frac{2}{\sqrt{\pi}n!}\int_0^\infty dy \cos(\varphi y) e^{-\frac{y^2}{4}} \left(\frac{y^2}{4}\ln\frac{y^2}{4}\right)^n \tag{4}$$

denote Molière series function for spatial and projected distributions. Molière found analytical solutions of these series functions successively up to $n = 2$ [2]. We got the analytical solutions for general n ($n \geq 1$):

$$\begin{aligned} f^{(n)}(\vartheta) &= 2e^{-\vartheta^2}\frac{\Gamma^{(n)}(n+1)}{\Gamma(n+1)}\sum_{j=0}^{n} {}_nC_j(-\vartheta^2)^j/j! \\ &\quad + 2e^{-\vartheta^2}\int_0^1 \left\{\frac{(1-t)^n}{t^{n+1}}e^{\vartheta^2 t}\right\}^* \sum_{j=0}^{n-1} {}_nM_j \left(\ln\frac{t}{1-t}\right)^{n-1-j} dt, \end{aligned} \tag{5}$$

$$\begin{aligned} f_{\rm P}^{(n)}(\varphi) &= \frac{2}{\sqrt{\pi}}e^{-\varphi^2}\frac{\Gamma^{(n)}(n+1)}{\Gamma(n+1)}\sum_{j=0}^{n} {}_{n-\frac{1}{2}}C_{j-\frac{1}{2}}(-\varphi^2)^j/j! \\ &\quad + \frac{2}{\sqrt{\pi}}e^{-\varphi^2}\int_0^1 \left\{\frac{(1-t)^{n-\frac{1}{2}}}{t^{n+1}}e^{\varphi^2 t}\right\}^* \sum_{j=0}^{n-1} {}_nM_j \left(\ln\frac{t}{1-t}\right)^{n-1-j} dt, \end{aligned} \tag{6}$$

using definite integrals [8], where

$${}_nM_j \equiv {}_nC_{j+1}(-)^j \sum_{k=0}^{[j/2]} {}_{j+1}C_{2k+1}\frac{\Gamma^{(j-2k)}(n+1)}{\Gamma(n+1)}(-\pi^2)^k, \tag{7}$$

and the function $g^*(t)$ denotes the function $g(t)$ with principal part or terms of negative power removed [8].

Goldstein indicated the solution for series function in power series for spatial distribution of $n = 2$ [3]. We find Goldstein solution for general n, for spatial and projected distributions. Putting $x \equiv \vartheta^2$ and $y \equiv \varphi^2$, we have

$$\begin{aligned}
\left\{\frac{(1-t)^n}{t^{n+1}}e^{xt}\right\}^* &= \frac{1}{t^{n+1}}\sum_{k=0}^{n} {}_nC_k(-t)^k \sum_{l=n+1-k}^{\infty}\frac{1}{l!}x^l t^l \\
&= \sum_{l=0}^{\infty} t^l \sum_{k=0}^{n} {}_nC_k \frac{(-)^k x^{n+l+1-k}}{(n+l+1-k)!}, \qquad (8) \\
\left\{\frac{(1-t)^{n-\frac{1}{2}}}{t^{n+1}}e^{yt}\right\}^* &= \frac{1}{t^{n+1}}\sum_{k=0}^{n} {}_{n-\frac{1}{2}}C_k(-t)^k \sum_{l=n+1-k}^{\infty}\frac{1}{l!}y^l t^l \\
&= \sum_{l=0}^{\infty} t^l \sum_{k=0}^{\infty} {}_{n-\frac{1}{2}}C_k \frac{(-)^k y^{n+l+1-k}}{(n+l+1-k)!}, \qquad (9)
\end{aligned}$$

so definite integrals I_n and J_n in Eqs. (5) and (6), respectively, can be expressed in power series as

$$\begin{aligned}
I_n &= \sum_{k=0}^{\infty} {}_nC_k(-)^k \sum_{l=0}^{\infty}\frac{x^{n+l+1-k}}{(n+l+1-k)!}\sum_{j=0}^{n-1} Q_{lj}\ {}_nM_{n-1-j} \\
&= \sum_{l=0}^{\infty} G_{ln} \sum_{k=0}^{n} {}_nC_k \frac{(-)^k x^{n+l+1-k}}{(n+l+1-k)!}, \qquad (10) \\
J_n &= \sum_{k=0}^{\infty} {}_{n-\frac{1}{2}}C_k(-)^k \sum_{l=0}^{\infty}\frac{y^{n+l+1-k}}{(n+l+1-k)!}\sum_{j=0}^{n-1} Q_{lj}\ {}_nM_{n-1-j} \\
&= \sum_{l=0}^{\infty} G_{ln} \sum_{k=0}^{n+1+l} {}_{n-\frac{1}{2}}C_k \frac{(-)^k y^{n+l+1-k}}{(n+l+1-k)!}, \qquad (11)
\end{aligned}$$

thus we have the Goldstein expansion for the Molière series of higher orders,

$$f^{(n)}(\vartheta) = 2e^{-x}\left\{\frac{\Gamma^{(n)}(n+1)}{\Gamma(n+1)}\sum_{j=0}^{n} {}_nC_{n-j}\frac{(-x)^j}{j!} + \sum_{l=0}^{\infty} G_{ln}\sum_{k=0}^{n} {}_nC_k\frac{(-)^k x^{n+l+1-k}}{(n+l+1-k)!}\right\}, \qquad (12)$$

$$f_{\mathrm{P}}^{(n)}(\varphi) = \frac{2}{\sqrt{\pi}}e^{-y}\left\{\frac{\Gamma^{(n)}(n+1)}{\Gamma(n+1)}\sum_{j=0}^{n} {}_{n-\frac{1}{2}}C_{n-j}\frac{(-y)^j}{j!} + \sum_{l=0}^{\infty} G_{ln}\sum_{k=0}^{n+1+l} {}_{n-\frac{1}{2}}C_k\frac{(-)^k y^{n+l+1-k}}{(n+l+1-k)!}\right\}, \qquad (13)$$

where

$$Q_{lj} \equiv \int_0^1 t^l \left(\ln\frac{t}{1-t}\right)^j dt, \quad \text{and} \quad G_{ln} \equiv \sum_{j=0}^{n-1} Q_{lj}\ {}_nM_{n-1-j}. \qquad (14)$$

Especially at $n = 2$, we have Goldstein's result [3]

$$G_{l2} = \frac{2}{l+1}[\psi(l+1) + C - \psi(3)]. \qquad (15)$$

Goldstein coefficients G_{ln} are tabulated in Table 2.

3 Importance of Molière series function of the higher orders

We investigate the meaning and the role of Molière series of the higher orders.

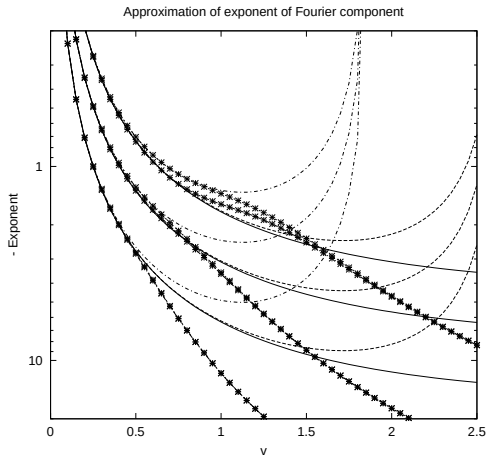

Figure 3: Comparison of Molière series expansion expressed as $-\ln(2\pi\tilde{f})$ for $B = 2, 3, 4$ (from top to bottom). Curve moves downward when we take account the term of the 4-th power in the exponent (28). Solid lines show Fourier frequency distribution with exact solution (20), and thin lines show those with the exponent taken up to the 2-nd power (broken line) and up to the 4-th power (dot line).

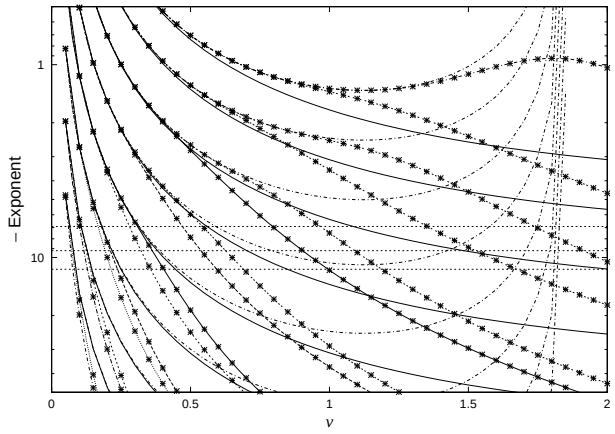

Figure 4: Comparison of Molière series expansion expressed as $-\ln(2\pi\tilde{f})$ for $B = 2, 3, \cdots, 9$ (from top to bottom). The curves with the first 7 terms move upward from those with the first 3 terms. Solid lines show Fourier frequency distribution with exact solution (20), and thin lines show those with exponent taken up to the 2-nd power (29). Horizontal lines corresponds to 10^{-3}, 10^{-4}, and 10^{-5} level of $1/(2\pi)$.

3.1 The single scattering cross-section with the rational-type screening model and the diffusion equation

We start from the single scattering cross-section with the rational-type screening model:

$$\frac{N}{A}\sigma(\chi)2\pi\chi d\chi dx = \frac{1}{\pi\Omega}\frac{K^2}{E^2}\frac{1}{(\chi^2+\chi_{\rm a}^2)^2}2\pi\chi d\chi dt, \tag{16}$$

where

$$\chi_{\rm a}^2 = \frac{K^2}{E^2}e^{-\Omega+1-2C}. \tag{17}$$

Then the diffusion equation for the angular distribution $f(\theta,t)2\pi\theta d\theta$ becomes

$$\frac{d}{dx}\,f(\vec{\theta},x) = \frac{N}{A}\iint\{f(\vec{\theta}-\vec{\theta}',x)-f(\vec{\theta},x)\}\sigma(\vec{\theta}')d\vec{\theta}'. \tag{18}$$

Applying Fourier transforms, we have

$$\frac{d}{dt}\ln 2\pi\tilde{f}(\vec{\zeta},t) = \frac{1}{\pi\Omega}\frac{K^2}{E^2}\int_0^\infty\frac{J_0(\zeta\chi)-1}{(\chi^2+\chi_{\rm a}^2)^2}2\pi\chi d\chi = \frac{K^2/E^2}{\Omega\chi_{\rm a}^2}[\chi_{\rm a}\zeta K_1(\chi_{\rm a}\zeta)-1], \tag{19}$$

so under the fixed-energy condition, we have the exact solution for the angular distribution in the Fourier frequency space [10, 11, 12] as

$$\tilde{f}(\zeta,t) = \frac{1}{2\pi}\exp\left\{\frac{t}{t_0}[\chi_{\rm a}\zeta K_1(\chi_{\rm a}\zeta)-1]\right\}, \tag{20}$$

where t_0 denotes the mean free path of the screened single scattering,

$$t_0 = \Omega e^{-\Omega+1-2C}, \tag{21}$$

and K_1 is modified Bessel function of the first order [13].

We investigate the meaning of the solution (20). Expanding the Eq. (20), we have

$$\begin{aligned} \tilde{f}(\zeta,t) &= \frac{1}{2\pi} e^{-\frac{t}{t_0}} \exp\left\{ \frac{t}{t_0} v K_1(v) \right\} \\ &= \frac{1}{2\pi} e^{-\frac{t}{t_0}} \sum_{k=0}^{\infty} \frac{1}{k!} \left(\frac{t}{t_0} \right)^k \{ v K_1(v) \}^k , \end{aligned} \tag{22}$$

where we introduced

$$v \equiv \chi_{\rm a} \zeta. \tag{23}$$

The first term of the summation is a constant, which turns to the δ-function diverging at $\vec{\theta} = 0$, corresponding to the survival probability of the incident charged particle. The second term $\chi_{\rm a}\zeta K_1(\chi_{\rm a}\zeta)$ shows the Fourier transforms of the screened single scattering (16), so that the terms $\{\chi_{\rm a}\zeta K_1(\chi_{\rm a}\zeta)\}^k$ of $k \geq 2$ show the angular distribution for the k-times folded angular distribution of the screened single scattering (16). So we understand the solution of (20) shows the Poisson mean distribution of the k-times folded angular distribution of the screened single scattering, as known as the Wentzel summation method [11].

3.2 Change of angular distribution from single, plural, to multiple scattering

The solution $\tilde{f}(\zeta,t)$ of (20) is a decreasing function of ζ, decreasing from $\frac{1}{2\pi}$ to $\frac{1}{2\pi}e^{-t/t_0}$ at ζ from 0 to ∞, as indicated in Fig. 1. The limiting value at $\zeta \to \infty$ corresponds to the survival probability of incident particle and gives δ-function at $\theta = 0$.

We derived angular distribution $f(\theta,t)2\pi\theta d\theta$ by applying numerical Fourier transforms [8] on Eq. (20) as Andreo et al. did [7]:

$$\theta^2 \times 2\pi f(\theta,t) = \left(\frac{\theta}{\chi_{\rm a}} \right)^2 \int_0^{\infty} v J_0((\theta/\chi_{\rm a})v) \left\{ \exp\left(\frac{t}{t_0}[vK_1(v) - 1] \right) - e^{-t/t_0} \right\} dv, \tag{24}$$

where we subtracted e^{-t/t_0} from Eq. (20) to separate the above δ-function from the angular distribution. We show the results in Fig. 2 for traversed thickness of

$$t = e^{2j-1}\Omega e^{-\Omega} = e^{2j-2+2C} t_0 \qquad (j = 0, 1, 2, \cdots, 7). \tag{25}$$

Ordinate shows the probability density multiplied by θ^2 and abscissa is taken in logarithmic scale, then the area enclosed by the curve shows the value proportional to the probability excluding the survival probability, $1 - e^{-t/t_0}$. We find in Fig. 2 clearly that the angular distribution starts with the single scattering at very thin thickness and θ^2-weighted angular distribution gradually moves to larger angle with increase of traversed thickness.

3.3 Meaning of the Molière series expansion

We examine property of the exponent of Eq. (20) quantitatively. We introduce a new variable $u \equiv \theta_{\rm M}\zeta$. As it satisfies

$$t/t_0 = (1/B)e^{B-1+2C}, \tag{26}$$

so we have

$$u \equiv \theta_{\rm M}\zeta = \sqrt{Bt/t_0}\chi_{\rm a}\zeta = \sqrt{e^{B-1+2C}}\chi_{\rm a}\zeta. \tag{27}$$

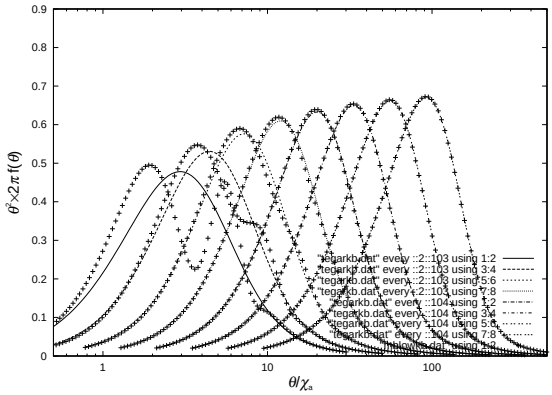

Figure 5: Molière angular distributions with the first 3 terms for $B = 2, 3, \cdots, 9$ from left to right. Solid lines show the exact distributions (24),

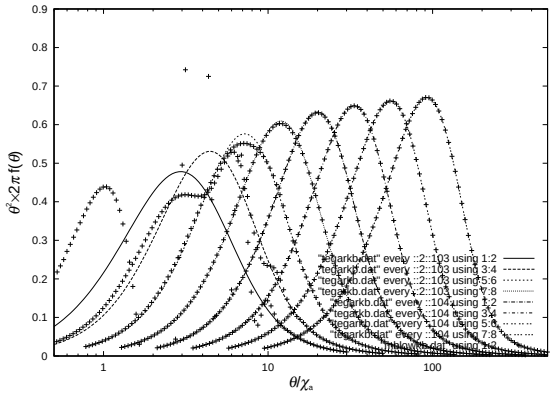

Figure 6: Molière angular distributions with the first 7 terms for $B = 2, 3, \cdots, 9$ from left to right. Solid lines show the exact distributions (24),

Then we can expand the exponent of Eq. (20) as

$$-\ln\left\{2\pi\tilde{f}(\zeta,t)\right\} = \frac{u^2}{4}\left[1-\frac{1}{B}\ln\frac{u^2}{4}\right] + \frac{e^{-B+1-2C}}{2}\left(\frac{u^2}{4}\right)^2\left[1-\frac{1}{B}\ln\frac{u^2}{4e^{3/2}}\right], \tag{28}$$

up to the 4-th power of u with coefficients including logarithmic terms [13, 7, 12]. Approximated Fourier-frequency distributions expressed with the exponent of (20) expanded up to u^2 and u^4 are indicated in Fig. 1.

Molière approximated the frequency distribution by taking the exponent up to u^2 term with the logarithmic coefficient,

$$\tilde{f}(\zeta,t) \simeq \frac{1}{2\pi}\exp\left\{-\frac{u^2}{4}\left[1-\frac{1}{B}\ln\frac{u^2}{4}\right]\right\}, \tag{29}$$

and expanded the exponential function, separating the gaussian factor of $e^{-u^2/4}$:

$$\tilde{f}(\zeta,t) \simeq \frac{1}{2\pi}\exp\left\{-\frac{u^2}{4}\right\}\sum_{k=0}^{\infty}\frac{1}{k!}\left(\frac{1}{B}\frac{u^2}{4}\ln\frac{u^2}{4}\right)^k. \tag{30}$$

We call ordinarily the Eq. (30) as the Molière expansion and we get the angular distribution by applying inverse Fourier transforms term by term. Molière got the results of inverse transforms up to the third term ($k = 0, 1, 2$), and usually we use the angular distribution with the first three terms as Molière distribution.

The Molière expansion (30) up to $k = 2$ contains the term of u^4 other than gaussian factor of $e^{-u^2/4}$. We should remind the exact frequency distribution (20) has another u^4 term in the exponent, as indicated in Eq. (28). So we have the exact expansion up to the u^4 term as

$$\tilde{f}(\zeta,t) \simeq \frac{1}{2\pi}\exp\left\{-\frac{u^2}{4}\right\}\left\{\sum_{k=0}^{2}\frac{1}{k!}\left(\frac{1}{B}\frac{u^2}{4}\ln\frac{u^2}{4}\right)^k - \frac{e^{-B+1-2C}}{2}\left(\frac{u^2}{4}\right)^2\left[1-\frac{1}{B}\ln\frac{u^2}{4e^{3/2}}\right]\right\}. \tag{31}$$

Additive angular distributions can be easily calculated by using generalized Molière series function of $f_1^{(2)}(\vartheta)$ and $f_2^{(2)}(\vartheta)$ [14]. We compare in Fig. 3 the frequency distribution (31) with Molière expansion (30) up to $k = 2$, for $B = 2, 3$ and 4. Contribution of u^4-term in the exponent moves the curve downward and gives higher accuracy, though contribution becomes small at about $B > 4$ due to the decreasing coefficient of $e^{-B+1-2C}$.

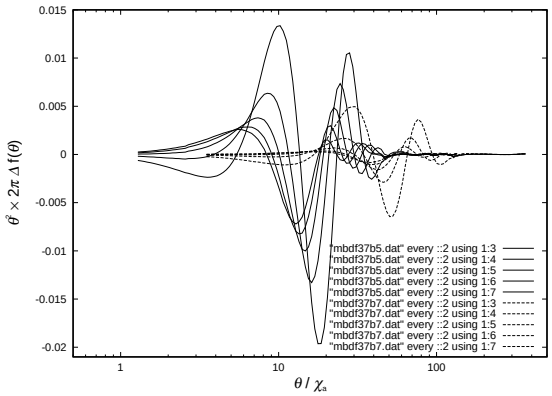

Figure 7: Decrease of the deviation of Molière angular distribution from the exact one with increase of the degree of higher term ($n = 2, 3, \cdots, 6$), for $B = 5$ (solid line) and $B = 7$ (dot line).

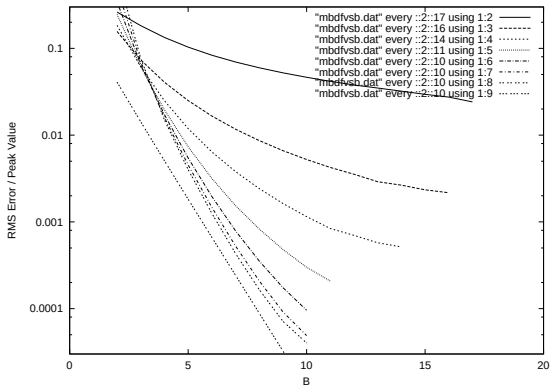

Figure 8: Decrease of the deviation of Molière angular distribution from the exact one with increase of B, for the degrees of higher term ($n = 0, 1, \cdots, 6$ from top to bottom). The line of far bottom indicates the contribution from the 4-th power term in the exponent (28).

3.4 Significance of Molière series of the higher orders

Molière expansion with the first 3 terms gives good angular distribution at B of large value, although accuracy decreases with decrease of B and it begins to oscillate at B of very small value due to the lack of Fourier components of the higher order [15, 16]. We want to confirm these facts visually in real angular space and in Fourier frequency space.

Let $f_{\rm n}(\vartheta)$ be the Molière expansion of angular distribution up to the n-th power of $\frac{1}{B}$,

$$f_{\rm n}(\vartheta) = \sum_{k=0}^{n} B^{-k} f^{(k)}(\vartheta). \tag{32}$$

We compare in Fig. 5 the first three terms of Molière expansion, $f_2(\vartheta)$, with the exact angular distribution derived by (24), where step size Δv of the numerical integration by trapezoidal method is about 0.001 for $B = 2, 3, \cdots, 7$, and 0.0005 for $B = 8, 9$. So accuracy of numerical integration in deriving the exact angular distribution is estimated as $\Delta I \simeq 10^{-8}$ from Takahasi-Mori theory of error estimation [17, 8]. We see good agreement at $B > 8$ and disagreement at $B < 5$. On the other hand we compare in Fig. 6 the first seven terms, $f_6(\vartheta)$, with the exact angular distribution. They agree well at $B > 6$ and not well at $B < 4$. So we find available region of Molière expansion in B is extended by using series terms of higher orders.

We discuss the accuracy of the Molière expansion in the Fourier frequency space. Let $\tilde{f}_{\rm n}(u)$ be the Molière expansion (30) up to the n-th power,

$$2\pi \tilde{f}_{\rm n}(u) = \exp\left\{-\frac{u^2}{4}\right\} \sum_{k=0}^{n} \frac{1}{k!} \left(\frac{1}{B}\frac{u^2}{4} \ln \frac{u^2}{4}\right)^k. \tag{33}$$

The exponent of the right-hand side of Eq. (20) decreases monotonously from 0 to $-t/t_0$ along with increase of ζ from 0 to ∞. So we plot in Fig. 4 $-\ln(2\pi\tilde{f})$ for the exact frequency distribution (solid line) of (20) and the approximated distribution (29) with the exponent taken up to u^2 (dot line) against $v \equiv \chi_{\rm a}\zeta$, for B from 2 to 9. And we compare $-\ln(2\pi\tilde{f}_2(u))$ and $-\ln(2\pi\tilde{f}_6(u))$ by plotting them in Fig. 4 (line with dots). $\tilde{f}_6(u)$ locates upward agreeing better with (29). We find $\tilde{f}_2$ deviates much from exact $\tilde{f}$ at $B < 7$, though $\tilde{f}_6$ agrees well with exact $\tilde{f}$ at $B > 5$.

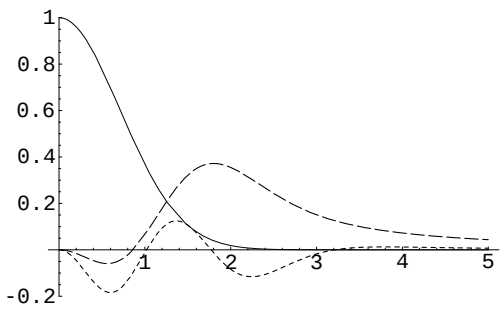

Figure 9: Integrated Molière terms, $F^{(0)}(\vartheta)$ (solid line), $F^{(1)}(\vartheta)$ (broken line), and $F^{(2)}(\vartheta)$ (dot line).

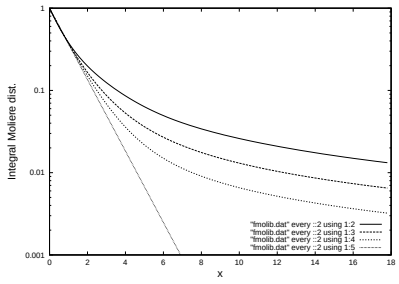

Figure 10: Integrated Molière angular distribution for $B = 5, 10, 20$ and infinity (thin line).

How accuracy increases with increase of Molière series term of the higher order? We indicate in Fig. 7 difference between $f_{\rm n}(\vartheta)$ with $n = 2, 3, \cdots, 6$ and the exact distribution (24) at $B = 5$ (solid line) and $B = 7$ (dot line). As we saw in Fig. 5, maximum value of $\vartheta^2 \times 2\pi f(\vartheta)$ was about 0.6, so we find applicable region of f_2 (the first 3 Molière terms) is $B > 7$ instead that of f_6 (the first 7 Molière terms) is extended to $B > 5$ under the accuracy of 10^{-3}.

Then how many terms of the higher order are necessary for required accuracy of angular distribution? We define the expected error by the root-mean-square difference of $\vartheta^2 \times 2\pi f(\vartheta)$ between $f_{\rm n}(\vartheta)$ and the exact distribution (24), as indicated in Figs. 5 and 6, at first 80 points among 100 equally divided steps of ϑ in logarithmic scale between 0.1 and 10.0. We indicate in Fig. 8 change of the expected error against B for $n = 0, 1, 2, \cdots, 6$, by the fractional error to the maximum value of $\vartheta^2 \times 2\pi f(\vartheta)$. The error decreases with increase of n, and the error decreases with increase of B. We find in this figure, applicable region is $B \geq 10$ for usual Molière series of the first three terms, f_2, and the first six terms or more of Molière series, $f_{\rm n}$ with $n \geq 5$, are required for $B = 6$ under the permission of fractional error of 10^{-3}. We also indicated in Fig. 8 the contribution of u^4-term in the exponent (28) (far bottom). We find the contribution is negligible compared with our expansion up to $n = 6$.

4 Integrated Molière spatial angular distribution

We derive integrated Molière spatial angular distribution from Goldstein solution for the Molière series of higher orders (12):

$$\begin{aligned} F(\vartheta) &\equiv \int_\vartheta^\infty f(\vartheta)\vartheta d\vartheta = \frac{1}{2}\int_x^\infty f(\vartheta)dx \\ &= F^{(0)}(\vartheta) + B^{-1}F^{(1)}(\vartheta) + B^{-2}F^{(2)}(\vartheta) + \cdots . \end{aligned} \tag{34}$$

$F^{(n)}(\vartheta)$ for $n \geq 1$ is expressed as

$$F^{(n)}(\vartheta) = e^{-x}\left\{ \frac{\Gamma^{(n)}(n+1)}{\Gamma(n+1)} \sum_{k=1}^{n} \frac{x^k}{k!} \sum_{j=k}^{n} {}_nC_j(-)^j + \sum_{l=0}^{\infty} G_{ln} \sum_{k=l+2}^{n+l+1} \frac{x^k}{k!} \sum_{j=0}^{n+l+1-k} {}_nC_j(-)^j \right\}. \tag{35}$$

The results for $n = 0$, 1, and 2 are practically expressed as and agree with

$$F^{(0)}(\vartheta) = e^{-x}, \tag{36}$$

$$\begin{aligned} F^{(1)}(\vartheta) &= \left\{ \gamma - 1 + \int_0^x \frac{e^x - 1 - x}{x^2} dx \right\} xe^{-x} \\ &= e^{-x} - 1 + \{E_i(x) - \ln x\} xe^{-x}, \end{aligned} \tag{37}$$

$$F^{(2)}(\vartheta) = \{\psi'(3) + \psi(3)^2\} \left\{ \frac{x}{2} - 1 \right\} xe^{-x}$$

Table 1: Counts of correction before convergence.

B	$\xi = .1$	$\xi = .2$	$\xi = .3$	$\xi = .4$	$\xi = .5$	$\xi = .6$	$\xi = .7$	$\xi = .8$	$\xi = .9$
5	4	3	2	2	2	2	2	2	2
10	3	2	2	2	2	2	2	2	2
20	3	2	2	2	2	2	2	2	2

$$+ 2e^{-x} \sum_{l=0}^{\infty} \frac{\psi(l+1) + \gamma - \psi(3)}{l+1} \left\{ \frac{x^{l+3}}{(l+3)!} - \frac{x^{l+2}}{(l+2)!} \right\}, \tag{38}$$

as indicated in Fig. 9. Integrated Molière angular distribution is indicated in Fig. 10, for B of 5, 10, 20, and ∞.

5 An effective sampling of Molière angular distribution

An important application of integrated Molière distribution will be sampling of the distribution by the Newton method. Molière spatial angle ϑ or the square of it $x \equiv \vartheta^2$ can be sampled from the uniform random number ξ, from

$$F(x) - \xi = 0. \tag{39}$$

As it satisfies

$$\frac{d}{dx} F(x) = -\frac{1}{2} f(x) \tag{40}$$

from Eq. (34), Eq. (39) is solved from

$$\Delta x = \frac{2(F(x) - \xi)}{f(x)}, \tag{41}$$

by the Newton method.

We have prepared the table of both $F^{(n)}(x)$ and $f^{(n)}(x)$ for $n = 0, 1, 2$ and for x from 0 to 18 with every 0.2 interval. For given random number ξ, we took the first approximation of x by solving $F^{(0)}(x) = e^{-x} = \xi$. Next we correct x successively by the Newton method, using the values of both function derived by linear interpolation with values at the nearest two x. We investigated how many corrections are needed before corrected x again stays in the same 0.2 interval, for ξ of 0.1, 0.2, $\cdots$, 0.9, for B of 5.0, 10.0, and 20.0. We confirm rapid convergences in determining $x = \vartheta^2$ corresponding to random numbers of ξ.

6 Conclusions and discussions

We have found Goldstein solution of the Molière series function for general higher orders. The solution showed more stable convergence than traditional solutions by definite integral and by numerical Fourier transforms, and we have come to derive Molière series functions without ambiguity of convergence in numerical integrals.

We investigated the significance of Molière series of the higher orders, visually and quantitatively. Under the permission of fractional error of10^{-3} in $\theta^2 \times f(\theta)$, region in $B \geq 10$ is applicable for usual Molière series of the first three terms and the first six terms are required in Molière series at $B = 6$.

We can easily obtain integral Molière distribution for spatial angle, from the Goldstein solution. We applied the integral distribution on sampling of the Molière angular distribution by the Newton method. Adequate angles for given random number are obtained effectively after about 2 or 3 times correction of required angle.

References

[1] G. Molière, Z. Naturforsch. **2a**, 133(1947).

[2] G. Molière, Z. Naturforsch. **3a**, 78(1948).

[3] H.A. Bethe, Phys. Rev. **89**, 1256(1953).

[4] M. Messel and D.F. Crawford, *Electron-Photon Shower Distribution Function Tables for Lead Copper and Air Absorbers* (Pergamon, Oxford, 1970).

[5] W.R. Nelson, H. Hirayama, and D.W.O. Rogers, "The EGS4 Code System," SLAC-265, Stanford Linear Accelerator Center (Dec. 1985).

[6] D. Heck, J. Knapp, J.N. Capdevielle, G. Shatz, and T. Thouw, Forschungszentrum Karlsruhe Report FZKA6019(1998).

[7] P. Andreo, J. Medin, and A.F. Bielajew, Med. Phys. **20**, 1315(1993).

[8] T. Nakatsuka, K. Okei, and N. Takahashi, *"Proceedings of the Thirteenth EGS Users' Meeting in Japan,"* KEK Proceedings 2006-4, 19(2006).

[9] T. Nakatsuka, *"Proceedings of the Second International Workshop on EGS,"* KEK Proceedings 2000-20, 330(2000).

[10] H. Snyder and W.T. Scott, Phys. Rev. **76**, 220(1949).

[11] W.T. Scott, Rev. Mod. Phys. **35**, 231(1963).

[12] A.F. Bielajew, Nucl. Instrum. Methods Phys. Res. **B86**, 257(1994).

[13] *Handbook of Mathematical Functions with Formulas, Graphs, and Mathematical Tables*, edited by M. Abramowitz and I. A. Stegun (Dover, New York, 1965).

[14] T. Nakatsuka, *"Proceedings of the Tenth EGS4 Users' Meeting in Japan,"* KEK Proceedings 2002-18, 1(2003).

[15] A.F. Bielajew, R. Wang, and S. Duane, Nucl. Instrum. Methods Phys. Res. **B82**, 503(1993).

[16] T. Nakatsuka, and K. Okei, *"Proceedings of the Eleventh EGS4 Users' Meeting in Japan,"* KEK Proceedings 2003-15, 1(2004).

[17] H. Takahasi and M. Mori, Rep. Compt. Centre, Univ. Tokyo, **3**, 41(1970).

Table 2: Goldstein coefficient G_{ln}.

l	$n=1$	$n=2$	$n=3$	$n=4$	$n=5$	$n=6$
0	1/ 1	-1.845569	5.584964	-17.470753	57.632370	-197.929291
1	1/ 2	0.077216	-0.975871	6.202903	-29.798979	132.547638
2	1/ 3	0.384810	-0.906698	3.090225	-8.482770	17.383913
3	1/ 4	0.455274	-0.558083	1.289029	-1.470656	-4.577640
4	1/ 5	0.464220	-0.273301	0.411593	0.732135	-7.335560
5	1/ 6	0.453516	-0.062308	-0.004650	1.300750	-6.071469
6	1/ 7	0.436347	0.093338	-0.186336	1.293957	-4.268216
7	1/ 8	0.417518	0.209587	-0.244291	1.096999	-2.729008
8	1/ 9	0.398905	0.297694	-0.235392	0.857639	-1.576980
9	1/10	0.381237	0.365374	-0.190225	0.632550	-0.765374
10	1/11	0.364761	0.417950	-0.125860	0.441508	-0.217230
11	1/12	0.349515	0.459160	-0.052094	0.288996	0.137346
12	1/13	0.335450	0.491677	0.025357	0.173287	0.353643
13	1/14	0.322479	0.517450	0.103131	0.090379	0.473179
14	1/15	0.310504	0.537925	0.179271	0.035716	0.526423
15	1/16	0.299431	0.554191	0.252661	0.004911	0.535488
16	1/17	0.289170	0.567079	0.322709	-0.005976	0.516320
17	1/18	0.279641	0.577234	0.389139	-0.000361	0.480361
18	1/19	0.270771	0.585159	0.451876	0.018846	0.435776
19	1/20	0.262496	0.591254	0.510961	0.049193	0.388352
20	1/21	0.254758	0.595836	0.566512	0.088626	0.342139
21	1/22	0.247507	0.599163	0.618685	0.135427	0.299928
22	1/23	0.240698	0.601444	0.667657	0.188164	0.263591
23	1/24	0.234292	0.602848	0.713614	0.245642	0.234331
24	1/25	0.228254	0.603516	0.756743	0.306866	0.212863
25	1/26	0.222552	0.603563	0.797226	0.371002	0.199552
26	1/27	0.217158	0.603088	0.835237	0.437358	0.194509
27	1/28	0.212048	0.602171	0.870941	0.505354	0.197666
28	1/29	0.207199	0.600879	0.904494	0.574505	0.208829
29	1/30	0.202591	0.599271	0.936040	0.644408	0.227716
30	1/31	0.198207	0.597395	0.965716	0.714724	0.253991
31	1/32	0.194029	0.595292	0.993646	0.785174	0.287280
32	1/33	0.190043	0.592998	1.019947	0.855521	0.327192
33	1/34	0.186236	0.590543	1.044727	0.925573	0.373330
34	1/35	0.182596	0.587952	1.068086	0.995166	0.425294
35	1/36	0.179111	0.585249	1.090116	1.064169	0.482695
36	1/37	0.175772	0.582453	1.110902	1.132471	0.545153
37	1/38	0.172569	0.579579	1.130525	1.199984	0.612304
38	1/39	0.169493	0.576643	1.149056	1.266635	0.683797
39	1/40	0.166538	0.573657	1.166564	1.332367	0.759300
40	1/41	0.163696	0.570632	1.183111	1.397134	0.838497
41	1/42	0.160959	0.567576	1.198757	1.460901	0.921092
42	1/43	0.158324	0.564499	1.213554	1.523641	1.006803
43	1/44	0.155782	0.561407	1.227554	1.585336	1.095366
44	1/45	0.153331	0.558307	1.240803	1.645974	1.186536
45	1/46	0.150964	0.555204	1.253343	1.705547	1.280079
46	1/47	0.148677	0.552102	1.265217	1.764053	1.375778
47	1/48	0.146466	0.549005	1.276461	1.821492	1.473432
48	1/49	0.144327	0.545918	1.287110	1.877870	1.572851
49	1/50	0.142257	0.542843	1.297198	1.933194	1.673857

The joint distribution of the angular and lateral deflections due to multiple Coulomb scattering

K. Okei[†] and T. Nakatsuka[‡]
[†]*Kawasaki Medical School, Kurashiki 701-0192, Japan*
[‡]*Okayama Shoka University, Okayama 700-8601, Japan*

Abstract

The joint probability density function of the deflection angle and the lateral displacement under Molière's multiple Coulomb scattering theory is obtained using FFT (Fast Fourier Transform). The joint distributions generated with the Monte Carlo method which has been developed by us and with EGS5 are examined by comparison with the numerical solutions.

1 Introduction

Charged particles passing through matter suffer deflections due to the Coulomb scattering, and the process is the main source of the angular and lateral spreads. However, in Monte Carlo simulations at high energies, sampling all deflections is unfeasible because of the huge number of events. Hence, multiple scattering theories are employed [1, 2, 3].

Molière's theory [4, 5, 6] is widely used in Monte Carlo codes such as EGS4 or GEANT3 [1, 2] to simulate the multiple Coulomb scattering of high energy charged particles. Since the joint probability density function of the deflection angle and the lateral displacement under the Molière theory is not known, the Monte Carlo particle transport step must be approximate. Though, to assess the validity of the approximation, we must know a more accurate joint distribution to be compared with Monte Carlo simulations. Because a detailed Monte Carlo method which sample all Coulomb scattering is only applicable for the case where the step size is not very large, we have calculated the joint probability density function numerically using FFT (Fast Fourier Transform) [7, 8].

In this work, the joint distributions generated with the Monte Carlo method which has been developed by us [9] and with EGS5 are examined by comparison with the numerical solutions.

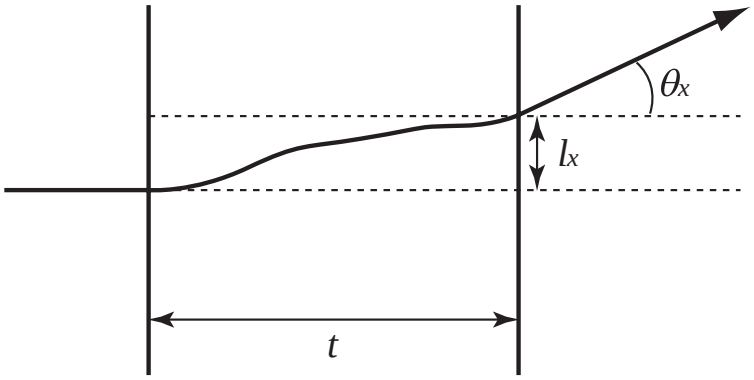

Figure 1: A schematic diagram of the projected trajectory of a charged particle with multiple scattering.

2 The joint probability density function of the deflection angle and the lateral displacement

Fig. 1 shows a schematic diagram of the projected trajectory of a charged particle with multiple scattering. Let $f(\theta_x, l_x)$ be the joint probability density function of the deflection angle θ_x and the lateral displacement l_x after a charged particle traversing a layer of matter of finite thickness t. We neglect the difference between t and the actual path length since we only consider the case where the small angle approximation is valid.

Although $f(\theta_x, l_x)$ under the Molière theory is not known, the transport equation for its Fourier transform $\tilde{f}(\zeta, \eta)$ is solved [7, 8]. We therefore apply FFT to obtain $f(\theta_x, l_x)$.

For example, the left panel of fig. 2 shows the contour plot of $f(\theta_x, l_x)$ calculated for 200 MeV electrons penetrated 0.1 cm of iron. (Each contour is drawn with a logarithmically equal interval.) Note that θ_x and l_x are reduced variables scaled by $\chi_c\sqrt{B}$ and $t\chi_c\sqrt{B_{\rm L}/3}$ respectively, where χ_c and B have usual meanings in Molière's theory and $B_{\rm L}$ is the expansion parameter for the lateral distribution. (See eq. (21) of ref. [10].) The corresponding Gaussian approximation which is often used is also shown for comparison in the right panel of fig. 2.

It can be seen that the Gaussian approximation can be used only for the central region of the distribution. To see this further, fig. 3 shows the conditional lateral distribution $f(l_x|\theta_x)$ for $\theta_x = 0, 1, 2, 3$ (left) and the conditional angular distribution $f(\theta_x|l_x)$ for $l_x = 0, 1, 2, 3$ (right). The dotted curve shows the corresponding Gaussian approximation. As θ_x becomes large, $f(l_x|\theta_x)$ becomes flatter since it is dominated by a single large deflection of angle θ_x at a certain random depth $t' \sim t - l_x/\theta_x$ uniformly distributed between 0 and t.

Thus, we see that the joint probability density function of the deflection angle and the lateral displacement cannot be represented by the Gaussian distribution for $|\theta_x| \gtrsim 1.5$ or $|l_x| \gtrsim 1.5$.

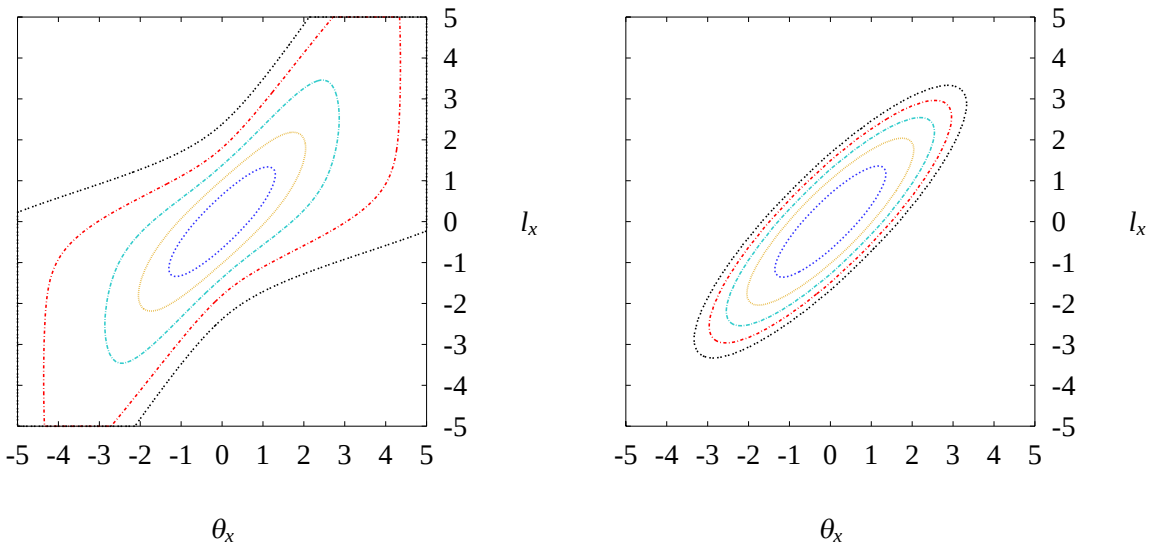

Figure 2: The joint probability density function calculated for 200 MeV electrons penetrated 0.1 cm of iron. Left: Molière (FFT), Right: Gaussian approximation.

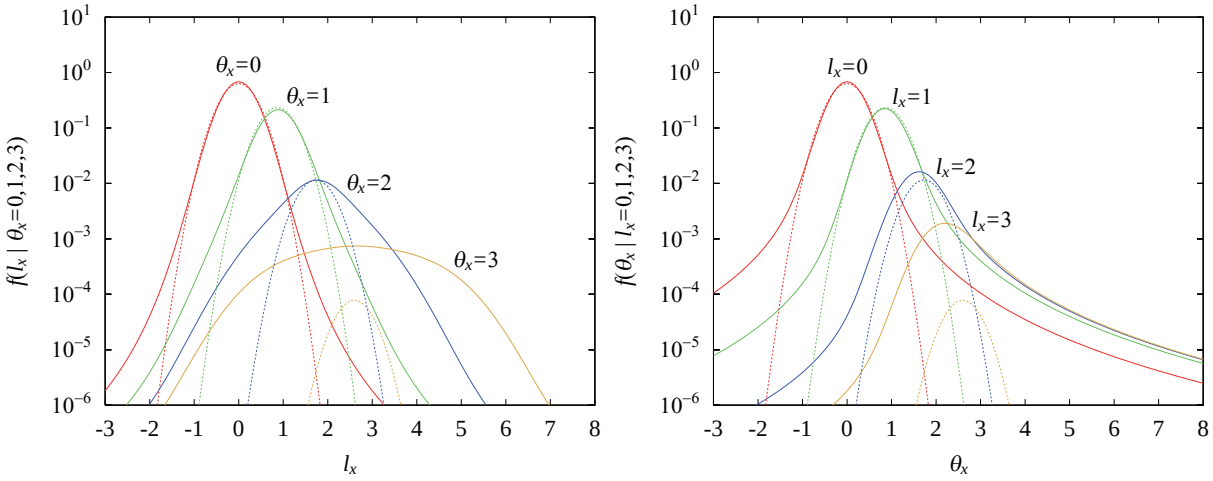

Figure 3: The conditional lateral distribution $f(l_x|\theta_x)$ for $\theta_x = 0, 1, 2, 3$ (left) and the conditional angular distribution $f(\theta_x|l_x)$ for $l_x = 0, 1, 2, 3$ (right). The dotted curve shows the corresponding Gaussian approximation.

3 Comparison with Monte Carlo

In this section, the joint distributions generated with the Monte Carlo methods which has been developed by us [9] and with EGS5 are examined.

First, we compare the joint distribution obtained by our Monte Carlo method, which is constructed by dividing the differential scattering cross section into the moderate scattering and the large angle scattering and exploiting the central limit theorem, with $f(\theta_x, l_x)$ calculated by FFT. The left panel of fig. 4 shows the contour plot of $f(\theta_x, l_x)$ generated by the Monte Carlo method for 200 MeV electrons penetrated 0.1 cm of iron. This seems similar to the contour plot obtained from FFT (the left panel of fig. 2).

The conditional probability density function $f(l_x|\theta_x)$ of the lateral displacement l_x given $\theta_x = 0 \pm 0.1, 1 \pm 0.1, 2 \pm 0.1$ and 3 ± 0.1 obtained from the Monte Carlo method (symbols with error bars) is also compared with the one from FFT (curves) in the right panel of fig. 2. We see that the agreement is excellent for all θ_x.

Second, the joint distributions generated by EGS5 are examined. The same figures as fig. 2 are shown in fig. 5 and 6. The simulations were performed with `CHARD`=0 (the default, fig. 5) and `CHARD`=0.1 (fig. 6). The parameter `CHARD` is used for selecting electron step sizes (see ref. [3] for detail). The distributions obtained with the default option, `CHARD`=0 show poor agreement with FFT results whereas the simulation with `CHARD`=0.1 seems to be quite good.

Finally, we compare the multiple scattering angular and lateral distributions generated by our Monte Carlo method (labeled "Gauss+Large"), EGS5 with `CHARD`=0 (labeled "EGS5 default") and EGS5 with `CHARD`=0.1 in fig. 7. The all angular distributions obtained from the Monte Carlo methods are in good agreement with each other and with the Molière distribution. However, the lateral distribution generated by the EGS5 default option, `CHARD`=0, is significantly deviated from the others.

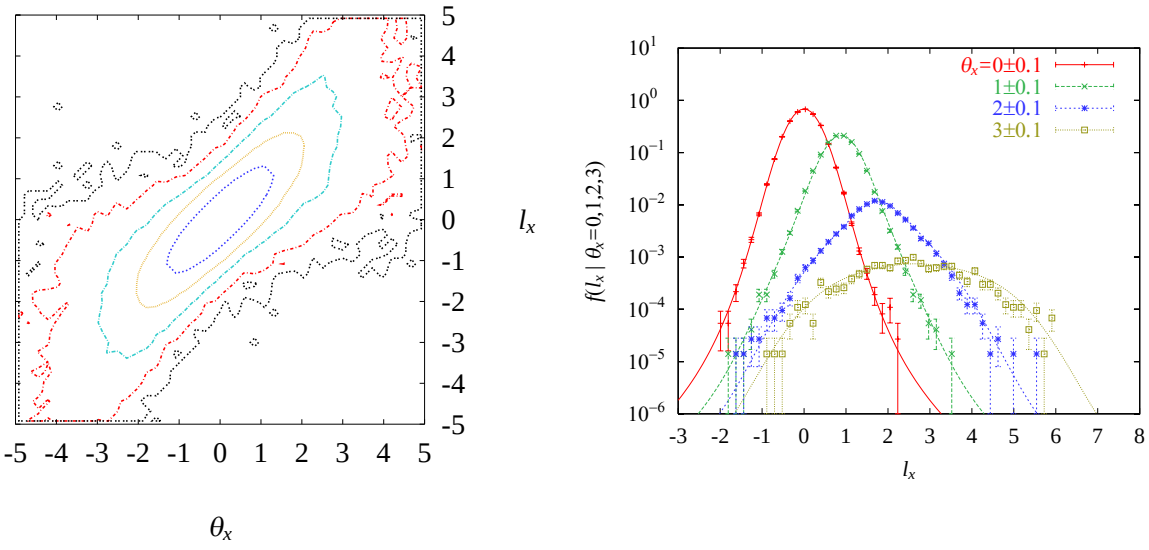

Figure 4: Left:The contour plot of $f(\theta_x, l_x)$ generated by our Monte Carlo method. Right:The conditional lateral distribution $f(l_x|\theta_x)$ for $\theta_x = 0 \pm 0.1, 1 \pm 0.1, 2 \pm 0.1$ and 3 ± 0.1 obtained from the Monte Carlo method (symbols with error bars) and from FFT (curves).

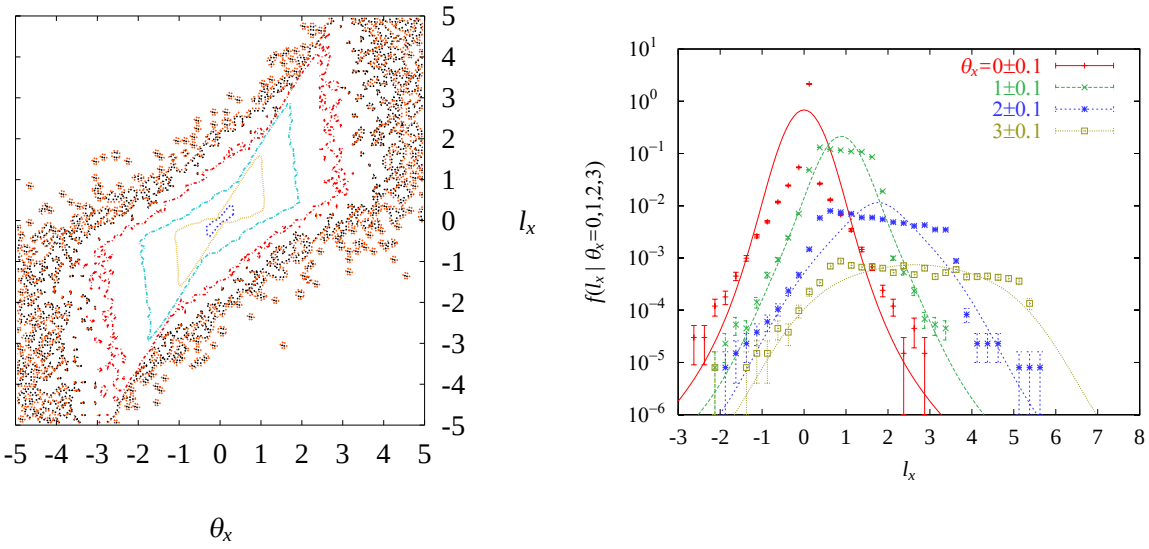

Figure 5: The same as fig. 4 but generated by EGS5 with `CHARD`=0 (default).

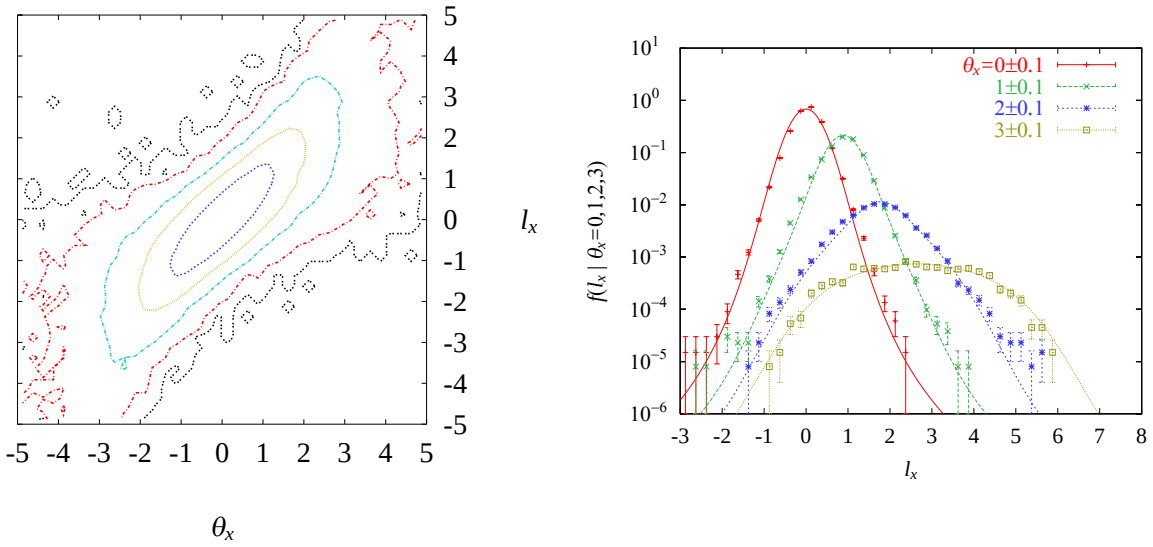

Figure 6: The same as fig. 4 but generated by EGS5 with CHARD=0.1 .

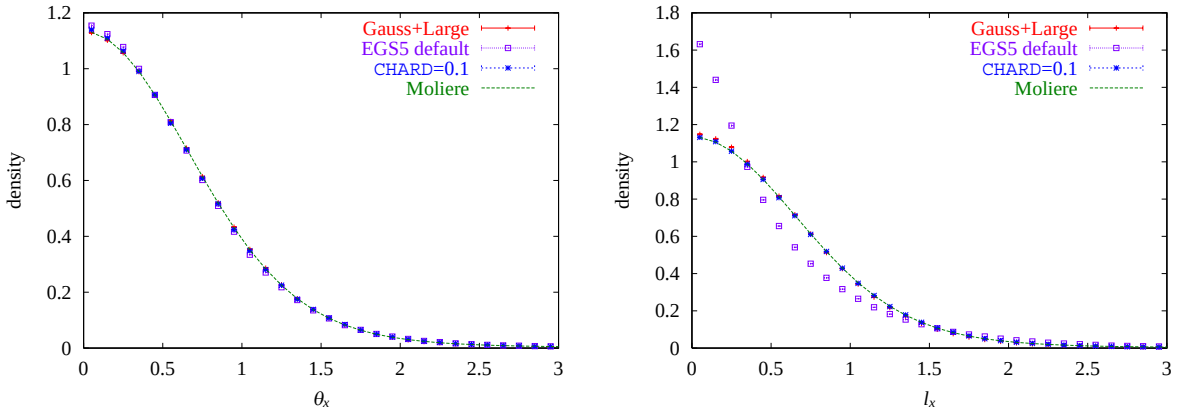

Figure 7: The multiple scattering angular (left) and lateral (right) distributions.

4 Discussion

Here we discuss the results obtained from the EGS5 Monte Carlo simulations which were performed with CHARD=0 and 0.1. The difference is attributed to the different number of sampling steps for a given thickness. Fig. 8 shows the distribution of the variable IMSCAT (number of times calling subprogram MSCAT) for the default EGS5 option (CHARD=0) and CHARD=0.1. The simulation with CHARD=0 was performed by one or two steps, whereas eleven or twelve steps were spent for CHARD=0.1.

Fig. 9 shows the contour plot of $f(\theta_x, l_x)$ generated by EGS5 with CHARD=0. This plot uses only events with IMSACAT=1 to see the joint distribution of one step. It can be seen that a single sampling step of EGS5 multiple scattering cannot mimic events such as $\theta_x < 0$ and $l_x > 0$, or

$\theta_x > 0$ and $l_x < 0$. However, multiple steps of multiple scattering can generate better results as the case of CHARD=0.1.

In order to know how many number of steps are needed, simple Monte Carlo simulations were performed. In the simulations, changing the number of sampling steps, we examined the resultant lateral distributions. Scattering angles were sampled from Gaussian so that the lateral distribution can be compared with Gaussian.

Fig. 10 shows the resultant lateral distributions and fig. 11 shows the kurtosis of the distributions. These figures show that more than ten sampling steps are needed to generate the correct lateral distribution.

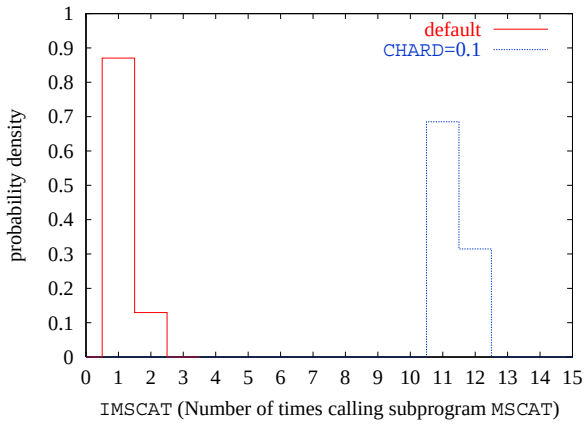

Figure 8: The number of times calling subprogram MSCAT for CHARD=0 (solid histogram) and 0.1 (dotted histogram).

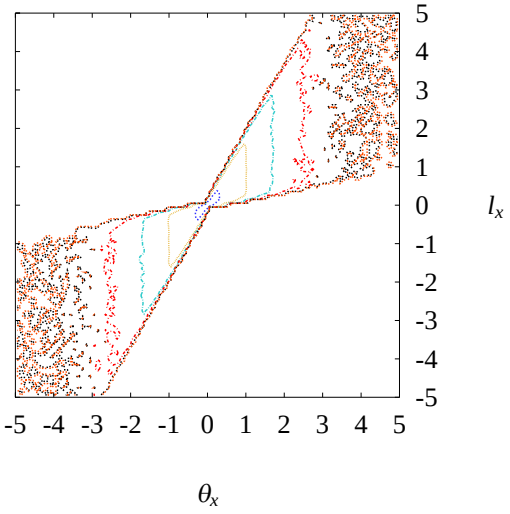

Figure 9: The same as the left panel of fig. 5 but only events with IMSACAT=1 were selected.

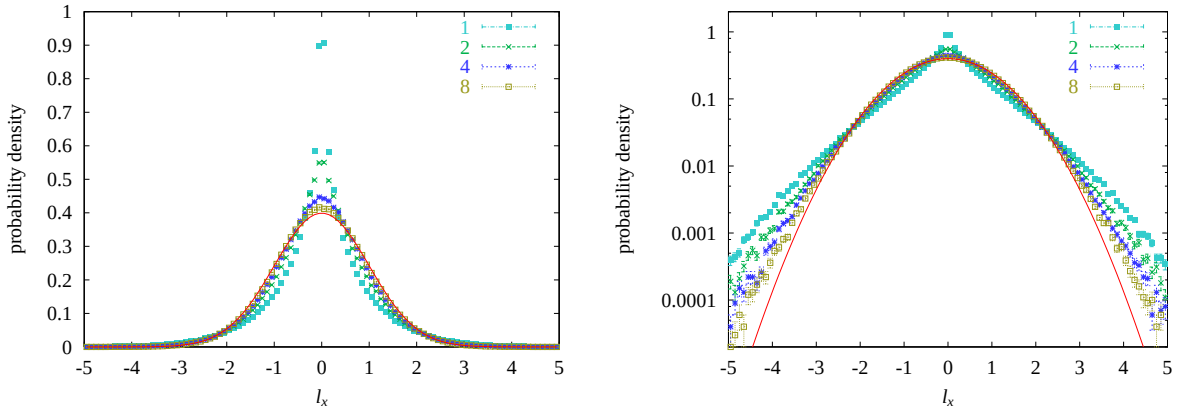

Figure 10: The lateral distributions resulted from the Monte Carlo simulations with the scattering angles of Gaussian. Left: linear ordinate, Right: logarithmic ordinate.

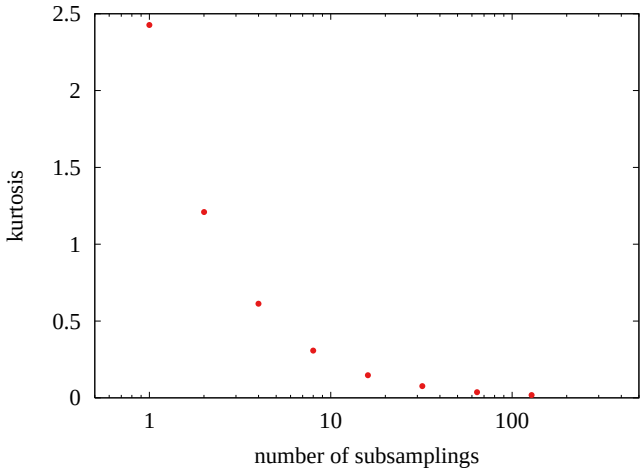

Figure 11: Kurtosis of the lateral distributions resulted from the Monte Carlo simulations with the scattering angles of Gaussian.

5 Conclusion

We have calculated the joint probability density function of the deflection angle and the lateral displacement due to multiple Coulomb scattering numerically using FFT. To examine the joint distributions obtained by Monte Carlo methods, they were compared with the numerical solutions. The Monte Carlo methods which has been developed by us and EGS5 with `CHARD` option can generate the correct joint distributions for 200 MeV electrons penetrated 0.1 cm of iron, but EGS5 with the default option. It was shown that the difference of the EGS5 simulations is attributed to the different number of sampling steps. In conclusion, the numerical solutions of the joint distribution is useful as a benchmark.

References

[1] W.R. Nelson, D.W.O. Rogers and H. Hirayama, The EGS4 Code System, Stanford Linear Accelerator report SLAC-265 (1985).

[2] GEANT Detector Description and Simulation Tool, CERN Program Library Long Writeup, PHYS325 (1993).

[3] H. Hirayama et al., The EGS5 Code System, SLAC-R-730 (2005) and KEK Report 2005-8 (2005).

[4] G. Molière, Z. Naturforsch. **2a**, 133 (1947).

[5] G. Molière, Z. Naturforsch. **3a**, 78 (1948).

[6] H.A. Bethe, Phys. Rev. **89**, 1256 (1953).

[7] T. Nakatsuka and K. Okei, *Proc. 13th EGS Users' Meeting in Japan*, KEK Proceedings 2006-4, 18 (2006).

[8] T. Nakatsuka, K. Okei and N. Takahashi, *Journal of Okayama Shoka Univ.* vol. 43-1, 1 (2007).

[9] K. Okei and T. Nakatsuka, *Proc. 3rd International Workshop on EGS*, KEK Proceedings 2005-7, 57 (2005).

[10] T. Nakatsuka, *Proc. 26th International Cosmic Ray Conference* **1** 522(1999).

Testing the K, L Shell Fluorescence Yield and Coster-Kronig Coefficients from EADL and from Campbell's Paper

I. Orion*, Y. Namito, Y. Kirihara and H. Hirayama

KEK High Energy Accelerator Research Organization
Oho, Tsukuba-shi, Ibaraki 305-0801, Japan

Abstract

The latest data of fluorescence and Coster-Kronig yields in use in EGS5 was adopted from *The Table of Isotopes eighth edition*. Since the fluorescence and Coster-Kronig yields from the Table of Isotopes were taken from several previous sources, it became reasonable to inspect these yields with a more updated database. In this work, we report the results of the fluorescence yields comparisons performed between the data from The Table of Isotopes and EADL the data from the Livermore Evaluated Atomic Data Library. The EADL data, in general, showed several percents difference in comparison with the previously used data and in some points the difference was tremendous. The updated database in EGS5 was tested and compared to previous simulation results for K-X-rays emission spectra of copper titanium and iron targets. The total counts of each fluorescence emission was calculated using EGS5 and was compared with experimental measurements results for polarized photon beams with incident energies of 20, 30 and 40 keV. The use of EADL database for atomic fluorescence K X-rays emission in the simulations, improved the matching between measured-to-calculated counts ratios. The EADL L subshell fluorescence emissions led to some discrepancies, and therefore alternative L subshell and Coster-Kronig yields were examined to be used in the EGS5 Monte Carlo simulation code system. Campbell summarized the differences in the L shell fluorescence yields and Coster-Kronig yields from several databases and provided recommended values. The use of the Campbells' yields values in the EGS5 simulations resulted improved measured-to-calculated counts ratios for the L fluorescence emission in gadolinium, tungsten and lead targets.

1. Introduction

The EGS5 Monte Carlo code system, as the successor of the EGS4 (1985)[1], has the routines and database ready to simulate detailed L-shell fluorescence emission [2,3]. The ability to simulate L-shell emission using EGS5 has been established due to improved subroutines, and an atomic data file, containing the emissions energies for each level and the transition probabilities. Fluorescence yields are the probabilities for vacancies filling in the atomic shells, following radiative emissions. For a vacancy in shell i, the fluorescence yield ω is obtained with the consideration of non-radiative probabilities, Auger and Coster-Kronig electrons emissions:

$$\omega_i + f_i + a_i = 1$$

* Ben-Gurion University of the Negev, Beer-Sheva, Israel
email: iorion@bgu.ac.il

For L-shell vacancy, f represents the Coster-Kronig yields of the non-radiative emission process resulting vacancies in other L subshells.

This work aims to introduce data from the EADL [4] in order to evaluate the atomic database with both previous EGS4 simulation results, and previous experimental data that were measured at the KEK Photon Factory synchrotron.

2. Method

2.1 The EADL Data Library

The EADL data library is part of the DLC-179 RSIC data library, which contains the Lawrence Livermore evaluated atomic data (EADL), electron data (EEDL) and photon data libraries (EPDL). The scope of EADL is to provide atomic relaxation data for use in Monte Carlo particle transport simulation codes for Z = 1 -100. The EADL includes three main data tables: 1. Subshell data; 2. Transition probability data; 3. Whole atom data [4].

In this work, values from the transition probabilities data were extracted into the EGS5 and tabulated in the file: egs5_block_data_atom.f. The modified tables are:

1. The K and L shell fluorescence yields: ω_K, ω_1, ω_2, ω_3
2. L shell Coster-Kronig transitions: f_{12}, f_{13}, f_{23}

2.2 The Experimental Data

Several highly pure material thick targets were irradiated at the BL-14C in the KEK-PF synchrotron facility. The beamline was equipped with a monochromator to produce mono-energetic photons incident beam of 10 keV, and up to 40 keV. Two planar HPGe detectors for low-energy X-rays were set, one horizontally to the beam – target plane, and the other vertically to the plane [5]. The measurements results of the previous experiments were compared with this current study simulation results.

2.3 The Monte Carlo simulations

The Monte Carlo simulation user-code has been modified to an EGS5 user-code from the previous EGS4 version. The user-code includes a source description with specific polarization ratios versus incident photon energy. The emitted X-rays flux has been tallied with a 0.1 keV binning for each detector. 5 degrees angular aperture has been set toward each detector.

The simulation flux results are analyzed using an earlier prepared HPGE response function arrays. This procedure provides a simulated spectral response of each detector for each run. The simulation results are treated using a spectral Gaussian broadening code, in several cases where spectral results had to be compared with detector spectral measurements.

3. Results and Discussion

3.1 K-X emission

The fluorescence yields ω_K ratios of the EADL over the Table of Isotope 8th Ed., which was taken from Bambynek-1984 [10] along all elements Z number are plotted in Fig. 1. Three targets used in this study were Fe, Cu and Ti, and their location is shown in Fig. 1, which allows us to predict a difference in their calculations results.

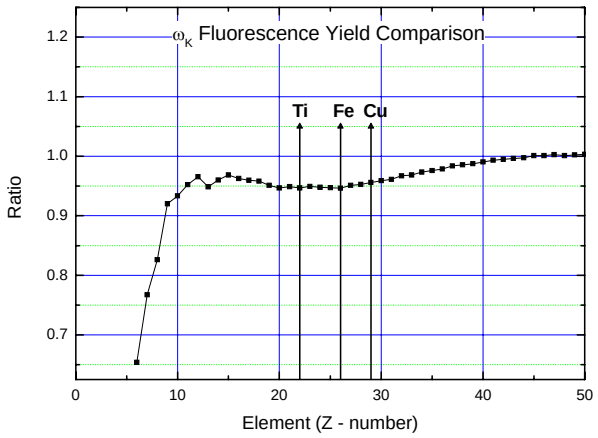

Figure 1: The fluorescence yields ω_K ratios of the EADL over the Bambynek 1984 yields. The tested targets are shown as arrows.

The K-X emissions of these materials were measured in high performance of spectral resolution and counts. Total K fluorescence counts measured-over-calculated ratios are shown versus the incident photon beam energy. In Fig. 2 the simulations results were obtained using the Bambynek 1984 fluorescence values taken from The Table of Isotopes - 8th edition. The results of the horizontal detector (H) and the vertical detector (V) ratios were averaged for each point. The results of K fluorescence counts measured-over-calculated ratios using the EADL data are shown in Fig. 3. The pulse-height distributions of each detector from the Monte Carlo simulations results and the measurements on iron target are shown in Fig. 4.
The M/C ratios showed an improved agreement for all the K-X emission results, and the EGS5 spectral results present very good agreement with the measured spectra in both detectors.

3.2 L-X emission

The total L-X peak counts were compared to the M/C counts ratios for three targets: Gd, W and Pb, as shown in Fig 5. Also the individual L emissions, Lα, Lβ and Lγ emission peaks, were compared to the experimental results, in Fig.6.
The Lα, Lβ and Lγ emission peaks M/C results, using the EADL data, are presented in Fig. 7. From Fig.6 and Fig. 7, we found that the Lβ and Lγ M/C ratios in Gd were improved with the EADL data, however the Lα M/C ratio diverge away. A similar trend is observed in lead. The tungsten results show this discrepancy for all the emission peaks M/C ratios. The explanations how the EADL data led to the L emissions mismatch are described in section 3.3.

In order to test Campbell (2003) recommendations, we modified again the fluorescence yields and Coster-Kronig yields due to Campbell data [7]. The resulted total L-emissions, and the Lα, Lβ and Lγ emission peaks were compared to the experimental results for each case, as shown in Fig. 8, and in Fig. 9.
The Campbell recommended database led to the closest agreement in most of the cases for the Lα, Lβ and Lγ emission peaks.

3.2 Investigation of the Coster-Kronig yields and energies

To find a reason of discrepancy between measured and calculated L-X rays when EADL fluorescence yield and Coster-Kronig coefficients are used, we compared ω_1, ω_2, ω_3 with other databases. A large difference in ω_1 was found, as shown in Fig.10. ω_1 in EADL for Z = 74 is about a half value compared to Krause [6] and Campbell, and therefore responsible for the reduce in the calculated Lγ intensity, which increases the Lγ M/C ratio.

In Fig 11, L_1-L_3 Coster-Kronig yield (f_{13}) is plotted. Again, there is a large difference between EADL and other data. Campbell pointed out that "EADL and DHS should give the same results, because they are based on the same Chen and Scofield rates". Campbell also pointed out that "the use of approximate Coster-Kronig energies in the EADL" is the reason of the difference [7].

To investigate this point more closely, we plotted the L_1-L_3-M_5 Coster-Kronig energy in Fig.12, because this is a dominant part of f_{13}. "DHFS+Corr." is "a Dirac-Hartree-Fock-Slater calculation and correction" from Chen [8]. "E(L1,Z)-E(L3,Z)-E(M5,Z+1)" is Eq.(4) of Chen. E (a,b) is the binding energy, a and b represent shell and atomic number respectively. E (M5,Z+1) is used to account for the effect of vacancy. This is presented here to provide a simplified equation of the Coster-Kronig energy.

The f_{13} values in DHS jumps up at Z=75 because "DHFS+Corr." of L1-L3-M5 Coster-Kronig energy is non-negative there [9]. The f13 values in EADL jumps up at Z=69, corresponding to non-negative value of L_1-L_3-M_5 Coster-Kronig energy at $Z \geq 69$ in EADL. This have shifted the f_{13} jump point f from Z=75 to Z=69, therefore overestimate of f_{13}, and underestimate of ω_1 were caused.

On the other hand, overestimated f_{13} caused overestimation of L_3 hole, then overestimation of Lα from L_3 hole happened. This is a reason of small M/C values of Lα when EADL was used.

References

[1] W. R. Nelson, H. Hirayama, D. W. O. Rogers, "The EGS4 code system", SLAC-265 (Stanford University, 1985).

[2] H. Hirayama, Y. Namito, A. F. Bielajew S. J. Wilderman and W. R. Nelson, "The EGS5 code system" SLAC-R-730 / KEK Report 2005-8 (2006).

[3] H. Hirayama, Y. Namito and S. Ban, "Implementation of an L-shell photoelectron and an L X-ray for elements into the EGS4 code", Proceeding of the 6th EGS4 Users' Meeting in Japan, KEK Tsukuba, Japan July 29-31, 1996 pp 10-16.

[4] T. Perkins and D.E. Cullen, "ENDL type format for the LLNL evaluated atomic data library, EADL, for the evaluated electron data library, EEDL, and for the evaluated photon data library, EPDL" UCRL-ID-117796 (July 1994).

[5] Y. Namito and H. Hirayama, "New photon transport physics in EGS5", pp. 19- 26, Proceedings of the Third International Workshop on EGS, August 2005 KEK, Tsukuba, Japan. KEK Proceedings 2005-3 (2005).

[6] M. O. Krause, J. Phys. Chem. Ref. Data **8,** 307 (1979); data was presented in: R. B. Firestone, *"Table of Isotopes"*, 8th Ed., John Wiley & Sons (1996).

[7] J. L. Campbell, "Fluorescence yields and Coster–Kronig probabilities for the atomic L subshells", Atomic Data and Nuclear Data Tables **85** 291-315 (2003).

[8] M.H.Chen, et al, "Theoretical L-shell Coster-Kronig Energies $11 \leq Z \leq 103$", Atomic Data and Nucl. Data Tables, **19**, 97-151 (1977).

[9] T.Papp, "On the accuracy of L subshell ionization cross sections: II. Coster-Kronig transition probabilities", ATOMKI, Annual Report, 37, Institute of Nuclear Research of the Hungarian Academy of Sciences, Debrecen, Hungary (2005).
[10] W. Bambynek, post-deadline abstract in the Proceedings of the Conference on X-ray and Inner shell Processes in Atoms, Molecules and Solids, Leipzig, Aug 20-24 (1984).

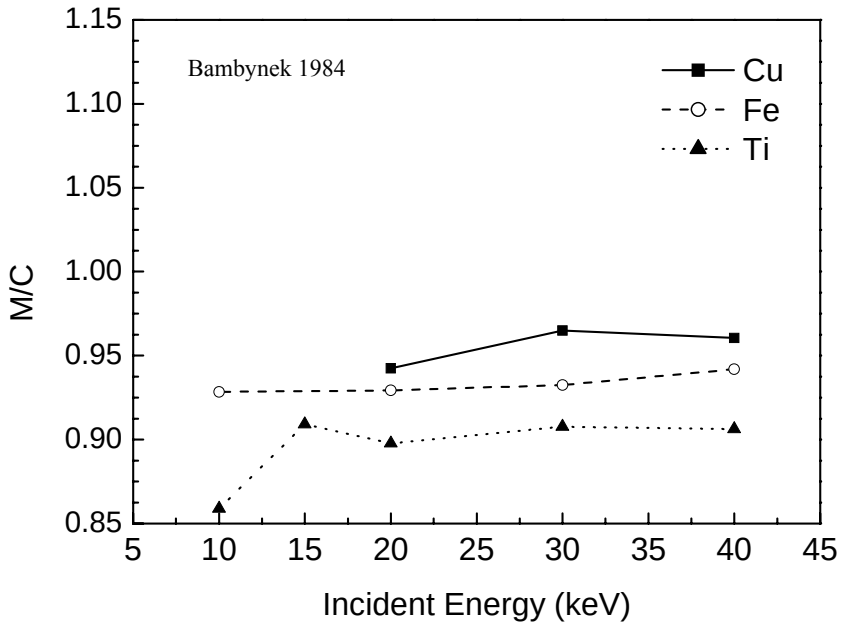

Figure 2: The K – X emission Measured/Calculated ratios in Cu, Fe and Ti using the Bambynek 1984 database.

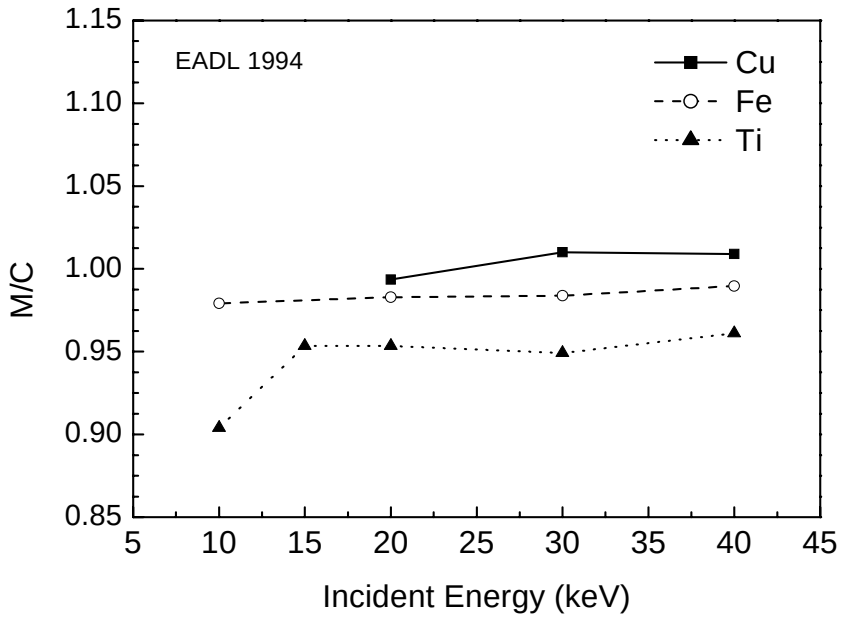

Figure 3: The K – X emission Measured/Calculated ratios in Cu, Fe and Ti using the EADL 1994 database.

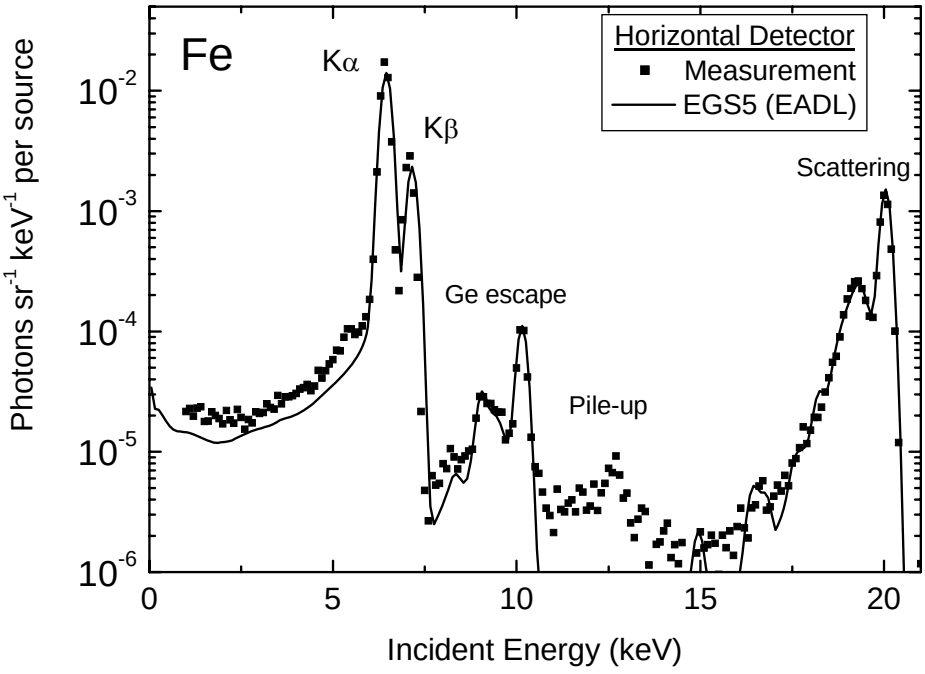

Figure 4: Spectrum comparison of the K – X lines of iron target for the horizontal detector. The calculated results were obtained using the EADL K fluorescence yields.

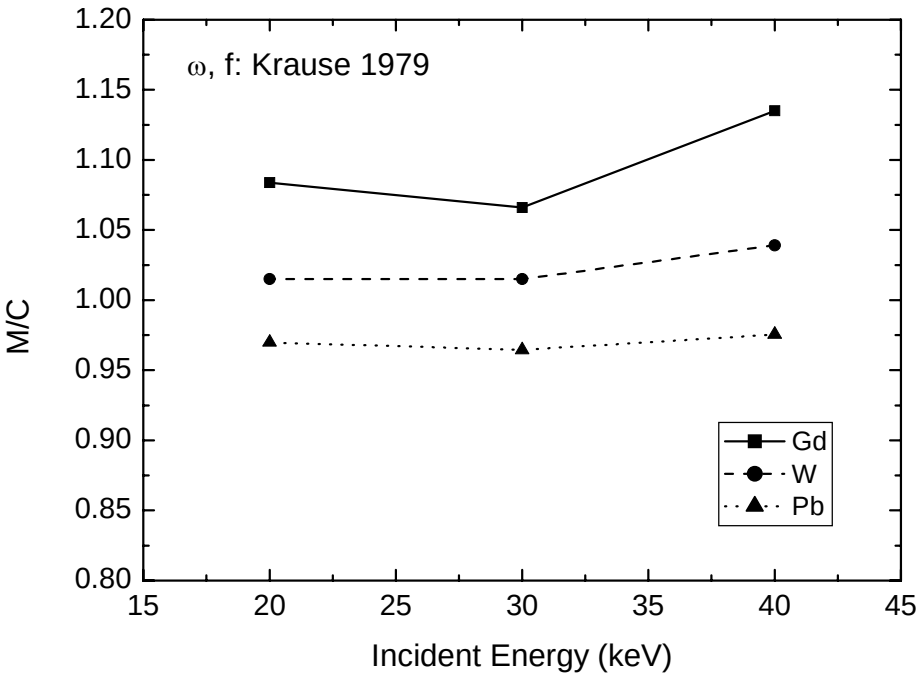

Figure 5: The Measured over Calculated total L – X emission counts ratios in gadolinium, tungsten and lead using the Krause 1979 yields, which was adopted in Table of Isotope 8th edition.

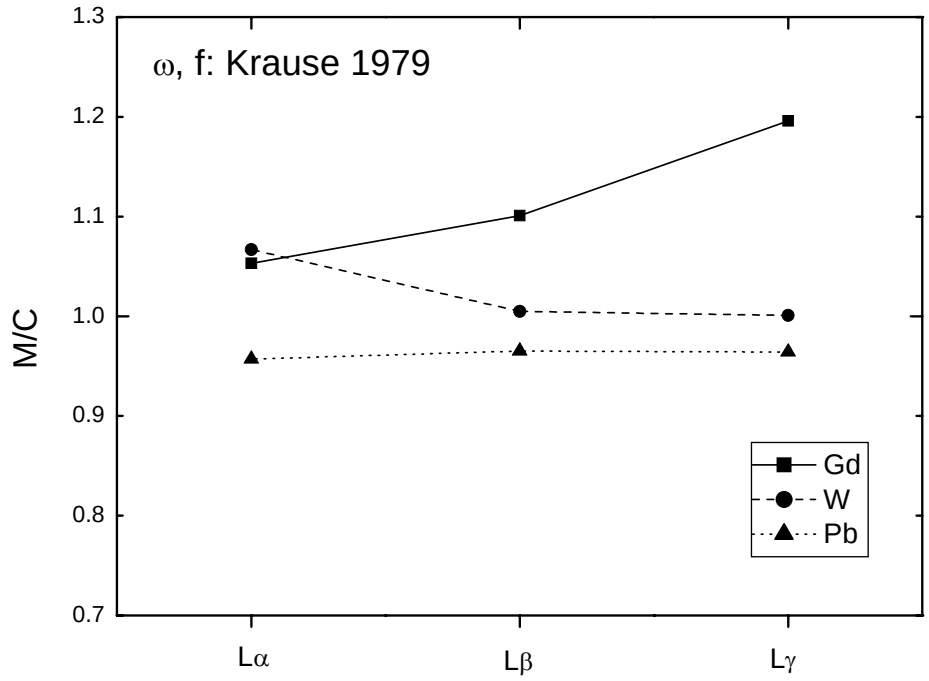

Figure 6: The Measured over Calculated Lα, Lβ and Lγ peaks counts ratios in gadolinium, tungsten and lead using the Krause 1979 yields. The points are the mean values of the results of incident energy at 20, 30, and 40 keV.

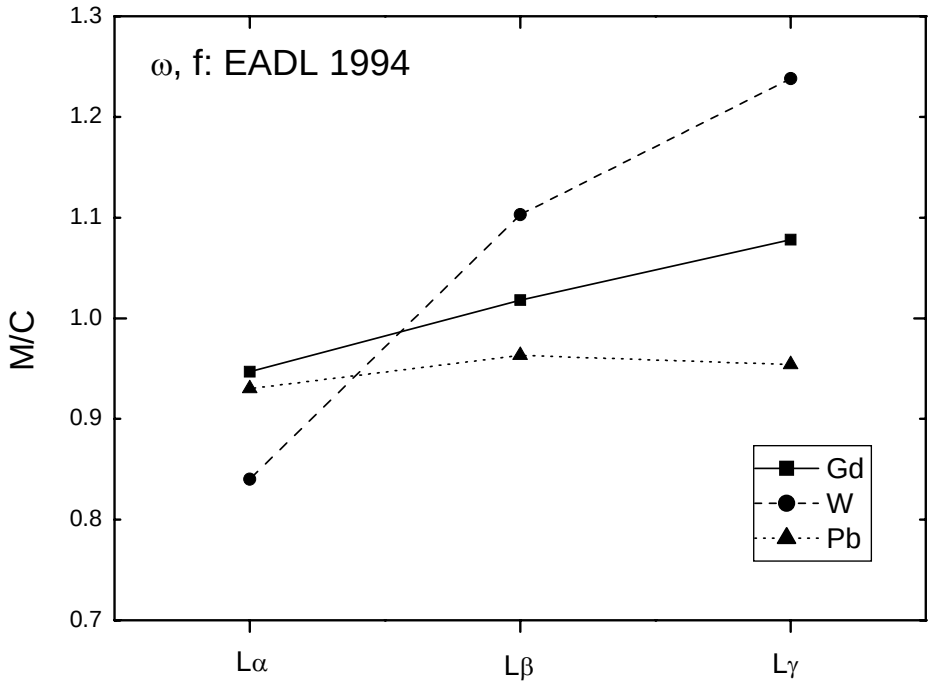

Figure 7: The Measured over Calculated Lα, Lβ and Lγ peaks counts ratios in gadolinium, tungsten and lead using the EADL 1994 yields. The points are the mean values of the results of incident energy at 20, 30, and 40 keV.

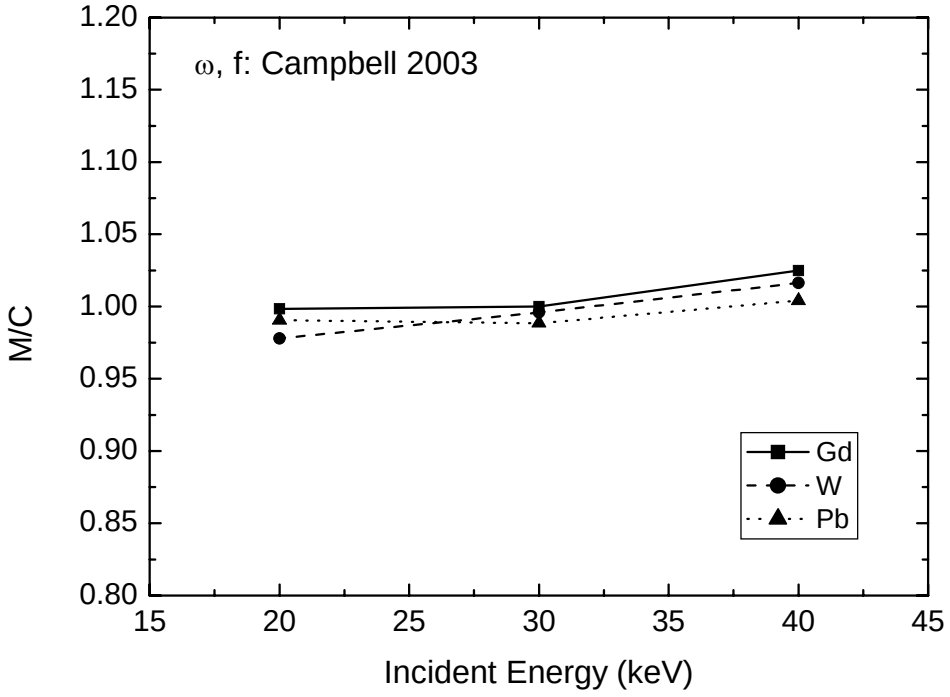

Figure 8: The Measured over Calculated total L – X emission counts ratios in gadolinium, tungsten and lead using the Campbell 2003 yields.

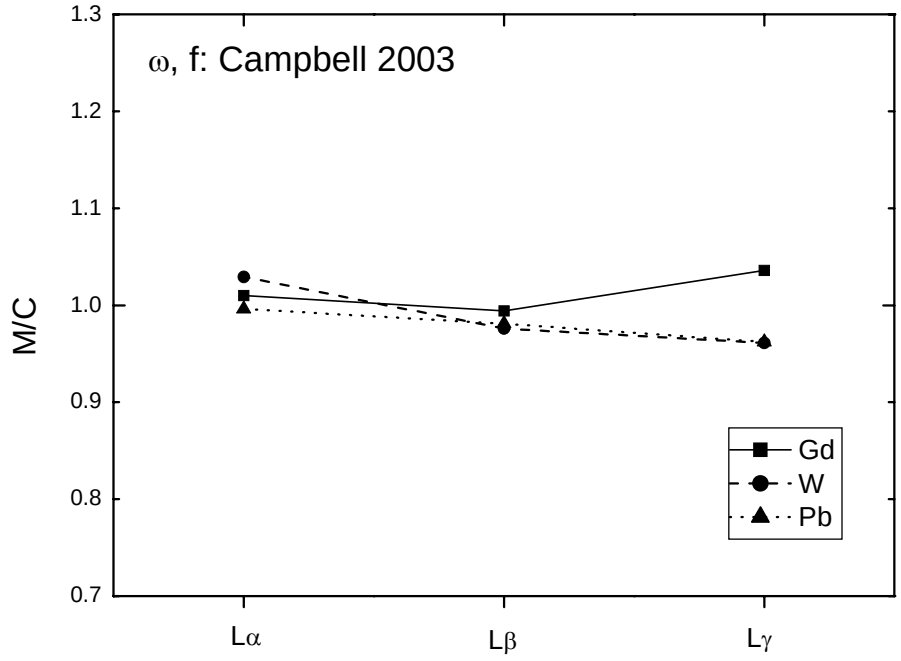

Figure 9: The Measured over Calculated Lα, Lβ and Lγ peaks counts ratios in gadolinium, tungsten and lead using the Campbell 2003 yields. The points are the mean values of the results of incident energy at 20, 30, and 40 keV.

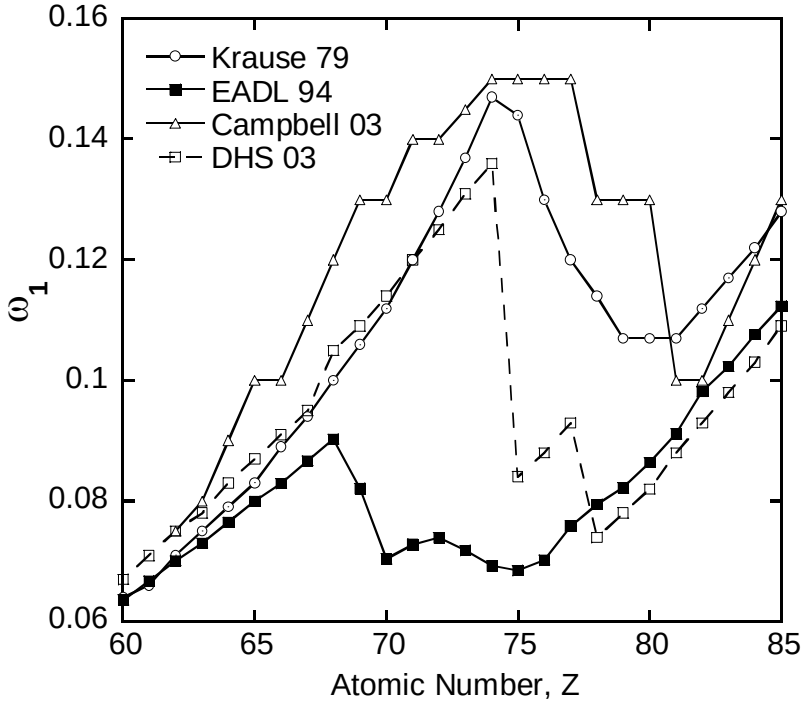

Figure 10: L1 fluorescence yield. EGS5 currently uses ω1 from "Table of Isotope 8th" which is identical to Krause. Campbell 03 is the recommended values in [7]. DHS 03 is Dirac-Hartree-Slater calculation values shown in Campbell 03.

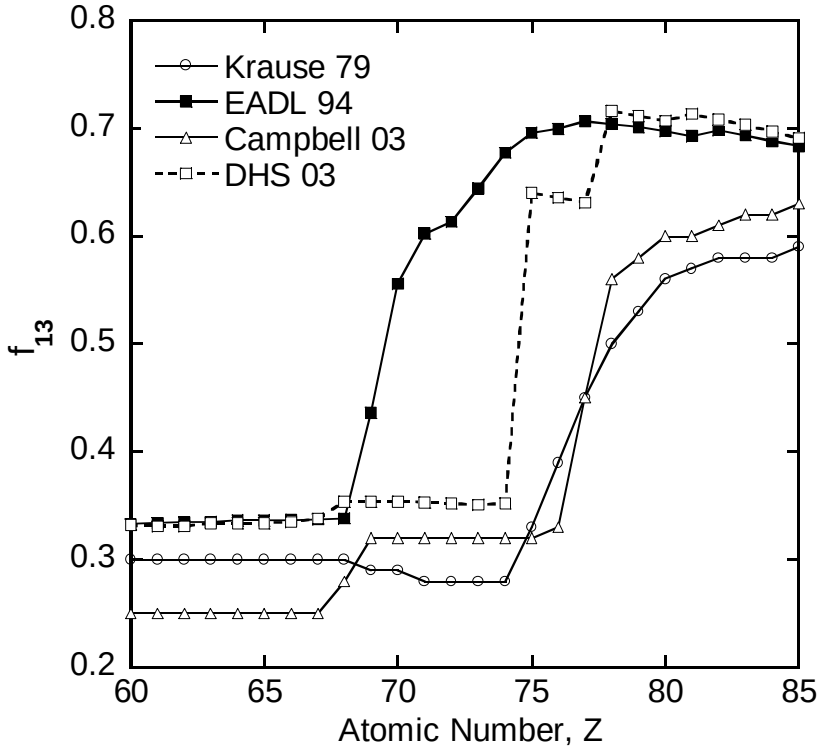

Figure 11: L1-L3 Coster-Kronig yield. EGS5 currently uses f13 from "Table of Isotope 8th" which is identical to Krause. Campbell 03 is the recommended values in [7]. DHS 03 is Dirac-Hartree-Slater calculation values shown in Campbell 03.

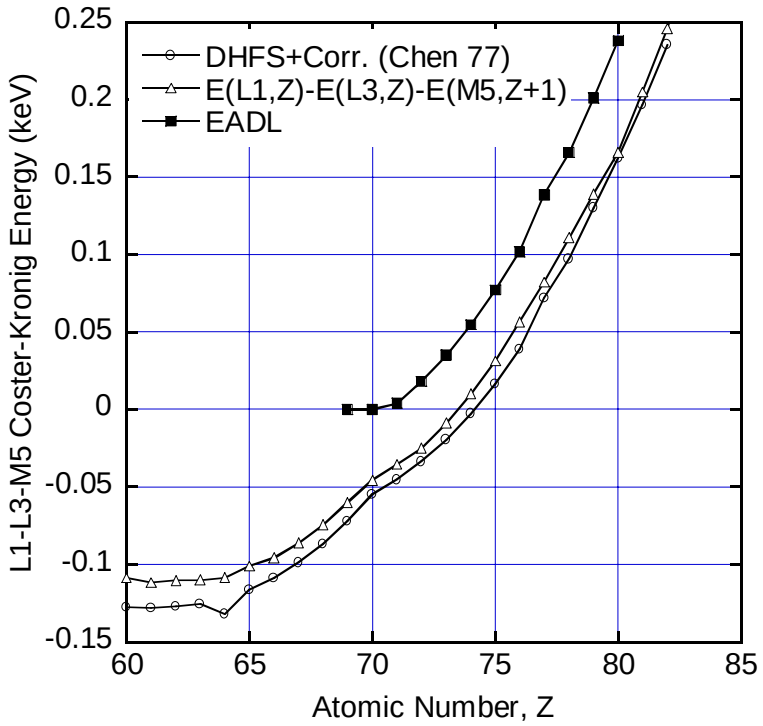

Figure 12: L1-L3-M5 Coster-Kronig energy. "DHFS+Corr." is the Dirac-Hartree-Fock-Slater calculation and corrections from Chen [8]. "EADL" is a L1-L3-M5 Coster-Kronig energy taken from EADL database [4]. "E(L1,Z)-E(L3,Z)-E(M5,Z+1)" is Eq.(4) of Chen. E(a,b) is the binding energy, a and b represent shell and atomic number respectively. E(M5,Z+1) is used to account for the effect of vacancy. This is presented here to provide a simplified equation of the Coster-Kronig energy.

INCORPORATING THE ELECTROMAGNETIC FIELD IN THE EGS5 CODE

Tatsuo Torii[1], Takeshi Sugita[2]

[1] Tsuruga Head Office, Japan Atomic Energy Agency, 2-1 Shiraki, Tsuruga, 919-1279 JAPAN
[2] Science and System Laboratory, 1342-6 Sumiyoshi, Kasama, 309-1716 JAPAN

Abstract

In recent years, radiation bursts called terrestrial gamma-ray flashes (TGFs) have been observed over thunderclouds by X- and γ-ray observation satellites. Accordingly, a set of modules designed to analyze the effects of electrons on the thundercloud electric field and global electric fields was developed, and the subroutine ELECTR was modified. These modules and the modified subroutine were then incorporated into the EGS5 code. Furthermore, in the EGS5 the density of substances was set for each computational region, but the code was modified to allow the density to be changed continuously by simulating the global atmosphere. The magnetic field was compared with the user code UCBEND and it was confirmed to agree well.

1. Introduction

In order to analyze the behavior of charged particles in thunderclouds, subroutines and a user code have been developed to analyze the effects of the external electric field with the PRESTA-CG [1,2]. To apply these new developments in the EGS5 code [3] and shed light on the mechanism of TGFs observed over thunderclouds [4,5], the code was extended to analyze the effects of the external magnetic field. To encompass the upper atmosphere from the vicinity of the ground to the altitude of 400 km, it is necessary to analyze the intensity and direction of the electromagnetic field that continuously changes with altitude and the behavior of electrons and photons in the space with atmospheric density that varies by 12 orders of magnitude. We have therefore decided to compute a reaction by determining the electromagnetic field and the atmospheric density at the reaction point of each particle.

Although the aim is to analyze the behavior of electrons and photons in the electromagnetic field in the air, we developed a highly versatile computer code by incorporating the CG method into the EGS5 code as with the PRESTA-CG so that it can analyze the behavior of electrons and photons in an arbitrary geometry and in an arbitrary electromagnetic field. This report outlines this newly developed code.

2. The Procedure to Incorporate the Electromagnetic Field into the EGS5 Code

The procedure to incorporate the capabilities to evaluate continuous changes in atmospheric density and evaluate electric and magnetic fields into the EGS5 code is described below. Basic equations for the effects of electric and magnetic fields are formulated with reference to Bielajew's method [6]:

(1) Basic equations for the electric and magnetic fields;

① The equation to calculate the direction vector

$$\vec{u}_f = \vec{u}_0 + \vec{\triangle u}_{ms,\,ret} + \vec{\triangle u}_{em}$$

$$\triangle \vec{u}_{em} = \frac{e\ s}{m_0 \gamma(E_0) v_0^2} (\vec{D}_0 - \vec{u}_0 (\vec{u}_0 \cdot \vec{D}_0) + \vec{v}_0 \times \vec{H}_0)$$

② The equation to calculate the particle position

$$\vec{x}_f = \vec{x}_0 + \vec{u}_0 s + \frac{s}{2} (\triangle \vec{u}_{ms,\ ret} + \triangle \vec{u}_{em})$$

③ The equation to calculate the final energy

$$E_f = E_0 - \triangle E_{ret} + e \vec{D}_0 \cdot (\vec{x}_f - \vec{x}_0)$$

$\vec{u}_f$: The new direction vector $\vec{u}_0$: The initial direction vector

$\triangle \vec{u}_{ms,\ ret}$: The deflection due to multiple scattering and inelastic collisions

$\triangle \vec{u}_{em}$: The deflection due to external electromagnetic filed

e : The charge of the particle s : The step length

$\vec{D}_0$: The macroscopic electric field strength m_0 : The mass

$\vec{H}_0$: The macroscopic magnetic field strength

$\gamma(E_0)$: $(1 - \vec{\beta} \cdot \vec{\beta})^{-1/2}$

$\vec{v}_0$: The initial velocity

$\vec{\beta}$: $\vec{v} / c$

$\vec{v}$: The velocity c : The velocity of photon

$\vec{x}_f$: The new particle position $\vec{x}_0$: The initial particle position

E_f : The new particle energy E_0 : The initial particle energy

$\triangle E_{ret}$: The energy loss due to inelastic collisions

(2) An equation to evaluate the loci of electrons and positrons moving in a vacuum in the electric field

The effects of the electric field with the code were confirmed in comparison with the loci of electrons and positrons in a vacuum as expressed by the following equation:

$$x_{\parallel} = \frac{m_0 c^2 \gamma_0}{eE} \left(\cosh\left(\frac{eE x_{\perp}}{m_0 c^2 \gamma_0 \beta_{\perp 0}}\right) - 1 + \beta_{\parallel 0} \sinh\left(\frac{eE x_{\perp}}{m_0 c^2 \gamma_0 \beta_{\perp 0}}\right)\right)$$

The results of the comparison are shown in Fig.1.

(3) An equation to evaluate the loci of electrons and positrons moving in a vacuum with an electric field

Where, the effects of the magnetic field with the code were confirmed in comparison with the locus defined by the following equation:

$$x_{\perp 1} = \frac{p^0_{\perp 2}}{eB}\left(\left(1-\cos\left(\frac{eB\,x_{\parallel}}{p^0_{\parallel}}\right)\right) + \frac{p^0_{\perp 1}}{eB}\sin\left(\frac{eB\,x_{\parallel}}{p^0_{\parallel}}\right)\right.$$

$$x_{\perp 2} = -\frac{p^0_{\perp 1}}{eB}\left(\left(1-\cos\left(\frac{eB\,x_{\parallel}}{p^0_{\parallel}}\right)\right) + \frac{p^0_{\perp 2}}{eB}\sin\left(\frac{eB\,x_{\parallel}}{p^0_{\parallel}}\right)\right.$$

In these equations, $p^0_{\perp 1}$, $p^0_{\perp 2}$ and $p^0_{\parallel}$ are the initial values of momentum.

The results of the locus are shown in Fig.2.

(4) The module modified in association with the calculations of the electric and magnetic fields by inputs from a file

Related modules are shown below. Inputs are set by =EM_FILE:FILE and =BM_FILE:FILE:

egs/egs5_electr.f
include/user_cg/cghead.f
include/user_cg/emfield_common.f
user_cgcode/read_emfiled.f

(5) The module modified in order to meet continuous changes in atmospheric density

The EGS5 code sets the concentration of substances by computational regions, but the newly developed code is capable of continuously changing the atmospheric density.
Related modules are shown below. Inputs are provided by setting irhofg to -1 and designating the filename:

egs/egs5_electr.f
egs/egs5_photon.f
include/user_cg/cghead.f
include/user_cg/rhofield_common.f
user_cgcode/read_rhofiled.f
user_cgcode/rd90opt.f
user_cgcode/rdoptary.f
user_cgcode/rdoptcg.f
user_cgcode/rdoptrtz.f
user_cgcode/rdoptsph.f
user_cgcode/rdoptxyz.f

(6) Determining the length of particles moving in the subroutine ELECTR
The length of particles moving in the subroutine ELECTR is determined as follows.
In calculations designed to evaluate the effects of the electromagnetic field, the routines STPEME and STPBME were used to include the energy flight direction at the moving point of particles and errors in evaluation were restricted:

tstep=MIN(tmscat,tinel,thard)
①The multiple scattering length; ②The length to the energy change point; ③The length to the collision reaction point

ustep=tstep
:
if (ustep.gt. dnear(np)) call howfar
:
④ The length to the region boundary
:
⑤ The moving length at which the maximum value of the electric field-caused energy variability becomes constant (STPEME)
:
⑥ The moving length at which the maximum value of the magnetic field-caused angle variability becomes constant (STPBME)

The minimum value of these six lengths is set as the moving length of particles.

3. Examples of Calculations

(1) Irradiation of 100 MeV electrons from the altitude of 15 km
For the atmospheric density, data derived from the "U.S. Standard Atmosphere 1976" were used. For the electric field data, data calculated by the FEM code were used.

Fig.3 shows the results of calculations (the track) performed for energy irradiation with 100 MeV electrons from the altitude of 15 km.

(2) Comparative calculations under the UCBEND [3] conditions
Fig.4 shows a diagram of the track determined under the same conditions as those of the user code UBEND generally attached to the EGS5 code.

(3) The behavior of electrons at a medium latitude (in the vicinity of the Monju reactor)
The typical behavior of electrons at a medium latitude (in the vicinity of the Monju reactor) is shown in Fig.5.

4. Conclusion

(1) In order to analyze the TGF event, a set of modules designed to analyze the effects of electrons on the electric field of a thundercloud and the terrestrial magnetism was developed and the subroutine ELECTR was modified. These modules and the modified subroutine were then incorporated into the EGS5 code. The following results were obtained.
・The electric field: Results similar to those of the calculations performed by the theoretical equation (in a vacuum) and with the EGS4 were obtained.
・The magnetic field: Results similar to those obtained under the UCBEND conditions were obtained.
(2) In the EGS5 the density of substances was set for each computational region, but the code was modified to allow the density to be changed continuously by simulating the global atmosphere.
(3) Trial calculations were performed to analyze the effects of electrons on the thundercloud electric field and the terrestrial magnetism in winter thunderclouds in a medium altitude region (in the vicinity of the Monju reactor).

References

[1] T. Torii, and T. Sugita, Development of PRESTA-CG incorporating combinatorial geometry in EGS4/PRESTA, JNC TN1410 2002-201, JAEA, Japan, 2002.
[2] T. Torii et al., Geophys. Res. Lett., **31**, L05113, doi:10.1029/2003GL019067, 2004.

[3] H. Hirayama et al., The EGS5 code system, SLAC-R-730, 2005.
[4] G. J. Fishman, et al., Science, **264**, 1313, 1994.
[5] D. M. Smith, et al., Science, **307**, 1085, 2005.
[6] A. F. Bielajew, Electron Transport in E and B Fields, in Monte Carlo Transport of Electrons and Photons, T. M. Jenkins, et al. (eds.), Plenum Pr. N.Y., 1988.

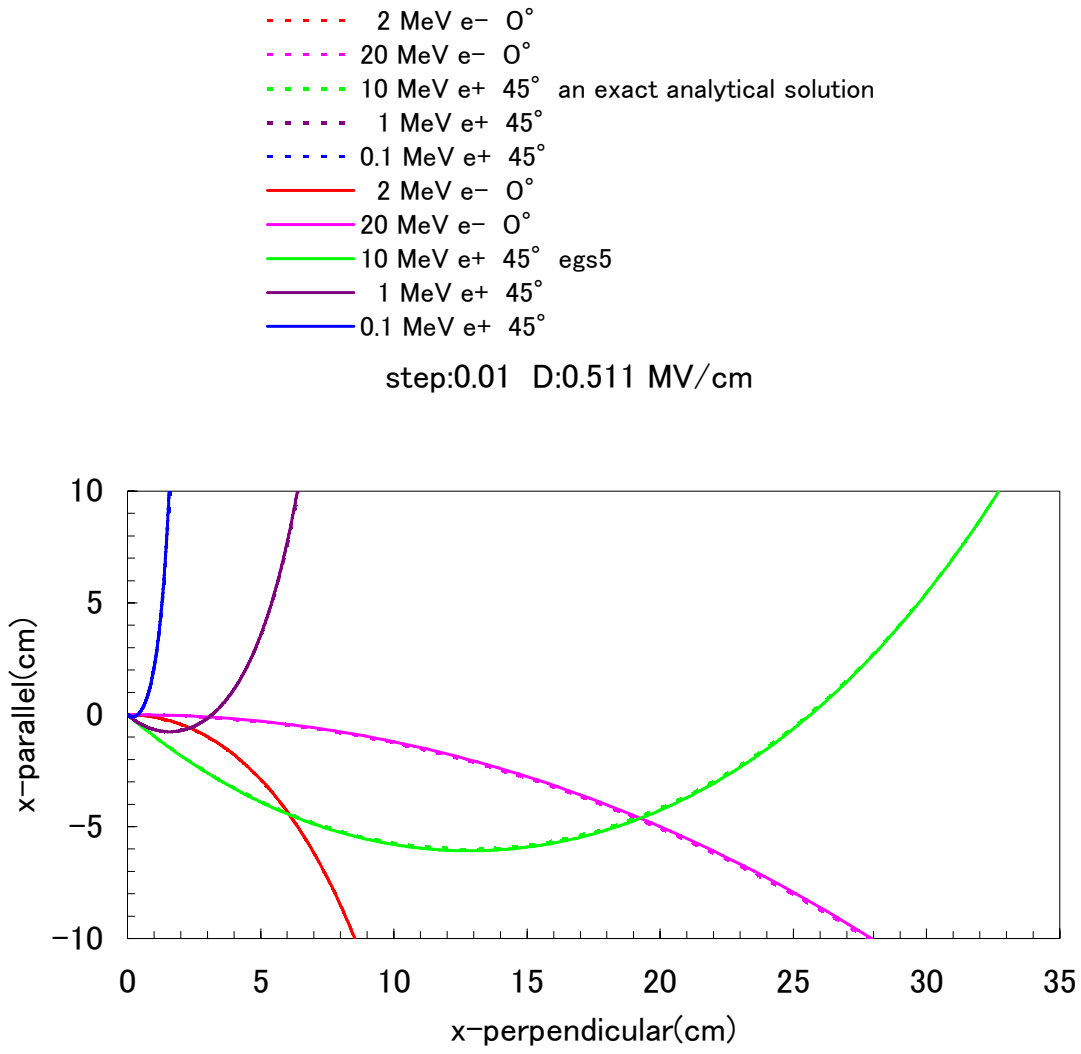

Fig.1 Electrons and Positrons Moving in the Vacuum with the Electric Field

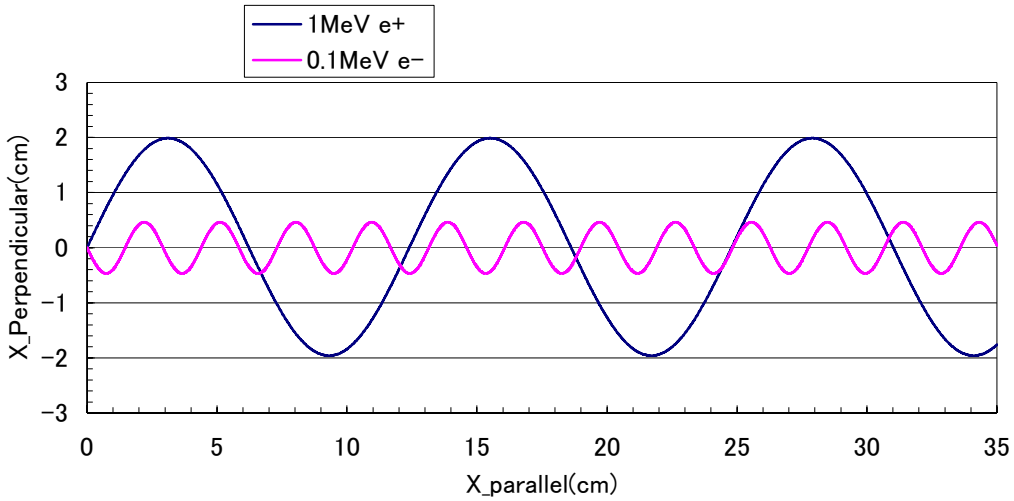

Fig.2 The Track of Charged Particles in 0.17 Tesla

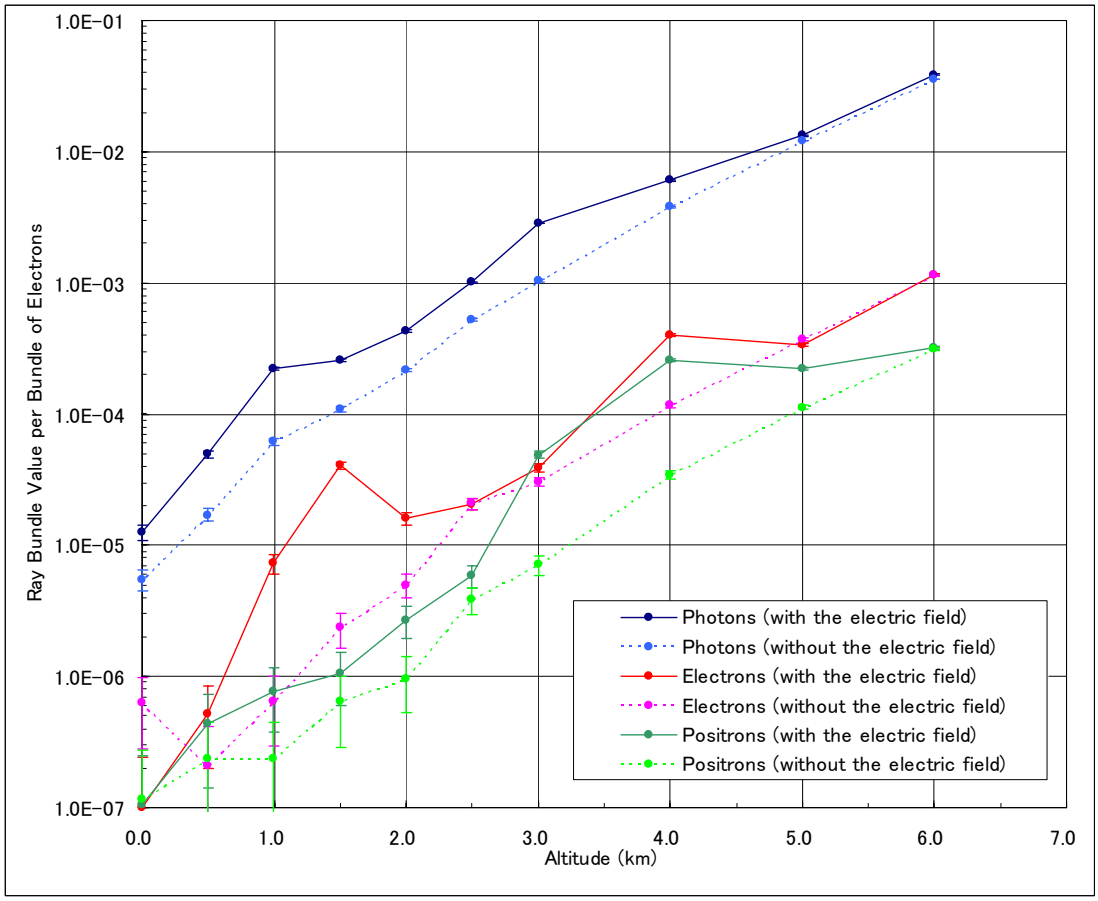

Fig.3. Data on Bundles of Rays when 100 MeV Electrons Are Emitted from the Altitude of 15 km
(Comparison of the Electric Fields)
(estepe = 0.1; continuous changes in the electric field; continuous changes in atmospheric density)

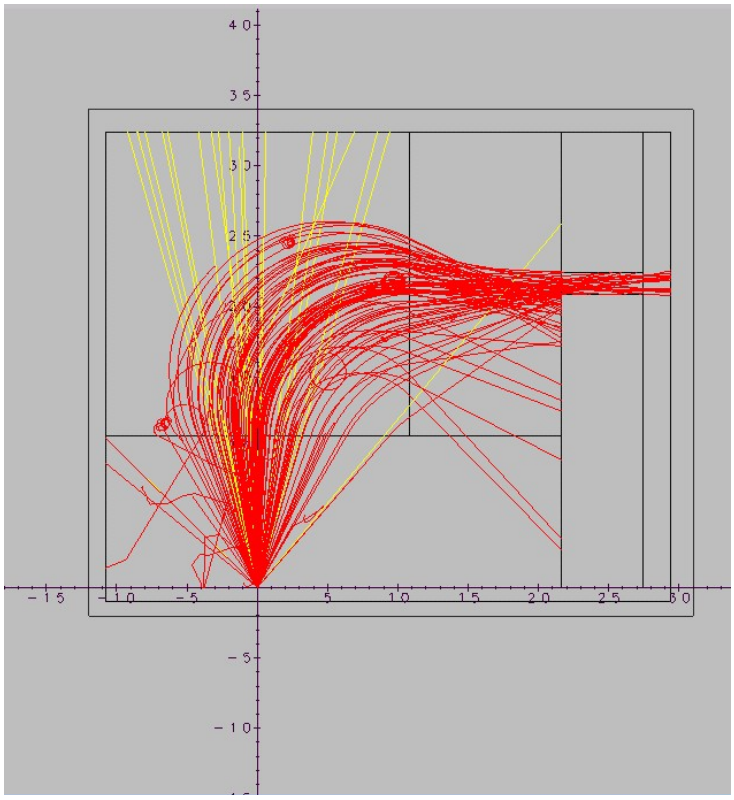

Fig.4 Calculations under the UCBEND Conditions
(8.5 MeV electrons were used to irradiate a copper plate of 0.381 mm; The intensity of the magnetic field in the Y-direction was 0.26 T.)
(Magnetic field region: X: -10.8–10.8 cm, Z: 10.8381–32.4381 cm)

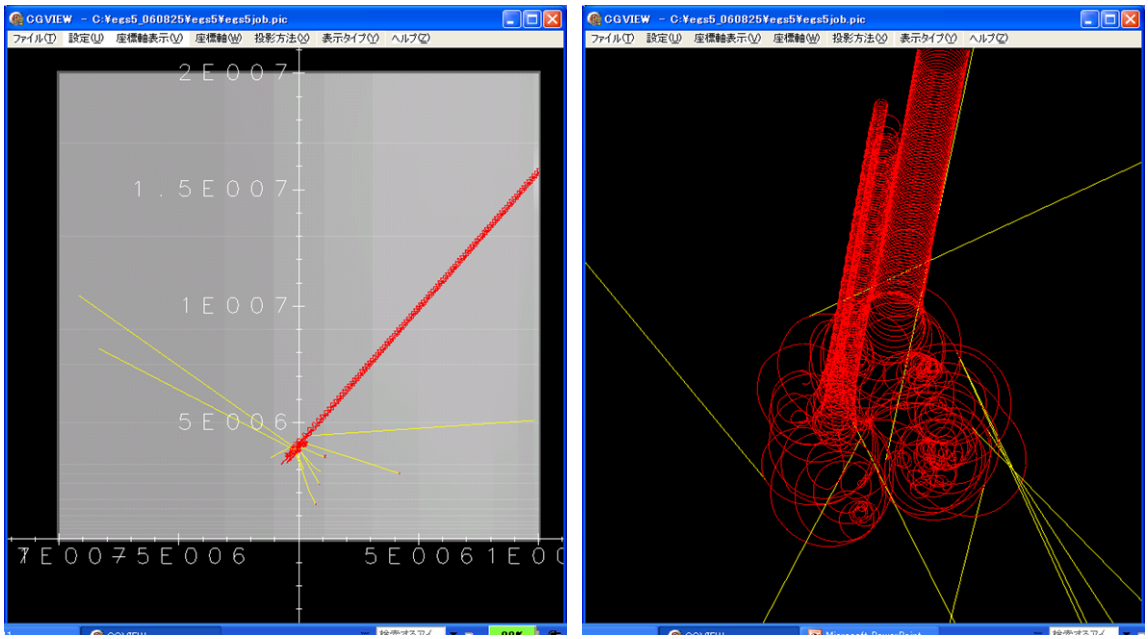

Fig.5 The Effects of Electrons on Terrestrial Magnetism at a Medium Latitude (around Tsuruga City)
(20 MeV electrons were emitted isotropically from a height of 40 km, 20 particles)

UPGRADE OF CGVIEW
(PARTICLE TRAJECTORY AND GEOMETRY DISPLAY PROGRAM)

T. Sugita[1],A. Takamura[1], Y. Namito[2], H. Hirayama[2]

[1]Science System Laboratory, Ibaraki 309-1716 JAPAN
[2]High Energy Accelerator Research Organization, Ibaraki 305-0801 JAPAN

Abstract

In a calculation using the EGS code, it is important and convenient to check geometry for calculation and particle trajectory visually for validating of the calculation conditions. Also, a graphical interface is useful for understanding the interactions. For these purposes, EGS particle trajectory and geometry 3D-display program CGVIEW has made.

1. Introduction

The EGS Shower Display system (CGVIEW) is used to display three-dimensional particle trajectories of electrons, positrons and photons on a windows PC or a Linux. The data of particles' trajectories are calculated by using the EGS code system.

It is possible to describe a complicated geometry using "Combinatorial Geometry (CG)" in the EGS calculation. The EGS Shower Display system (CGVIEW) is used to display three-dimensional particle trajectories of electrons, positrons and photons together with the geometry described in CG. It is possible to check if the geometry is properly input or not on a three-dimensional display using CGVIEW. The time to prepare the geometry may be reduced by using CGVIEW.

In CGVIEW Ver.2.2, we have added new functions there are animation display, check geometry data and saving file option.

2. Outline of new functions

2.1 Animation display

By this job you can be showing an animation that be split by the lifetime of particle.

2.1.1 Specify time option

By checking **[Specify]** in **[Specify time option]** frame in Fig.1,the Animation display is enabled with a file including lifetime data. Time range is setting to specify starting and ending lifetime of the particles. An absolute value of Time step is setting to specify the lifetime step that is wrote at one display. If Time step is a minus quantity then the starting time is always the specified starting lifetime. The unit is same as a file using unit.

2.1.2 Showing an animation

You can be showing an animation by checking the [Animation] menu in Fig.2. You can abort using double click at message area.

2.1.3. File Format of PICT file.

a)At geometry data

[CG System]
(1)CSTA
write CG data input start Symbol
CSTA = Fixed Format
CSTA-TIME = Fixed Format with lifetime data
CSTA-FREE = Free Format
CSTA-FREE-TIME = Free Format with lifetime data
CSTA-CSV = CSV Format
CSTA-CSV-TIME = CSV Format with lifetime data

Added for animation

[Excepted CG System]
(1)GSTA
write except CG data input start Symbol
GSTA = Fixed Format
GSTA-TIME = Fixed Format with lifetime data
GSTA-FREE = Free Format
GSTA-FREE-TIME = Free Format with lifetime data
GSTA-CSV = CSV Format
GSTA-CSV-TIME =CSV Format with lifetime data

Added for animation

b) At Particle trajectory data
(1)Format('0',i5) PHIS
(2)Format(i1,1p3E13.6,1pE10.3,i4,1p2E10.3)
PTYP, PX, PY, PZ, PENR, PZONO, PWGT, PTIME
(3)Format('-1')
(4)Format('9',i5) PLAT

Added for animation

2.2 Check geometry data

CGVIEW can be used to help check geometry data for an EGS calculation. Input Start Position and Direction for particle. CGVIEW checks a geometry data at middle point of boundaries(show Fig.3). if zones overlap, no define zone or outside zone's material number is not 0 then CGVIEW prints an error message.

Select **[Environment]-[Geometry Check]** in the main menu to open a window to check geometry data. If error then a message is printed in output (show Fig.4) and they are displayed by white lines (show Fig.5).

2.3 Saving file option

It is possible to print a currently displayed picture of a particle trajectory and geometry. In the main menu, select **[File]-[Print]** in fig.6. A dialog appears to select a printer. If you Checks a output to file. Then you can output to File that example is PostScript file .(Only Windows)

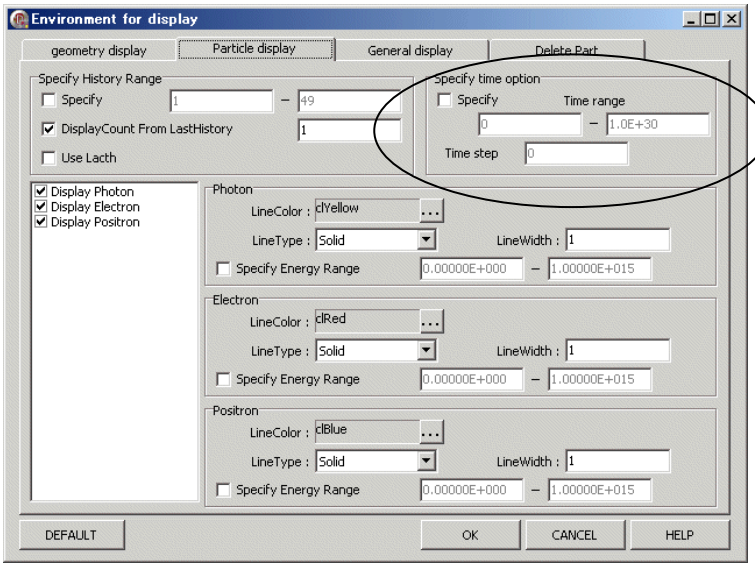

Fig.1 Window to specify a particle display

Fig.2 [Animation] menu

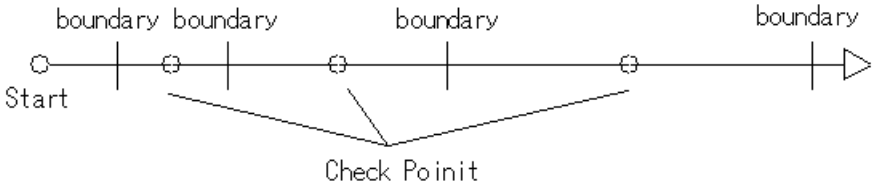

.

Fig.3 Check Geometry

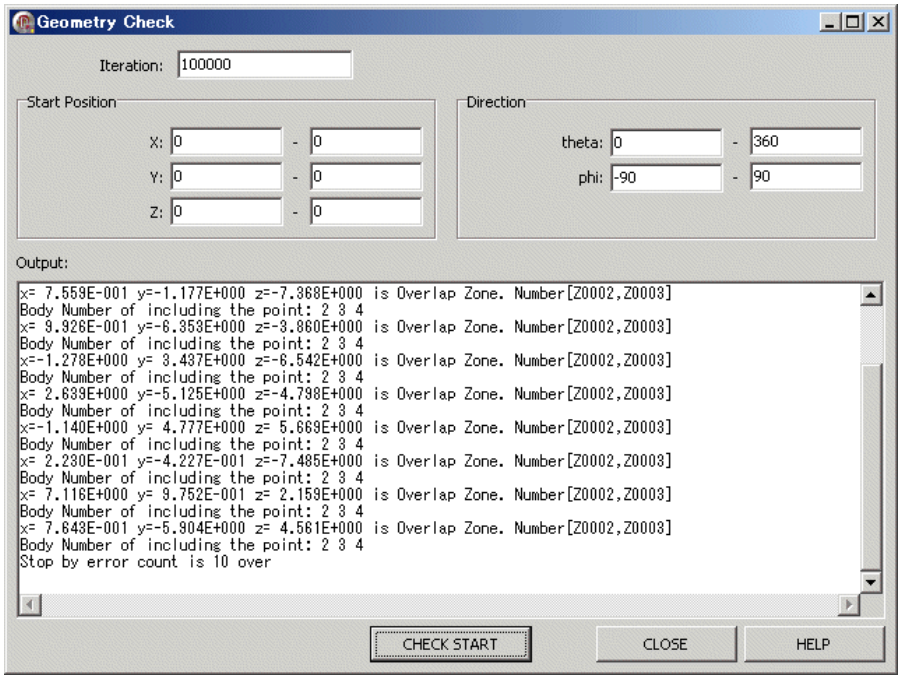

Fig.4 Output of error messages

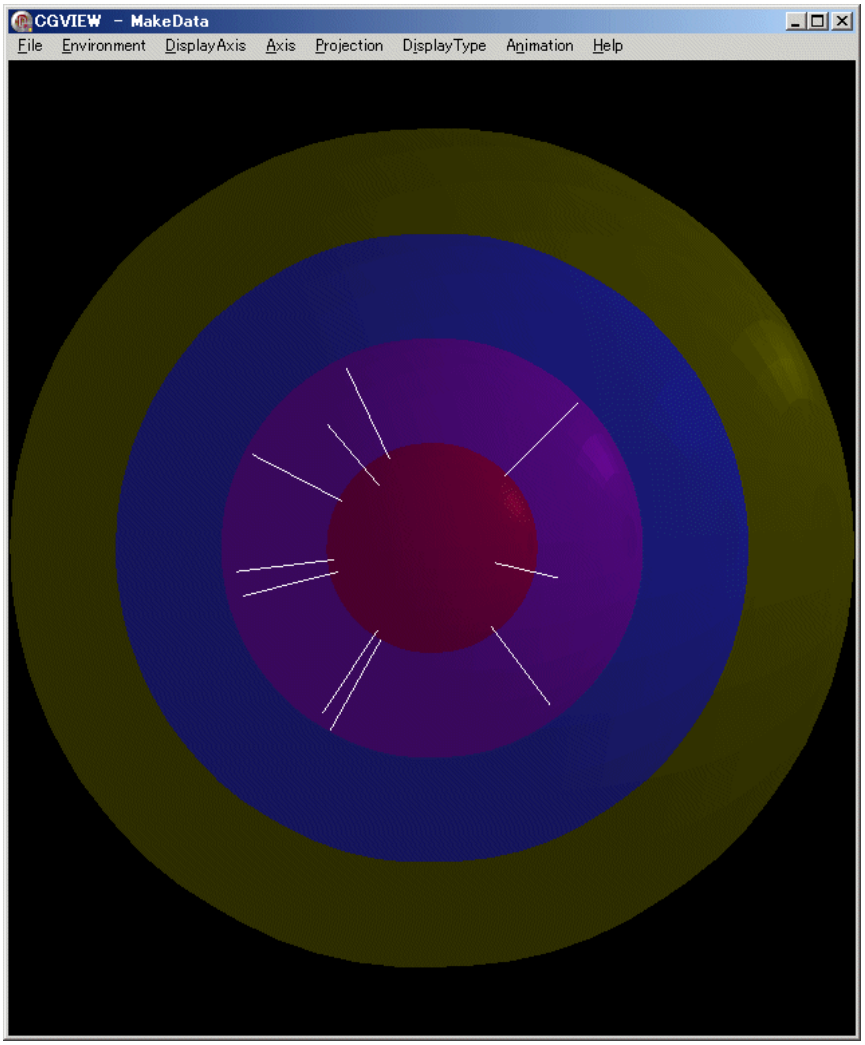

Fig.5 Sample display with white lines

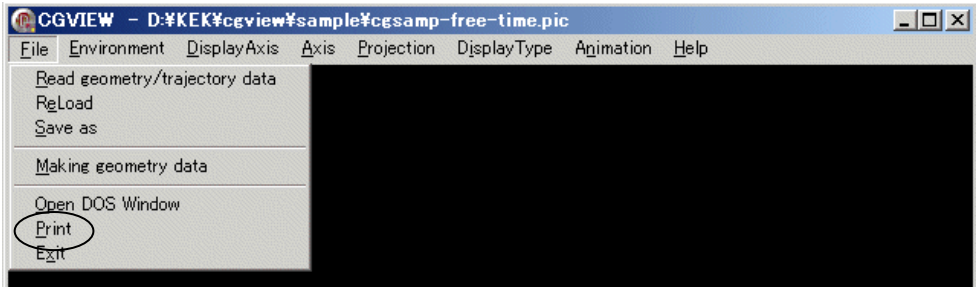

Fig.6 [Print] menu

FUNDAMENTAL EXAMINATION OF FILM DOSIMETRY IN RADIOTHERAPY II

C. Nejigaki[1], K. Tabushi[2], T. Shimosato[1,3], and Y. Aoyama[1,4]

[1]Department of Radiological Technology, Graduate School of Medicine, Nagoya University
1-1-20 Daikou – Minami, Higashi area, Nagoya, Japan
[2]Nagoya University School of Health Science
[3]Department of Radiology, Hamamatsu University School of Medicine
[4]Department of Radiology, Nagoya University School of Medicine
e-mail: stardust.seen.from.rooftop@gmail.com

Abstract

In radiotherapy the dose delivery techniques are evolved rapidly. Intensity-modulated radiotherapy (IMRT) has non-uniform complex distribution and varying two-dimensional (2D) dose distribution. Therefore it is necessary to obtain 2D data. The radiographic film is more commonly used in this situation. The radiographic film features high resolution, and obtaining 2D data easily. In radiographic film dosimetry, the film is a few deflected from the beam axis at each facility. Because of this, it is considered that when the primary photons incident the film directly, the primary photons scattered by the film first, so that a dose distribution obtained from the film do not correspond with deposition energy produced from particles scattered in a water equivalent phantom. However, the adequate length of shift and the affect of shift do not clarify. Moreover, this study verifies the affect that the radiographic film deflected from the beam axis and that difference of measuring methods by experimental measurement and Monte Carlo code EGS5. Experimental measurement and simulation performed two different arrangements. First method was that a film protruded from the upper edge of the phantom. Second method was that the upper edge of a film matched that of the phantom. In each method, films were exposed in two patterns; one was the film was set under the beam axis and the other was the film was set 2 cm off from the beam axis. Density distributions obtained by the films were converted to percentage depth dose (PDD) curves. PDD curves obtained in the first method were not in good agreement with that of the ion chamber but PDD curves in the second was in good agreement in experimental measurement. However, PDD curves measured by the films accorded with PDD curve measured by ion chamber. Moreover, first method was more available than second.

1. Introduction

In radiotherapy, as intensity-modulated radiotherapy (IMRT) and dynamic delivery techniques, the dose delivery techniques are evolved rapidly. IMRT has non-uniform complex distribution and varying two-dimensional (2D) dose distribution. Therefore it is necessary to obtain 2D data to verify the 2D dose distribution. The radiographic film is more commonly used in this situation. The radiographic film features high resolution, and obtaining 2D data easily. These features indicate that the radiographic film is available, but the radiographic film dosimetry has some problems such as film handling, quality control and energy dependence.

In radiographic film dosimetry, the film is a few deflected from the beam axis at each facility. If the film under the beam axis, the primary photon was incident into the film first and scattered by the film. Therefore the dose distributions obtained from the film did not differ from the dose distribution in water equivalent phantom. Thus, the film was set a few off from the beam axis. However the adequate length of the shift and the affect of the shift do not clarify and the standard of measuring method by radiographic film dosimetry is not firm. This study verifies the affect of the radiographic film deflected from the beam axis and that of difference in two measuring methods by experimental measurement and Monte Carlo code EGS5.

2. Materials and Methods

2.1 Film measurements

The radiographic film used in this study was Kodak X-Omat V film in Ready Pack. 10 MV X-ray beam were delivered from a Varian Clinac 21EX, 100 cm SSD, for field size of 10 x 10 cm^2. The water equivalent phantom was used tough water phantom (30 x 30 x 30 cm^3). Film calibration was carried out at depth of 10 cm and nine monitor units (30, 50, 80, 100, 150, 200, 250, 300, 350 MU). Monitor unit was calibrated by ion chamber and confirmed MU-dose linearity. To obtain the 2D dose distribution, this measurement was executed in two methods. As shown in Fig.1, the first method was that the film protruded from the surface of phantom, and as shown in Fig.2, the second was that the upper edge of film matched with the surface of phantom. Furthermore, the film was exposed in three patterns, under the beam axis, deflected 1cm from beam axis, and deflected 2 cm from beam axis. The exposed films were processed under the same conditions using automatic film processor. All film was analyzed by DD-system (R-TECH. INC). All film was digitalized by using of a scanner (EPSON Offirio ES 100000G) and all digitized film data was read digital values. Later, the density-dose correction curve was made out and percentage depth dose (PDD) curves were created by DD-system.

2.2 Monte Carlo simulation using EGS5

The simulation geometry reflected the film measurement arrangement with accuracy. The elemental composition of film, fraction by weight, was H: 0.023948, C: 0.222374, N: 0.099407, O: 0.473944, Br: 0.076736 and Ag: 0.103592; and the density was 1.731 g / cm^3 [1]. The composition of the paper used in Ready Pack for prevention of light-transmittance was assumed cellulose (C_6HO_8) and the density was 0.8050 g / cm^3. This paper wrapped the film and its thickness was 0.3 mm. The tough water phantom was used in simulation, and the elemental composition of tough water phantom, fraction by weight, was H: 0.0821, C: 0.6633, N: 0.0221, O: 0.2065, Cl: 0.0040, Ca: 0.0220. Incident energy spectrum was obtained from published data for 10 MV from a Varian Clinac 21 EX and the irradiation field size was 10 x 10 cm^2 in all simulations [2].

3. Results and Discussions

3.1 Film measurement

Fig.3 (a) shows PDD curves measured by the film that protruded from the surface of the phantom (first method). Fig.3 (b) shows the PDD curves measured by the film that upper edge of the film matched with the surface of the phantom (second method). PDD curve measured by the ion chamber was plotted in, too. The PDD curves measured by the films, shown in Fig.3 (a) and (b), do not agree with the curve measured by ion chamber. Fig.4 (a) and (b) show that the variability between the PDD curves measured by the films and the curve measured by ion chamber. The variability is defined as follows:

$$Variability = \frac{PDD_{film} - PDD_{ion-chamber}}{PDD_{ion-chamber}} \times 100\% . \quad (1)$$

As shown in Fig.4, the tendencies of almost all curves vary at about 10 cm depth obviously. This is expected that the film has over-response to low-energy photons [3]. In this study, the density-dose correction curve is made at 10 cm depth but low-energy photons are more abundant at deeper parts than 10 cm depth. Therefore the PDD curves obtained from the films overestimate the dose at deep parts of the phantom.

The affect of the film deflected from the beam axis is not significantly in both of the measuring methods. Consideration to the facility of the measurement setting, the film had better set under the beam axis.

3.2 Monte Carlo calculation

Fig.5 (a) shows the PDD curves calculated by EGS5 that reflect the geometry of the first method and Fig.5 (b) shows the PDD curves calculated by EGS5 that reflect the geometry of the second. The calculated PDD curves that are shown in Fig.5 (a) differ from the curve measured by the ion chamber. Meanwhile the PDD curves that are shown in Fig.5 (b) are in good agreement with the curve measured by the ion chamber. Moreover in the both of measuring methods, the affect of the film deflected from the beam axis is not significant.

Fig.6 shows the variability calculated by the equation (1) in the second method. Though the variability is large with depth except build up region in three patterns, the variability is less than 5% in the setting of the film under the beam axis and deflected 2 cm from the beam axis. These indicate that the second method is better than the first in point of that the PDD curves obtained from the films are closer to the curve measured by the ion chamber.

4. Conclusions

In this study, two measuring methods and three patterns are investigated. In the measurement, the PDD curves measured by the two measuring methods and three patterns are not significantly different from the curve measured by the ion chamber. In the Monte Carlo simulation, however, the PDD curves measured by the first method are significantly different from the curve measured by the ion chamber. Additionally, the curves measured by three patterns of film locations are not significantly difference. Moreover the PDD curves calculated by EGS5 in the second method are in good agreement with the curve measured by the ion chamber. These indicate that the second measuring method is more available for film dosimetry than the first and the film had better be set under the beam axis. However, the film has over-response to low-energy photons; it is necessary to improve a method of making density-dose correction curve.

References

1) Å. Palm, A. S. Kirov and T. LoSasso, “Predicting energy response of radiographic film in a 6 MV x-ray beam using Monte Carlo calculated fluence spectra and absorbed dose,” Med. Phys. 31 (12), 3168-3178 (2004).
2) Daryouth Sheikh-Bagheri and D.W.O. Rogers, “Monte Carlo calculation of nine megavoltage photon beam spectra using the BEAM code,” Med. Phys. 29 (3), 391-402 (2002).
3) Inhwan J. Yeo, C-K Chris Wang and Sandra E. Burch, “A filtration method for improving film dosimetry in photon radiation therapy,” Med. Phys. 24 (12), 1943-1953 (1997).

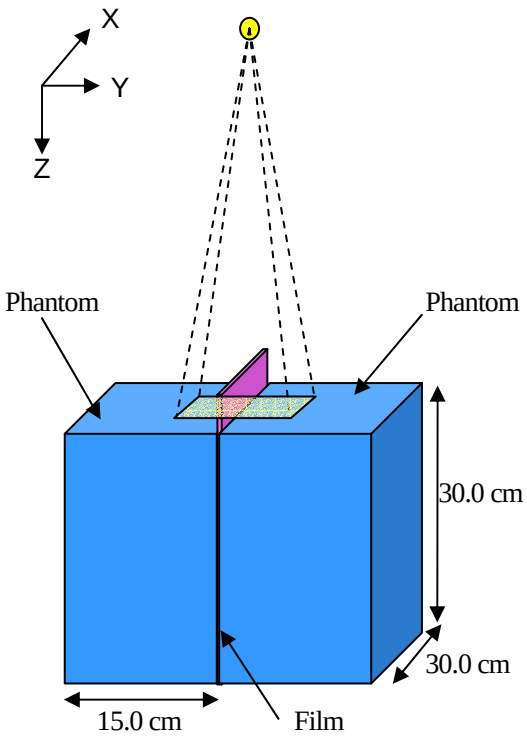

Fig. 1. The geometry that the film was protruded from the surface of the phantom (the first method).

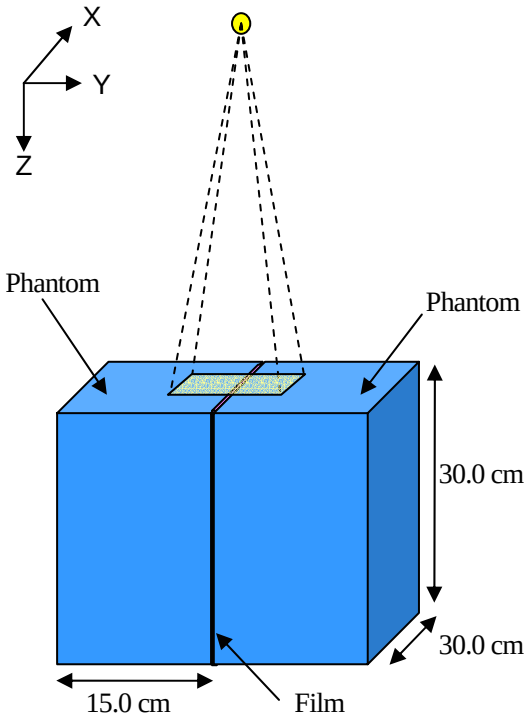

Fig. 2. The geometry that the upper edge of the film was matched with the surface of the phantom (the second method).

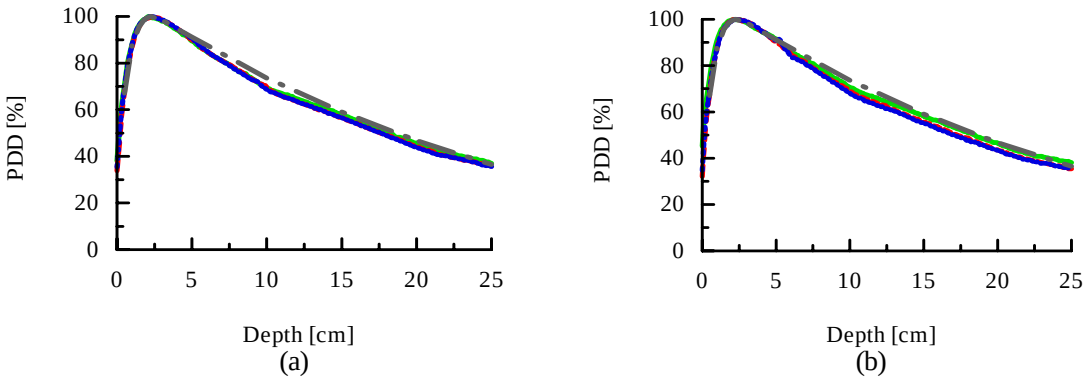

Fig. 3. The PDD curves measured by the films and the ion chamber are shown: (a) the first method (b) the second method. The solid line (green) is the PDD curve measured by the film that set under the beam axis. The dash line (red) is the PDD curve measured by the film that deflected 1 cm from the beam axis. The dot line (blue) is the PDD curve measured by the film that deflected 2 cm from the beam axis. The long dash-dot line (gray) is the PDD curve measured by the ion chamber.

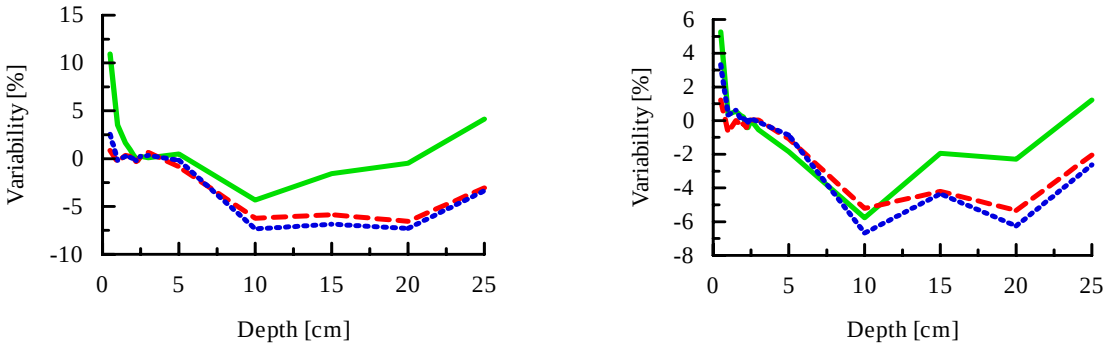

Fig. 4. The variability curves that calculated by the equation (1) are shown: (a) in the case of the first method, (b) in the case of the second method. The solid line (green) is the variability measured by the film that set under the beam axis. The dash line (red) is the variability measured by the film that deflected 1 cm from the beam axis. The dot line (blue) is the variability measured by the film that deflected 2 cm from the beam axis.

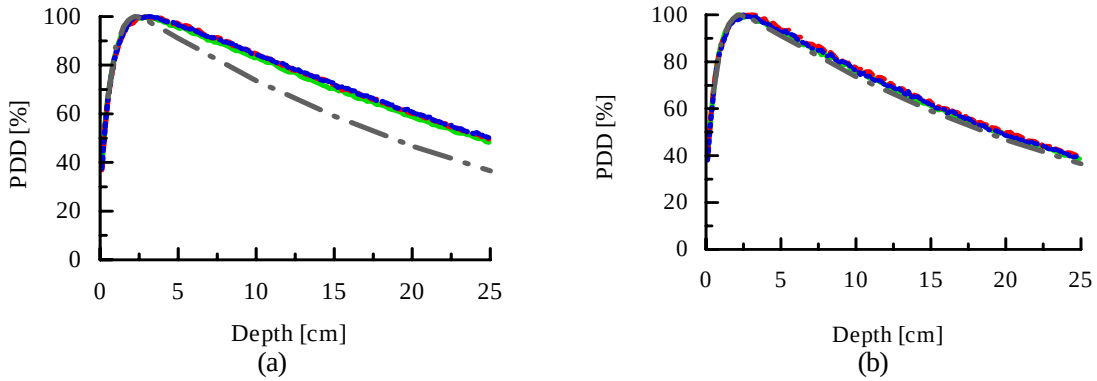

Fig. 5. The PDD curves that calculated by EGS5 and the curve measured by the ion chamber are shown: (a) reflection of the geometry of the first method, (b) reflection of the geometry of the second method. The solid line (green) is the PDD curve calculated by EGS5 that the film sets under the beam axis. The dash line (red) is the PDD curve measured by the film that deflected 1 cm from the beam axis. The dot line (blue) is the PDD curve measured by the film that deflected 2 cm from the beam axis. The long dash-dot line (gray) is the PDD curve measured by the ion chamber.

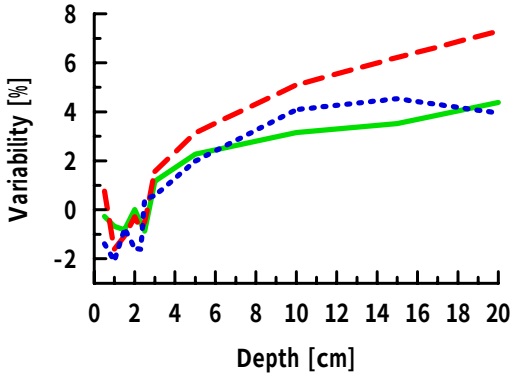

Fig. 6. The variability curves that calculated by the equation (1) are shown. The solid line (green) is the variability calculated by EGS5 that geometry is setting the film under the beam axis. The dash line (red) is the variability calculated by EGS5 that geometry is setting the film deflected 1 cm from the beam axis. The dot line (blue) is the variability calculated by EGS5 that geometry is setting the film that deflected 2 cm from the beam axis.

Investigation of a Shielding Plate used for Intraoperative Electron Beam Radiation Therapy of Breast Cancer

T. Oshima[1], K. Tabushi[2], Y. Aoyama[1, 3], C. Nejigaki[1] and H. Shibata[1]

[1]Department of Radiological Technology, Graduate School of Medicine, Nagoya University
1-1-20 Daikou-Minami, Higashi ward, Nagoya, Japan
[2]Department of Radiological Technology, School of Health Science, Nagoya University
[3]Division of Radiology, Nagoya University Hospital
e-mail: j070204m@mbox.nagoya-u.ac.jp

Abstract

Intraoperative electron beam radiation therapy (IOERT) is one option of radiotherapy following breast-conserving surgery. IOERT in breast-conserving therapy includes some issues and one of them is the undesirable dose to the some normal tissue which surround breast such as the pectoralis major muscle and the lung. The goal of this study is to investigate the feasible material and structure for a plate which prevents the unfavorable dose using Monte Carlo simulation code EGS5. Metal was chosen as the main material of the plate and poly-methyl methacrylate (PMMA) was positioned on the back side of metal to absorb the electrons scattered backward (backscattered electron) in metal. Three types of metal, aluminum (Al), cuprum (Cu) and lead (Pb), were selected as the material. The shielding capability of each metal and the magnitude of the dose yielded by backscattered electrons (backscatter dose) were explored to choose the suitable metal for the plate. The appropriate thickness of PMMA and that of metal were examined after the favorable metal was determined. The favorable metal for the plate was Cu since Al could not prevent the dose sufficiently and Pb scattered electrons backward excessively. To absorb the backscatter dose, the thickness of PMMA should be 7 mm and the 3 mm Cu was necessary to shield the electron beam which had already transited the breast tissue. In this work, the optimum metal and structure for the plate which prevent the undesirable dose to the normal tissue were determined.

1. Introduction

Intraoperative electron beam radiation therapy (IOERT) is one option of radiotherapy following breast-conserving surgery [1]. IOERT has not been a major option due to the difficulty of transferring patients from an operating room (OR) to a sanitized treatment room within the Department of Radiation Oncology to perform IOERT [2]. That difficulty was, however, settled by the introduction of mobile linear accelerators. Mobile accelerators can be placed in OR and IOERT can be implemented in OR. IOERT operated in OR, however, includes some issues and one of them is the undesirable dose to the some normal tissue which surround breast.

On IOERT after breast-conserving surgery, the residual breast cancer is irradiated and at the same time the pectoralis major muscle and the lung are also exposed. Some complications associated with IOERT are sometimes occurred due to the dose to these normal tissue. However, this unfavorable dose can be shielded by locating a plate on the pectoralis major muscle. In this work, the optimum material and structure for the shielding plate were explored using the Monte Carlo (MC) simulation code EGS5.

2. Materials and Methods

2.1 Material selection and structure of the plate

Consorti el al. implemented IOERT with a 1-cm-thick poly-methyl methacrylate (PMMA) disk positioned on the pectoralis major muscle to prevent any irradiation of the chest wall [3]. As shown in Fig. 1, however, a PMMA disk could not adequately reduce the dose to the chest wall. Therefore, metal was selected as a main material of the plate. It is known that the electron beam is scattered in metal and a few percent of electrons are scattered backward as the backscattered electrons. As the backscattered electron causes the unnecessary dose to the normal breast tissue, a PMMA was positioned on the back side of the metal, where electron beam enter, to prevent the dose yielded by backscattered electron (back scatter dose). Consequently, the structure of the plate is shown in Fig. 2. In this study, aluminum (Al), cuprum (Cu) and lead (Pb) were selected as metal for the plate, though these are usually used for the photon shielding. The thickness of metal and PMMA is described in the next part.

2.2 EGS5 simulation

Since the backscatter dose could not actually be measured and it was difficult to make three types of the plate consisting of each metal and PMMA, the plates were simulated with MC simulation code EGS5 and the central axis depth dose curves and the backscatter dose curves were obtained. The plate was placed in a 30 x 30 x 30 cm^3 water phantom and the back surface of the plate was matched to the level at the depth of R_{90} (d_{R90}), at which the PDD on the central axis was 90 %, so that the planning target volume was covered with 90 % isodose. The d_{R90} was determined from the measured percent depth dose curve. The geometry is shown in Fig. 3. The electron beam energy was 6 MeV and 12 MeV and their energy spectra and angular distributions used in this simulation were made from the phase space data on the surface of the water phantom at 100 cm source surface distance (SSD) for 10 x 10 cm^2 irradiation field [4]. Though the electron beam generally includes not only electrons which get to the surface of the phantom directly or are scattered in treatment head but also contamination photons, the photons were excluded from electron beam in this simulation as it seemed to be difficult to shield the photons with the plate. Each thickness of metal was 3 mm and 6 mm for 6 and 12 MeV, respectively, so as to shield the electron beam sufficiently and the thickness of PMMA were 5 mm and 10 mm for each energy. The value of d_{R90} and the thickness of metal and PMMA were summarized in Table 1. The electrons, which were going into PMMA region from metal region and had the opposite z component of direction cosine against the incident electron, were defined as backscattered electrons in this simulation using the latch option.

2.3 Evaluation of the shielding capability and backscatter dose

To evaluate the shielding capability of each metal, the distance from the front surface of metal to the point at which the relative dose behind metal fell below 1 % was defined as d_F. If the value of d_F is observed, this indicates a plate can not prevent the electron dose enough. And the distance from back surface of metal to the point at which the relative backscatter dose fell less than 1 % was defined as d_B to estimate the magnitude of backscatter dose. If the value of d_B is beyond the thickness of PMMA, this represents the normal breast tissue is affected by the backscatter dose. The actual distance of d_F and d_B on the depth dose curve is shown in Fig. 4. According to d_F and d_B, the favorable metal was selected.

2.4 Determination of the optimum thickness of metal and PMMA for making a practical plate

After the favorable metal was selected, the additional simulations were executed for 12 MeV electron beam to decide the optimum thickness of PMMA which absorbed the backscatter dose and that of the metal which prevented the electron dose. First, the thickness of metal was stabilized at 6 mm and that of PMMA was varied from 6 mm to 8 mm. Second, the thickness of PMMA was fixed at the determined thickness and that of the metal was changed from 1 mm to 3 mm.

3. Results and discussions

3.1 The shielding capability of metal and the magnitude of the backscatter dose

Figs. 5 (a) and (b) show the MC simulated central axis total depth dose curves and the backscatter dose curves in the combination of each metal and 5 and 10 mm PMMA for 6 MeV electron beam in the water phantom. Each curve was normalized to the maximum among the values calculated by subtracting the backscatter dose from the total depth dose to assess the magnitude of the backscatter dose. Figs. 6 (a) and (b) are the same curves as Fig. 5 for 12 MeV. In figs. 5 and 6, a transparent area represents the region in which PMMA was located and a dark area represents metal region. The values of d_F and d_B were calculated by linear interpolation of each curve and summed up in Table 2.

As shown in Figs. 5 (a), (b) and Fig. 6 (a), the transit dose was observed in the combination of Al and two types of PMMA thickness for 6 MeV and that of Al and 5 mm PMMA for 12 MeV. Thus, the d_F of Al was observed in these three cases while those of Cu and Pb were not observed as shown in Table 2. This implies that Al is not suitable for a shielding material of the plate. On the other hand, in the combination of each metal and 5 mm PMMA for 12 MeV and that of Pb and 5 mm PMMA for 6 MeV the d_B exceeded the thickness of PMMA as shown in Table 2. Furthermore, the Pb's d_B was the largest in the any combination of each metal and two types of PMMA thickness for each energy. Although Cu and Pb were feasible metal for the plate in terms of the shielding capability, Pb was not appropriate regarding the backscatter dose due to its excessive d_B. As the plate will be inserted between the breast tissue and the pectoralis major muscle, a thinner plate is desirable. Therefore, Cu is more favorable metal for the plate since it scattered less electrons backward than Pb.

3.2 The optimum thickness of PMMA and Cu

Table 3 shows the values of Cu's d_B obtained by the additional MC simulation and the linear interpolation. In the simulation, the PMMA thickness was varied while the Cu thickness was fixed. As shown in Table 3, d_B in 7mm PMMA corresponds with the PMMA thickness. Thereby, the optimum thickness of PMMA for absorbing the backscatter dose from Cu was 7 mm.

The values of Cu's d_F obtained via the incremental simulation and the interpolation were shown in Table 4. The thickness of Cu was changed and that of PMMA was 7 mm in the simulation. Almost all electrons were shielded by the plate in 3 mm Cu while there were the transit dose in 1 mm and 2 mm Cu as shown in Table 4. Consequently, 3 mm thickness was the suitable for shielding electron beam.

4. Conclusions

The optimum metal and structure for the plate were determined in this study using the MC simulation. However, it has to be considered that the plate can not prevent the dose caused by contamination photons. In the near future, the practical plate based on this data will be made and the verification of the practical plate will be executed.

References

1) R. Orecchia, M. Ciocca, R. Lazzari, C. Garibaldi, M. C. Leonardi, A. Luini, M. Intra, G. Gatti, P. Veronesi, J. I. Petit and U. Veronesi "Intraoperative radiation therapy with electrons (ELIOT) in early-stage breast cancer," The Breast, **12**, 483-490 (2003).
2) A. S. Beddar, P. J. Biggs, S. Chang, G. A. Ezzell, B. A. Faddegon, F. W. Hensley and M. D. Mills, "Intraoperative radiation therapy using mobile electron linear accelerators" Report of AAPM Radiation Therapy Committee Task Group No. 72.
3) R. Consorti, A. Petrucci, F. Fortunato, A. Soriani, S. Marzi, G. Iaccarino, V. Landoni and M. Benassi "IN VIVO DOSIMETRY WITH MOSFET: DOSIMETRIC CHARACTERIZATION AND FIRST CLINICAL RESULTS IN

INTRAOPERATIVE RADIOTHERAPY," Int. J. Radiat. Oncol., Biol., Phys. **63**, 952-960 (2005).

4) G. X. Ding and D. W. O. Rogers "Energy spectra, angular spread and dose distributions of electron beams from various accelerators used in radiotherapy" PIRS-0439.

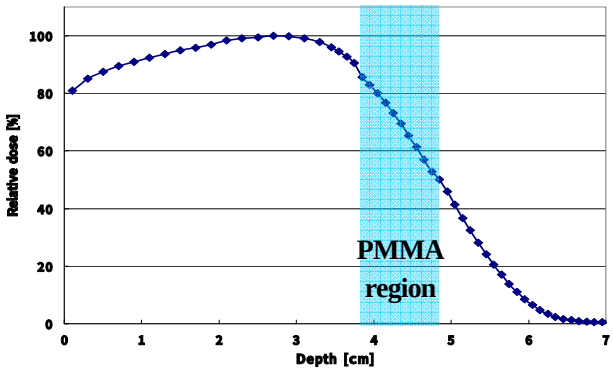

Fig. 1. The central axis depth dose curve in the water phantom for 6 MeV with a 1-cm-thick PMMA plate positioned at depth of R_{90}.

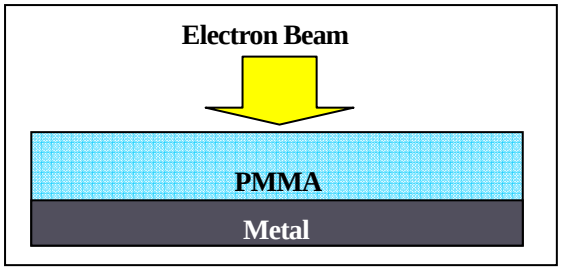

Fig. 2. The structure of the plate.

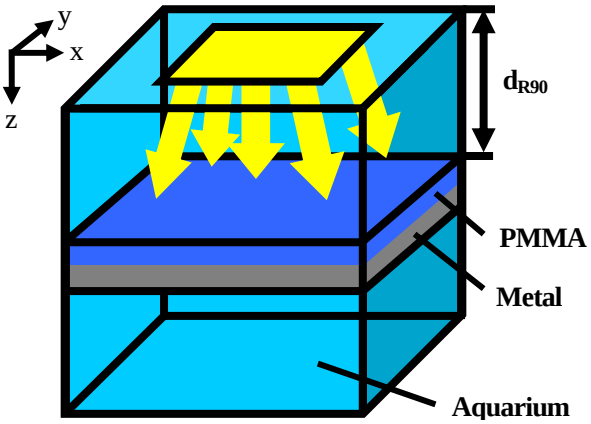

Fig. 3. Geometry.

Table 1. The combination of beam energy, d_{R90} and the thickness of PMMA and metal.

Beam energy [MeV]	6	12
d_{R90} [mm]	18	38
PMMA thickness [mm]	5.0, 10	
Metal thickness [mm]	3.0	6.0

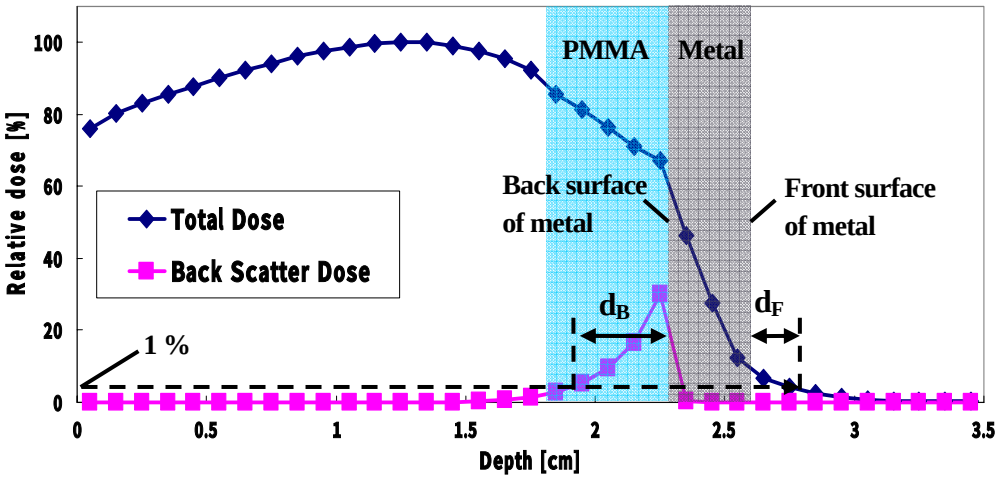

Fig. 4. The actual distance of d_B and d_F on the depth dose curve.

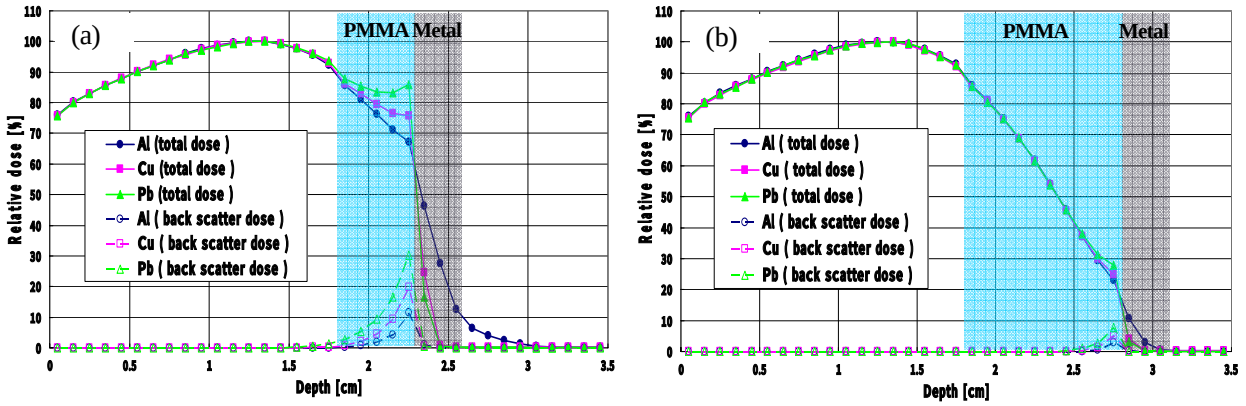

Fig. 5. The central axis depth dose curve in the water phantom for 6 with the plate consisting of: (a) the combination of 5 mm PMMA and each metal (b) the combination of 10 mm PMMA and each metal.

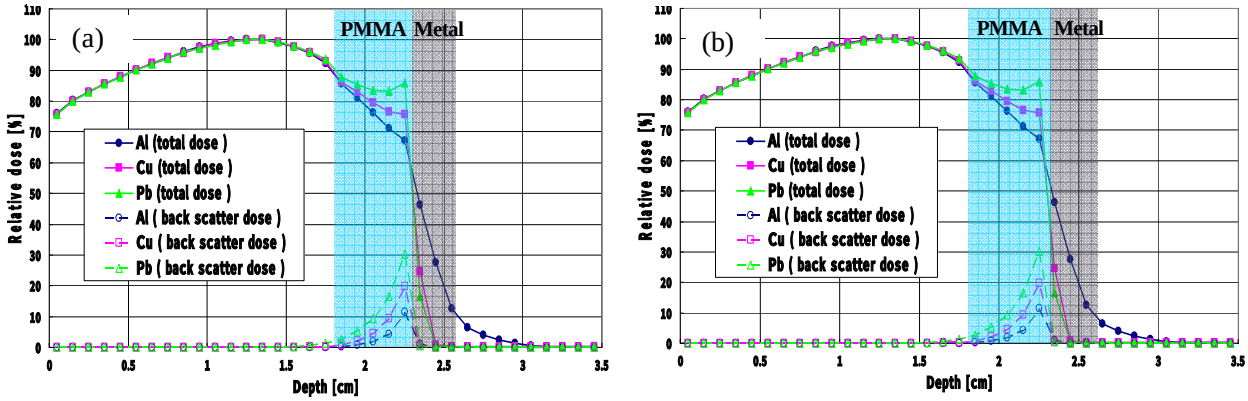

Fig. 6. The central axis depth dose curve in the water phantom for 12 with the plate consisting of: (a) the combination of 5 mm PMMA and each metal (b) the combination of 10 mm PMMA and each metal.

Table 2. The values of d_F and d_B calculated by linear interpolation of each curves on Figs. 5 and 6.

Energy [MeV]		6			12		
Metal		Al	Cu	Pb	Al	Cu	Pb
5 mm PMMA	d_F [mm]	3.86	-	-	10.2	-	-
	d_B [mm]	3.18	4.38	5.98	5.51	8.34	11.8
10 mm PMMA	d_F [mm]	-	-	-	4.06	-	-
	d_B [mm]	1.26	1.68	2.48	3.88	5.68	7.90

Table 3. The values of d_B obtained by the additional simulation in which the PMMA thickness was varied.

PMMA thickness [mm]	6.0	7.0	8.0
d_B [mm]	7.7	7.0	6.6

Table 4. The values of d_F obtained by the additional simulation in which the Cu thickness was varied.

Cu thickness [mm]	1.0	2.0	3.0
d_F [mm]	14.1	5.7	-

Comparison between EGS5 and GEANT4 in simulations with the model of cobalt teletherapy unit

H. Shibata, K. Tabushi[1], C. Nejigaki, and T. Oshima

Department of Radiological Technology, Graduate School of Medicine, Nagoya University
1 - 1 - 20 Daikou - Minami, Higashi-ku, Nagoya, Japan
[1]Nagoya University School of Health Science
e-mail: h.shibata0715@gmail.com

Abstract

Recently, hadrontherapy is gaining popularity among the public along increase in the hadrontherapy facilities. In that situation, it was thought that a Monte Carlo (MC) code which could transport the ion particles used in hadrontherapy had to be introduced into our laboratory. At the present, several MC codes such as GEANT and PHITS are well known for their handling the ion particles. GEANT4 is chosen and is in the middle of the introduction into our laboratory. Upon introducing GEANT4, the comparison between measured data and calculation results by GEANT4 and EGS5 codes were required. The cobalt teletherapy unit in our university was selected as a simulation model for the comparison, and simulations were performed on the condition that a field size of 10 x 10 cm^2 was set at a source-surface distance of 80 cm. Tough water phantom as the scoring regions was set at 80 cm away from source. In this work, the photon energy spectra on the surface of the phantom, the percent depth dose (PDD), and the off-center ratio (OCR) at the calibration depth were investigated. In the comparison of photon energy spectra, the significant difference was found. The PDD curves calculated with EGS5 and GEANT4 were agreed with each other, though the measured PDD curve disagreed with the simulated PDD curves in the build up region. The measured and simulated OCR curves were not agreed with each other around outside of the irradiation field. The causes of the errors described above are not obvious and are now being investigated.

1. Introduction

These days, hadrontherapy gains publicity with increasing the facilities, and the number of patients whom hadrontherapy is applied to will increase from now on. The occasions to investigate about the therapy with Monte Carlo (MC) simulations may appear. Though the MC code EGS5 [1] are used in our laboratory, it can handle only photon, electron and positron. In that situation, we had to introduce a Monte Carlo code that can transport the ion particles.

It becomes popular that the MC codes such as GEANT [2] and PHITS can handle ion particles and GEANT4 is now being introduced into our laboratory. GEANT4 provides various types of particles. For example, we can use not only ordinary particles like photon, electron and positron but also hadrons such as proton and carbon ion and optical photon. GEANT4 also provides diverse physics processes related to them. On GEANT4, geometry is constructed by combining predefined solids by Boolean operations, and that method is similar to the method using CGVIEW on EGS5. This method enables to construct complex structures [3].

On the introduction of GEANT4, the basic validation of it was previously performed. The calculated percent depth dose (PDD) curve in tough water phantom with Co-60 gamma ray from isotropic point source was compared to the PDD curve by EGS5, and that showed good agreement between them. In this work, GEANT4 ver. 4.8.3 and EGS5 ver. 1.0.2 were used, and the calculation results using the model of the cobalt teletherapy unit were compared between by

GEANT4 and EGS5. In particular, the photon energy spectra on the surface of the phantom, the PDD curves, and the off-center ratio (OCR) curves at the calibration depth were investigated. The cobalt teletherapy unit in our university was selected as the model for the comparison because the kinetic energy of Co-60 gamma ray was relatively low in energy range of radiotherapy and the measured data could be taken easily from the past examined data.

2. Materials and Methods

2.1 Modeling of the cobalt teletherapy unit

The cobalt teletherapy unit (ISOTRON RTGS-21, SHIMADZU) was modeled by referring its design. Figures 1(a) and (b) show the overviews of the geometries constructed with GEANT4 and EGS5, respectively. The cylinders were used for the cobalt source and its stainless container, and the inner tungsten shield wall and the outer lead one were modeled with rectangular solids. The exit window below the container was shaped as cone. The collimators of the real cobalt teletherapy unit have 6 tungsten plates which are joined to a tungsten square bar. As shown in figure 2(a), the collimators were re-created in the simulation with GEANT4. As shown in figure 2(b), we substituted trapezoidal boards for them by EGS5 because their structure was too complex to construct by writing subroutine HOWFAR for computing efficiency. Tough water phantom for scoring regions was 15 cm in half width and 30 cm thick, and the surface of it was set at 80 cm away from the bottom of the source. We set a field size of 10×10 cm^2 at the surface of the phantom by controlling the positions of collimators. The cut-off energies of photon and electron were 10 keV and 521 keV, respectively.

2.2 Simulations

2.2.1 Calculation of the photon energy spectra

The photon energy spectra were calculated on the surface of the tough water phantom, and the photons moving into the phantom were scored. Incident Co-60 gamma rays were uniformly irradiated from inside of the source region, and as shown in figure 3, the three patterns of incident directions were examined for computing efficiency. One of them was the isotropic source at each irradiation point inside the cobalt source. Another was the hemispheroidal isotropic source which was domed on the side of the phantom, and the other was the cone-shaped source of which incident directions were limited so that incident Co-60 gamma rays were able to go through the exit window.

2.2.2 Percent Depth Dose

Calculation of PDD curves was performed with the each model of the cobalt teletherapy unit on EGS5 and GEANT4. The boxels were allocated on the center axis of beam in tough water phantom and calculated PDD curves on the axis as shown in figure 4. The boxel sizes were 0.5 x 0.5 x 0.1 cm^3 from the 0.1 cm to 1.2 cm depth, and 0.5 x 0.5 x 0.5 cm^3 from 1.5 cm depth to 29.5 cm depth. The pattern of incident beam was the cone-shaped source so that the fraction of the incident particles moving into the phantom was increased.

The measured data were the past data of our laboratory which was measured with the ion chamber.

2.2.3 Off-center ratio at the calibration depth

Boxels which size were 0.5 x 0.5 x 0.5 cm^3 were placed on a grid at the calibration depth in the phantom perpendicular to the center axis of the beam for calculating the OCR curves as shown in figure 5. The dose distribution was calculated from deposit energies in the boxels and the OCR curve was obtained from it. In common with the calculation of the PDD curve, the pattern of incident beam was the cone-shaped source.

The measurement data were obtained by the film dosimetry. The film was placed in the phantoms at right angle to the center axis of the beam in the calibration depth and exposed by Co-60 gamma ray. It was processed with DD system(R-TEC.INC.), and the OCR curve was obtained.

3. Results and Discussions

3.1 Calculation of the photon energy spectra

Figures 6(a) and 6(b) show photon energy spectra at the surface of the phantom calculated with EGS5 and GEANT4 respectively, and figures 7(a) and 7(b) show the part of the low fraction in spectra. Each spectrum on the figures was calculated with three patterns of incident beam described above. The peaks of fluorescent X-rays and annihilation gamma-rays were found on each spectrum, respectively as shown in figure 7(a). In comparisons among three spectra, the fraction of low energy photons was increased by broadening the incident beam, and the fraction of the photons of which kinetic energies were from about 200 keV to 300 keV notably changed. It was speculated that these were the photons which were scattered by the Compton Effect in the upper part of the teletherapy unit. As shown in figure 7(b), the peaks of fluorescent X-rays and annihilation gamma rays were also seen, and the fraction of low energy photons increased by spreading incident beam too.

The number of photons of which kinetic energies were around 250 keV was not increased so much on the spectrum which was computed with the isotropic source by GEANT4 as compared to the spectra calculated by EGS5 (figure 8). In the comparison of spectra calculated with the cone shaped source, they show agreement with each other. The difference between spectra by EGS5 and GEANT4 was become significant by broadening the incident photon beam. The cause of this phenomenon has not become clear.

3.2 PDD

Figure 9 shows the PDD curves measured with an ion chamber and computed with EGS5 and GEANT4. The maximum depths were 0.5 cm and 0.7 cm calculated with EGS5 and GEANT4, respectively. The measured maximum depth of 0.5 cm corresponded to that with EGS5. The disagreement of the maximum depth with GEANT4 was caused by statistical error and should be improved as a result of the calculation carried on. The simulated PDD curves agreed well with each other, and they also showed an agreement with the measured PDD curve except in the build-up region.

3.3 OCR at calibration depth

Figure 10 shows the OCR curves at calibration depth which were measured by the film dosimetry and calculated with EGS5 and GEANT4. The OCR curves computed with EGS5 and GEANT4 were fitted with each other. The measured OCR curve was agreed with the simulated OCR curves in the irradiation field, but the disagreement was seen around the both field edge. It might be caused by the characteristic of the film dosimetry.

4. Conclusions

In this work, the comparisons between EGS5 and GEANT4 were performed on the subjects of the photon energy spectra at the surface of the tough water phantom, the PDD curves, and the OCR curves. In the comparison of photon energy spectra, the significant difference was found when the spectra were computed with the isotropic source. The spectra simulated with the cone shaped source agreed with each other. The PDD curves and OCR curves computed with EGS5 and GEANT4 did not show the significant difference between each curve, respectively. By comparison between the measured PDD curve and the simulated PDD curves, it illustrated agreement except in the build up region. The measured OCR curve was agreed with the calculated OCR curves in the irradiation field, but the measured OCR curve showed higher values than the simulated ones around outside of the field. The validation of GEANT4 in our laboratory is in progress and the causes of various differences are investigated now.

References

1) H. Hirayama, Y. Namito, A.F. Bielajew, S.J. Wilderman and W.R. Nelson, “The EGS5 Code System,” SLAC-R-730 (2005)

2) GEANT4 Collaboration, "GEANT4 User's Guide for Application Developers" [online], available at http://geant4.web.cern.ch/geant4/support/userdocuments.shtml
3) Emily Poon and Frank Verhaegen, "Accuracy of the photon and electron physics in GEANT4 for radiotherapy applications," Med. Phys. **32**, 1696-1711 (2005).

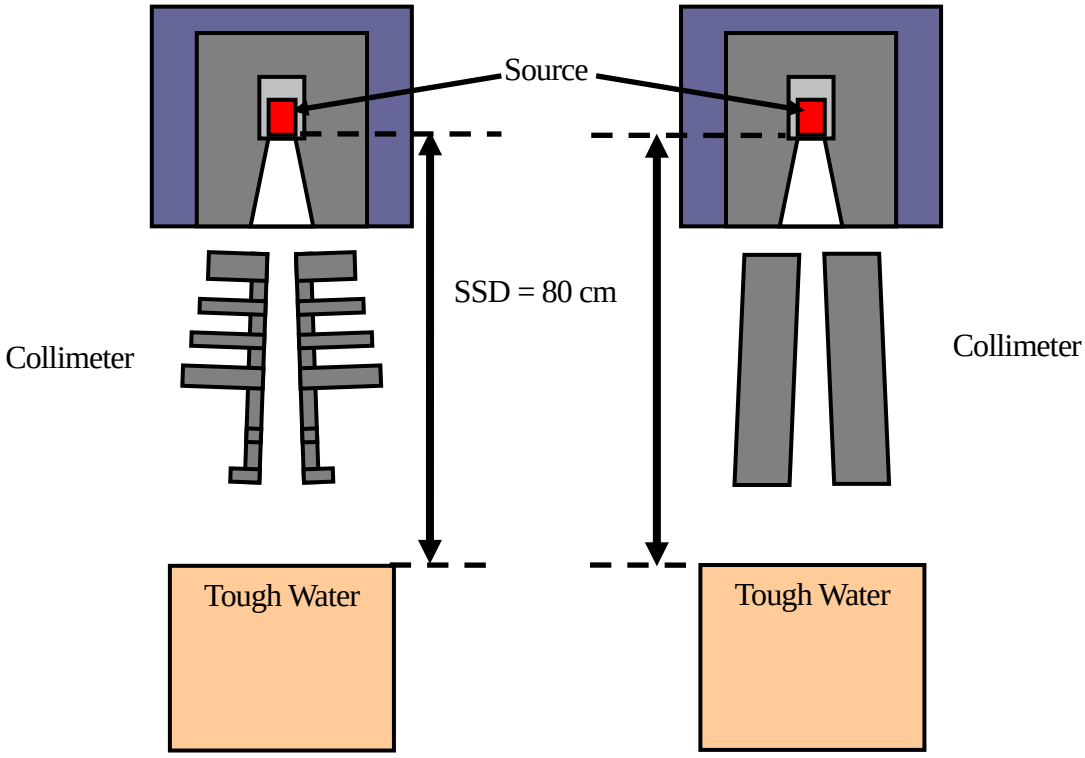

figure 1. Overview of the geometries that the cobalt teletherapy unit was modeled:
(a) with GEANT4 (b) with EGS5

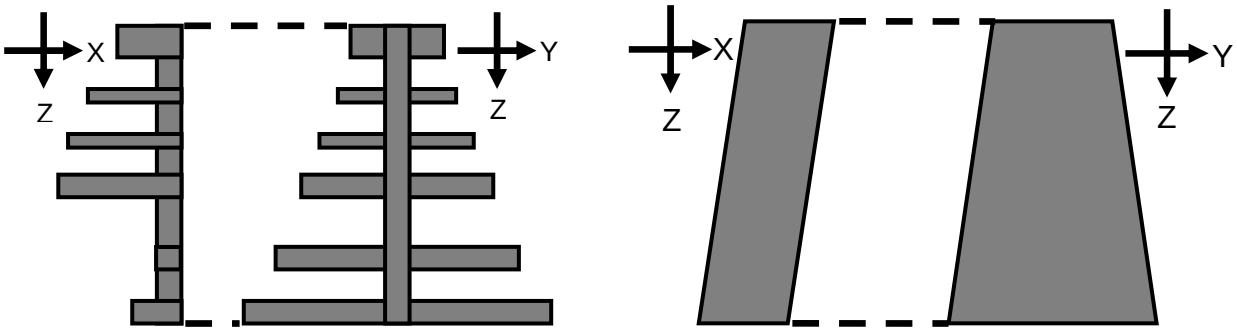

figure 2. Overview of the simulated collimeter:
(a) with GEANT4 (b) with EGS5

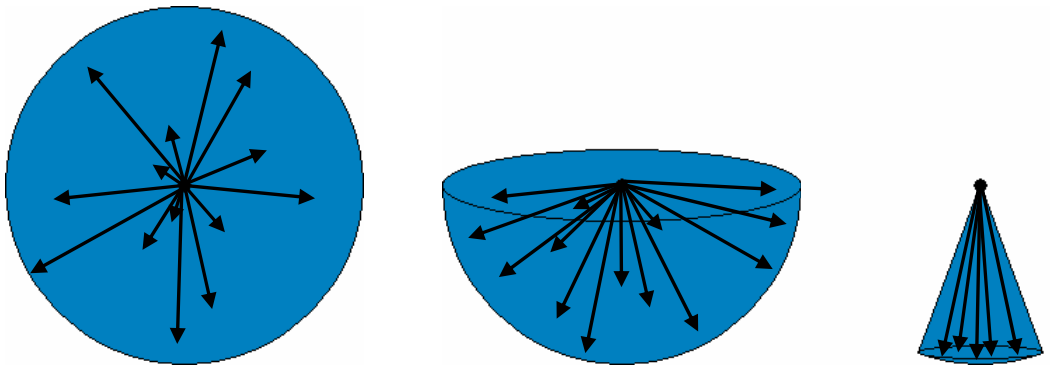

(a) (b) (c)

figure 3. The three pattern of the incident directions:
(a) isotropic source (b) hemispheroidal isotropic source (c) cone shaped source

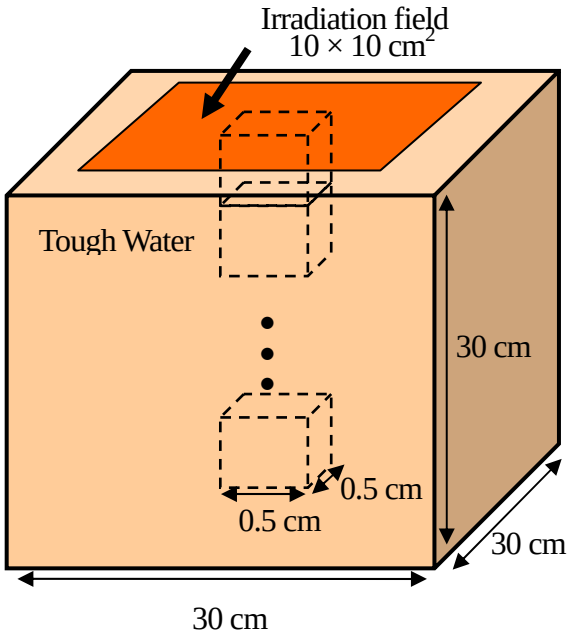

figure 4. The geometry of scoring region for calculating the PDD curves

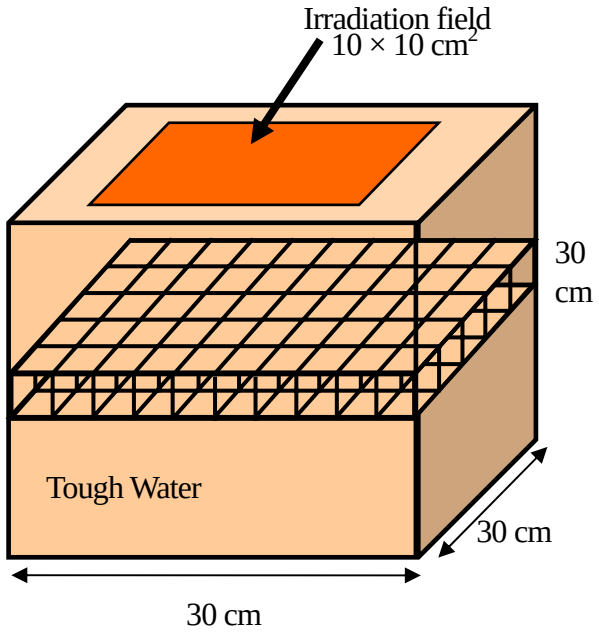

figure 5. The geometry of scoring region for calculating the OCR curves

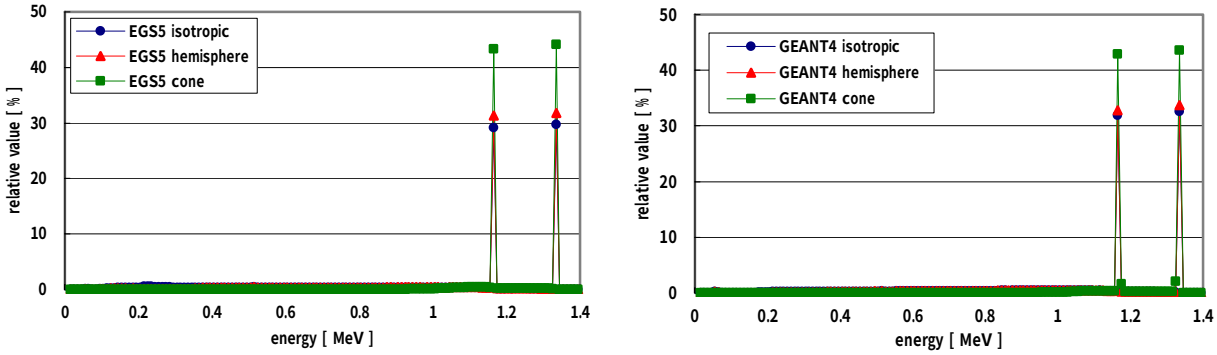

(a) (b)

figure 6. The photon energy spectra scored at the surface of the tough water phantom:
(a) calculated with EGS5 (b) calculated with GEANT4

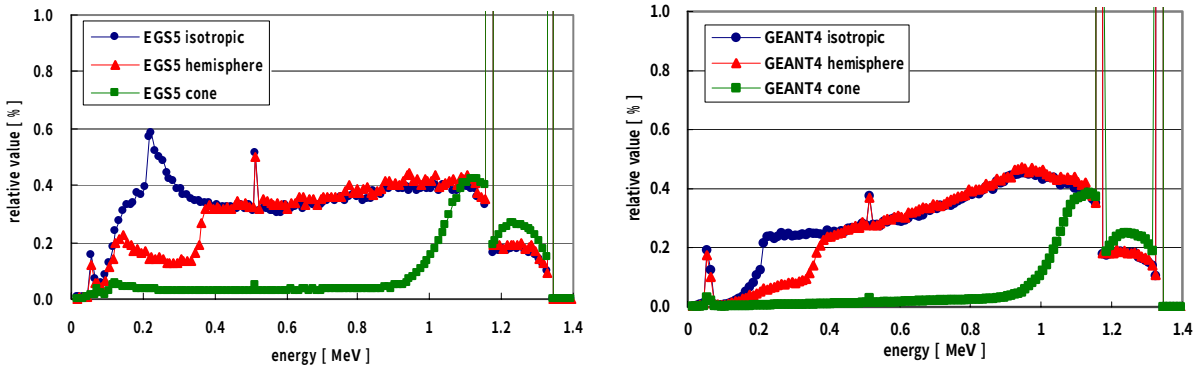

(a) (b)

figure 7. The part of the low fraction in photon energy spectra:
(a) calculated with EGS5 (b) calculated with GEANT4

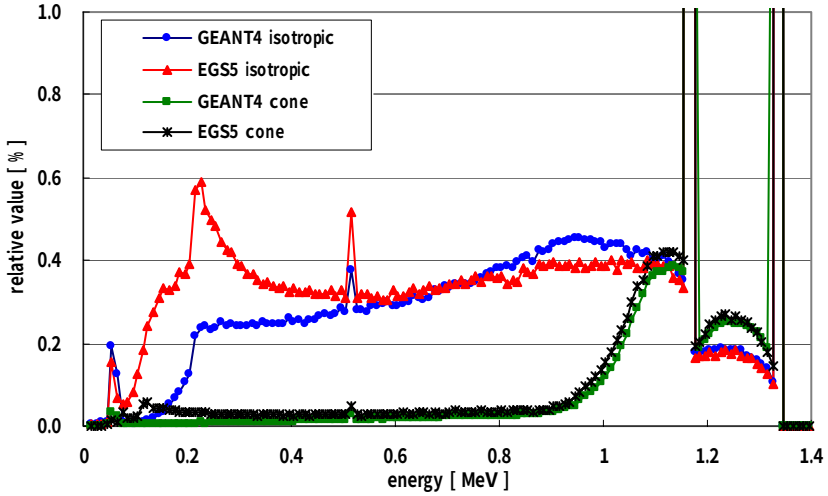

figure 8. Comparison of the photon energy spectra between by EGS5 and by GEANT4

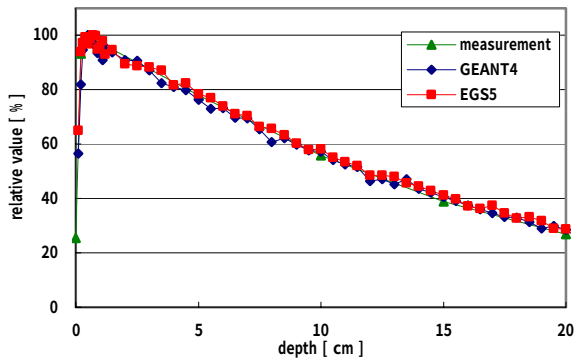

figure 9. The PDD curves measured and simulated

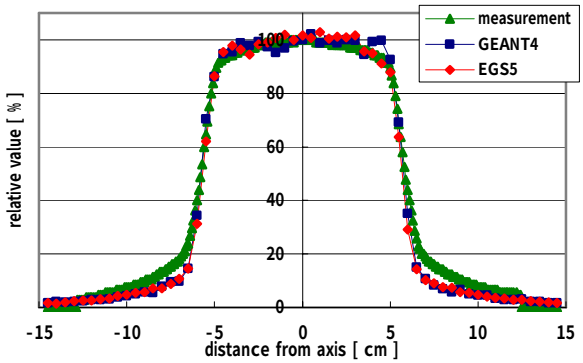

figure 10. The OCR curves measured and simulated

EVALUATION OF ORGAN DOSES IN A VOXEL MOUSE

S. Kinase[1] and K. Saito[1]

[1]Radiation Effect Analysis Group,
JapanJapan Atomic Energy Agency
Tokai-mura, Naka-gun, Ibaraki-ken, 319-1195, Japan
e-mail: kinase.sakae@jaea.go.jp

Abstract

Self-absorbed fractions (self-AFs)-the fraction of energy emitted as a specified radiation type in a source tissue which is absorbed in the source (=target) tissue- were evaluated for photons and electrons in kidneys, liver and spleen of a voxel mouse. The sources were assumed to be monoenergetic in the energy range 10 keV-4 MeV, and be uniformly distributed in the organs. Self-S values (μGy/MBq·s) for ^{64}Cu in the kidneys, liver and spleen were assessed using the self-AFs. In addition, self-AFs and self-S values were evaluated for voxel humans in order to examine the differences between the mouse and humans. The self-AFs for photons and electrons were found to be dependent upon energy emitted in the source organ. It was also found that the self-S values for ^{64}Cu in the voxel mouse are 400 or more times larger than those in the voxel humans.

1. Introduction

Internal radiation dosimetry in mice is of considerable practical concern in preclinical studies of new radiopharmaceuticals. The dosimetry should be made as exactly as possible since the dose-response relationships in the animals such as mice would be translated to those in humans. Several studies have been conducted on the evaluation of doses, particularly AFs and S values in mice using simulations [1-8]. However, published data on self-AFs and self-S values for sophisticated models such as voxel mouse are limited. To perform reliable evaluation of internal doses in mice, Monte Carlo simulations of mouse dosimetry are required using voxel mouse. The purpose of the present study is to provide data relevant to the organ dosimetry in a voxel mouse using Monte Carlo simulations. Self-AFs for photons and electrons in the kidneys, liver and spleen of the voxel mouse were evaluated. Self-S values for ^{64}Cu in the kidneys, liver and spleen were assessed using the self-AFs. In addition, self-AFs and self-S values for voxel humans were evaluated and were compared with those for the voxel mouse, in order to examine the differences between the mouse and humans.

2. Materials and Methods

2.1 Voxel phantoms

The voxel mouse used is illustrated in Figs. 1 (a) and (b). The voxel mouse "Digimouse" was constructed from co-registered micro-CT and colour cryosection data of a normal nude male mouse [9]. The voxel mouse was developed at the University of Southern California. The voxel size is 0.1×0.1×0.1 mm^3. As for voxel humans, the adult male human "Otoko" [10], the adult female human "Onago" [11] were used. The Otoko and Onago phantoms were constructed from CT data of real Japanese human bodies. The voxel humans were developed at the Japan Atomic Energy Agency. The voxel size is 0.98×0.98×10.0 mm^3. The masses of the kidneys, liver and spleen for the phantoms are shown in Table 1.

2.2 Self-absorbed fractions

Self-AFs for photons and electrons in the kidneys, liver and spleen were evaluated for Digimouse, Otoko and Onago phantoms using the Monte Carlo code, EGS4 [12], in conjunction with an EGS4 user code, UCSAF[13]. In the present study, the self-AFs were evaluated for uniformly distributed monoenergetic sources of both photons and electrons. Twelve energies were simulated between 10 keV and 4 MeV. Photon and electron histories were run at numbers sufficient to reduce statistical uncertainties below 5%. The cutoff energy was set to 1 keV for both the photons and electrons. The Parameter Reduced Electron-Step Transport Algorithm (PRESTA) [14] to improve the electron transport in the low-energy region was used. The cross-section data for photons were taken from PHOTX [15, 16] and the data for electrons are taken from ICRU report 37 [17]. No variance reduction technique was used.

2.2 Self-S values

Self-S values for the kidneys, liver and spleen were calculated for Digimouse, Otoko and Onago phantoms using the results of the self-AFs for both photons and electrons. The nuclide considered was ^{64}Cu that is a cyclotron-produced radionuclide that decays by both β^+ (655 keV, 17.4%) and β^- (573 keV, 39.0%) emission, making it suitable for labeling monoclonal antibodies for positron emission tomography imaging and radioimmunotherapy of cancer. The self-AFs were converted into the self-S values considering the masses of the organs and the decay modes of the radionuclides. The self-AFs for electron were used for beta particle components. The self-AF for photon with energy 511 keV was used for two annihilation photons from ^{64}Cu. The beta spectra for ^{64}Cu was extracted from DECDC [18].

3. Results and discussion

3.1 Self-absorbed fractions

Figures 2 (a)-(c) show the self-AFs for photons in the kidneys, liver and spleen of the Digimouse, Otoko and Onago phantoms in the energy range from 10 keV to 4 MeV. The self-AFs decrease with increasing photon energy on the whole. The self-AFs for the Digimouse phantom are significantly smaller than those for the Otoko and Onago phantoms. This is due to the different shape and size of the organs.

The self-AFs for electrons in the kidneys, liver and spleen of the Digimouse are shown in Figs. 3 (a)-(c). The self-AF for the Digimouse is almost unity in the electron energy range from 10 keV to 100 keV, followed by a sharp fall. For the organs in small animals such as mice, all electrons are not always absorbed within the organs that emit them. Figures 3 also show that the electron self-AFs for the Digimouse are inconsistent with those for the Otoko and Onago phantoms in the higher energy region. The apparent inconsistency is attributable to the different size of the organs.

3.2 Self-S values

Figure 4 shows the self-S values for the kidneys, liver and spleen of the Digimouse, Otoko and Onago phantoms, for ^{64}Cu. It can be seen that, as expected, the self-S values for the Digimouse phantom are much larger than those for the Otoko and Onago phantoms. The self-S value for the Digimouse phantom is 400 or more times larger than those in the voxel human phantoms. This is, as already known, due to the different masses of the organs.

4. Conclusions

The self-AFs for photons and electrons in the kidneys, liver and spleen of a voxel mouse and two voxel humans were evaluated using Monte Carlo simulations in the energy range from 10 keV to 4 MeV. Furthermore, the self-S values for ^{64}Cu in the organs of the voxel phantoms were evaluated using the obtained self-AFs. It was found that the photon self-AFs for the voxel mouse are significantly smaller than those for the voxel humans and that the electron self-AFs for

the voxel mouse are inconsistent with those for the voxel humans in the high-energy region above 100 keV. The self-S values for the voxel mouse were found to be much larger than those for the voxel humans.

Acknowledgments

We wish to express our sincere thanks to Dr. Dogdas and Prof. Leahy for allowing us to use the Digimouse.

References

1) T. E. Hui, D. R. Fisher, J. A. Kuhn, L. E. Williams, C. Nourigat, C. C. Badger, B. G. Beatty and J. D. Beatty, A mouse model for calculating cross-organ beta-doses from yttrium-90-labeled immunoconjugates. *Cancer* 73, 951-957 (1994).
2) A. A. Flynn, A. J. Green, R. B. Pedley, G. M. Boxer, R. Boden and R. H. J. Begent, A mouse model for calculating the absorbed beta-particle dose from ^{131}I- and ^{90}Y-labeled immunoconjugates, including a method for dealing with heterogeneity in kidney and tumor. *Radiat. Res.* 156, 28-35 (2001).
3) K. S. Kolbert, T. Watson, C. Matei, S. Xu, J. A. Koutcher and G. Sgouros, Murine S factors for liver, spleen, and kidney, *J. Nucl. Med*. 44, 784-791 (2003).
4) C. Hindorf, M. Ljungberg and S-E. Strand, Evaluation of parameters influencing S values in mouse dosimetry. *J. Nucl. Med*. 45, 1960-1965 (2004).
5) M. G. Stabin, T. E. Peterson, G. E. Holburn and M. A. Emmons, Voxel-based mouse and rat models for internal dose calculations, *J. Nucl. Med*. 47, 655-659 (2006).
6) A. Bitar, A. Lisbona, P. Thedrez, C. S. Maurel, D. L. Forestier, J. Barbet and M. Bardies, A voxel-based mouse for internal dose calculations using Monte Carlo simulations (MCNP). *Phys. Med. Biol.* 52, 1013-1025 (2007).
7) R. Taschereau and A. F. Chatziioannou, Monte Carlo simulations of absorbed dose in a mouse phantom from 18-flurorine compounds. *Med. Phys*. 34, 1026-1036 (2007).
8) S. Kinase, M. Takahashi and K. Saito, Evaluation of self-absorbed doses for the kidneys of a voxel mouse. Submitted to *J. Nucl. Sci. and Technol*.
9) B. Dogdas, D. Stout, A. F. Chatziioannou and R. M. Leahy, Digimouse: a 3D whole body mouse atlas from CT and cryosection data. *Phys. Med. Biol.* 52, 577-587 (2007).
10) K. Saito, A. Wittmann, S. Koga, Y. Ida, T. Kamei, J. Funabiki and M. Zankl, Construction of a computed tomographic phantom for a Japanese male adult and dose calculation system, *Radiat. Environ. Biophys*. **40**, 69-76 (2001).
11) K. Saito, S. Koga, Y. Ida, T. Kamei and J. Funabiki, Construction of a voxel phantom based on CT data for a Japanese female adult and its use for calculation of organ doses from external electrons. *Jpn. J. Health Phys*. (in press).
12) W. R. Nelson, H. Hirayama and D. W. O. Rogers, The EGS4 code system, SLAC-265 (1985).
13) S. Kinase, M. Zankl, J. Kuwabara, K. Sato, H. Noguchi, J. Funabiki and K. Saito, Evaluation of specific absorbed fractions in voxel phantoms using Monte Carlo simulation, *Radiat. Prot. Dosim*. **105 (1-4)**, 557-563 (2003)
14) A. F. Bielajew and I. Kawrakow, The EGS4/PRESTA-II electron transport algorithm: Tests of electron step-size stability, Proceedings of the XII'th Conference on the Use of Computers in Radiotherapy 153-154 (Madison, WI:Medical Physics Publishing) (1997).
15) RSIC. DLC-136/PHOTX Photon interaction cross section library (contributed by National Institute of Standards and Technology) (1989).
16) Y. Sakamoto, Photon cross section data PHOTX for PEGS4, KEK Proceedings 93-15, 77-82 (in Japanese).
17) ICRU. Stopping powers for electrons and positrons. ICRU Report 37 (Bethesda, MD, USA: ICRU) (1984).
18) A. Endo, Y. Yamaguchi and K. Eckerman, Nuclear decay data for dosimetry calculation revised data of ICRP Publ.38. JAERI 1347 (2005).

Table 1. Masses of kidneys, liver and spleen in the Digimouse, Otoko and Onago phantoms

	Digimouse (kg)	Otoko (kg)	Onago (kg)
kidneys	5.15×10^{-4}	2.66×10^{-1}	2.57×10^{-1}
liver	2.09×10^{-3}	1.19	1.45
spleen	1.44×10^{-4}	7.57×10^{-2}	9.06×10^{-2}

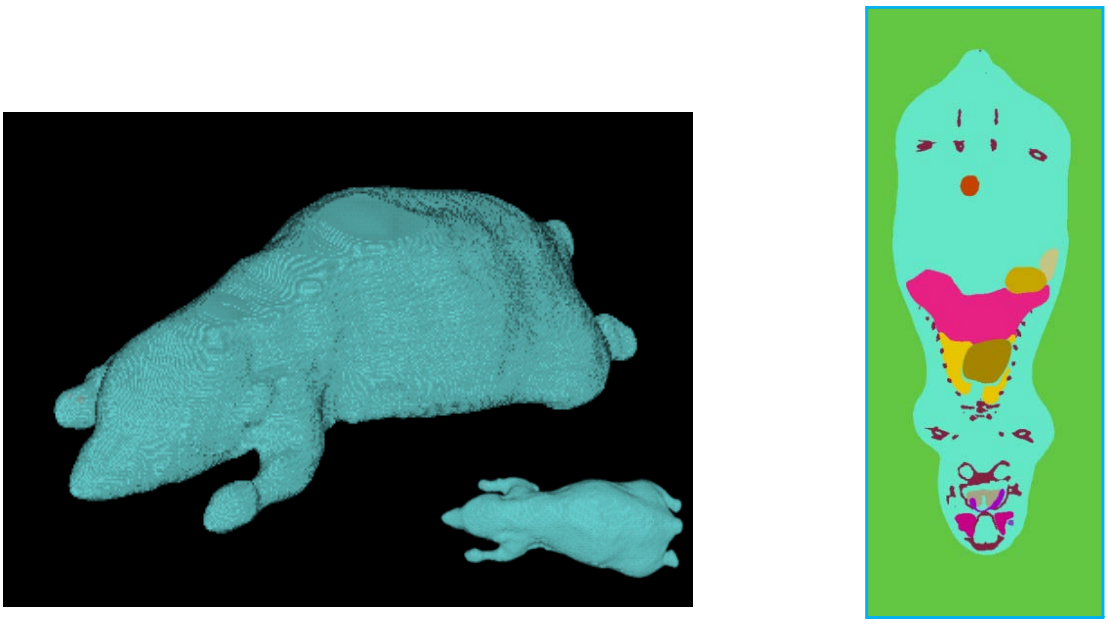

(a) 3D images (b) Cross section

Figure 1. Image of Digimouse.

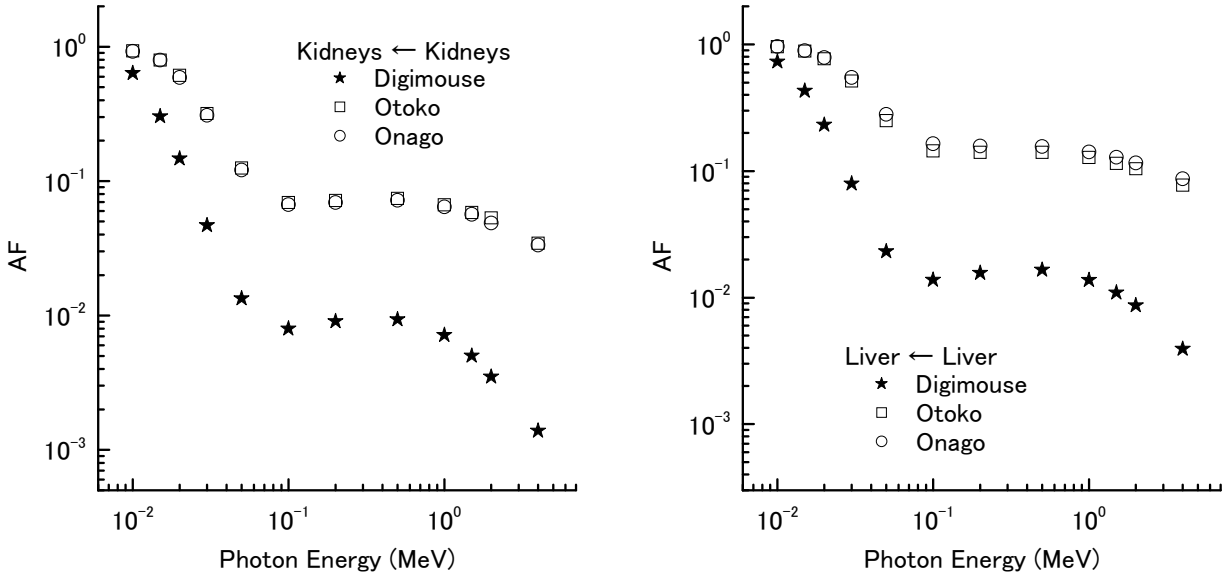

(a)

(b)

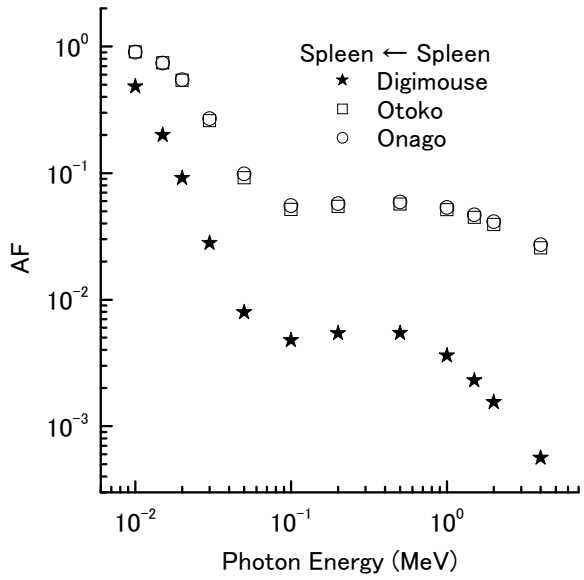

(c)

Figures 2. Self-AFs in the kidneys (a), liver (b) and spleen (c) for the Digimouse, Otoko and Onago phantoms in the photon energy 10 keV-4MeV.

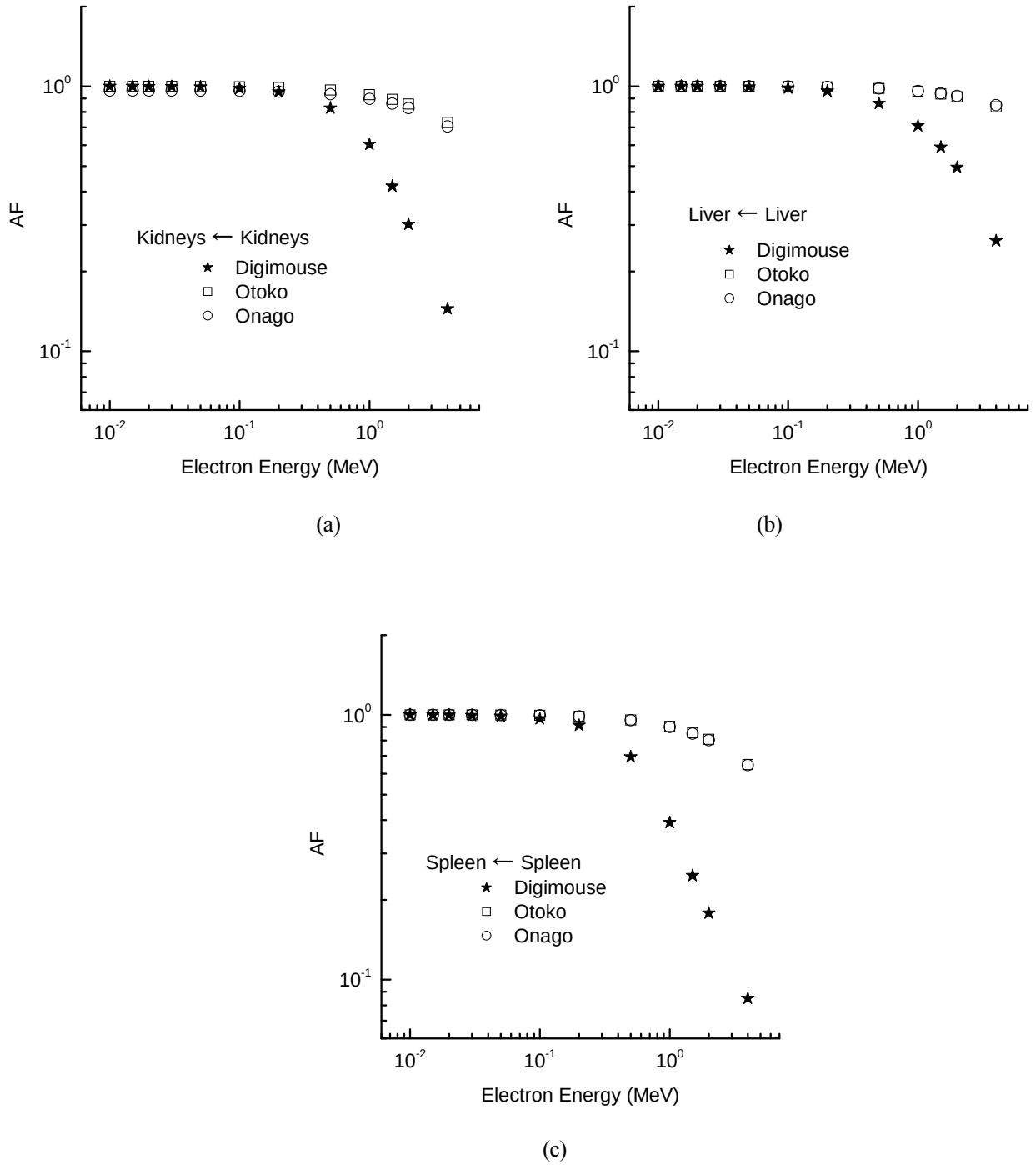

Figures 3. Self-AFs in the kidneys (a), liver (b) and spleen (c) for the Digimouse, Otoko and Onago phantoms in the electron energy 10 keV-4MeV.

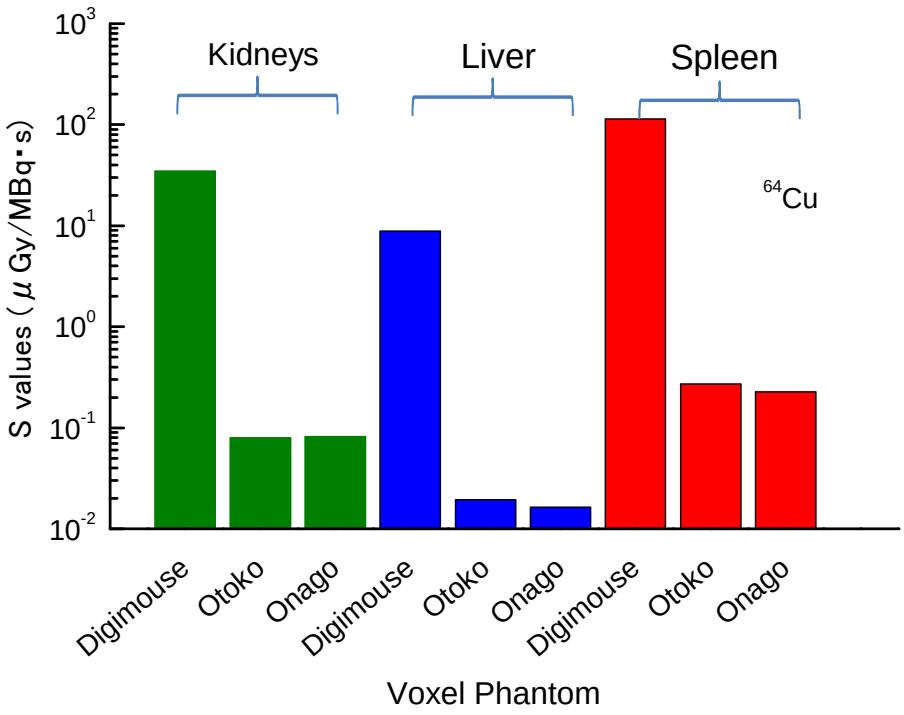

Figure 4. Self-S values for ^{64}Cu in the kidneys, liver and spleen of the Digimouse, Otoko and Onago phantoms.

Influence of "CHARD" set for very small regions composed of different media on the absorbed doses of small glass regions from ^{90}Y beta ray source implanted in a small phantom using EGS5

Y. Sato [1], H. Yamabayashi [1], T. Nakamura [1, 2]

[1] Oarai Research Center, Chiyoda Technol Corporation,
Oarai-machi, Higashi-ibaraki-gun, Ibarak, 311-1313, Japan
[2] Cyclotron and Radioisotope Center, Tohoku University,
Aoba, Aramaki, Aoba-ku, Sendai, 980-8578, Japan

Abstract

A method for optimization of electron multiple-scattering step-sizes selection is provided by setting a value of the variable CHARD related to the controlling of electron multiple-scattering step-sizes in the EGS5 user code.

In this work, the influence of CHARD set for very small regions composed of different media was examined on the absorbed doses of small glass regions from ^{90}Y beta ray source implanted in a small phantom using EGS5.

As the results, even if the value of CHARD was set to the less or more value than the recommended value of that related to the size of the smallest scoring region for a given material, the calculated absorbed doses for glass regions were largely affected by the statistical uncertainties rather than by the variable CHARD for very small regions composed of different media.

1. Introduction

A method for optimization of electron multiple-scattering step-sizes selection is provided by setting a value of the variable CHARD related to the controlling of electron multiple-scattering step-sizes in the EGS5 user code [1].

We had tried to validate a user code to simulate the beta particle transport in mice in the Monte Carlo code system (EGS5) by comparing with the absorbed dose measured using a number of small Fluorescent Glass Dosimeters and one capsule of $^{90}YCl_3$ solution implanted in a small Tough-Water phantom simulating a mice[2]. In that calculation, it had been used the recommended values of CHARD related to the size of the smallest scoring region of regions for each given material, for instance, glass, air, ABS and so on. The Rather good agreement had been represented between measurement and calculation obtained at the positions close to the source, but large discrepancy at the positions away from the source [2].

It is known that there is sensitivity on lower photon energy in a Fluorescent Glass Dosimeter [3, 4]. Therefore, in preliminary examination, an approach to correcting photon energy spectrum had been performed at the positions much away from the source, which is at the area interacted with only photons. However, the differences between the measured doses and the simulated doses could not have been explained by the correction of incident photon energy into glass regions.

In this working, we focused attention on the parameters in user code in simulation, especially the treatment of electron transport and energy deposition through multiple scattering in very small multi-layer system of glass, Tough-water and source used. Therefore, the influence of CHARD set for very small regions composed of different media was examined on the absorbed doses of small glass regions from ^{90}Y beta ray source implanted in a small phantom using EGS5.

2. Materials and Methods

2·1 Phantom

As the first step of this examination, a small physical phantom simply simulating a mouse had been used in this experiment [2]. The phantom is made of Tough-Water phantom produced by Kyoto Kagaku Co., Ltd. consisting of a water equivalent material [5]. The phantom is composed of three blocks (each block of 30 mm x 30 mm x 14 mm), and has a hole in the central area for embedding a cylindrical Tough-Water capsule (outer diameter of 10mm, outer length of16mm, inner diameter of 6mm, inner length of 11mm) inserting a radioactive source as shown in Fig. 1. The source is $^{90}YCl_3$ solution (267.7 mg) of 6.6 MBq activity, when the phantom is irradiated. Each phantom block has eight holes for embedding a number of small Fluorescent Glass Dosimeters around the source region.

2·2 Measurement

The dosimeters used in this experiment are a number of small Fluorescent Glass Dosimeters[9] (Dose Ace; GD-302M, AGC TECHNO GLASS CO., LTD.). In this working, it was used that the measured values taken out previously by these dosimeters [2].

2·3 Calculation with Monte Carlo code

The internal dose distribution in this phantom was calculated using the Monte Carlo code (EGS5) to validate the simulation of beta ray transport by comparing with the experiment. In this calculation, the user code was prepared for the computational parameters of geometry, mass densities, and elements of materials of the phantom. A computational geometry simulating this phantom used in the experiment had been made by using the Combinatorial Geometry (CG) [2].

The absorbed doses separately from beta rays and bremsstrahlung X-rays in a number of very small areas were estimated using the method to discriminate beta rays and bremsstrahlung X-rays [2]. In this calculation, the cutoff energies of electrons, ECUT, and photons, PCUT, were set at 521 keV and 10 keV. The number of histories of the simulations were 10^7 and 2×10^7 two ways without and with the flag for turning on splitting of bremsstrahlung photons as the variance reduction technique because of low-probability bremsstrahlung photon production.

In each calculation, the values of CHARD were set to the less or more values than the recommended value of that related to the size of the smallest scoring region for a given material in user code. Figure 2 shows the values (in cm) set as default of CHARD for some major regions.

3. Results and Discussions

The influence of CHARD set for very small regions composed of different media was examined on the absorbed doses of small glass regions from ^{90}Y beta ray source implanted in a small phantom using EGS5.

A comparison of calculated absorbed doses and measured absorbed doses in simulation and measurement is shown in Figure 3. In Figure 3 (1), the maximum calculated absorbed dose was less than 1.1 times the minimum calculated absorbed dose at Block 2 No. 1 close to the source and the statistical uncertainties of the doses at the position were less than 1.5%, and the similar results were obtained in Figure 3 (2), (3), (4), (5). These shows that the calculated doses at Block 2 No. 1 are scarcely affected by the variable CHARD for glass regions, air thin layer regions, ABS thin layer regions, water solution region, or Tough-water regions and the differences between the simulated doses and the measured doses may result from the other causes.

However, the statistical uncertainties of the calculated absorbed doses were larger than 16.8% and less than 54.3% at the other positions, that is, Block 1 No. 1, Block 3 No. 1, Block 3 No. 5 in Figure 3 (1), (2), (3), (4), (5). Therefore, it was not possible to judge whether the calculated absorbed doses of small glass regions were significantly affected by the variable CHARD.

So the absorbed doses were calculated with the flag for turning on splitting of bremsstrahlung photons to reduce statistical uncertainties. An instance of the calculated results is shown in Table 1. We are concerned here only with the CHARD of ABS regions at Block 3 No. 5 much away from the source.

The calculated absorbed dose with the statistical uncertainty 54.3% was 5.28×10^{-12} mGy when the value of CHARD was 0.05. However, even if the value of CHARD was 0.05 or 0.01, the calculated absorbed doses with the variance reduction technique were approximately larger than 3.56×10^{-12} mGy and less than 3.68×10^{-12} mGy and the statistical uncertainties of the calculated values were less than 2.9%. Nevertheless, the calculated values were approximately three times the measured value. These show that the calculated absorbed dose for glass regions are largely affected by the statistical uncertainties rather than by the variable CHARD for ABS regions and the differences between the simulated doses and the measured doses may result from the other causes.

4. Conclusions

In this working, the influence of CHARD set for very small regions composed of different media was examined on the absorbed doses of small glass regions from ^{90}Y beta ray source implanted in a small phantom using EGS5.

The calculated absorbed dose for glass regions were largely affected by the statistical uncertainties rather than by the variable CHARD for very small regions composed of different media.

The differences between the simulated doses and the measured doses may result from the other causes. We have started to improve this discrepancy in the simulation.

Acknowledgments

The authors would like to thank Dr. H. Hirayama and Dr. Y. Namito for their very helpful comments and discussions.

References

1) H. Hirayama, Y. Namito, A.F. Bielajew, S.J. Wilderman and W.R. Nelson, "The EGS5 Code System," SLAC-R-730 and KEK Report 2005-8 (2007)

2) Y. Sato, H. Yamabayashi and T. Nakamura, *Proc. 13th EGS User's Meeting in Japan*, KEK Proceedings 2006-4, 94 (2006)

3) K. Ejiri, K. Minami, M. Shimo, K.Terada, S. Maeda, Y. Takeuchi, H. Toyama and K. Katada, The Design by the Monte Carlo Method of the Filter for Fluorescence Glass Dosimeters, IRPA 11, Madrid Spain 23-28 May (2004).

4) K. Shimomura, K. Tabushi, S. Kito, Y. Shiota, N. Kadoya, S. Ban, and Y. Namito, KEK Proceedings 2005-10, p.99-103 (2005).

5) Kyoto Kagaku Co., Ltd, MEM 55 Vol.1α 2004-2005, p.95 (2004)

Table 1 Comparison between the absorbed doses calculated considering statistical precision and the measured value at Block3 No. 5

Simulation						Measurement
CHARD of ABS regions (cm)	Histories	IBRSPL*1)	NBRSPL*2)	Statistical errors at Block3 No. 5 (%)	Calculated values at Block3 No. 5 (mGy)	Measured value at Block3 No. 5 (mGy)
0.05	10^7	0	-	54.3	5.28×10^{-12}	1.26×10^{-12}
0.05	2×10^7	1	132	2.52	3.68×10^{-12}	
0.01	10^7	0	-	26.5	3.69×10^{-12}	
0.01	10^7	1	198	2.90	3.57×10^{-12}	
0.01	2×10^7	1	198	2.00	3.56×10^{-12}	

*1) Flag for turning on (=1) splitting of bremsstrahlung photons (default=0 implies no splitting).

*2) Number of bremsstrahlung photons for splitting when IBRSPL=1.

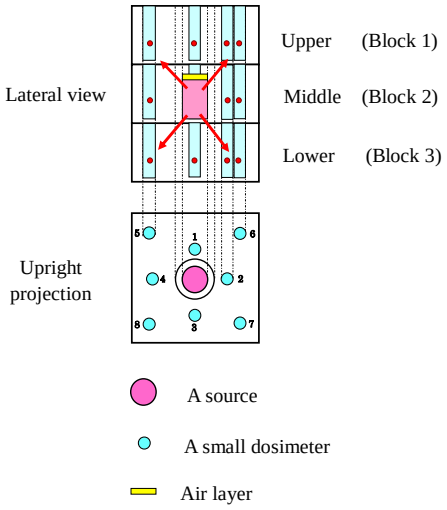

Figure 1. Geometrical configuration of dosimeters and a source.

```
chard(1) = 0.025d0    !  for glass regions
chard(2) = 0.005d0    !  for Air thin layer regions
chard(4) = 0.05d0     !  for ABS thin layer regions
chard(5) = 0.6d0      !  for Water solution region
chard(6) = 0.1d0      !  for Tough-water regions
```

Figure 2. Default values (in cm) of CHARD for some major regions.

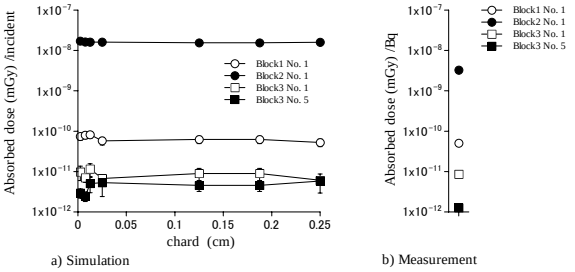

(1) Variable CHARD for Glass regions only

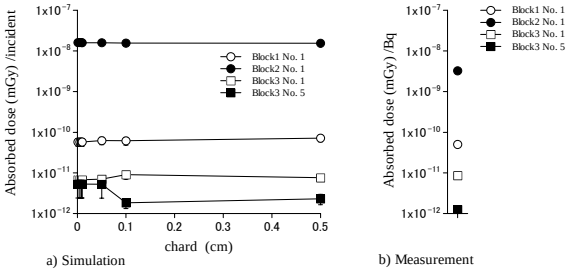

(2) Variable CHARD for Air thin layer regions only

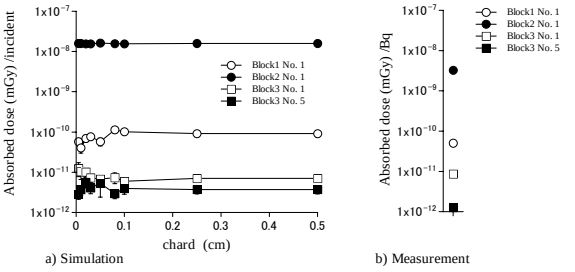

(3) Variable CHARD for ABS thin layer regions only

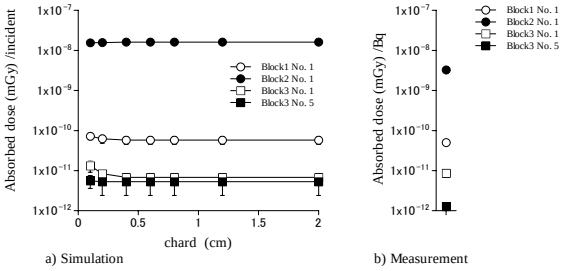

(4) Variable CHARD for Water solution region only

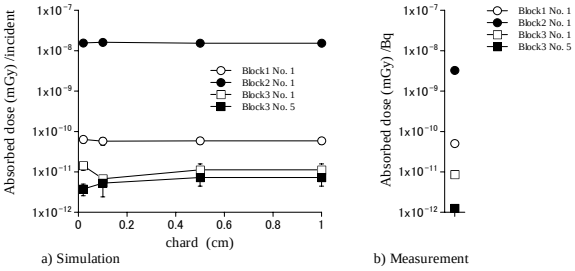

(5) Variable CHARD for Tough-water regions only

Figure 3. Comparison between the absorbed doses calculated considering the variable CHARD related to the controlling of electron multiple-scattering step-sizes and the measured absorbed doses

The effect of scattered photons for x-ray air-kerma calibrations

Tadahiro Kurosawa, Yuuichirou Morishita, Tsuyoshi Matsumoto, Norio Saito
National Metrology Institute of Japan, AIST
1-1-1 Umezono, Tsukuba 305-8568 Japan
Tadahiro-kurosawa@aist.go.jp

Abstract

The parallel-plate free-air ionization chambers are used for X-rays air-kerma rate standards at National Metrology Institute of Japan (NMIJ), National Institute of Advanced Industrial Science and Technology (AIST). The diaphragms are used to free-air chambers to fix the air volume of ionizing region in chambers. It means that absolute air-kerma rates are defined for collimated x-ray beams, because most of scattered photons are collimated by diaphragms. On the other hand, calibrated chambers are measured with non-collimated conditions. The variation of calibration constants was observed at different calibration distances and different diaphragm sizes for A6 Exradion chambers calibrations. The difference of the calibration constants are about 1.5% for 250kV X-ray beams. We thought that these results could be explained by the effect of scattered photons from the filters. In this study, we evaluate the contribution of scattered photons for free-air chambers and cavity chambers by Monte Carlo simulations, and suggest a new correction factor for evaluation of x-ray standards. The difference of calibration constants decreases below 0.4%.

1. Introduction

The parallel-plate free-air ionization chambers[1] are used for X-rays air-kerma rate standards at National Metrology Institute of Japan (NMIJ), National Institute of Advanced Industrial Science and Technology (AIST). The diaphragms are used to free-air chambers to fix the air volume of ionizing region in chambers. It means that absolute air-kerma rates are defined for collimated x-ray beams, because most of scattered photons are collimated by diaphragms. On the other hand, calibrated chambers are measured with non-collimated conditions.

The variation of calibration constants was observed at different calibration distances and different diaphragm sizes for A6 Exradion chamber calibrations. The difference of the calibration constants are about 1.5% for 250kV X-ray beams. We thought that these results could be explained by the effect of scattered photons from the filters. In this study, we evaluate the contribution of scattered photons for free-air chambers and cavity chambers by Monte Carlo simulations[2] and suggest a new correction factor for evaluation of x-ray standards. The difference of calibration constants decreases below 0.4%.

2. Measurements

The calibrations for A6 Exradin chamber were done at medium-energy x-ray standards of NMIJ with various conditions. The voltages of x-ray tube are 250, 150, and 75 kV, and effective energies are 175, 105, and 52.5 keV respectively. 25mm diameter diaphragms was used and calibrations were done at 2.0, 2.5 and 3.0 m that were distances from x-ray target to detectors. The measurements were also done with changing beam collimators to define the effect of collimator size. Three different collimators were applied for this measurements. A small one makes field size to be 12 cm diameter at 1.2 m from a x-ray tube to a detector. That of medium one is 18 cm and large one is 24cm diameter. Figure 1, 2 and 3 show the calibration constants for

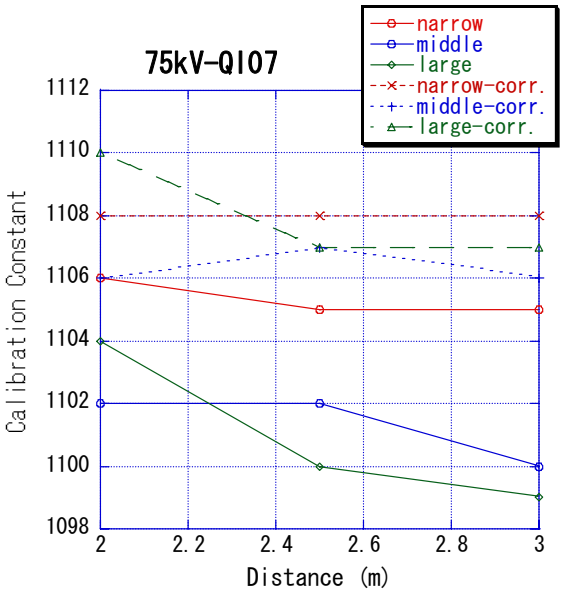

Figure 1 Calibration constants of A6 Exradin chamber for 75kV x-rays. Solid lines are measured values and dotted lines are corrected values by k_{outer}.

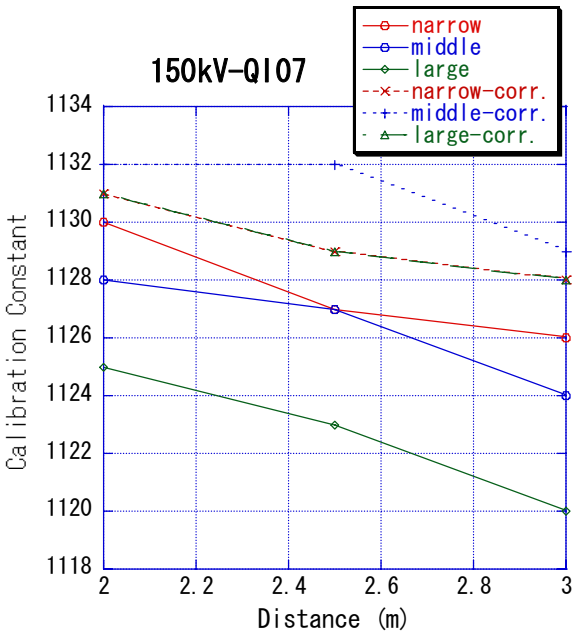

Figure 2 Calibration constants of A6 Exradin chamber for 150kV x-rays. Solid lines are measured values and dotted lines are corrected values by k_{outer}.

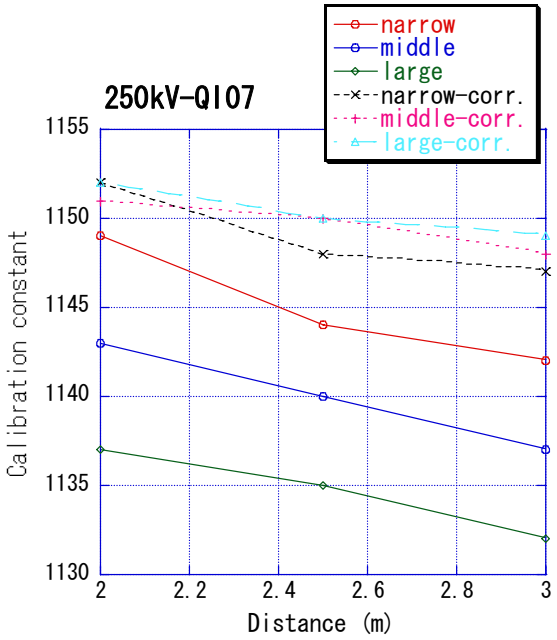

Figure 3 Calibration constants of A6 Exradin chamber for 250kV x-rays. Solid lines are measured values and dotted lines are corrected values by k_{outer}.

A6 chambers. The calibration values becomes larger for short distance than longer ones, and also becomes larger for small collimator for each beam qualites. The variation of calibration constants becomes large for high energy beam qualities. It can be said that these differences are caused by scattered photons. The aperture of free-air chamber woks like collimator for scattered photon that produced at filters and air. On the other hand, calibrated chambers can detect the photons that comes any directions.

3. Monte Carlo Simulations

The simulations are done to evaluate the difference of calibration constants with various conditions. The EGS5[2] was used for the Monte Carlo simulations. The simulations are sepalated two steps as shown in Figure 4. First step is calculation for source photons penetrated through Be-window of x-ray tube. The information (energy, position and angles) of each photons are recorded on a file. Next step is simulations for detector using previous result. The photon fluences are scored at reference plane that pass through a hole of diaphragm or that comes any direction with the size of A6 chamber separately.

The new correction factor for the effect of diaphragm are calculated by the following equation,

$$k_{outer} = \frac{\int \phi_t(E) f(E) dE}{\int \phi_d(E) f(E) dE} \qquad (2)$$

where ϕ_t is a photon fluence without diaphragm at reference position that include scattered photons from filter and air. ϕ_d means collimated photon flucence by the diaphragm.

In this simulations, the photons are separately scored as direct photons, scattered photons at additional filters and scattered photons at air region behind filters to define the effect of scattered photons that are produced at filters or air.

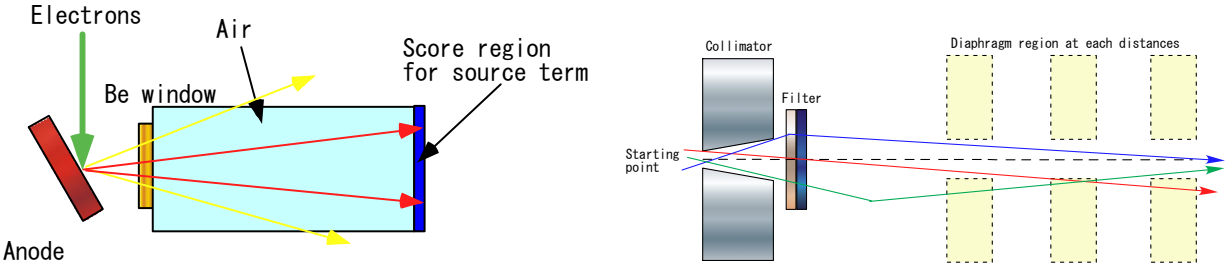

Figure 4. Simulation geometry for EGS5 calculations. Left one is for the source term calculations, and right hand is for detector term calculations. The photons that come to score region are recorded on a data file with particle information. These data are used as source history for detector term calculations.

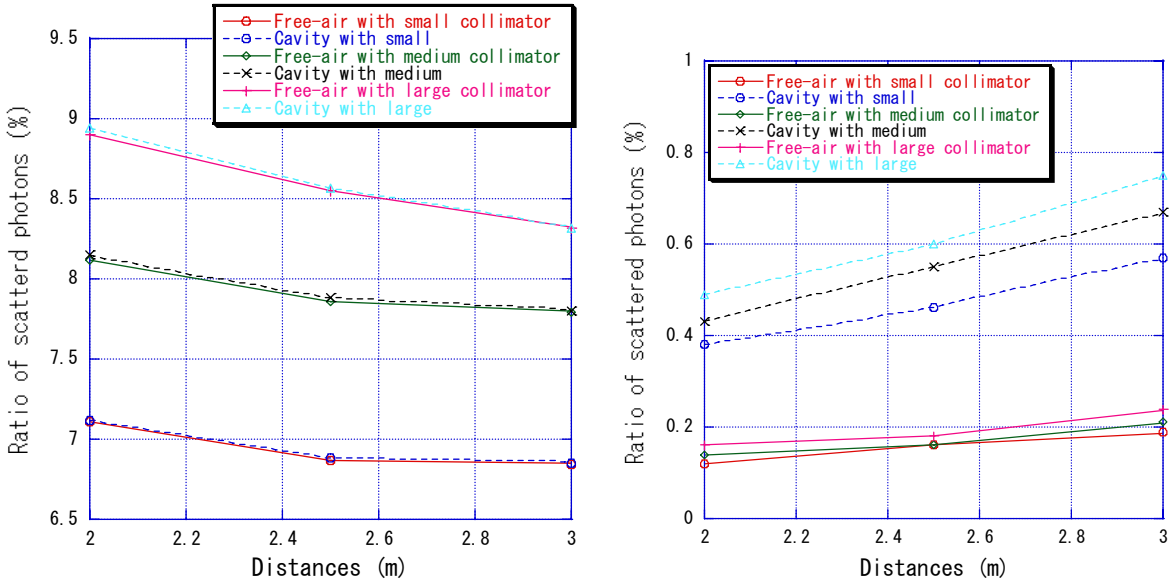

Figure 5. The ratio of scattered photons for 250kV beam quality. Left hand is the ratio of scattered photons that produced in the filters, and right hand is a result for scattering in the air.

4. Calculation results

4.1 Calibration constants corrected by new correction factors

Figure 1 to 3 shows the calibration constants corrected by new correction factors. The difference of calibration constants at various distances before correction by k_{outer} were 1.5% for 250kV, 0.8% for 150kV and 0.7% for 75kV, and these of corrected values became within 0.4% for 250kV, 0.4% for 150kV and 0.4% for 75kV respectively. The k_{outer} could be reduced the variations of calibration constant related by calibration distances.

4.2 Contributions of scattered photons in irradiation facility

In this simulations, the photons are separately scored as direct photons produced by x-ray anode, scattered photons at additional filters and scattered photons at air region behind filters. Fig. 5 shows contributions of these events for 250kV beam quality. For both chambers, the scattered photons increase with increasing x-ray tube voltage. It relate that the energy of photons produced at x-ray tube becomes highly enough to interact Compton scattering and thickness of filters also becomes thick to make its beam quality. The scattered photons produced at air increase with increasing the size of beam collimators and distances from the tube to the detectors. But the amount of these scattered photons for free-air chamber and cavity chambers are different. It can be said that the diaphragm of free-air chambers works as collimator for scattered photons. It is interesting that the differences of scattered photons are less than 0.5% between the free-air chamber and the cavity chamber in these simulations. The main difference is the photon fluence that comes to a detector directory. It's assumed that scattered photons which are produced at before filters becomes dominant for x-ray reference field.

5. Summary

The calibration constants for A6 Exradin cavity chamber were measured with changing x-ray energy, beam collimators and distances for medium-energy x-rays to estimate the scattering photon effect. The difference of these values becomes up to 1.5 %. The simulations for new correction factor k_{outer} were calculated to correct the different conditions for free-air chamber measurements and for cavity chamber. in this study. The corrected calibration constants by k_{outer} agree within 0.4 %. If air-kerma rates at reference point were determined by only measured results by free-air chambers, these values means collimated air-kerma rates by diaphragm.

References

[1] T. Matsumoto and J.Naoi, "Reestablished exposure standard for medium energy x-rays", Bulletin of the Electrotechnical Laboratory, 47, 822-845(1983)

[2] Hirayama H. et.al, "The EGS5 code system", SLAC-R-730 (2005)

CHARACTERISTICS OF ENERGY RESPONSE FOR FLAT-PANEL DETECTORS
-COMPARISON BETWEEN DIRECT AND INDIRECT CONVERSION METHODS -

K. Koshida, M. Takada, A. Suzuki, and K. Noto

Division of Health Science,
Kanazawa University Graduate School of Medical Science, Kanazawa 920-0942, Japan
e-mail:kosida@mhs.mp.kanazawa-u.ac.jp

Abstract

In place of film, X-rays can be received by an array of detector elements and converted to electronic information. This conversion is achieved using two types of detector in the direct conversion method and the indirect conversion method. However, there are inadequacies in methods using digital equipment, such as computed radiography and flat-panel detector (FPD) systems. The conditions used in conventional analog X-ray photography are often used with this new equipment. However, the effectiveness of these methods may be improved by optimizing the exposure conditions for the digital equipment. With Monte Carlo simulation, we examined the relations between the absorbed dose of the detector and the energy to validate the photography conditions by examining the energy characteristics in the direct and the indirect-conversion methods of FPD. In direct-conversion FPD, the response decreased in the order RQA 7 (90 kV), RQA 5 (70 kV), RQA 9 (120 kV), and RQA 3 (50 kV). On the other hand, for indirect-conversion FPD, the response decreased in order RQA 7 (90 kV), RQA 9 (120 kV), RQA 5 (70 kV), and RQA 3(50 kV). For both direct-conversion and indirect-conversion FPDs, measurement values agreed well with simulation values, with error between measurement and simulation values of less than 13.9%. The effectiveness of detectors may improve if appropriate exposure conditions can be established corresponding to the digital equipment.

1. Introduction

With recent developments in radiological equipment, there has been a shift from conventional analog methods to digital methods, with a corresponding shift away from the use of analog film. Equipment for both direct-conversion and indirect-conversion methods using flat-panel detectors (FPD) have been developed [1-15]. However, there has been insufficient research regarding methods using digital equipment, such as computed radiography and FPD. At present, the conditions conventionally used in analog X-ray photography are often used with digital equipment. The effectiveness of these methods may be improved by establishing exposure conditions appropriate for the digital equipment.

Volk [2] reported that flat-panel X-ray detector technology allows a significant reduction in radiation dose as compared with screen-film radiography without loss of diagnostic accuracy. Ludwig [12] estimated that exposure dose with the flat-panel detector can be reduced by 50% with diagnostic performance comparable to that of a conventional speed class 400 screen-film system. However, the energy range in their study is unknown because the energy response differs according to X-ray energy range.

We used the Monte Carlo simulation method to examine the relations between the absorbed dose of the detector with energy, and performed validation of the photography conditions by examining the energy characteristics in the

direct- and the indirect-conversion methods using FPD systems.

2. Materials and Methods

2.1 Equipment and dose meter used for estimation of energy response

The FPD equipment used for estimation of energy responses were a RADIO TEX Safire X-ray imaging system equipped with direct-conversion FPD (Shimadzu, Kyoto, Japan) and an AXIOM Aristos MX/NX imaging system equipped with indirect-conversion FPD (Siemens Medical Solutions, Malvern, PA). An X-ray system (UD 150L-R II; Shimadzu) was used to determine the basic characteristics. Three types of grid were used with the front FPD: 1) grid density 80 lines, grid ratio 15:1, paper spacer; 2) grid density 60 lines, grid ratio 13:1, carbon fiber spacer; and 3) grid density 40 lines & 60 lines, grid ratio 12:1 & 14:1, aluminum spacer. The dose was measured with an ion chamber (RAMTEC-1000D; Toyo Medic Co., Tokyo, Japan).

2.2 Range of photon energy

In the Monte Carlo simulation, the mono energy ranges were from 10 keV to 150 keV, and continuous X-rays were from 50 kV to 130 kV. Moreover, in previous experiments using the IEC61267 standard [16], continuous X-rays were from 50 kV to 120 kV. The radiation quality for determination of detective quantum efficiency and corresponding parameters are shown in Table 1.

2.3 Irradiation conditions and response definition in Monte Carlo simulation

In Monte Carlo simulation, the target angle of irradiation of the FPD was 12°, and the total filtration thickness was 2.5 mm aluminum equivalent. The target–FPD distance was 1.0 m, and the number of photons was 500,000.

The response was defined as follows: Response = Absorbed dose in FPD (Gy) / Air kerma (Gy)

As the absorbed dose in FPD, the material of direct-conversion FPD was amorphous Selenium, and that of indirect-conversion FPD was CsI. The collection efficiency of the ion current to the electric plate, the luminous efficiency, and the fluorescence yield were not taken into consideration. The collection efficiency and the luminous efficiency were both considered to be 100%.

3. Results

3.1 Characteristics of FPD digital value (output) to air kerma (input)

Figure 1(a) and (b) show the characteristics of direct-conversion FPD between the air kerma (input) and the digital value (output), and that of indirect-conversion FPD, respectively. The relations between the air kerma and the digital value can be expressed by linear equations. However, the digital values were constant: 16383 for direct-conversion FPD and 4095 for indirect-conversion FPD. In direct-conversion FPD, the slope of the linear expression decreased in the order 90 kV > 70 kV > 120 kV > 50 kV. On the other hand, for indirect-conversion FPD, the slope of the linear expression decreased in the order 90 kV > 120 kV > 70 kV > 50 kV.

3.2 Response in Monte Carlo simulation

3-2-1. Direct-conversion FPD

Figure 2 shows the relation between photon energy and response in direct-conversion FPD. In this figure, the solid line shows the response to photons for mono energy and the dashed line shows the response to continuous X-rays without the additional filter. The dotted lines show the radiation quality within the aluminum filter (RQA 3, RQA 5, RQA 7, and RQA 9 in Table 1), continuous X-rays within the water phantom (20 cm), and continuous X-rays without the aluminum filter or water phantom.

The response of direct-conversion FPD was highest on RQA 7 (90 kV), and was good in the range from 70 kV to 100 kV. On the other hand, low-voltage X-rays showed good contrast, but the response of RQA less than 70 kV became worse suddenly.

3-2-2. Indirect-conversion FPD

Figure 3 shows the relation between photon energy and response in indirect-conversion FPD. In this figure, the solid line shows the response to photons for mono energy and the dashed line shows the response to continuous X-rays without the additional filter. The dotted lines show the radiation quality within the aluminum filter (RQA 3, RQA 5, RQA 7, and RQA 9 in Table 1), continuous x rays within the water phantom (20 cm), and without the aluminum filter or water phantom. The response of indirect-conversion FPD became highest on RQA 7 (90 kV), and was good in the range from 70 kV to 120 kV. On the other hand, the low voltage X-rays showed good contrast, but the response of RQA less than 70 kV became worse suddenly, in the same was as in direct-conversion FPD.

3.3 Comparison of simulation response and measurement response

Figure 4(a) and (b) show the ratio of each response. Each response was normalized to 1.0 in RQA 7. Measurement values for both direct-conversion and indirect-conversion FPDs agreed well with the simulation values, with error of less than 13.9%.

4. Discussion

When using the conventional screen-film system, there are several conversion processes between X-rays incident on the cassette and the image on the film, and it is difficult to prevent loss of information and generation of noise. The role of the FPD in an X-ray imaging system corresponds to the film in the cassette. In place of the film, X-rays are received by an array of detector elements and converted directly to indirectly to electronic information depending on the type of detector used. Indirect-conversion FPDs have been developed by combining pre-existing image intensifier technologies, and several manufacturers have already produced systems based on this method. On the other hand, direct-conversion FPDs incorporate a detector capable of converting X-rays that pass through the patient without prior conversion to electrical signals. However, there are inadequacies in methods using digital equipment, such as computed radiography and FPD, as the conditions used in conventional analog X-ray photography are often used with this new equipment. The effectiveness of detectors may improve if the exposure condition could be established corresponding to the digital equipment.

In this study, comparison of the dose absorbed by FPDs and the responses of computer simulations clearly indicated good agreement between the two methods, with error rates of less than 13.9%. Therefore, by simulation, the exposure conditions can be defined corresponding to the digital equipment used for direct and indirect conversion methods. This technique will facilitate further improvements in the usage of digital equipment. Moreover, the range of X-rays may be extended to lower and higher energies.

5. Conclusions

In direct-conversion FPD, the response decreased in the order RQA 7 (90 kV) > RQA 5 (70 kV) > RQA 9 (120 kV) > RQA 3 (50 kV). On the other hand, for indirect-conversion FPD, the response decreased in the order RQA 7 (90 kV) > RQA 9 (120 kV) > RQA 5 (70 kV) > RQA 3 (50 kV). For both direct- and indirect-conversion FPDs, measurement values agreed well with those of simulations, with an error rate of less than 13.9%. The responses of direct- and indirect-conversion FPD became highest on RQA 7 (90 kV) and lowest on RQA 3 (50 kV). Thus, RQA7 was most suitable with regard to the quality of the response.

References

1) W. Zhao, J.A. Rowlands, "X-ray imaging using amorphous selenium: feasibility of a flat panel self-scanned detector for digital radiology," Med Phys. 22, 1595-1604 (1995).
2) M. Volk, M. Strotzer, J. Gmeinwieser, J. Alexander, R. Frund, J Seitz, C. Manke, M. Spahn, and S. Feuerbach, "Flat-panel x-ray detector using amorphous silicon technology. Reduced radiation dose for the detection of foreign bodies," Invest Radiol. 32, 373-377 (1997).
3) W. Zhao, I. Blevis, S. Germann, J.A. Rowlands, D. Waechter, and Z. Huang, "Digital radiology using active matrix readout of amorphous selenium: construction and evaluation of a prototype real-time detector," Med Phys. 24, 1834-1843 (1997).
4) M. Strotzer, J. Gmeinwieser, M. Spahn, M. Volk, R. Frund, J. Seitz, V. Spies, J. Alexander, and S. Feuerbach, "Amorphous silicon, flat-panel, x-ray detector versus screen-film radiography: effect of dose reduction on the detectability of cortical bone defects and fractures," Invest Radiol. 33, 33-38 (1998).
5) M. Strotzer, J. Gmeinwieser, M. Spahn, M, Volk, R. Frund, J. Seitz, V. Spies, J. Alexander, and S. Feuerbach, "Detection of simulated chest lesions with normal and reduced radiation dose: comparison of conventional screen-film radiography and a flat-panel x-ray detector based on amorphous silicon," Invest Radiol. 33, 98-103 (1998).
6) K. Nakagawa, Y. Aoki, Y. Sasaki, A. Akanuma, and S. Mizuno, "C-MOS flat-panel sensor for real time X-ray imaging, " Radiat Med. 18, 349-353 (2000).
7) J.M. Boone, J.A. Seibert, J.M. Sabol, and M. Tecotzky, "A Monte Carlo study of x-ray fluorescence in x-ray detectors," Med Phys. 26, 905-916 (1999).
8) M. Strotzer, M. Volk, T. Wild, P. von Landenberg, and S. Feuerbach, "Simulated bone erosions in a hand phantom: detection with conventional screen-film technology versus cesium iodide-amorphous silicon flat-panel detector," Radiology. 215, 512-515 (2000).
9) H.G. Chotas, and C.E. Ravin, "Digital chest radiography with a solid-state flat-panel x-ray detector: contrast-detail evaluation with processed images printed on film hard copy," Radiology. 218, 679-682 (2001).
10) M. Volk, M. Strotzer, N. Holzknecht, C. Manke, M. Lenhart, J. Gmeinwieser, J. Link, M. Reiser, and S. Feuerbach, "Digital radiography of the skeleton using a large-area detector based on amorphous silicon technology: image quality and potential for dose reduction in comparison with screen-film radiography," Clin Radiol. 55, 615-621 (2000).
11) C.E. Floyd Jr, R.J. Warp, J.T. Dobbins 3rd, H.G. Chotas, A.H. Baydush, R. Vargas-Voracek, and C.E. Ravin, "Imaging characteristics of an amorphous silicon flat-panel detector for digital chest radiography," Radiology. 218, 683-688 (2001).
12) K. Ludwig, H. Lenzen, K.F. Kamm, T.M. Link, S. Diederich, D. Wormanns, and W. Heindel, "Performance of a flat-panel detector in detecting artificial bone lesions: comparison with conventional screen-film and storage-phosphor radiography," Radiology. 222, 453-459 (2002).
13) J.M. Goo, J.G. Im, H.J. Lee, M.J. Chung, J.B. Seo, H.Y. Kim, Y.J. Lee, J.W. Kang, and J.H. Kim, "Detection of simulated chest lesions by using soft-copy reading: comparison of an amorphous silicon flat-panel-detector system and a storage-phosphor system," Radiology. 224, 242-246 (2002).
14) K. Kishimoto, "Evaluation of flat-panel detector for general radiography systems," Nippon Hoshasen Gijutsu Gakkai Zasshi. 58, 455-461 (2002).
15) J.T. Dobbins 3rd, E. Samei, H.G. Chotas, R.J. Warp, A.H. Baydush, D.E. Floyd Jr, and C.E. Ravin, "Chest radiography: optimization of X-ray spectrum for cesium iodide-amorphous silicon flat-panel detector," Radiology. 226, 221-230 (2003).
16) International Electrotechnical Commission, "Medical diagnostic X-ray equipment—Radiation conditions for use in the determination of characteristics," IEC 61267 (Geneva: IEC) (1994).

Table 1 Radiation quality for the determination of detective quantum efficiency and corresponding parameters

RADIATION QUALITY NO.	Tube Voltage [kV]	HVL [mm]	Additional Aluminum [mm]
RQA 3	50	4.0	10.0
RQA 5	70	7.1	21.0
RQA 7	90	9.1	30.0
RQA 9	120	11.5	40.0

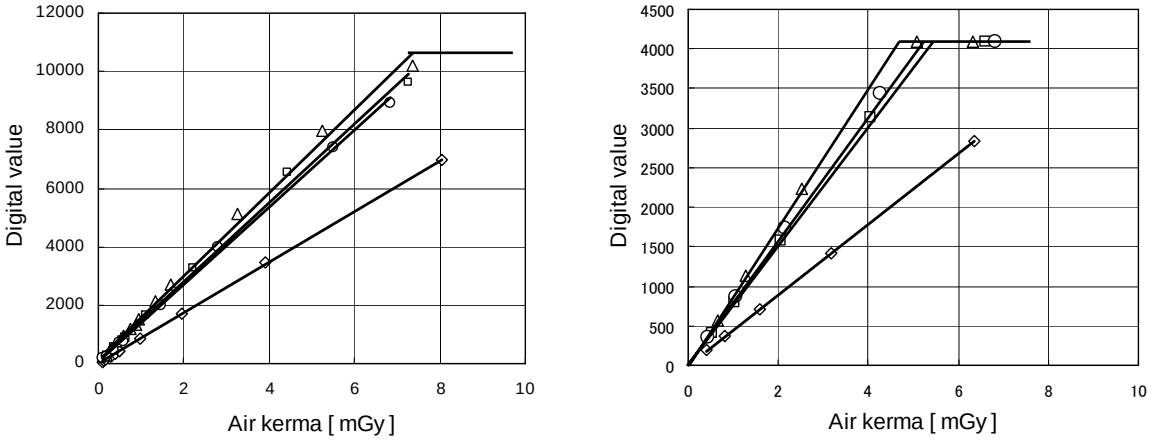

(a) Direct-conversion FPD (b) Indirect-conversion FPD

Figure 1 Characteristics of direct-conversion and indirect-conversion FPDs.
[◇: 50 kV (RQA 3), □: 70 kV (RQA 5), △: 90 kV (RQA 7), and ○: 120 kV (RQA 9)]

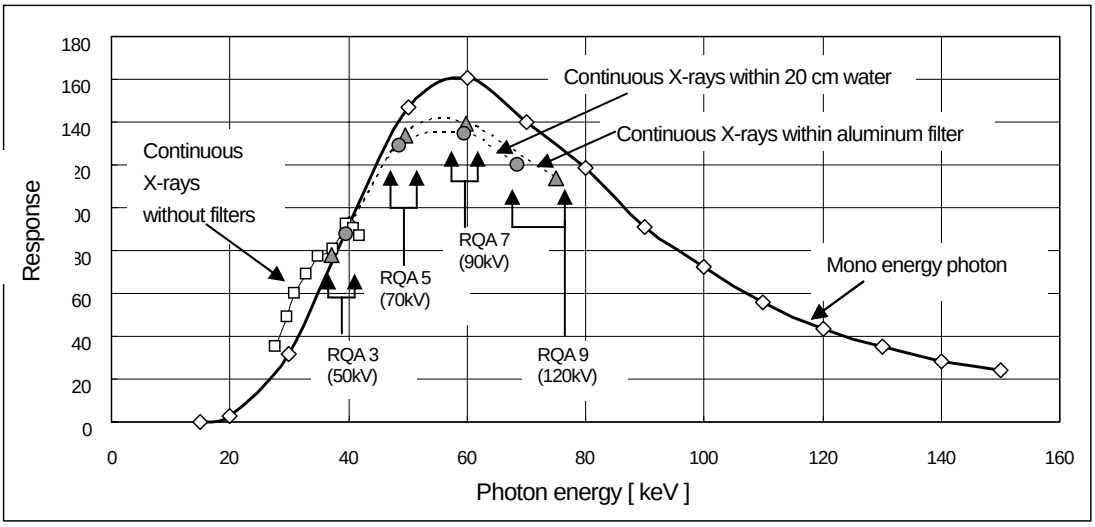

Figure 2 Relation between photon energy and response for direct-conversion FPD

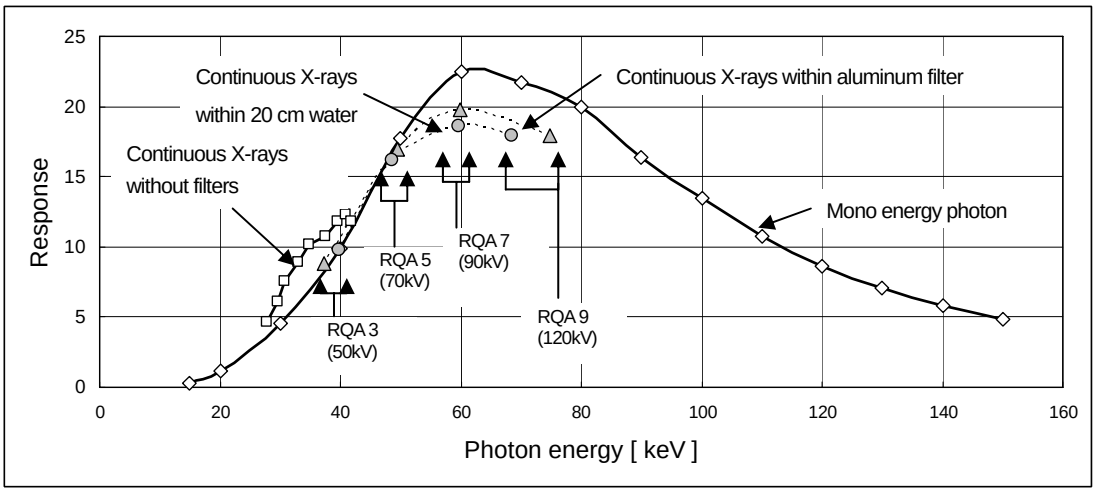

Figure 3 Relation between photon energy and response for indirect-conversion FPD

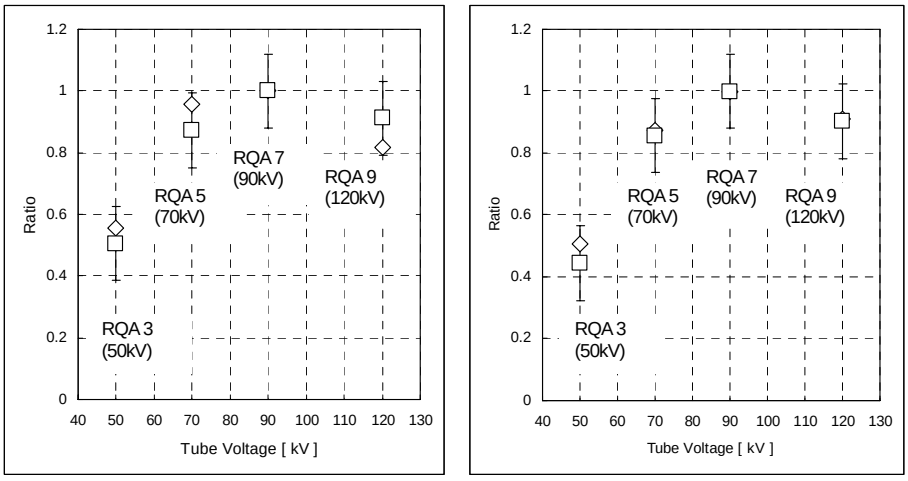

(a) Direct-conversion FPD (b) Indirect-conversion FPD

Figure 4 Ratio of each response. Each response was normalized to 1.0 in RQA 7. (□: measurement; ♢: simulation)

ANALYSIS OF X-RAY ENERGY CHANGE AT VARIOUS POINTS IN TWO TYPES OF CYLINDRICAL PHANTOM UNDERGOING X-RAY CT SCAN USING MONTE CARLO SIMULATION

Y.Sasada[1],and S.Koyama[2]

[1]Department of Radiological Technology, Graduate School of Medicine, Nagoya University

1-1-20 Daikou-Minami, Higashi area, Nagoya, Japan

[2]Nagoya University School of Health Sciences

e-mail:yuradio8172@yahoo.co.jp

Abstract

Technologies for multi-detector helical computed tomography (CT) have been rapidly developing. These technologies include the increase of detector row number along the x-ray tube rotation axis and the thinner slice reconstruction of axial image. Increasing of detector row number has produced wider beam width along the axis. In the CT dosimetry, CT chamber of 10cm long inserted in a cylindrical phantom is generally used. Length of the chamber, however, is not enough for present wider beam width. For the complete CT dosimetry small dosimetry device like Thermo Luminescence Dosimeter (TLD) or semiconductor dosimeter should be used. In generally these devices have strong energy dependence of x-ray sensitivity. The energy spectrum of x-rays is different according to the x-ray beam angle, since a beam-shaping filter is mounted at the x-ray tube aperture. The purpose of this study is to analyze x-ray energy change at various points in a phantom using EGS4 and to review the calibration factor of the dosimeter. In the result of the calculation, at the center point of phantom axial plane in the x-ray beam along the z axis, effective energy change was about 8% at maximum compared to it of the incident x-ray. When the measured value of TLD like $CaSO_4$ or Mg_2SiO_4 is corrected by calibration factor for the incident x-ray energy, it found that absorbed dose will be underestimated of a few percentages.

1. Introduction

Computed tomography (CT) is an important diagnostic imaging modality with rapid technical developments [1]. New technologies for multi-detector helical CT have been rapidly developing. These technologies include the increase of detector row number along the x-ray tube rotation axis and the thinner slice reconstruction of axial image. Increasing of detector row number has produced wider beam width along the axis. In the CT dosimetry, CT chamber of 10cm long inserted in a cylindrical phantom is generally used. Length of the chamber, however, is not enough for present wider beam width [2]. For the complete CT dosimetry, another dosimetry method using small dosimetry device like Thermo Luminescence Dosimeter (TLD) or semiconductor dosimeter should be used. In generally these devices have strong energy dependence of x-ray sensitivity.

In most CT scanner, beam-shaping filter is mounted at the x-ray tube aperture (figure 1) that corrects the x-ray attenuation through the object and adjusts the beam quality at the CT detector for each x-ray path. Energy spectrum of x-rays after passing the beam-shaping filter, therefore, is different according to the x-ray beam angle. In addition, the spectrum of the x-ray through the object material is changed in the object. In this study, the x-ray energy change at various points in

two types of cylindrical phantom undergoing x-ray CT scan was calculated using Monte Carlo simulation Method, and the effect of energy correction was analyzed in use of the dosimetry devices which have strong energy dependence.

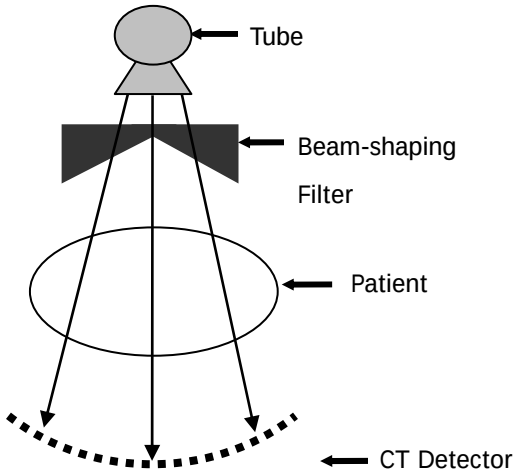

Figure 1 Geometrical position of beam-shaping filter in x-ray CT

2. Methods

2.1 Monte Carlo simulation

Energy spectrum in the phantom was calculated using the Low-Energy Photon-Scattering Expansion for the EGS4 Code (LSCAT) which is one of Monte Carlo method. Number of photons was set to become less than 5% of fractional standard deviation (FSD) and made a cutoff-energy of the photon to 5keV.

2.2 Source and spectrum

Distance between x-ray tube rotation axis and the source was set to 60cm and the source turned every 10 degrees. Here the horizontal line and vertical line through the x-ray tube rotation axis on the axial plane is assumed x axis, and y axis respectively. The orthogonal axis of x and y axis is assumed z axis. Beam hardning of the x-ray through the beam-shaping filter was divided by three steps and three kinds of spectrum were used (Figure 2, Figure 3).

2.3 Abdominal phantom for the CT and Thoracoabdominal Phantom

Figure 4 shows the geometry of abdominal phantom for the CT (cylindrical phantom 1). The phantom material was polymethylmethacrylate (PMMA) with 32cm diameter, the length along z axis of 40 cm. Calculation was also performed for water material. Figure 5 shows the geometry of thoracoabdominal phantom (cylindrical phantom 2) of Japan Industrial Standard (JIS; Z4915; JIS phantom). The material of JIS phantom was PMMA with the length along z axis of 40 cm.

2.4 Deviation of calibration factor

Deviation of the calibration factor (D_{cf}) which was shown in the result was calculated using the following formula (1).

$$D_{cf} = (C_{incidence} - C_{point}) \div C_{point} \times 100 \quad (1)$$

$C_{incidence}$ is calibration factor for the effective energy of the incident x-rays at the surface of the phantom.

C_{point} is calibration factor for the effective energy at the point in the phantom. The effective energy was calculated by the x-ray spectrum which was obtained by Monte Carlo Method.

3. Results

Table 1 shows effective energy of the x-ray before incidence on the surface of phantoms and them at the various points in the phantoms. At the center point of phantom axial plane in the x-ray beam along the z axis, effective energy change was about 8% at maximum compared to it of the incident x-ray.

Figure 6 shows the effective energy at various points in the cylindrical phantom. The effective energy of the center point was lower than that of the peripheral point in the phantom. And energy was decreased with increasing distance between the beam center and the detector along the z axis. It was thought that the contribution of the scattered radiation became larger than the primary radiation at the center of the phantom.

Figure 7 shows the D_{cf} at various points in the cylindrical phantom. When TLD was used as a detector, the maximum D_{cf} was about 13%. In case of the semiconductor dosimeter, D_{cf} was about 5% at maximum. Figure 8 shows the effective energy at various points in the JIS phantom. Figure 9 shows the D_{cf} in the JIS phantom. All the data had a similar tendency shown in these graphs.

Table 1 Effective energy at the various points

Effective energy of the x-ray before incidence on the surface of phantoms ; 52.5keV

Distance from the beam center (along z axis)	Cylindrical phantom 1				JIS phantom			
	PMMA	WATER	PMMA	WATER	PMMA			
	Inside 1cm (peripheral)		Rotation center		Inside 1cm(Y)	Inside 5cm(Y)	Rotation center	Inside 1cm(X)
0cm	54.0	56.5	51.0	55.0	53.0	51.2	50.6	56.0
1cm	47.5	50.2	46.9	49.8	46.5	45.5	45.2	48.3
5cm	45.0	49.1	45.0	48.1	45.1	44.2	43.3	45.7
9cm	44.2	49.0	44.0	48.0	44.3	43.0	42.4	44.8
13cm	44.0	48.4	43.2	48.0	43.6	42.5	41.9	44.2
17cm	44.0	48.2	43.2	48.0	43.6	42.5	41.9	44.2

4. Discussion

4.1 Trends in D_{cf} along the z axis

When using a TLD or a semiconductor dosimeter in Anthropomorphic Phantom which has long trunk, there is a possibility that the absorbed dose is underestimated by using a calibration factor at the effective energy for the incident x-rays.

4.2 Calibration by effective energy in the phantom

It was shown that absorbed dose at each point which was calibrated by the effective energy for the incident x-rays energy was underestimated. Effects of effective energy change, however, was very small, because the absorbed dose at the point apart from the beam center along z axis was also small compared to it at the beam center. Therefore, it was reviewed as follows (2), (3).

$$D_{cf} \times R_d = D_{act} \qquad (2)$$

D_{cf} is deviation of the calibration factor. R_d is a ratio of the absorbed dose at the each point to it at the beam center. D_{act} is actual deviation of the absorbed dose at the each point.

cf. a point apart from the beam center along the z axis is 5cm. D_{cf}=0.1, R_d=0.05.

$$0.1 \times 0.05 = 0.005 \qquad (3)$$

D_{act} is 0.005 (0.5%).

5. Conclusions

In this study, the analysis of x-ray energy change at various points in a phantom was performed using EGS4 and the calibration factor of the dosimeter was reviewed. In the result of the calculation, at the center point of phantom axial plane in the x-ray beam along the z axis, effective energy error was about 8% at maximum compared to it of the incident x-ray. When the measured value of TLD like $CaSO_4$ or Mg_2SiO_4 is corrected by calibration factor for the incident x-ray energy, it found that absorbed dose will be underestimated of a few percentages.

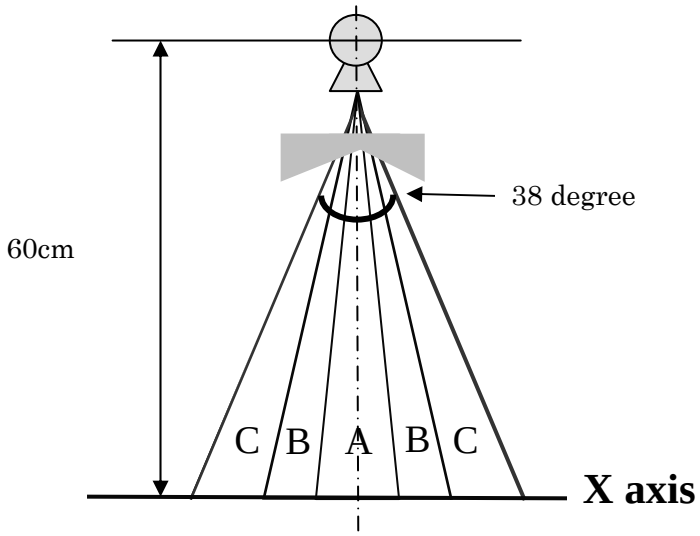

Figure 2 Geometrical settings of x-ray tube, beam-shaping filter and x-ray fan beam

Energy spectrum of x-rays after passing the beam-shaping filter is different according to the x-ray beam angle. The spectrum was divided by three steps A to C, each energy spectrum is shown in figure 3. The range A is ±5cm from the beam center on the x axis. The range B is outside of range A (+5 ~ +10cm, -5 ~ -10cm). The range C is outside of range B (+10 ~ +21cm*, -10 ~ -21cm*) * $21 \cong 60 \tan(38 \times 0.5 \times \pi \div 180)$

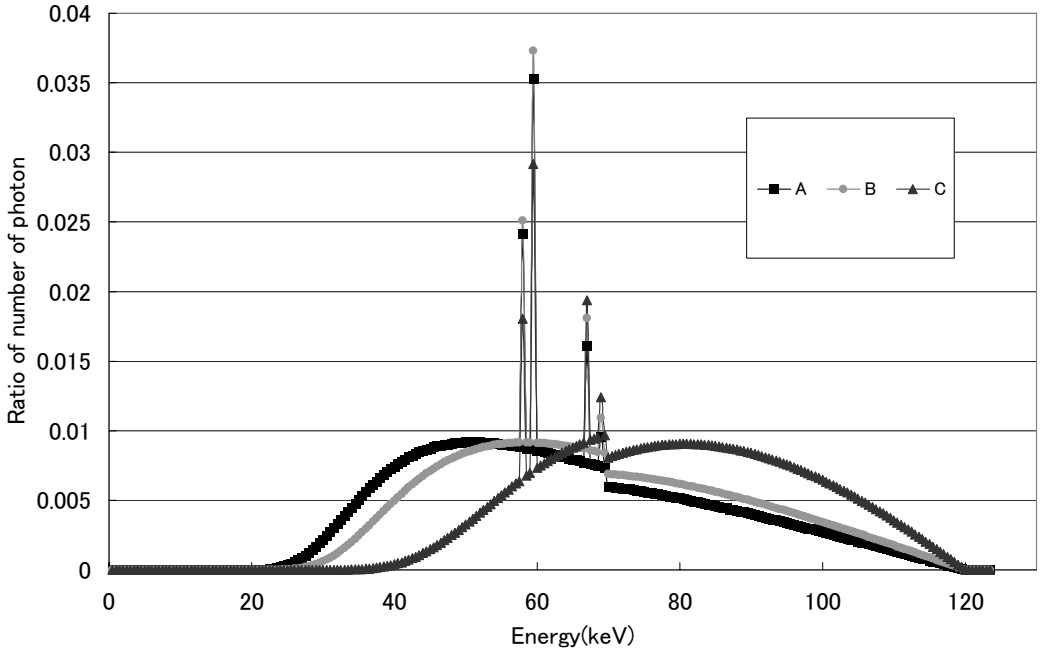

Figure 3 Spectrum after passing through Beam-shaping Filter

Spectrum A, B, and C were that of range A, B, and C in figure 2. These spectra were calculated by Birch-Marshall formula. Maximum energy of these spectra is 120keV. Effect energy of A is 52.5keV, B is 58.8keV, and C is 74.3keV. Each effective energy corresponded to actual half value layer of TOSHIBA: TCT300 scanner.

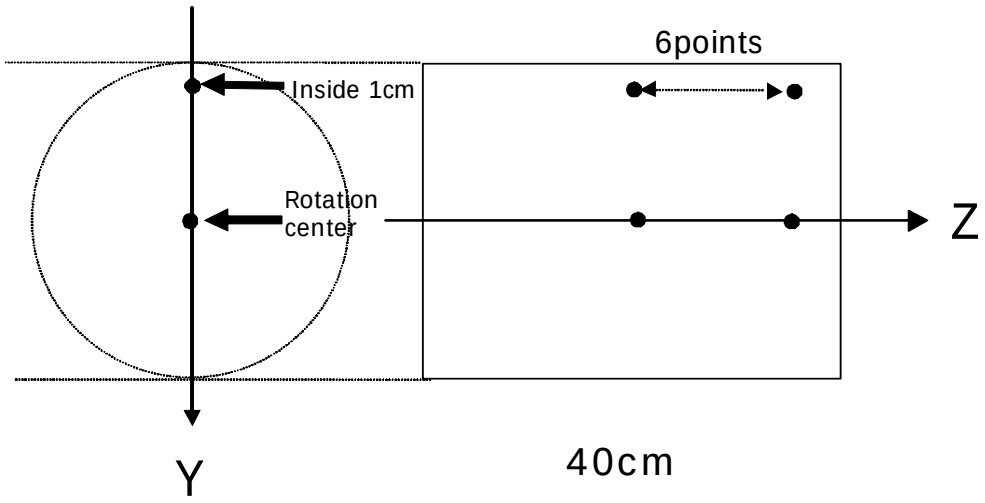

Figure 4 Cylindrical phantom 1

Detectors were set at 1cm inside from the surface of phantom on the y axis and at rotation center. Along the z axis, six detectors were set at beam center and at 1, 5, 9, 13, and 17cm apart from beam center. The shape of the detector was small cylinder. The size of these detectors was 1cm diameter with 0.4cm thickness.

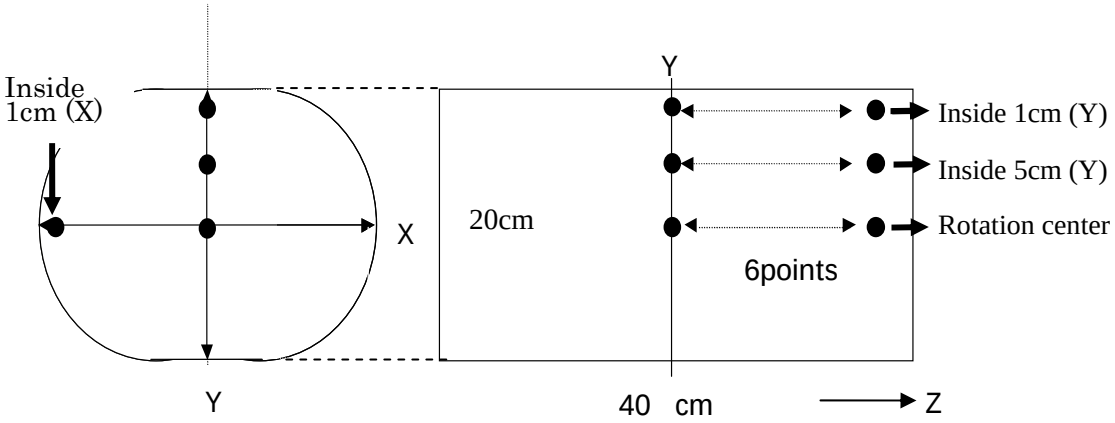

Figure 5　JIS phantom (cylindrical phantom 2)

Detectors were set at 1cm and 5cm inside from the surface of phantom on the y axis and at rotation center. Along the z axis, six detectors were set at beam center and at 1, 5, 9, 13, and 17cm apart from beam center. The shape of the detector was small cylinder.　The size of these detectors was 1cm diameter with 0.4cm thickness.

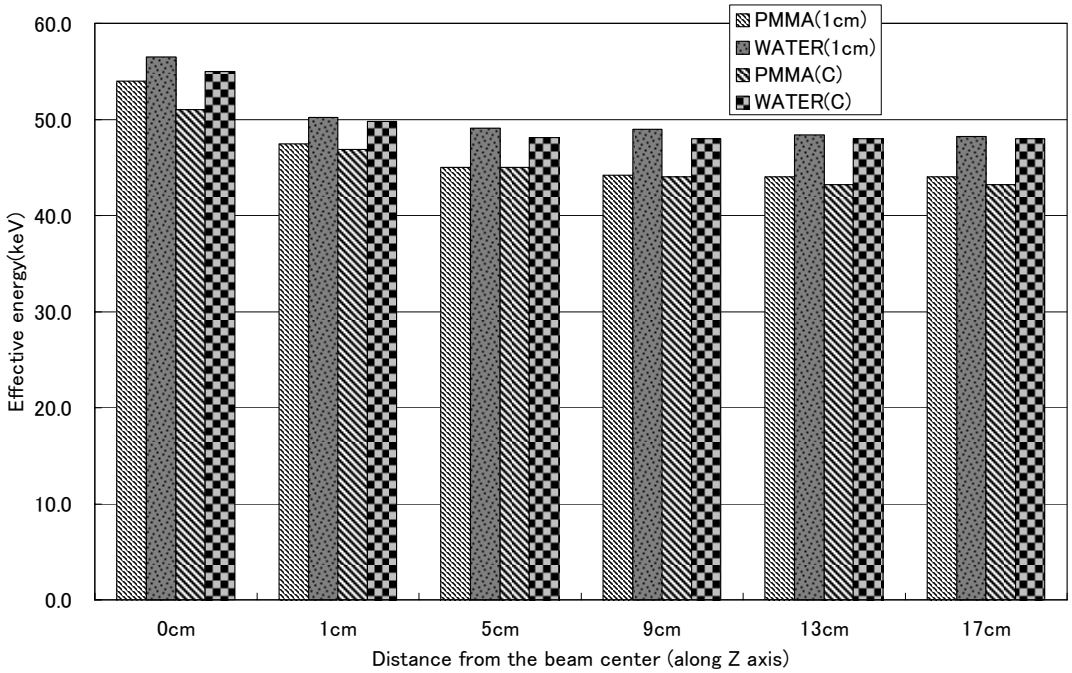

Figure 6　Effective energy at various points in the cylindrical phantom 1

"(1cm) " of the explanatory remarks shows the 1cm inside from the surface of phantom. "(C)" shows the rotation center.

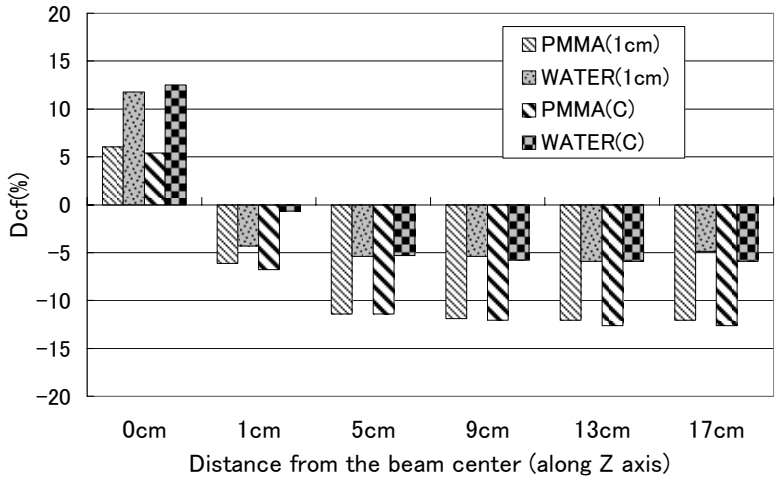

(a) TLD ($CaSO_4$)

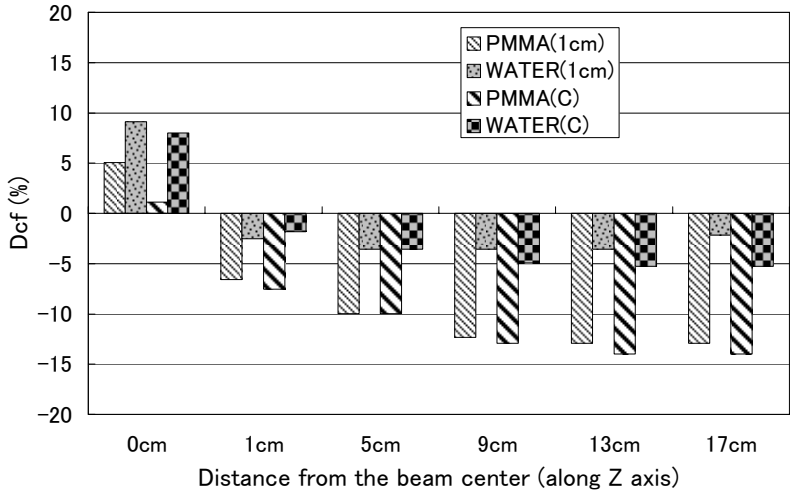

(b) TLD (Mg_2SiO_4)

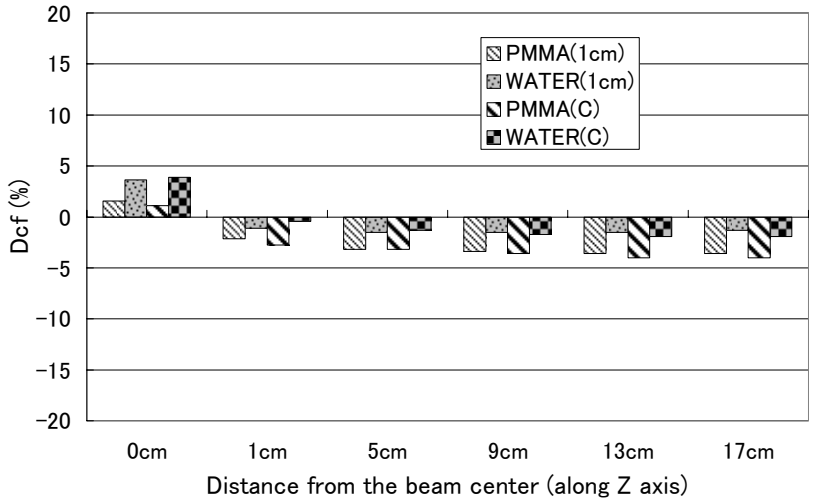

(c) semiconductor dosimeter

Figure7 D_{cf} at various points in the cylindrical phantom 1 (a) ~ (c)

(a) shows the $\mathbf{D_{cf}}$ of TLD ($CaSO_4$). (b) shows the $\mathbf{D_{cf}}$ of TLD (Mg_2SiO_4). (c) shows the $\mathbf{D_{cf}}$ of semiconductor dosimeter. The vertical axis shows $\mathbf{D_{cf}}$ (see formula 1) and the transverse axis shows the distance from the beam center along the z axis.

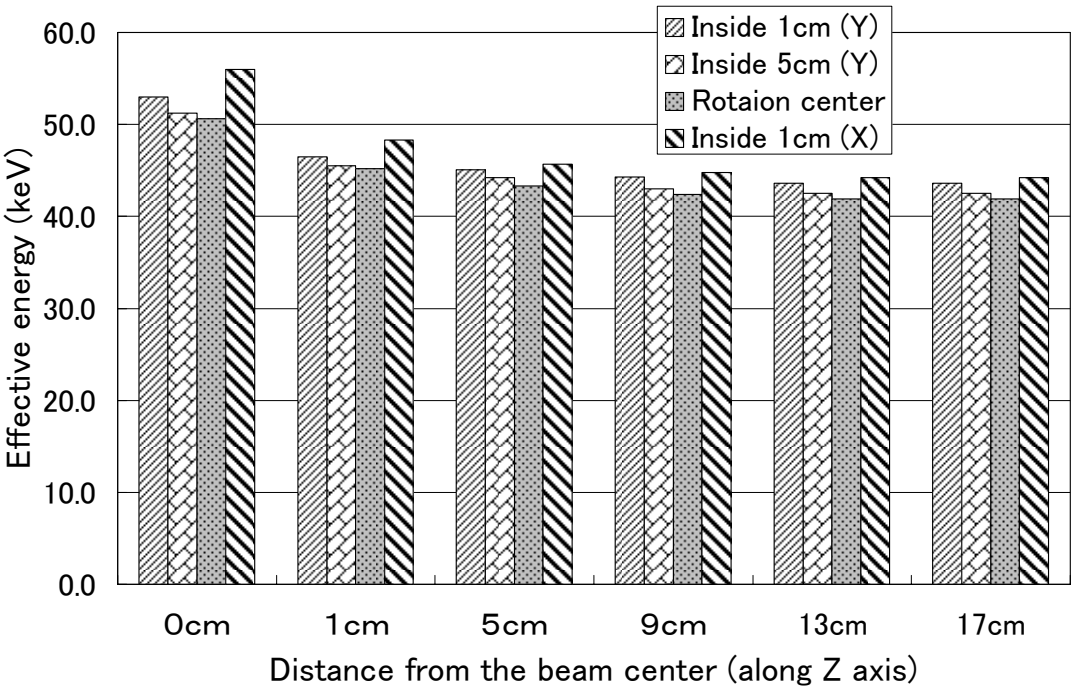

Figure 8　Effective energy at various points in JIS phantom

"Inside 1, 5cm (Y)" shows the position of the 1 and 5cm inside from the surface of phantom on the y axis. "(X)" shows along the x axis.

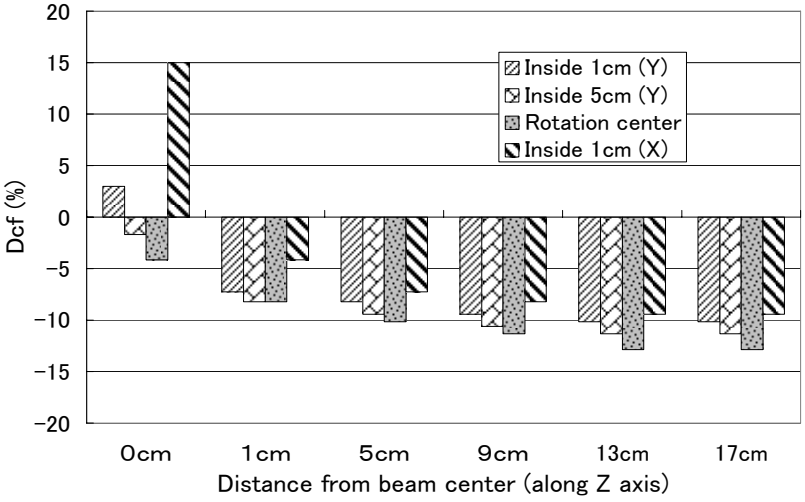

(a) TLD ($CaSO_4$)

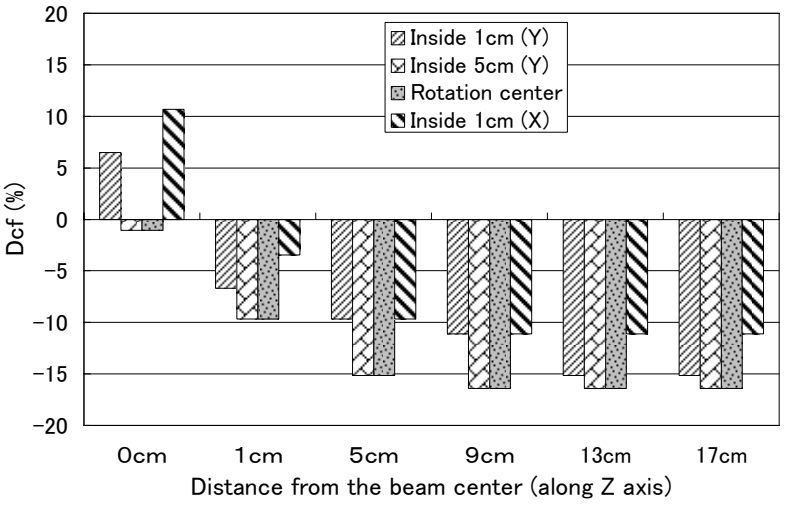

(b) TLD (Mg_2SiO_4)

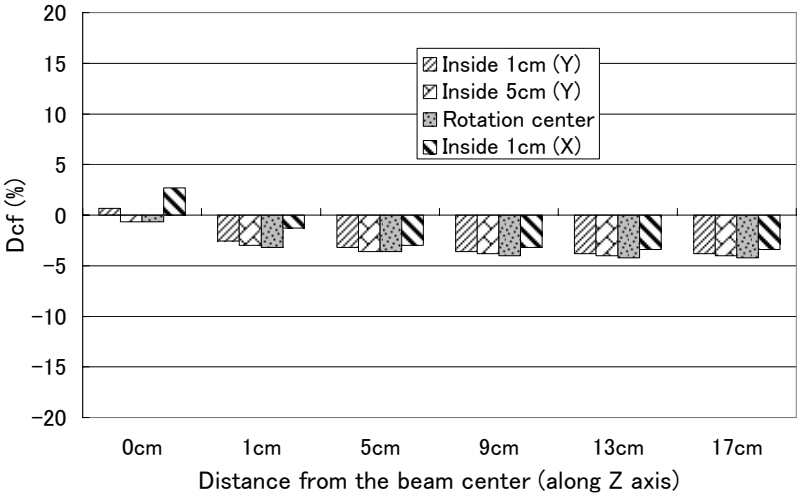

(c) semiconductor dosimeter

Figure 9 D_{cf} at various points in the JIS phantom (cylindrical phantom 2) (a) ~ (c)

(a) shows the $\mathbf{D_{cf}}$ of TLD ($CaSO_4$). (b) shows the $\mathbf{D_{cf}}$ of TLD (Mg_2SiO_4). (c) shows the $\mathbf{D_{cf}}$ of semiconductor dosimeter.

References

1) Flohr T, Stierstorfer K, et al : Image reconstruction and image quality evaluation for a 64-slice CT scanner with z-flying focal spot, Med Phys. 32, August 2005,2536-2547.
2) Robert L et al :Experimental validation of a versatile system of CT dosimetry using a conventional ion chamber: Beyond CTDI100, Med. Phys. 34 (8) , August 2007,3399-3413.
3) M. Tachibana et al : Effect of the Beam-shaping Filter of Computed Tomography Scanners on the Conversion of Absorbed Dose in Water and Polymethyl Methacrylate Phantom, Jpn.J.Radiol.Technol.57,51-58(2001).
4) JARP: Date Book of Medical Physics, Jpn.J.Med Phy40,(1994).
5) JSRP: DATE BOOK OF PHOTON ATTENUATION COEFFICIENTS(1995).
6) Y.NAMITO and H.HIRAYAMA: LSCAT: low-energy photon –scattering expansion for the EGS4 Code, KEK Internal(2000)
7) S J GOLDING et al : Radiation dose in CT: are we meeting the challenge?, The British Journal of Radiology, 75, 2002, 1-4

OPTIMIZATION OF DETECTOR THICKNESS FOR CALCULATION OF BACKSCATTER FACTOR USING MONTE CARLO SIMULATION

Y.Sakai[1], S.Koyama[2]

[1]Department of Radiological Technology, Graduate School of Medicine,
Nagoya University, 461-8673, Nagoya , Japan
[2]Nagoya University School of Health Sciences
e-mail:yohe1020@yahoo.co.jp

Abstract

In medical x-ray examination, patient exposure is usually evaluated by entrance skin dose. In the actual measurement of the entrance skin dose, exposure (C/kg) is measured free in air using ionization chamber, and it is converted to absorbed skin dose (Gy). To compensate the contribution of backscatter due to existence of back tissue, backscatter factor (BSF) is essential. However there are few data sets of BSF for diagnostic x-rays, it is necessary to develop a valid data set of BSF. In this study, optimum detector thickness to accumulate the primary and scatter x-rays was discussed when calculating the BSF using EGS4. Calculation method and parameters together with the result were compared with other works. The result of our calculation indicated that the optimum detector thickness to calculate BSF for diagnostic x-rays is 1 mm.

1. Introduction

In medical x-ray examination, it is necessary to evaluate an exposed dose correctly due to discussion of reducing patient exposure. To evaluate patient exposure, entrance skin dose was recommended by IAEA (International Atomic Energy Agency) guidance level and by JART (The Japan Association of Radiological Technologists) guidance level. In the actual measurement of the entrance skin dose, exposure (C/kg) is measured free in air using ionization chamber, and it is converted to absorbed skin dose (Gy). To compensate the contribution of backscatter due to existence of back tissue, backscatter factor (BSF) is essential. For a rigorously definition, BSF should be evaluated by using an infinitesimal detector at the surface of phantom which simulate soft tissue. However it is necessary a detector has some volume to accumulate the primary and scatter x-rays when BSF is calculated by using EGS4.

In this study, optimum detector thickness to accumulate the primary and scatter x-rays was discussed when calculating the BSF using EGS4.

2. Materials and Methods

Calculation method using EGS4 was showed in Figure 1 and Table 1 . The water phantom was 50 cm × 50 cm × 50 cm , and the SSD was 100 cm . The irradiation field size was 10 cm × 10 cm on the surface of the water Phantom . Detector width was 1 cm × 1 cm , and its thickness was changed from 0.5 mm to 10 mm (0.5mm , 1 mm , 3 mm ,5 mm , 10 mm) . The detector was placed on (or in) the surface of the water Phantom : on the surface was called " ON " , in the surface was called " IN" . （Figure 1 ） The irradiation condition was made as shown in Table 1 , tube voltage was 100 kV , X-ray tube was simulated TOSHIBA DRX-2425C and target angle was 12° . From the

condition of showing above , the beam energy was set for HVL to become 5mmAl by using the Birch's formula . Figure 2 showed the spectrum used in this simulation . Number of photon was 100 million , and LSCAT which was one of Monte Carlo code was used for the particle transportation . The BSF was calculated from the deposited energy ratio which was primary and scatter in the detector . It showed formula (1) .

$$BSF = \frac{Deposited\ \ Energy\ \ from\ \ primary\ \ and\ \ scatter}{Deposited\ \ Energy\ \ from\ \ primary} \quad (1)$$

Then , the thickness was examined to find out an appropriate number of particles and the calculation time . At this time, the number of particles was one million .

Figure 1 Geometry to calculate BSF

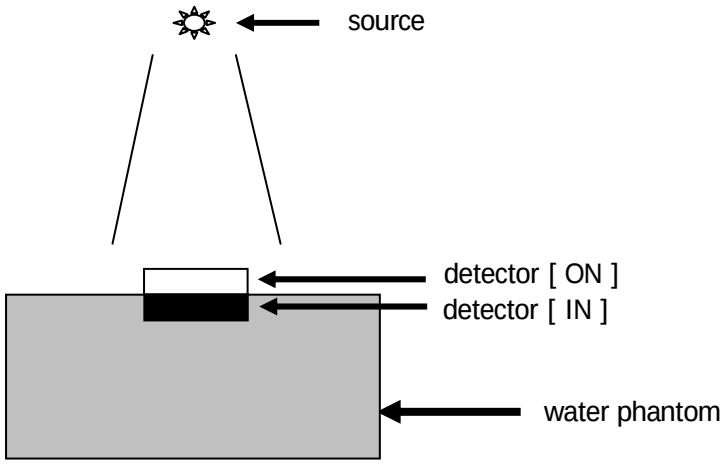

SSD was 100cm . Detector positions were [ON] and [IN] . Detector width was 1 cm×1 cm and thickness was from 0.5 mm to 10 mm (0.5mm , 1 mm , 3 mm ,5 mm , 10 mm) .Water phantom size was 50 cm×50 cm×50 cm . Irradiation field was 10 cm×10 cm .

Table 1 irradiation condition

Tube voltage[kV]	100
Target angle[°]	12
HVL[mmAl]	5
Efficient energy[KeV]	42

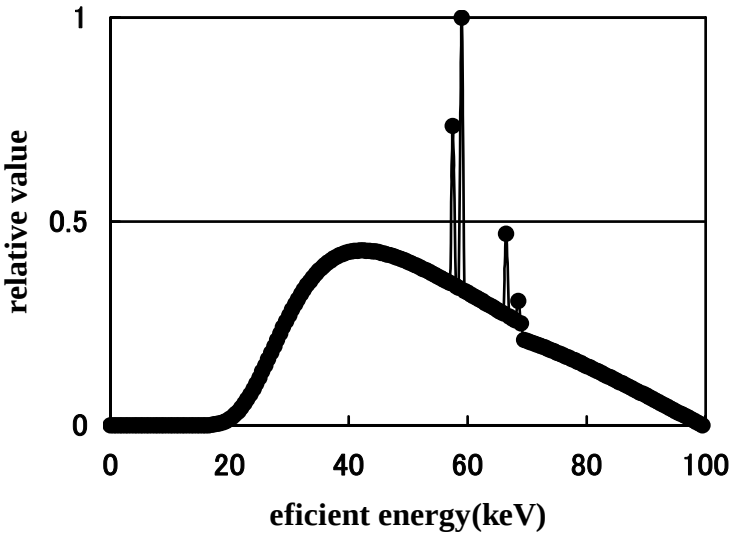

Figure 2 Spectrum using Monte Carlo simulation

This spectrum was made by Birch5 which was made by H Kato . Birch5 can make X-ray spectrum using Birch's formula .

3. Results

The result concerning the thickness and BSF were shown in Figure 3 . The detector emerges difference by the position while becoming thick . And BSF decreases with decreasing detector thickness . Increasing of BSF for large values of detector thickness might be due to incidence of scattered radiation from the side of detector . When the thickness of detector is large and it is in water phantom , BSF might be overvalued . Therefore , 0.5 mm or 1 mm may optimize the thickness of detector .

The result concerning the thickness and calculation time were shown in Figure 4 . Calculation time increases with decreasing detector thickness . Therefore , 1 mm or 3 mm may optimize the thickness of detector .

Figure 3 Relation between detector thickness and BSF

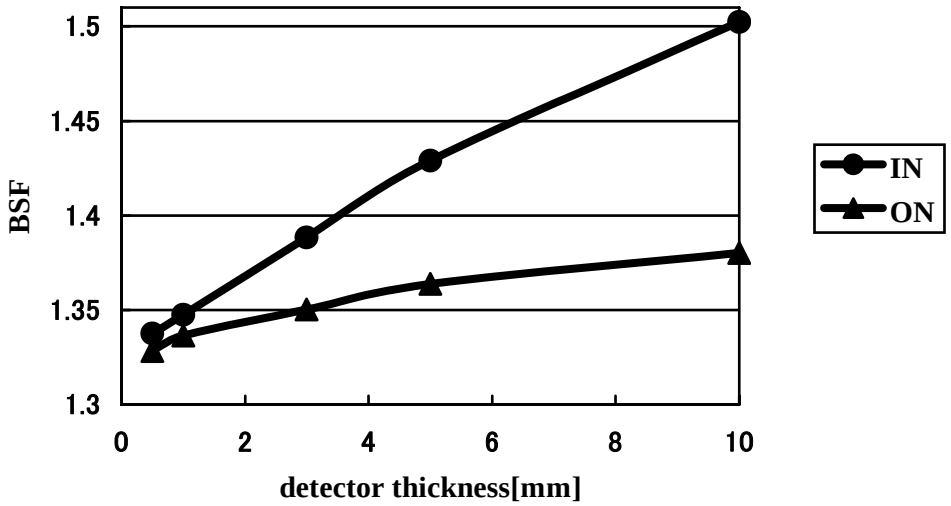

[ON] means that the detector was placed on water phantom . [IN] means that the detector was placed in water phantom . It showed Figure 1 . Increasing of BSF for large values of detector thickness might be due to incidence of scattered radiation from the side of detector . [IN] was particularly influenced .

Figure 4 Relation between detector thickness and number of batchCalculation time increases with decreasing

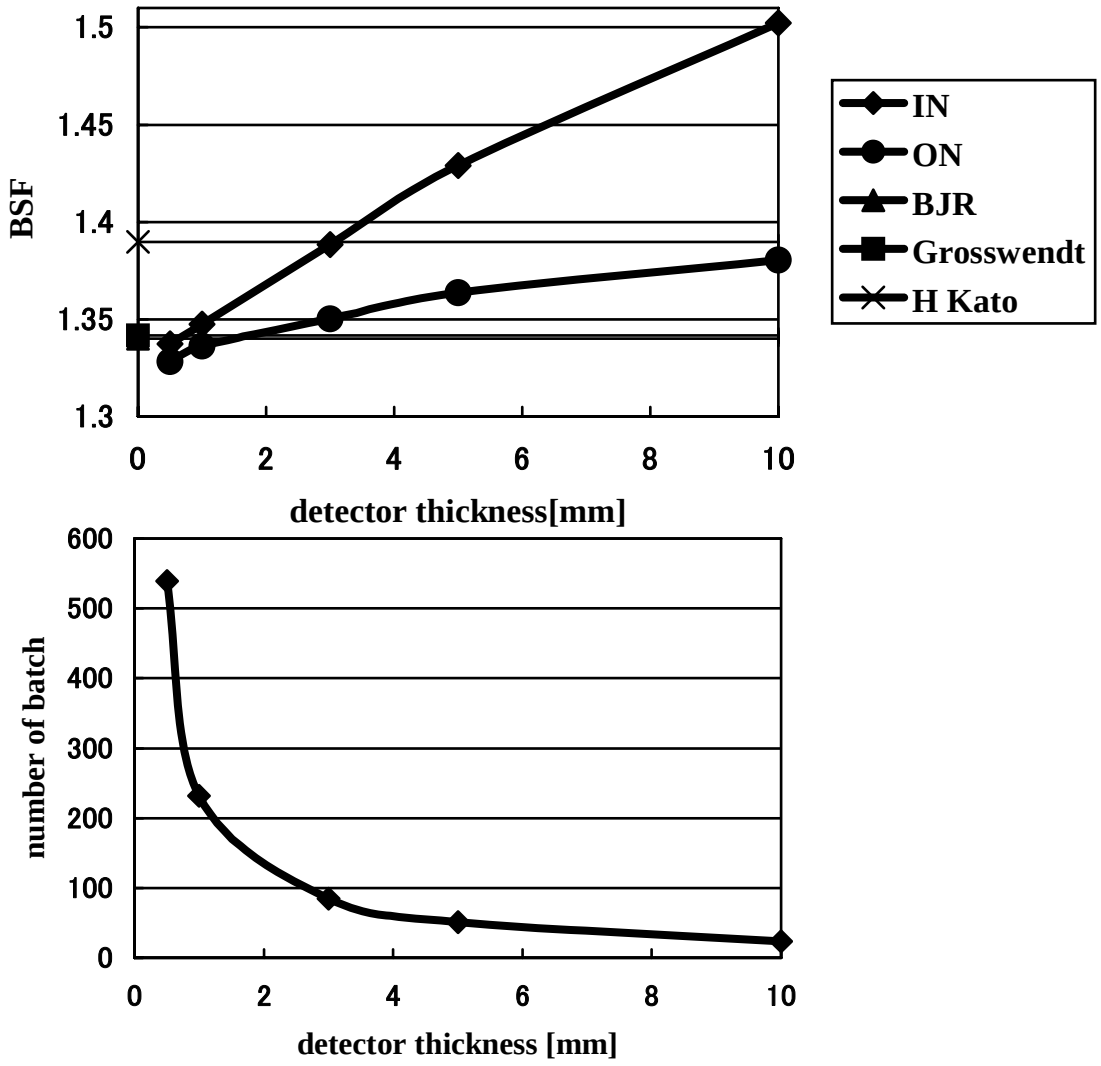

detector thickness .

figure 5 . A comparison of the present data and those published earlier (1) British Journal of Radiology 1983(BIR) , (2) B Grosswendt (1990) ,(3) H Kato (2001)

4. Discussion

A comparison of the present data and those published earlier (1) , (2) ,(3) were carried out in the following and it showed figure 5 .

First , the present data was compared with the reference (1) British Journal of Radiology 1983 . The reference (1) was similar value to present data in 1mm . The reference (1) , however , has problem that tube voltage is unknown .

Second , the present data was compared with the reference (2) B Grosswendt (1990) . The reference (2) was similar value to at present data in 1mm and the reference (1) .

Finally , the present data was compared with the reference (3) H Kato (2001) . The reference (3) was larger value than other three data . BSF of the reference (2) and (3) were calculated on the basis of same formula (1) . But both of them were not same values . BSF is not same value when energy spectrum is different even if method and HVL are same . This has been mentioned by the reference (3) . The statistical uncertainties was seen between the present data and the reference (3) though both of them were used same X-ray energy spectrum . It is necessary to obtain BSF with reference (3) in a similar method because method is different .

5. Conclusions

The optimum thickness of detector was 1 mm in this study , though the method that must reexamine . Then , when present data compared with other known data , it had difference . It is necessary to calculate BSF with knowing factor which influences BSF .

References

1) British Journal of Radiology 1983 Central axis depth dose data for use in radiotherapy . Br J Radiol , (suppl 17) ,(1983)
2) B Grosswendt :Dependence of the photon backscatter factor for water on source to phantom distance and irradiation field size . Phys Med Biol , 35(9) , 1233-1245 , (1990)
3) H Kato : Method of Calculating the Backscatter Factor for Diagnostic X-rays Using the Differential Backscatter Factor . JSRT , 57(12) , 1503-1510 , (2001)

Measurement of Monochromatic Radiation Using a Proportional Counter and Comparison with EGS5 Simulations

Y. Kirihara, Y. Namito†, H. Hirayama†, M. Hagiwara† and H. Iwase†
The Graduate University for Advanced Studies, Oho1-1, Tsukuba, Ibaraki 305-0801, Japan
†*KEK High Energy Accelerator Research Organization, Oho1-1, Tsukuba, Ibaraki 305-0801, Japan*

Abstract

We have performed a mono-energetic photon scattering experiment at the BL-14C in KEK Photon Factory (PF experiment). Photons scattered by C, Cu and Ti target were measured by a proportional counter located at $\theta = 90°$. The experimental data were compared with calculations using the EGS5 code. The calculation and measurement of Compton peaks had the difference within 7%, and K-X peak had the difference within 24% for Cu and 7% for Ti target. In addition, we have performed Cu, Rb, Mo and Ag K-X ray measurements from variable energy X-ray source using a Ge detector and a proportional counter and compared the measurement data of the two detectors (RI experiment). The intensities of K-X peaks of the two measurements had difference within 16%.

1 Introduction

Ge detectors are used for measurements of X-ray spectrum because of the excellent energy resolution. However, the efficiency decrease below 10 keV due to dead layers ($\sim$0.3μm). The efficiency in the simulation therefore possibly have a few % of uncertainly.

Proportional counters are also utilized for measurements of X-ray spectrum, and have no dead layers. The efficiency of proportional counters can be well estimated by the simulation. We measured mono-energetic photon spectrum by a proportional counter, and compared with the measurements of the Ge detector to estimate the dead layer thickness of the Ge detector.

In this paper, we simulated the measured response to the proportional counter of scattered mono-energetic synchrotron photons at the angle $\theta = 90°$ on several targets. They are compared to Monte Carlo simulations using the EGS5 code. In addition, we have performed K-X ray measurements from variable energy X-ray source using a Ge detector and a proportional counter. The intensity of the detectors were compared.

2 Experiments

2.1 PF Experiment

In the PF experiment, mono-energetic photons were delivered to the BL-14C in KEK Photon Factory (KEK-PF). The experimental flows are shown as follows (See also Fig. 1).

1. Synchrotron photons from a vertical wiggler were monochronized by a Si(1,1,1) double crystal monochrometer. The incident photon energies are 20, 30 and 40 keV.

2. Number of incident mono-energetic photon beams were measured by a free-air ionization chamber placed in the front of the target.

3. Mono-energetic photon beams were scattered by a target. Target materials were carbon, copper and titanium (shown in Table 1).

4. The scattered photons were detected by a proportional counter located at $\theta = 90°$.

Table 1: Target materials character

Material	C	Cu	Ti
Thickness (g/cm^2)	0.180	0.986	0.726
K_α X-ray (keV)	0.277	8.048	4.511

Each target was installed in a vacuum chamber and vacuum pipes were placed between the vacuum chamber and the proportional counter in order to reduce any scattering due to the air. Collimator of 5.01 mm ϕ and 10 mm length was placed in front of the proportional counter. The distance from the surface of the target to the collimator was 448 mm. The specification of the proportional counter used in the experiment is shown in Table 2.

Table 2: The specification of the proportional counter

Type	Gas Filling	Gss Press	Effective Width	Window Material	Areal Density
LND, Inc.:4244	Xe, (CO_2)	800 Torr	19.05 mm	Beryllium	9.0 mg/cm^2

Measured spectra were normalized by number of photons and the solid angle 9.78×10^{-5} sr. The energy calibration with a linear function was used by two well-known energy peaks, Compton and the K-X. At $\theta = 90°$, Compton peaks were obtained following formula:

$$E_c = \frac{E_\gamma}{1 + E_\gamma / mc^2} \quad (1)$$

where E_γ is an incident energy before the scattering, and mc^2 is the rest mass of electron. The K-X energies were shown in Table 1.

2.2 RI Experiment

In the RI experiment, We performed K-X ray measurements from an X-ray source using a Ge detector and a proportional counter. "Variable energy X-ray source (Amersham International Limited, code:AMC.2084)" was used for the X-ray source. The simple experimental arrangements are shown in Fig. 2. Cu, Rb, Mo and Ag K-X rays from the X-ray source were detected by the Ge detector and the proportional counter. Each K-X energy is shown in Table 3. Rayleigh and Compton scattering from Am-241 source were also detected. A collimator of 5.01 mm ϕ was placed in front of the detectors. The distance from the surface of the X-ray source to the detectors was 65 mm. The measured energy spectra from the Cu, Rb, Mo and Ag targets using the detectors are shown in Fig. 3. In the Ge detector, Rayleigh peak and Compton scattering peak can be shown. In the proportional counter, Xe escape peaks of Rayleigh and Compton can be shown.

Table 3: Incident K-X energy

Target Material	Energy (keV)	
	K_α	K_β
Cu	8.048	8.905
Rb	13.395	14.961
Mo	17.479	19.607
Ag	22.163	24.943

3 Calculations using the EGS5 code

3.1 Energy spectra at the PF experiment

The incident photons to the proportional counter were estimated using EGS5 calculations shown in Fig. 4. The source position was set uniformly distributed in the collimator ($\sim$5.01 mm ϕ). The direction of the incident photons was set parallel to the proportional counter.

The geometry of the proportional counter is shown in Fig. 5. The photon beam enter the effective region of Xe gas through the beryllium window. The insensitive region was also considered (See Fig. 5 caption for detail). In the simulation, the energy deposition ΔE in the effective region was scored.

There exists differences on energy resolution between the measured data and the calculations. Compared with the experiment data, the calculated peaks were broadened so that the FWHMs (full width at half maximum) were set to be same to the experimental data.

3.2 Efficiency of the detectors at the RI experiment

The efficiencies of the Ge detector and the proportional counter were calculated with changing the incident energy, and using the geometries shown in Fig. 6 and 7. The peak efficiencies are shown in Fig. 8.

4 Results and discussions

In the PF experiment, the calculated and measured energy spectra for the C, Cu and Ti targets are shown in Fig. 9. The calculated spectra reproduce the measured spectra inclined. The calculation and measurement of Compton peaks had the difference within 7%. The K-X escape peaks (7.6$\sim$10.5 keV) from Xe gas can be observed for targets at 40 keV. The K-X peak was also detected. The calculation and experiment had difference within 24% for Cu and 7% for Ti target. In the plateau region between the peaks of Compton and the K-X, discrepancies are large. This is due to pile ups effect of the K-X photons. If there is no pile ups in the measurement, the agreement of the plateau region will come better. On the other hand, the pile up component does not explain the disagreement on the K-X peaks, since it is only 2 $\sim$ 5% of the K-X peak. In the experiment, the collimator exist between the target and the proportional counter. If they are included in the calculation, the disagreement of the K-X peak will be improved. The rectangle geometry of the detector might cause an uncertainty on the electron collection in the experiment. A cylindrical proportional counter was prepared for the next beam time.

In the RI experiment, the intensities of Ge detector and the proportional counter for the Cu, Rb, Mo and Ag targets are shown in Fig. 10. The energy resolution of Ge detector is better than the proportional counter. The K-X peaks of the two measurements had difference within 16%.

Total counts, Compton counts and the K-X peak counts in the PF experiment were compared with the proportional counter measurement over EGS5 Calcuration (PPC/C) ratio in Fig. 11. The K-X peak counts in the RI experiment were also compared with the proportional counter over the Ge detector ratio in Fig. 11.

5 Conclusions

In this study, we measured the synchrotron radiation of mono-energetic incident photon using a proportional counter. The energy spectra measured by the proportional counter was simulated using the EGS5 code, and compared to the measured energy spectra. In addition, we measured K-X ray from variable energy X-ray source using a Ge detector and a proportional counter, and compared

to the intensities of the detectors. Total counts, Compton counts and the K-X peak counts were compared with the calculation over measurement ratio. The shape of Compton scattering and the K-X peaks were well reproduced by the EGS5 calculation. We should note the following points in future:

- Including collimator in the simulations.
- Using a different gas as a krypton gas.
- Using a cylinder shape of a proportional counter.

References

[1] Y. Namito, S. Ban, H. Hirayama, S. Tanaka, H. Nakashima, Y. Nakane, Y. Sakamoto, N. Sasamoto and Y. Asano, "Compton scattering of 20- to 40-keV photons", Phys. Rev. A **51**, 3036-3043(1995).

[2] Y. Namito, H. Hirayama and S. Ban: "Improvements of Low Energy Photon Transport for EGS5", In: *Proceedings of the 2nd International Workshop on EGS* Ed. H. Hirayama, Y. Namito and S. Ban, KEK Proc. **2000-20**,(2000) pp.11-22.

[3] H. Hirayama, Y. Namito, A. F. Bielajew, S. J. Wilderman and W. R. Nelson. The EGS5 Code System. Report SLAC-R-730, Stanford Linear Accelerator Center, Stanford, CA, (2005).

[4] T. M. Jenkins, W. R. Nelson, A. Rindi, A. E. Nahum, and D. W. O. Rogers, editors, *Monte Carlo Transport of Electrons and Photons*, Plenum Press, New York, (1988).

[5] Ed C. M. Lederer, V. S. Shireley, *Table of Isotopes* 7th edn (Wiley-Interscience, New York, 1978).

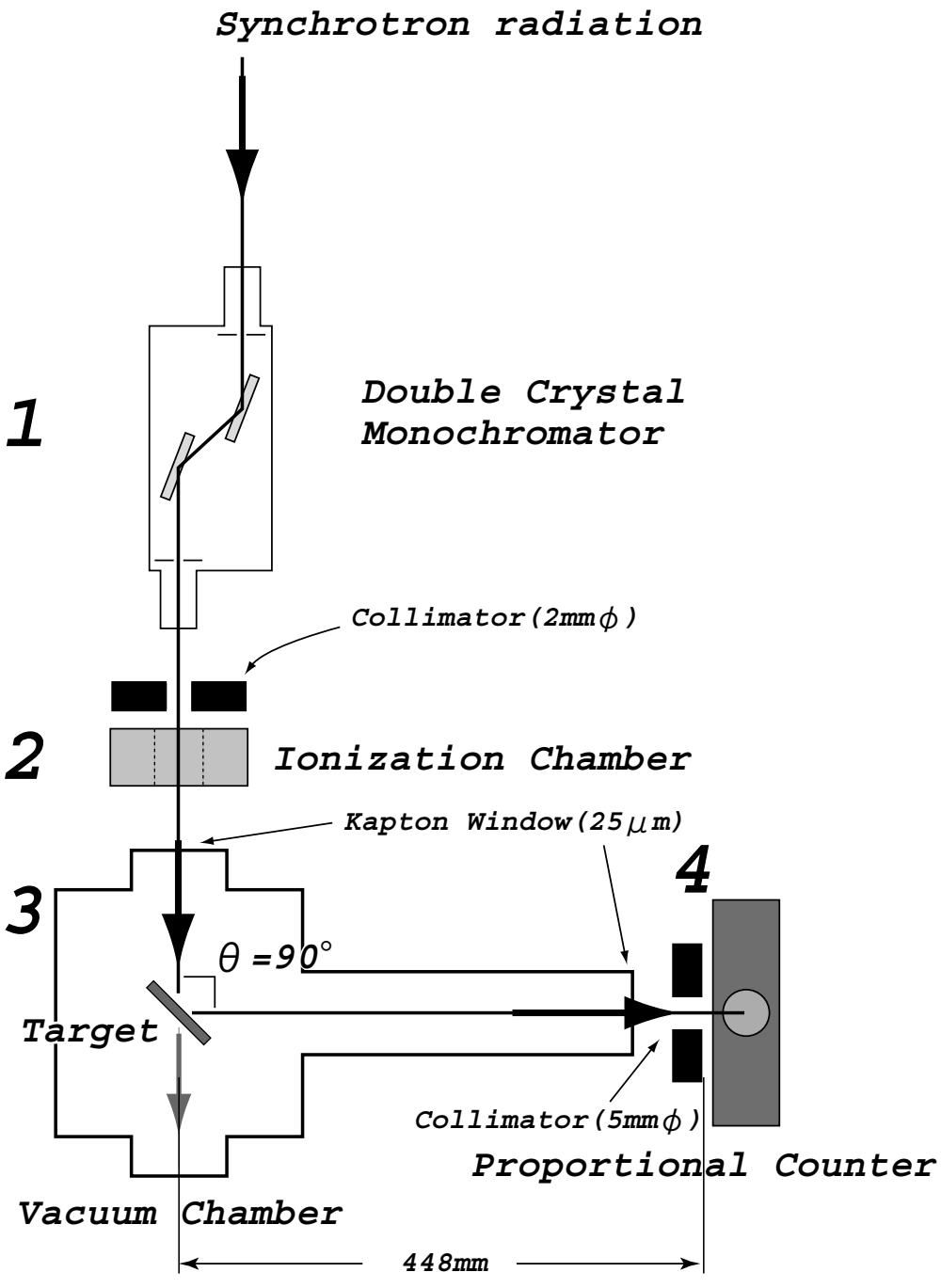

Figure 1: The PF experiment arrangement

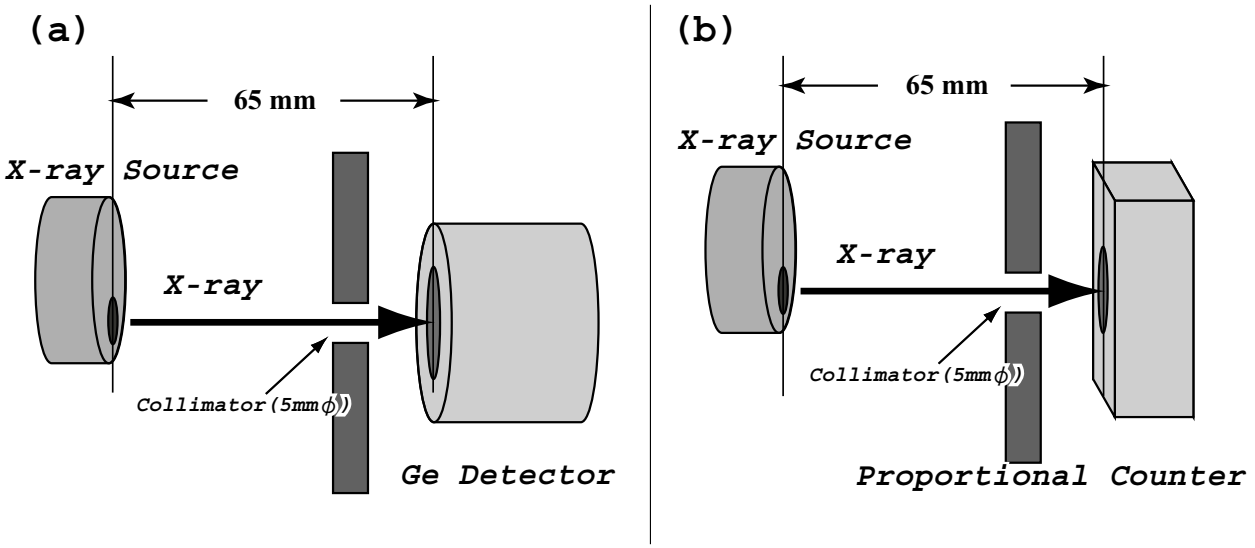

Figure 2: The RI experiment arrangement using (a) the Ge detector and (b) the proportional counter.

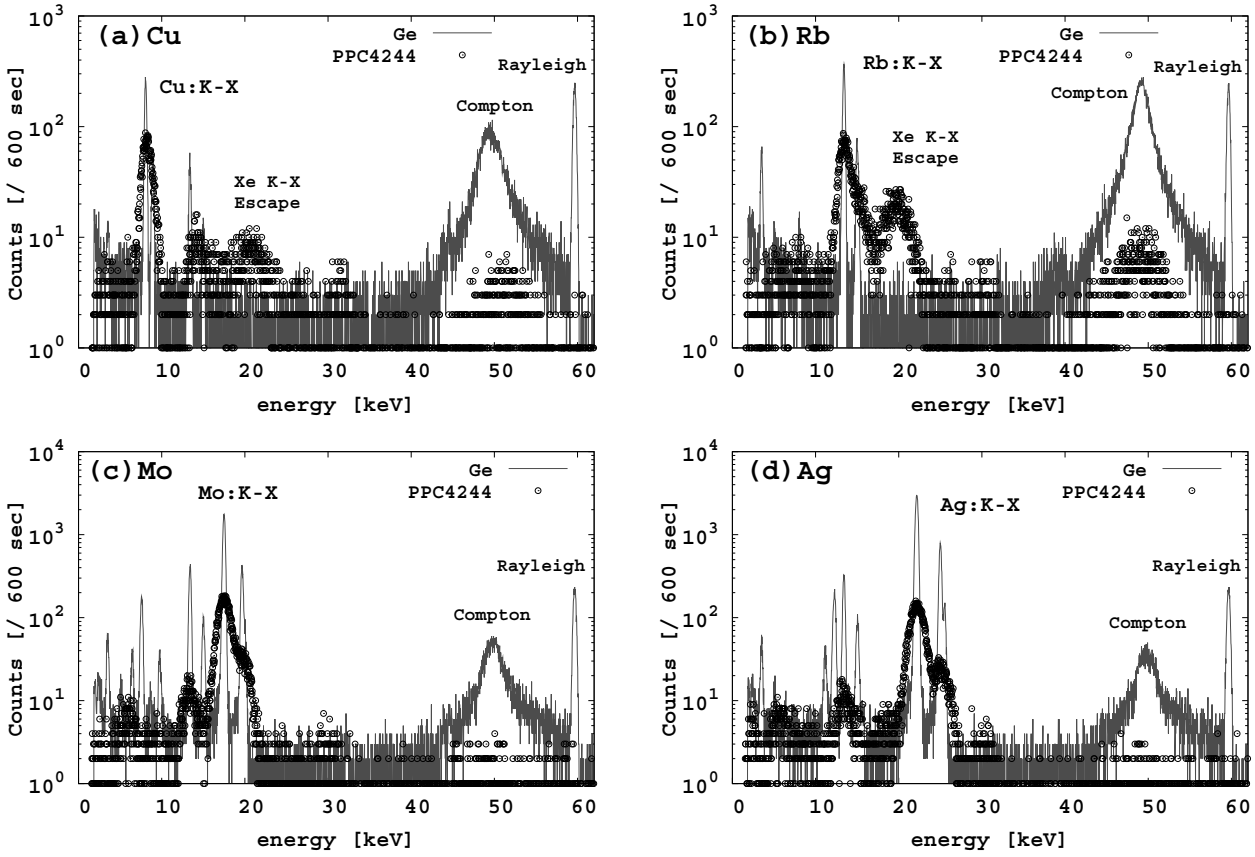

Figure 3: The energy spectra for (a) Cu, (b) Rb, (c) Mo and (d) Ag targets in the RI experiment. The Ge detector is shown by line. The proportional counter is shown by dot.

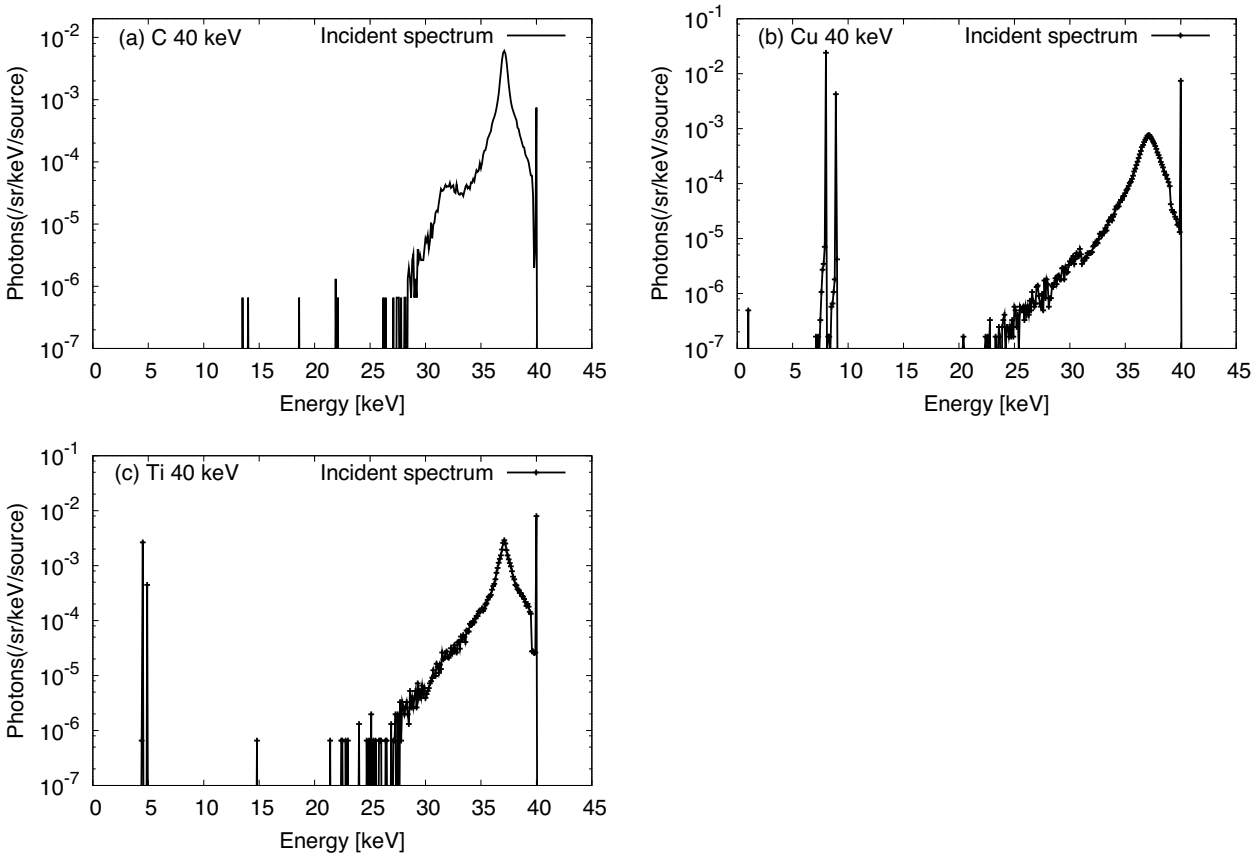

Figure 4: $\theta = 90°$ scattered spectra when incident photon energies were 40 keV. (a) Carbon, (b) Copper and (c) Titanium target.

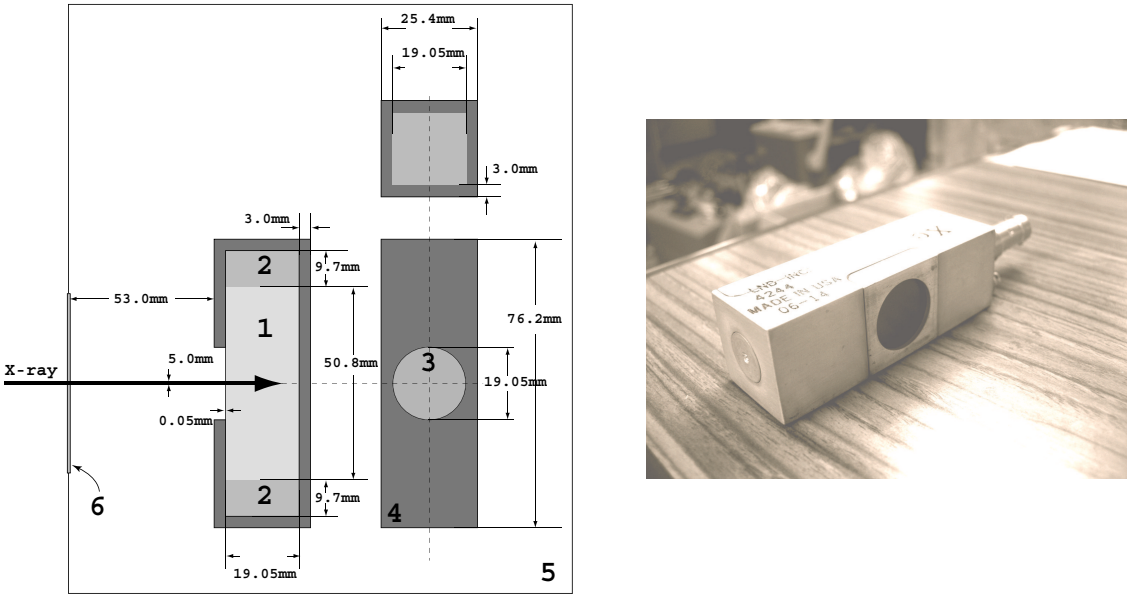

Figure 5: The geometry of the proportional counter at the PF experiment. 1. Xe effective region, 2. Xe ineffective region, 3. Beryllium window, 4. Aluminum cathode/container, 5. Air region and 6. Kapton vacuum window.

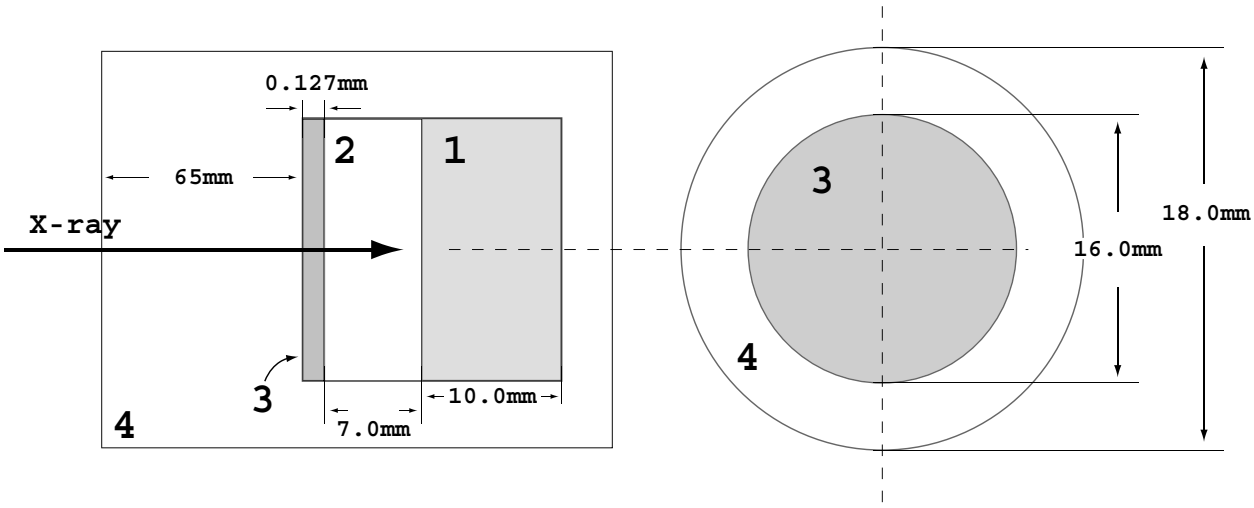

Figure 6: The geometry of the Ge detector at the RI experiment. 1. Germanium region, 2. Vacuum region, 3. Beryllium window and 4. Air region

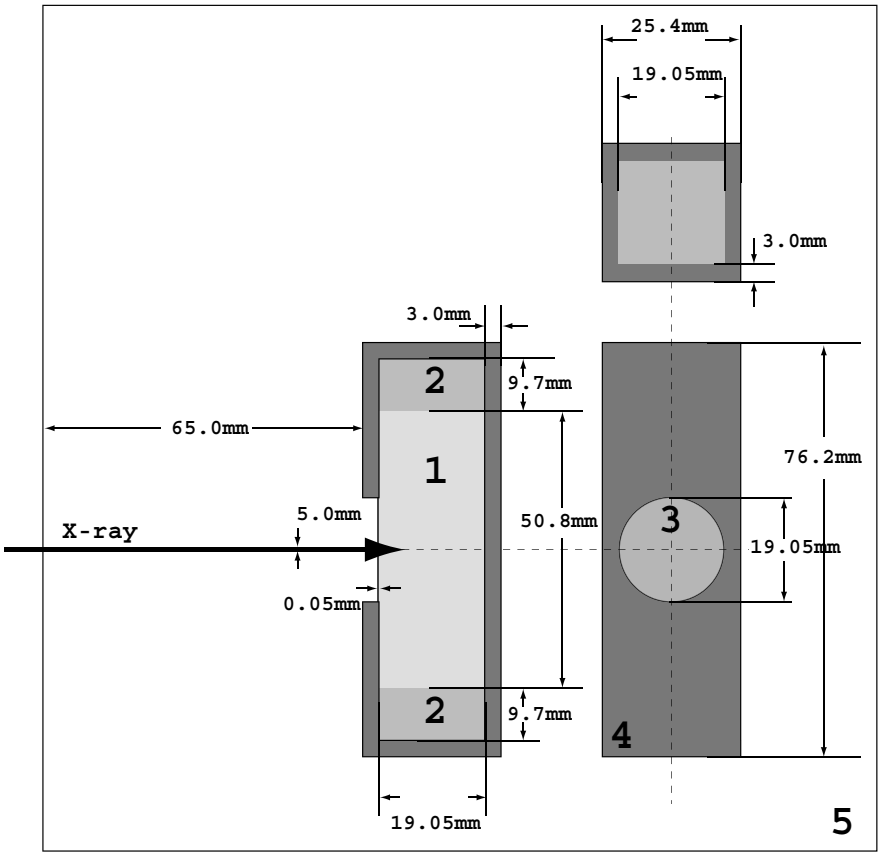

Figure 7: The geometry of the proportional counter at the RI experiment. 1. Xe effective region, 2. Xe ineffective region, 3. Beryllium window, 4. Aluminum cathode/container and 5. Air region.

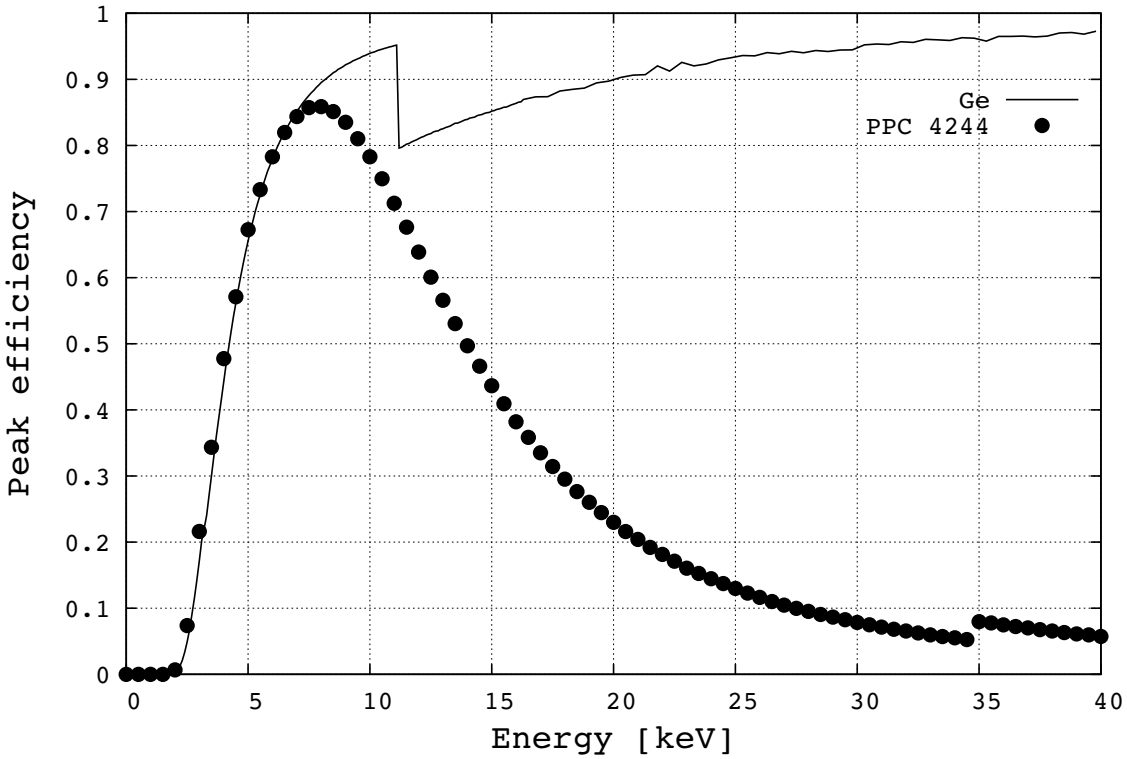

Figure 8: The peak efficiency of the detectors. The Ge detector is shown by line. The proportional counter is shown by dot.

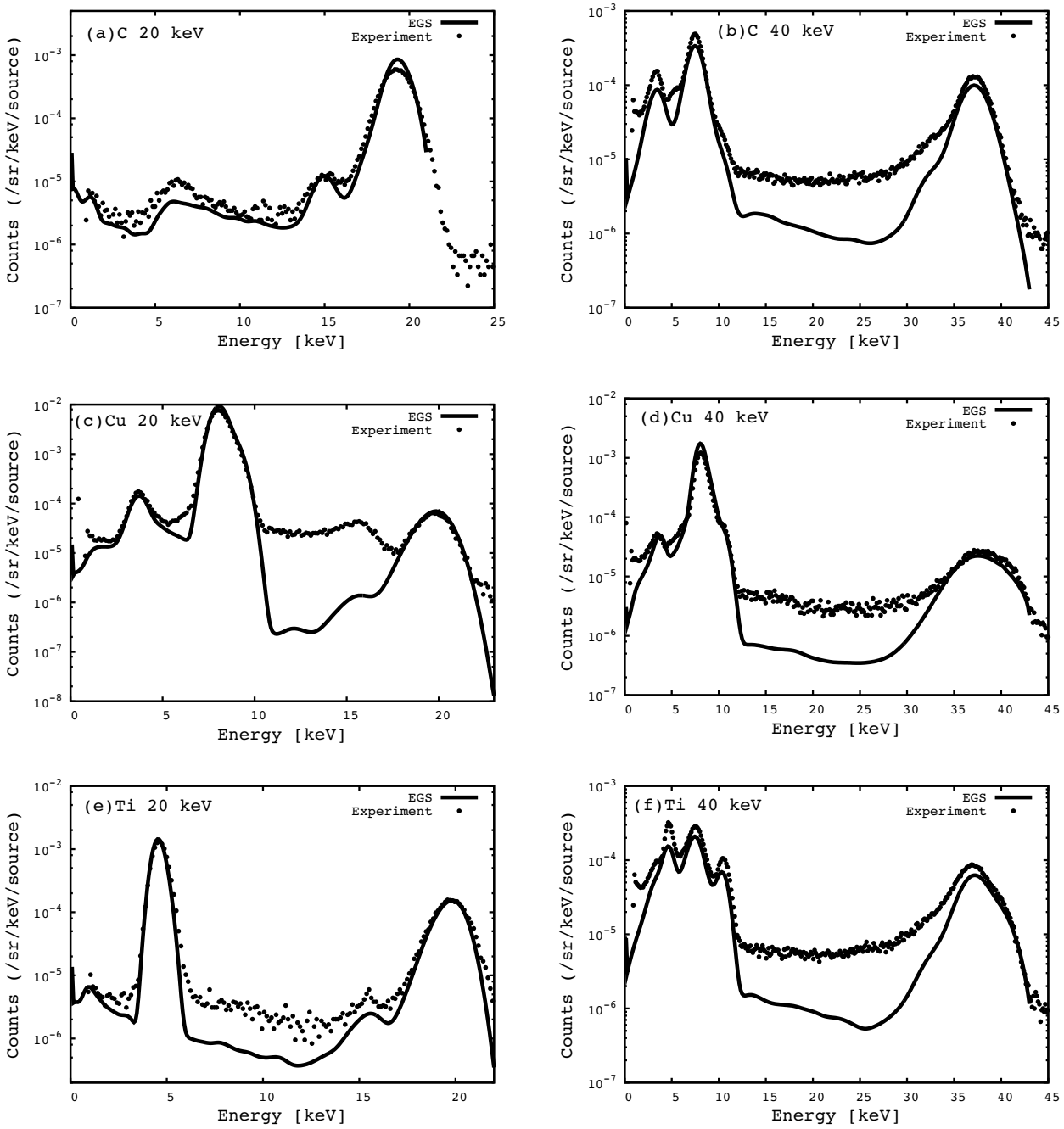

Figure 9: Comparison of the photon energy spectra. Measurement is shown by dot. EGS5 simulation is shown in solid line. Targets and incident energy are (a) C-20 keV, (b) C-40 keV, (c) Cu-20 keV, (d) Cu-40 keV, (e) Ti-20 keV and (f) Ti-40 keV.

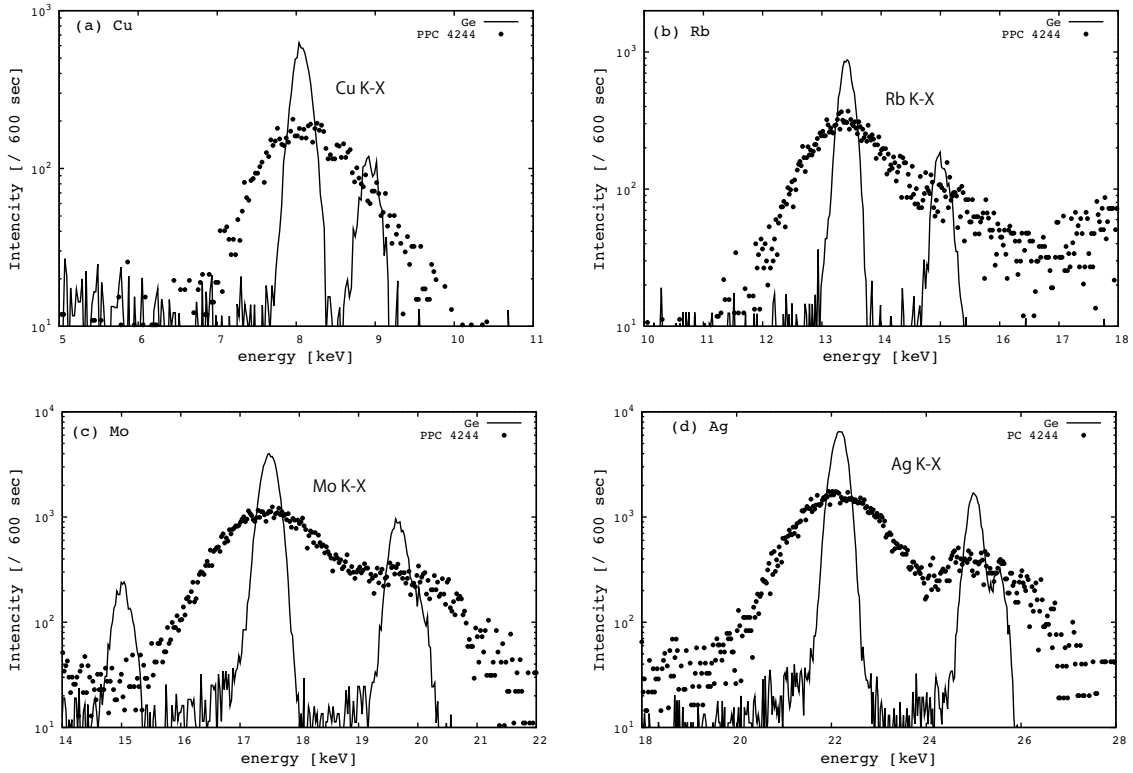

Figure 10: Comparison of the intensity in the RI experiment. The Ge detector is shown by line. The proportional counter is shown in solid dots. The targets are (a) Cu, (b) Rb, (c) Mo and (d) Ag.

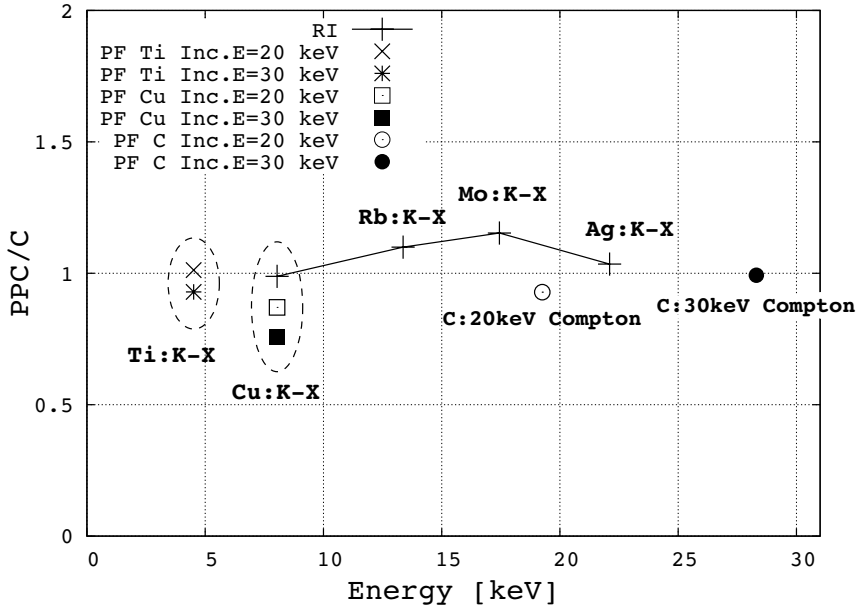

Figure 11: The proportional counter measurement over EGS5 Calculation in PF experiment and intensity of the Ge detector in RI experiment (PPC/C) on each part for different targets.

GENERATION OF LASER COMPTON GAMMA RAYS AND LIGHT OUTPUT RESPONSE OF INORGANIC SCINTILLATORS

M. Imamura[1], Y. Koba[1], H. Fukuda[1], G. Wakabayashi[1], T. Kaihori[2], H. Toyokawa[2], and Y. Uozumi[1]

[1]Department of Applied Quantum Physics and Nuclear Engineering, Kyushu University, Fukuoka 812-0395, Japan

[2]Research Institute of Instrumentation Frontier, National Institute of Advanced Industrial Science and Technology, Ibaraki 305-8568, Japan

e-mail:m-imamura@nucl.kyushu-u.ac.jp

Abstract

In recent years, the gamma rays using laser Compton scattering have gotten a lot of attention from the viewpoint of tunable energy, narrow energy spectrum, and high polarization. We describe experimental studies of light output response of some inorganic scintillators for high energy gamma rays using laser Compton gamma rays. The gamma rays energy of 5-30 MeV were generated using Nd:YVO_4 laser at electron storage ring TERAS. The energy spectra were measured using NaI(Tl), GSO(Ce), CsI(Tl) and LYSO(Ce) scintillators. Energy at the peak position was decided by using, simulating EGS5, and comparing it with the experimental data. According to the result, the light output response showed good linearity for all scintillators.

1. Introduction

The light output response of inorganic scintillators to gamma rays and various charged particles has been investigated extensively[1,2]. We previously investigated the light output response of GSO(Ce) scintillator for impinging protons[3], deuterons[4], ^{4}He[5] and ^{12}C particles[6]. According to the results, the light output was described well with the Birks equation[7] with common parameters.

About gamma rays, most of the measurement of a light output response for high energy gamma rays was not performed till now because of the radioisotope which we can use is generally up to 2 MeV and even though we can raise energy using bremsstrahlung X ray, it is unsuitable for the measurement of the light output response since an energy spectrum is wide. However, a laser Compton gamma ray, which is produced in the collision between relativistic electrons and a laser beam, was put to practical use. It has excellent characteristics of tunable energy, narrow energy spectrum, and high polarization. In this paper, we describe experimental studies of light output response of some inorganic scintillators for high energy gamma rays using laser Compton gamma rays.

2. Experiment

The experiments were performed at electron storage ring TERAS, National Institute of Advanced Industrial Science and Technology. At TERAS, electrons can be accelerated up to 800 MeV. We used Nd:YVO_4 laser (INAZUMA) manufactured by Spectra –Physics. The laser wavelength can be chosen from 1064 nm (fundamental wavelength), 532

nm (second harmonic) and 354.6 nm (third harmonic). The experimental arrangement is shown in Figure 1. The used electron energies, laser wavelengths and calculated maximum gamma ray energies are listed Table 1.We measured energy spectrum using four kinds of scintillators, NaI(Tl), GSO(Ce), CsI(Tl) and LYSO(Ce). The size of scintillators is listed in Table 2.

Figure 2 shows an example of energy spectrum measured by Cylindrical-NaI. A background has already deducted it in Figure 2, but the right side of a big peak can look at the second peak. This is a pile up event when two laser Compton gamma rays occurred in one laser pulse. Because there is it for the purpose of measurement of light output response this time, the first big peak was analyzed. However, we cannot decide energy corresponding to the first peak because energy of laser Compton gamma rays slightly spreads and we cannot decide what kind of reaction (photoelectric effect, Compton scattering and pair creation) is caused for reasons of high energy gamma rays. Therefore the energy corresponding to this peak was decided by using EGS5.

3. Simulation by EGS5

Energy according to the energy differential cross section of laser Compton scattering shown in Figure 3 is generated with laser electron interaction region of the EGS5 calculation system shown in Figure 4. After energy is decided by random numbers, the angle is calculated because the discharge angle of the laser Compton gamma scattering corresponds to energy by the one-on-one. It is necessary to generate it with the extension but not generation by certain one point because both electron beams and lasers have the extension. This time, it was assumed that an expanse followed Gaussian distribution and calculated. The variance of the beam axis was σ_z and the variance of a vertical direction to the beam axis was calculated as $\sigma_x=\sigma_y=\sigma_{xy}$. Because the value of these variances was cannot be decided according to experimental conditions, the best value was decided by comparing the EGS5 result with the experimental data of Cylindrical-NaI which has the biggest peak efficiency. For other scintillators, the value of the variances decided here was used. Moreover, after it calculates, it is necessary to add the energy resolution because the energy resolution of the detector is not considered in EGS5. The value of energy resolution decided the most suitable value by comparing it with the experimental data.

4. Result and Discussion

The comparison of the EGS5 result and the experimental data is shown in Figure 5 – 9. The value to which σ_{xy} and σ_z are decided is shown in Figure 5 that is the result of Cylindrical-NaI. When the energy of the gamma rays has risen, underestimation is seen in the low energy part though the EGS5 result can reproduce the experimental data comparatively well for all scintillators. Because energy at the peak position is decided from the EGS5 result, the relation of this energy and the channel that shows the amount of luminescence is shown in Figure 10. In this figure the points of ^{40}K(1.46 MeV) and ^{208}Tl(2.46 MeV) measured as a background are added for Cylindrical-NaI and the point of ^{137}Cs(662 keV) is added for other scintillators. As for the relation of the amount of luminescence into energy, it has been understood that there is linear in all measured scintillators.

5. Conclusion

We generated laser Compton gamma rays energy of 5 - 30 MeV using Nd:YVO_4 laser at TERAS and measured energy spectrum with NaI, GSO, CsI and LYSO scintillators. Energy at the peak position was decided by using EGS5, and the amount of luminescence into the energy was decided. According to the results, the light output response showed good linearity for all scintillators.

References

1) A. Meyer and R.B. Murray, Physical Review **128** (1962) 98.
2) N. Colonna et al., Nucl. Instr. and Meth. A **321** (1992) 529.
3) S. Aoki et al., IEEE Trans. Nucl. Aci. **NS-47** (2000) 1798.
4) F. Saiho et al., Nucl. Instr. and Meth. A **537** (2005) 594.
5) M. Imamura et al., Nucl. Instr. and Meth. A **564** (2006) 324.
6) Y. Koba et al., KEK Proceedings 2006-7 Radiation Detectors and Their Uses (2006) p. 161.
7) J.B. Birks, The Theory and Practice of Scintillation Counting, (New York, 1964) p. 187.

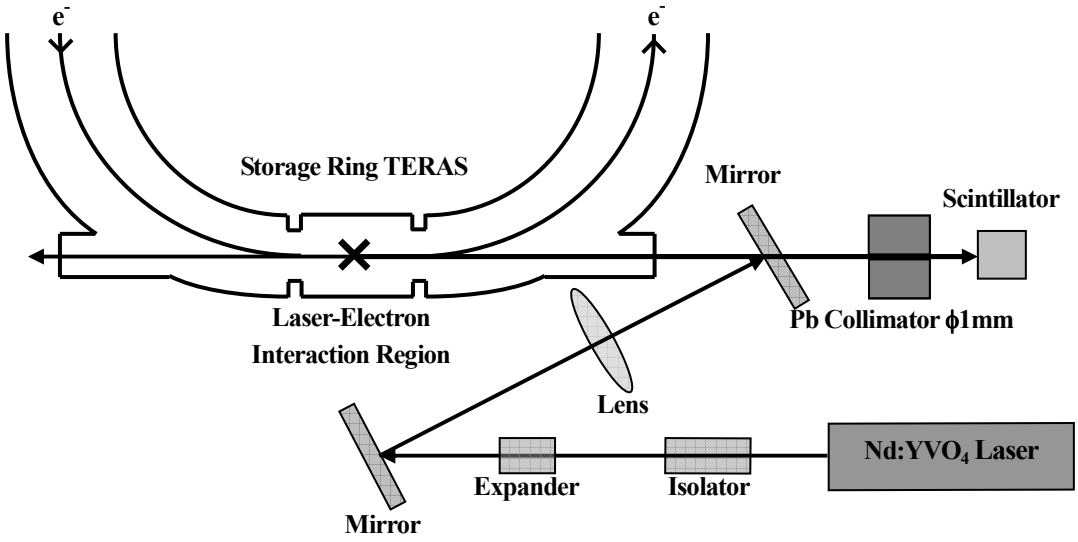

Figure 1. The experimental arrangement in the present measurement.

Table 1. The used electron energies, laser wavelengths and maximum gamma ray energies.

Electron energy (MeV)	Laser wavelength (nm)	Maximum gamma ray energy (MeV)
576	1064	5.83
760	1064	10.16
760	532	20.04
760	354.6	29.65

Table 2. The used size of scintillators.

Cylindrical-NaI(Tl)	ϕ203mm×305mm
NaI(Tl)	50.8mm×50.8mm×50.8mm
GSO(Ce)	43mm×43mm×43mm
CsI(Tl)	43mm×43mm×43mm
LYSO(Ce)	20mm×20mm×20mm

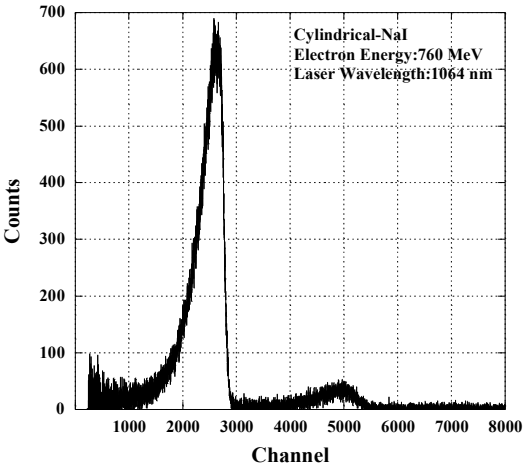

Figure 2. The energy spectrum measured by Cylindrical-NaI.

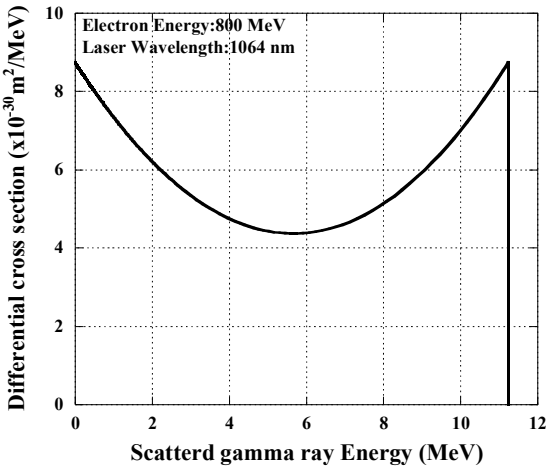

Figure 3. The energy differential cross section of laser Compton scattering.

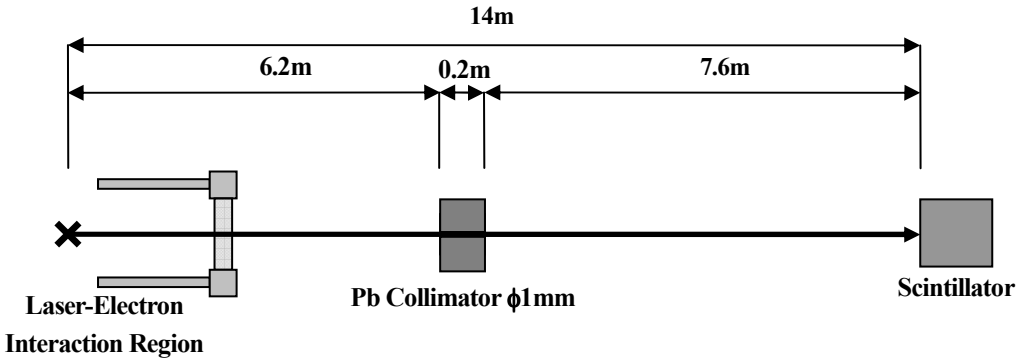

Figure 4. The calculation system of EGS5.

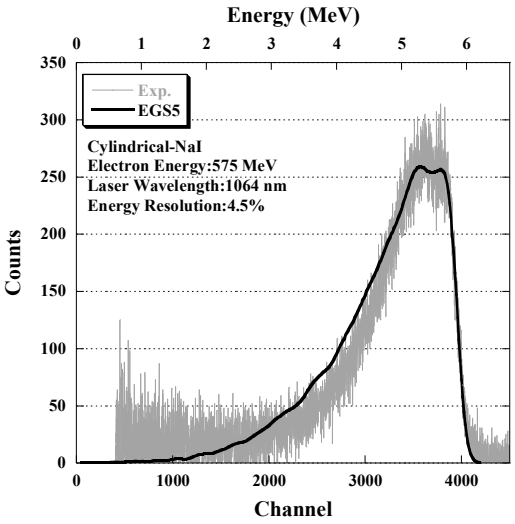

(a) 5.83 MeV, σ_{xy}=0.3 cm, σ_z=5.0 cm

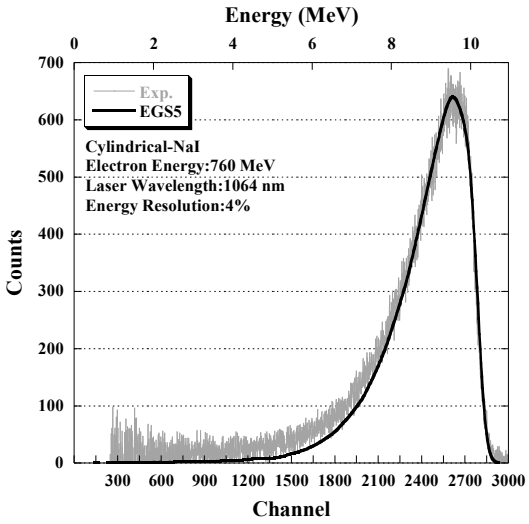

(b) 10.16 MeV, σ_{xy}=0.125 cm, σ_z=5.0 cm

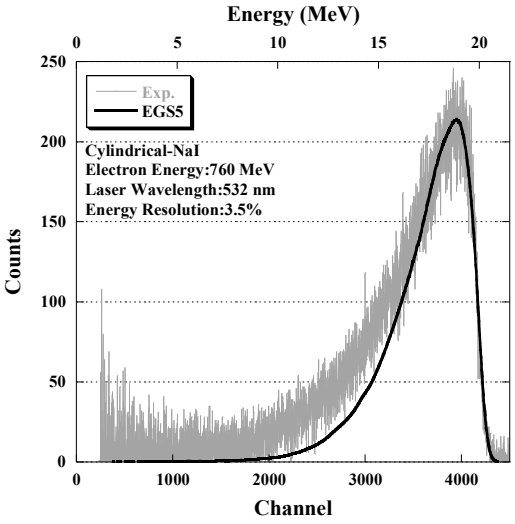

(c) 20.04 MeV, σ_{xy}=0.125 cm, σ_z=5.0 cm

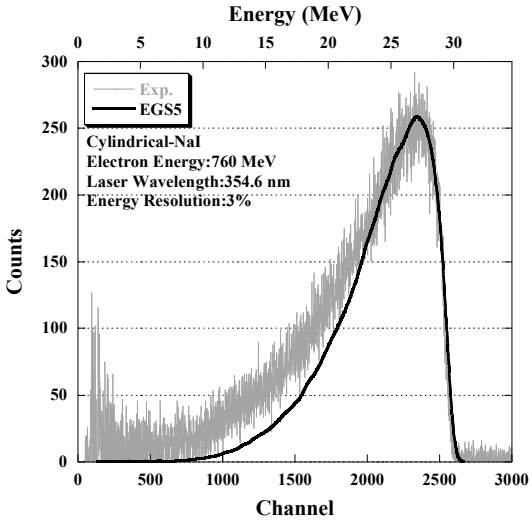

(d) 29.65 MeV, σ_{xy}=0.2 cm, σ_z=5.0 cm

Figure 5. The comparison of the EGS5 result and the experimental data for Cylindrical-NaI. It is shown the decided values of σ_{xy}, σ_z and energy resolusion

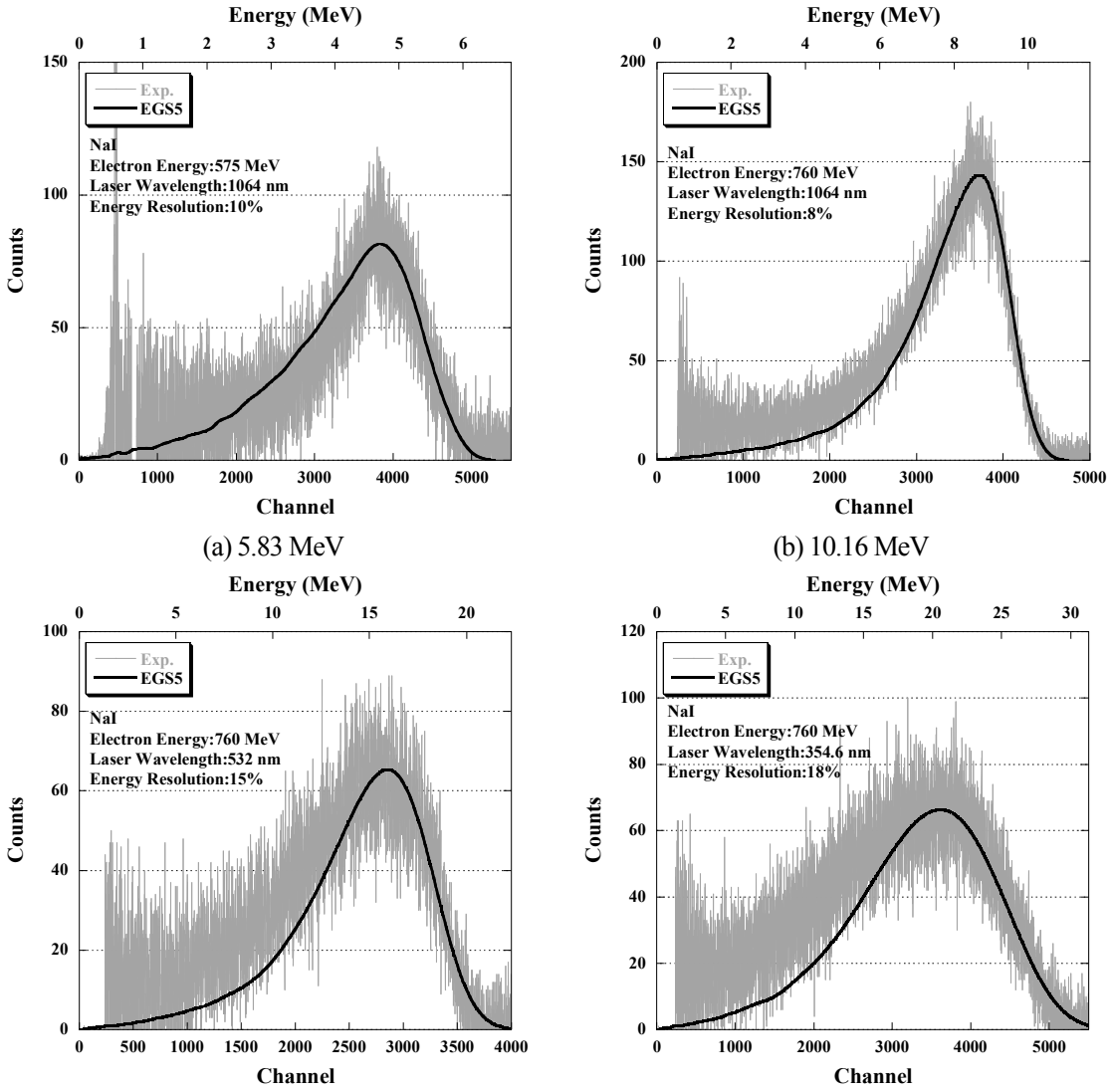

Figure 6. The comparison of the EGS5 result and the experimental data for NaI. It is shown the decided value of energy resolution.

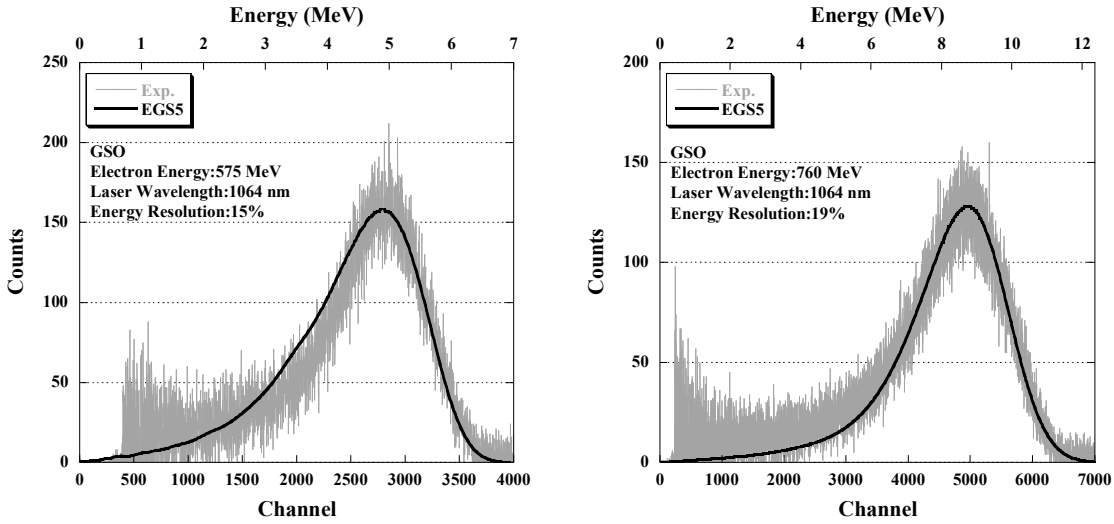

(a) 5.83 MeV

(b) 10.16 MeV

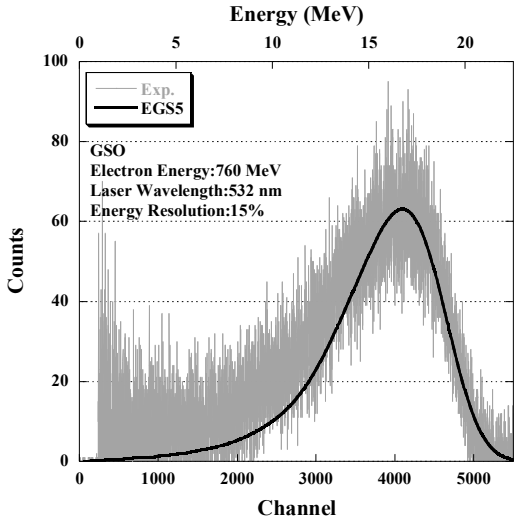

(c) 20.04 MeV

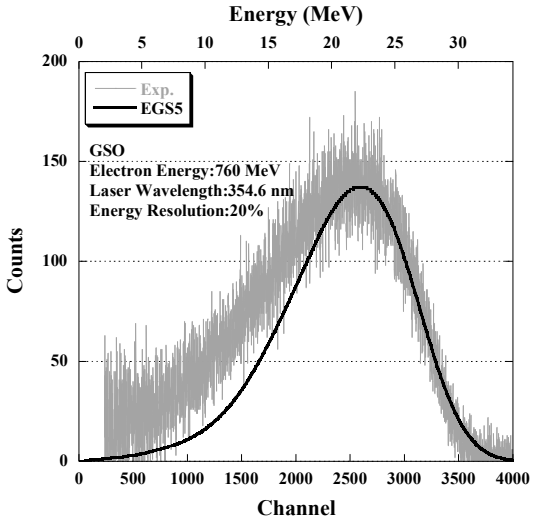

(d) 29.65 MeV

Figure 7. The comparison of the EGS5 result and the experimental data for GSO. It is shown the decided value of energy resolution.

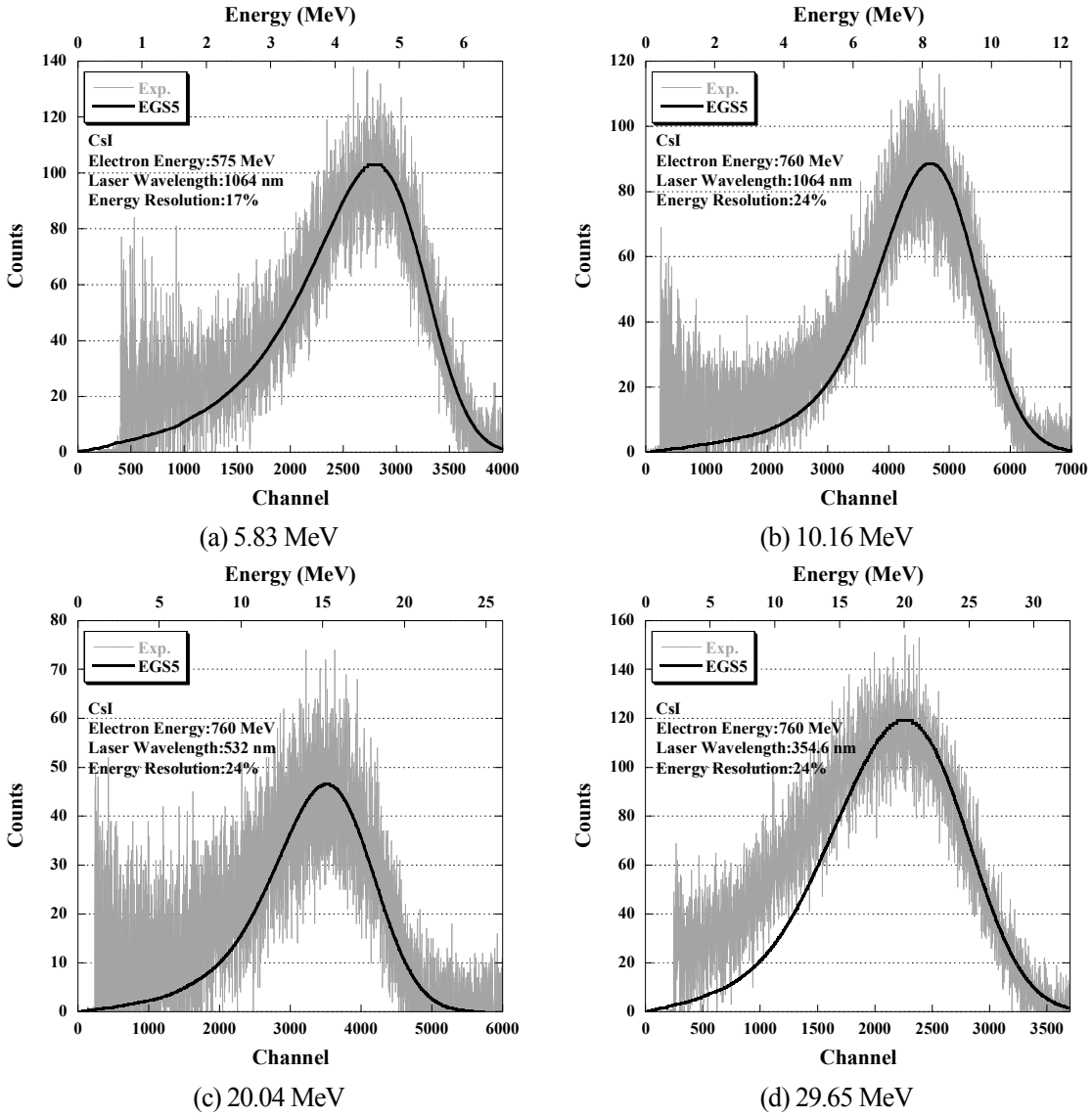

Figure 8. The comparison of the EGS5 result and the experimental data for CsI. It is shown the decided value of energy resolution.

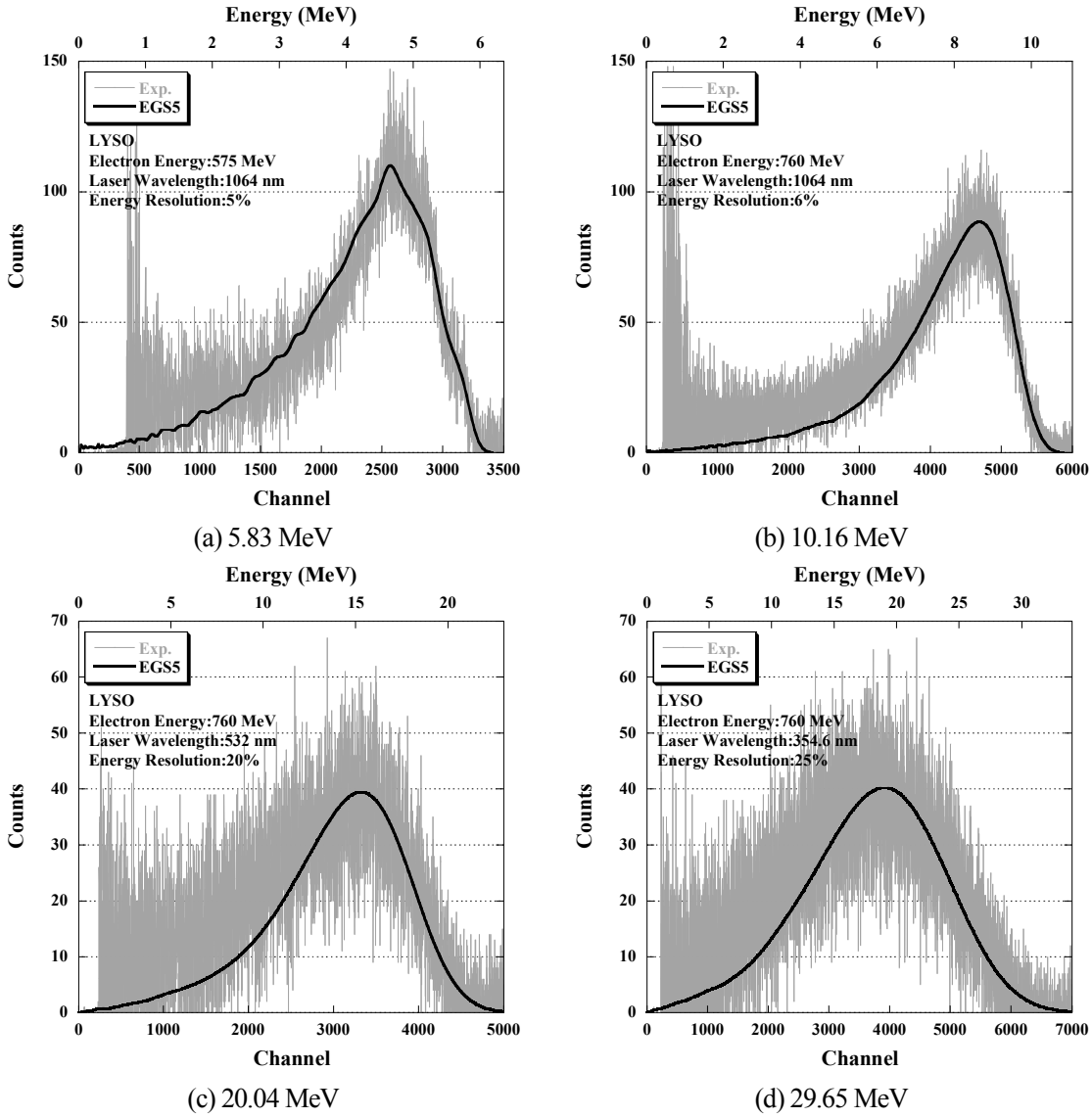

Figure 9. The comparison of the EGS5 result and the experimental data for LYSO. It is shown the decided value of energy resolution.

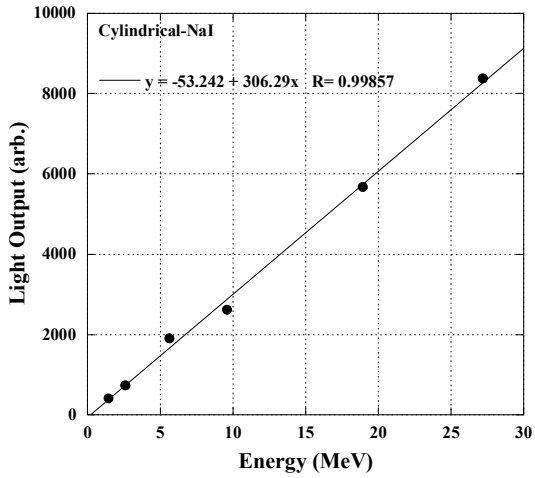

(a) Cylindrical-NaI

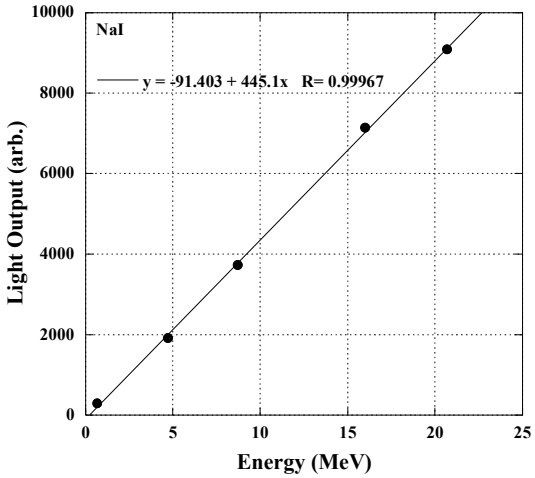

(b) NaI

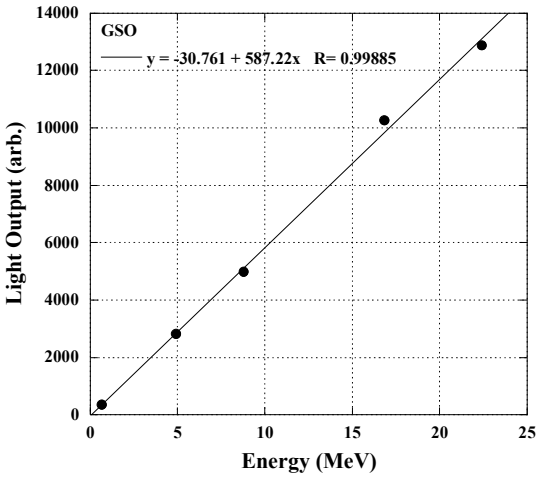

(c) GSO

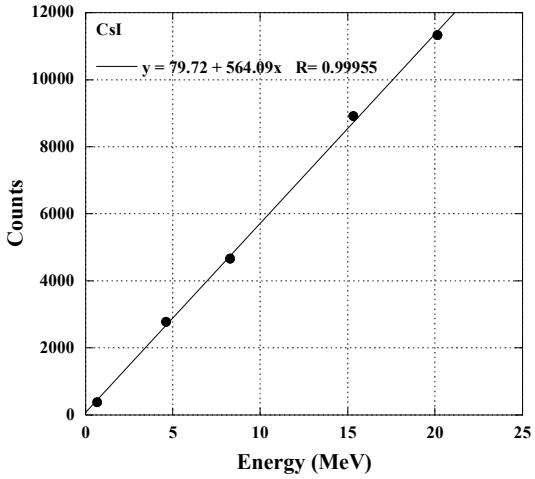

(d) CsI

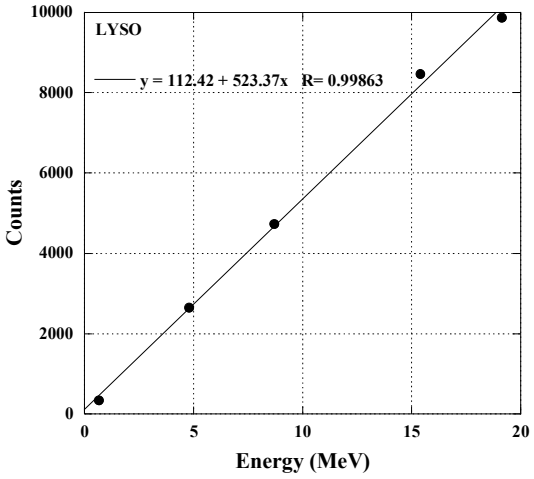

(e) LYSO

Figure 10. The light output response as a function of energy. The solid line is result of least square fitting.

Monte Carlo simulations for the study on the characteristics of polymer gel 3D dosimeter

K. Haneda[1], S. Usui[1], T. Tominaga[1], S. Hayashi[1], M. Yoshioka[1], H. Okudo[2], and Y. Tsunei[2]

[1]Department of Clinical Radiology,
Hiroshima International University, Hiroshima 739-2695, Japan
[2]CMagor in Medical Engineering and Technology, Hiroshima International University Graduate School,
Hiroshima 739-2695, Japan
e-mail: k-haneda@hs.hirokoku-u.ac.jp

Abstract

We evaluate the polymer gel's water equivalency by means of calculations on the attenuation and ionization of radiations, and Monte Carlo simulations on the transport of electrons and photons with energies 12 MeV and 6 MV respectively in water and polymer gel. And also the simulated results are compared to depth dose distributions measured with polymer gel dosimeters. The polymer gels, three gels, which compositions are deferent in a gelatin concentration, were investigated. The attenuation coefficients of photons and the stopping powers of electrons in the medium listed above were calculated in the energy range of 10 KeV to 100 MeV. The percentage depth doses in each polymer gel were calculated using the EGS5 Monte Carlo simulation code. The results show that solid water has the close values to water's in all listed items as expected, and also the values of 5% gel are almost same as solid water's value. The differences in each value were less than 4% even in the comparison of 15% gel's values with solid water's values. The stopping powers in all gels were about 1% smaller than in water without any energy dependence. The attenuation coefficients of photons were 1% smaller than in water above 0.1MeV, and decreased to 5% smaller with energy decreasing to 0.01MeV. The percentage depth dose curves of all gels can reproduce the curve of water within 1% differences as well as in the case of solid water for photons, but the density effect is not neglected for electrons as the gelatin concentration increasing, the absolute values of ordinate are well consistent against the depth in area density (g/cm^2). Our results confirmed the polymer gel's water equivalency and it can be said that the polymer gel dosimeter is well suited for the device for the clinical radiation measurements.

1. Introduction

Recent rapid advances dynamic radiotherapy treatments demand on more accurate methods of dosimetry than ever. In the stereo-tactic irradiations (STI) and intensity-modulated radiotherapy (IMRT) treatments, highly tailored multi-segmented x-ray beames give precise radiation doses to the target volume, and allow for higher radiation doses to be delivered to the tumor while sparing healthy tissue[1)]. The complex three dimensional (3D) pattern of radiation delivery can be determined using the 3D treatment planning and the 3D optimization by CT simulator. But the equipments routinly used in radiation dosimetry are still micro ion-chambers, metal oxide semiconductor FET detectors [2)],radiochromic films[3)] and such dosimeters which are limited to one or two dimensional measurements. Polymer gel dosimetry is an only method to measure 3D dose distribution directly[4, 5, 6)]. The polymer gel dosimeter is a device utilizing the radical polymerization reaction of organic monomers, and since its atomic constituent is similar to water and

muscle, it is regarded as a tissue equivalence dosimeter.

In this paper, we evaluate the polymer gel's water equivalency by means of calculations on the attenuation and ionization of radiations, and Monte Carlo simulations on the transport of electrons and photons with energies 12MeV and 6MV respectively in water and polymer gel. And also the simulated results are compared to depth dose distributions measured with polymer gel dosimeters.

2. Method

2.1 Medium in the consideration

Several mediums such as water, solid water, muscle and the polymer gel were considered in our calculations and simulations. In particular the polymer gel, three gels, which compositions are deferent in a gelatin concentration, were investigated (table 1). The chemical compositions of each medium are listed in table 2.

2.2 Calculations

The attenuation coefficients of photons and the stopping powers of electrons in the medium listed above were calculated in the energy range of 10 KeV to 100 MeV. They were based on the database program XCOM for the attenuation coefficients calculation and ESTAR for the stopping power calculation, which were provided by National Institute of Standards and Technology [7, 8].

2.3 Monte Carlo Simulation

The percentage depth doses in each polymer gel were calculated using the EGS5 Monte Carlo simulation code. The parameters of threshold energies were set as A_e=0.561 MeV, A_p =0.010 MeV, E_{cut}=0.561 MeV, and P_{cut}=0.01 MeV, where A_e and A_p were the discrete cutoff thresholds energy of electrons and photons for collision and radiative energy losses, E_{cut} and P_{cut} were user-defined cutoff energies for the termination of the tracking of electrons and photons for each region. The geometry was specified as the incident source distance be set 98.5cm from 10 $\times$ 10 cm^2 plane.

The energy spectrum of incident photons was determined from the data on the attenuation of nominal energy of 6MV photons measured at EXL-12 SP linac system, and the average incident energy was 1.715 MV. For the percentage depth doses calculations, the bin dimensions along the z-depth direction were set to 1.0$\times$1.0$\times$ 0.5 cm^3. The number of histories were 2.5 $\times$ 10^9 for photons and 10^8 for electrons which set the statistical uncertainty to 1.0%.

3. Results and discussions

First Table 3 summarize the values of density, electron concentration, electron density, and effective atomic number to compare the compositional properties of each gel with water. The values of a solid water as a standard water equivalent material are also listed together. It shows that increasing the concentration of gelatin, increasing its density and decreasing its effective atomic number. Solid water has the close values to water's in all listed items as expected, and also the values of 5% gel are almost same as solid water's value. The differences in each value were less than 4% even in the comparison of 15% gel's values with solid water's values.

Next the calculated stopping powers of electrons and attenuation coefficients of photons in each medium are presented in Figure 1 and Figure 3, and relative values to water's stopping powers and attenuation coefficients are in Figure2 and Figure 4. In these figures the abscissa indicate the energy of particles. As Figure 2 shows, the stopping powers in all gels were about 1% smaller than in water without any energy dependence. The attenuation coefficients of photons (Figure 4) were 1% smaller than in water above 0.1MeV, and decreased to 5% smaller with energy decreasing to 0.01MeV. However our results show the gel's water equivalency is much better than solid water as regard to stopping

powers of electrons and attenuation coefficients of photons.

Finally we show the EGS Monte Carlo Simulation results on the depth dose distributions of incident 6MV photons and 12MeV electrons in the materials. The calculated and measured percentage depth dose curves of photons and electrons in 10% gel are compared in Figure 5 and 6. Our calculated depth dose curves are well consist with the results measured by 10% gel dosimeters, and these results justify the setting conditions of our simulation's parameters.

The percentage depth dose curves calculated in each medium are compared in Figure 7(for photons) and Figure 8(for electrons). The curves of all gels can reproduce the curve of water within 1% differences as well as in the case of solid water for photons, but as to electrons, as the concentration of gelatin increase, the consistency in the percentage depth dose with water is getting worse due to its density effect. In Figures 9, for the sake of comparing the absolute value of ordinate, the abscissa indicates area density (g/cm^2) to normalize the depth with the deferent densities. As figure shows, all curves are well consist in ordinate with each other.

4. Conclusions

A water equivalency of the material is one of considerable property in the clinical dosimetry. We examined the polymer gel's property of water equivalence to radiations examined by means of comparison the results of Monte Carlo simulations on the transport of radiations in the gels and in water, and also in solid water as a standard used water equivalent material. As the results, the polymer gel with gelatin concentration less than 15% is regarded as water equivalence as well as or even better than solid water with respect to the attenuation coefficient and the stopping power in the medium. And their percentage depth dose curves are in well consistency with that of water for incident photons. Though the density effect is not neglected for electrons as the gelatin concentration increasing, the absolute values of ordinate are well consistent against the depth in area density (g/cm^2).

Our results confirmed the polymer gel's water equivalency and it can be said that the polymer gel dosimeter is well suited for the device for the clinical radiation measurements.

References

1) ICRU Report 24: Determination of absorbed dose in a patient irradiated by beams of X or gamma rays in radiotherapy procedures. International Commission on Radiation Units and Measurements, ICRU Publications (1976)
2) R. ramani, S. Russell, P. O'Brien, "Clinical dosimetry using MOSFETs" Int J Rad Onc Bio Phys. 37, 959-964(1997)
3) ISP Data Sheet: "GAF CHROMIC MD-55 DOSIMETRY MEDIUM" INTERNATIONAL SPECIAL PRODUCTS
4) M. F. Peter, C. K. Derek et al."Polymer gel for magnetic resonance imaging of radiation dose distributions at normal room atmosphere" Phys. Med. Biol. 46, 3105-3113(2001)
5) S. W. Cheng, Y. Xu, "Three-dimensional dose verification for intensity modulated radiation therapy using optical CT based polymer gel dosimetry" Med. Phys. 33, 1412-1419(2006)
6) K. Haneda, H. Okudo et al. "Comparison evaluation of polymer gel with a water phantom" Jpn. J. Med.Phys. 26, 199-206(2007)
7) M. J. Berger, J. S. Coursey et al. " Zucker: Stopping power and range tables for electrons, protons, and helium ions, NIST(1998)
8) M. J. Berger, J. H. Hubbell et al. "XCOM: Photon Cross Sections Database" NIST(1998)

Table 1 Composition of the polymer gel dosimeters

	Concentration		
Gel components	5%	10%	15%
Gelatin	5 wt%	10 wt%	15 wt%
Methacrylic acid	5 wt%	5 wt%	5 wt%
THPC	2 mM	2 mM	2 mM
Water	90 wt%	85 wt%	80 wt%

Table 2 Elemental composition for polymer gel dosimeters

Material	wC	wH	wO	wP	wCl	wN	wS	wCa
5%-gel	0.050	0.107	0.841	5.85×10^{-5}	6.70×10^{-5}	0.002		
10%-gel	0.072	0.104	0.820	5.85×10^{-5}	6.70×10^{-5}	0.004		
15%-gel	0.095	0.101	0.799	5.85×10^{-5}	6.70×10^{-5}	0.006		
Solid water	0.672	0.081	0.199		0.001	0.024		0.023
Muscle	0.123	0.104	0.729			0.035	0.005	
Water		0.112	0.888					

Table 3 The mass density, electron concentration, electron density and Effective atomic number for polymer gel disimeters

Material	Mass density*1		Electron concentration		Electron density		Effective atomic number	
	kg m^{-3}	%	× 10^{29} em^{-3}	%	× 10^{26} ekg^{-1}	%		%
Water	998		3.34		3.35		7.42	
5%-gel	1020	2.16	3.33	▲ 0.45	3.26	▲ 2.56	7.36	▲ 0.80
10%-gel	1039	4.12	3.32	▲ 0.71	3.19	▲ 4.63	7.34	▲ 1.11
15%-gel	1059	6.14	3.31	▲ 0.96	3.12	▲ 6.69	7.31	▲ 1.44
Solid water	1020	2.20	3.31	▲ 0.93	3.25	▲ 3.07	7.38	▲ 0.54

*1 Temperature= 23 ℃

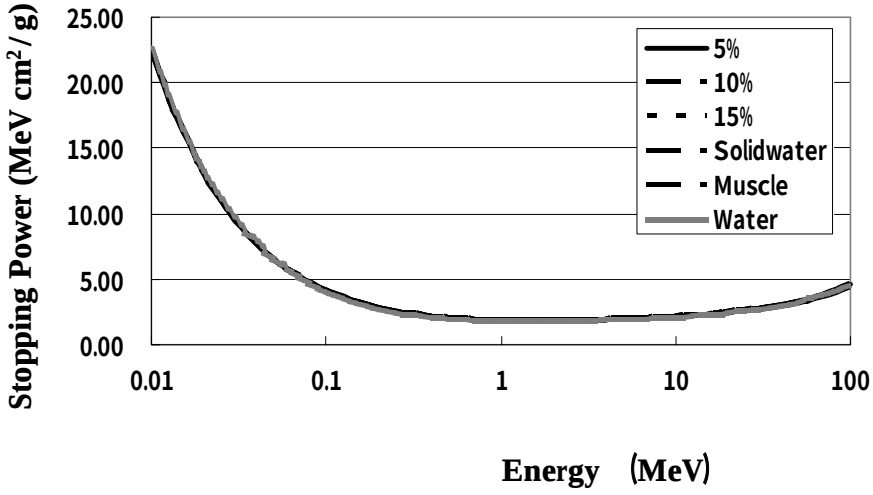

Fig. 1 Stopping power for various materials

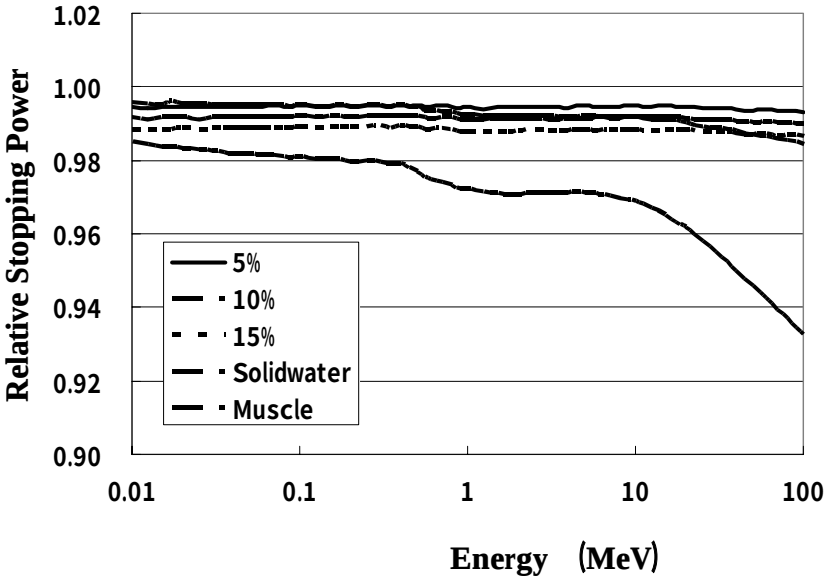

Fig. 2 Relative stopping power

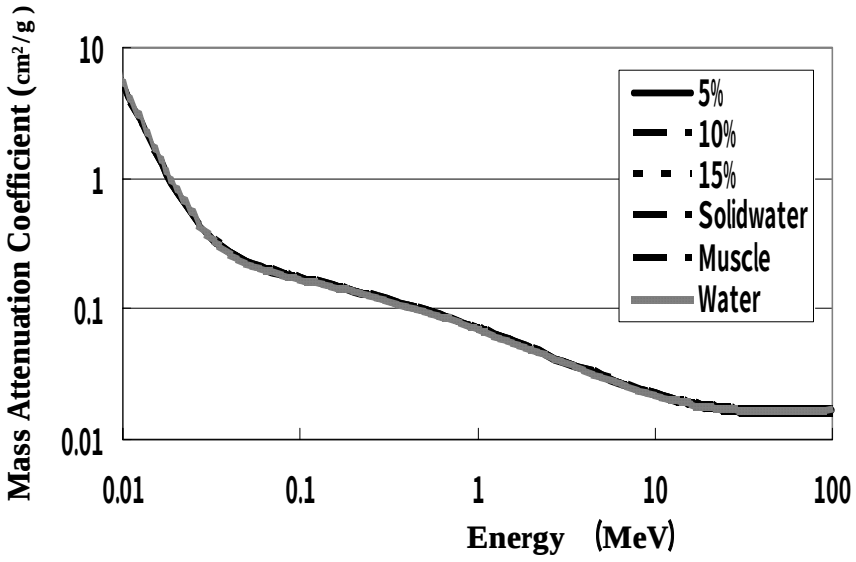

Fig. 3 Mass attenuation coefficient

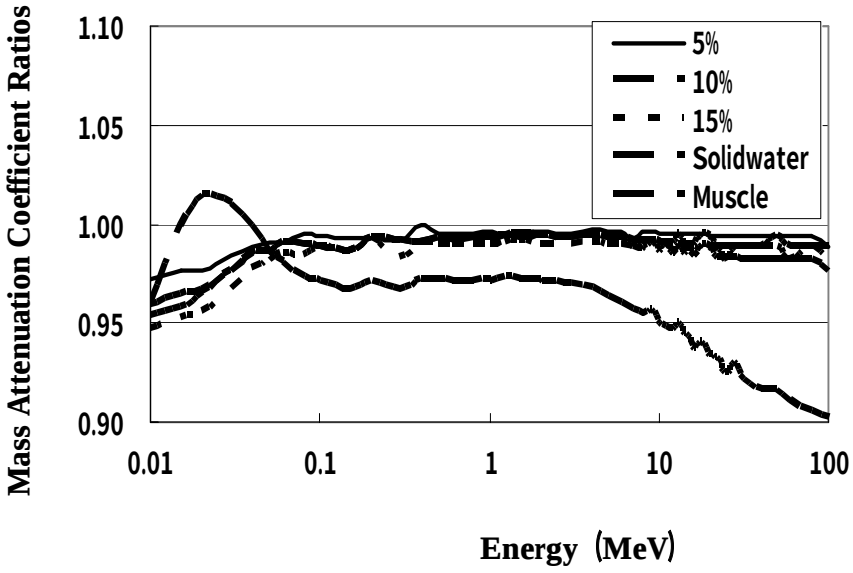

Fig. 4 Mass attenuation coefficient Ratios

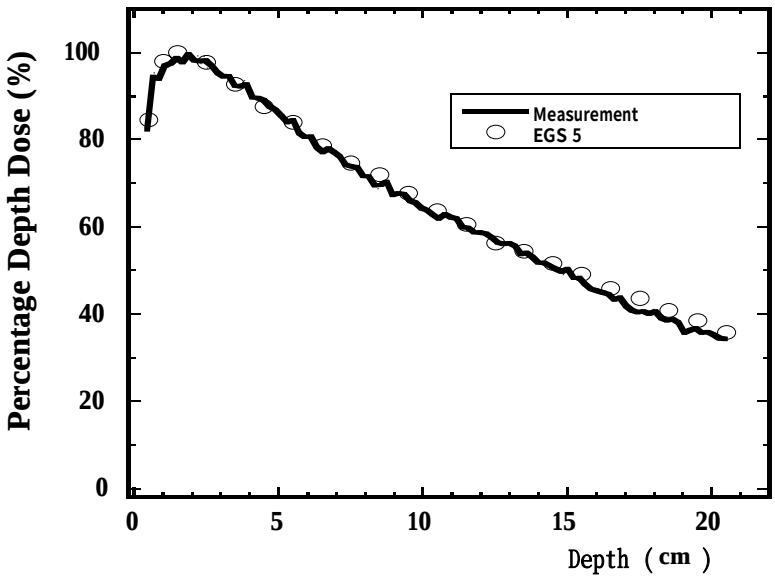

Fig. 5 Comparaison of Percentage Depth Dose for 6 MV photon beams from the simulation with EGS5 and that of the

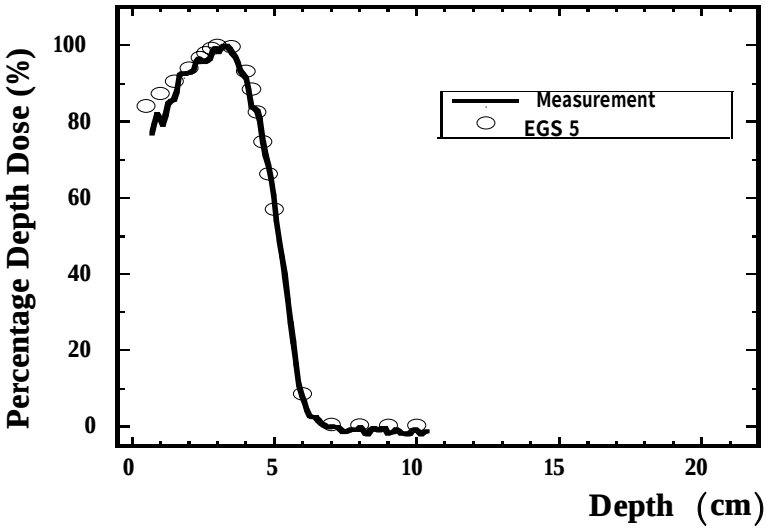

Fig. 6 Comparison of Percentage Depth Dose for 12 MeV electron beams from the simulation with EGS5 and that of the

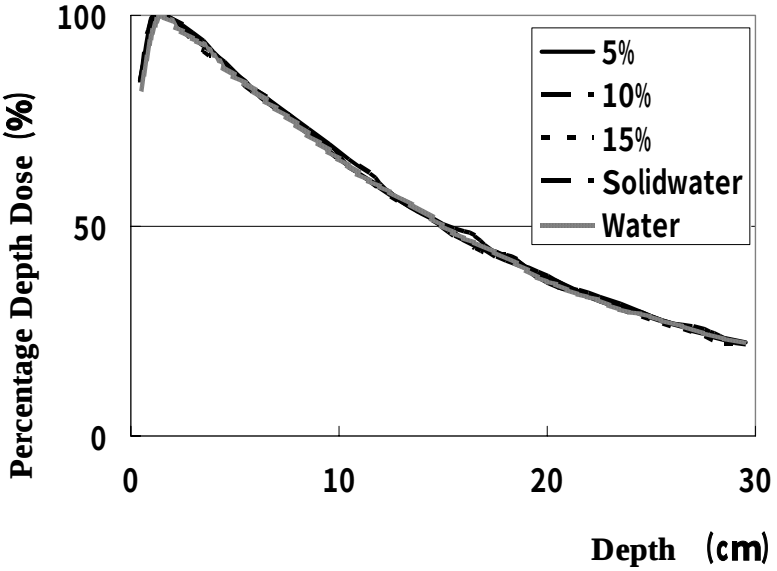

Fig. 7 Depth dose Monte Carlo output for 6 MV photon beams

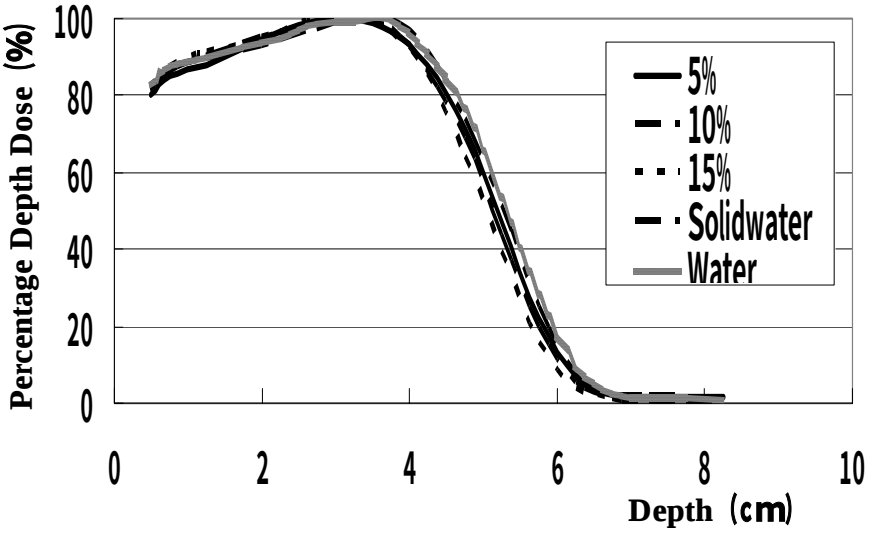

Fig. 8 Depth dose Monte Carlo output for 12 MeV electron beams

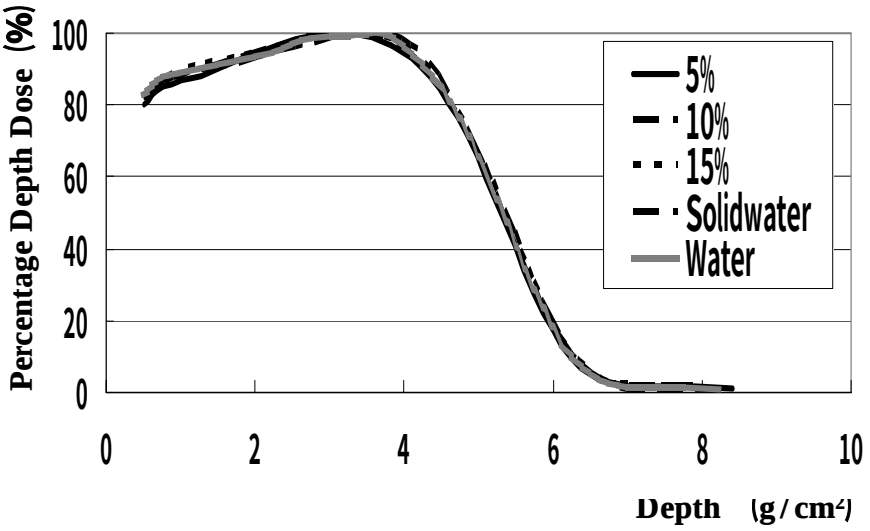

Fig. 9 Depth dose Monte Carlo output for 12 MeV electron beams; Depth Correction

EVALUATION OF EXTERNAL RADIATION EXPOSURE OF HUMAN INVOLVED IN EQUINE BONE SCINTIGRAPHY (No.2)

E. Kobayashi[1], K. Oono[1], M. Nishioka[1], T. Kakizaki[1], S.Wada[1], M. Natsuhori[2], Y. Namito[3], H. Hirayama[3], N. Ito[1]

1 School of Veterinary Medicine, Kitasato University,
Higashi,23-35-1,Towada, Aomori,034-8628,Japan
2 The University of Tennessee, Department of Small Animal Clinical Sciences
C247 Veterinary Teaching Hospital, Knoxville, TN 37996-4544,USA
3 High Energy Accelerator Research Organization,
Tsukuba, Ibaraki,305-0801,Japan

Abstract

The purpose of this study is to obtain the basic data for radiation safety in the veterinary nuclear medicine. Therefore, human external radiation dose in equine bone scintigraphy was evaluated by using EGS4. Using CGview, we made mathematical phantom of a horse. The phantom has heart, liver, kidney, bladder, lungs, muscle (water equivalent) and bone. The phantom radiation detectors were set up in a position of 0 m, 1 m and 2 m from surface of the body. An effective dose was calculated using a conversion factor by the energy and the fluence of the photon which pass through a detector. The equine bone scintigraphy used radiopharmaceutical labeled with ^{99m}Tc. The biodistribution of the medicine differs at the time after administration, and it influences on dose rate around the horse. Therefore we assumed that the pattern of biodistribution changed into three kinds with the passage of time, and we compared the calculation result and the actual measured value. In addition, created scattered radiation by mesurer himself may effect on dose rate when he stands near a horse. For this evaluation, we put a human phantom to left 30 cm of the horse phantom, and compared dose rate with the right side and the left side. Exposure dose of the general public is a problem after a horse left the hospital. It was assumed that there was a man in a position of 0m and 1m from surface of a horse until radioactivity became extinct after release. The cumulative radiation exposure dose after 24 hours was 42 μSv. It was about 4% of 1 mSv (the radiation dosage safety limit of the general public of the ICRP advice) and supposed that this dose was low enough.

1. Introduction

Now the equine bone scintigraphy using ^{99m}Tc is put into operation in Europe countries, USA, some Asian countries, and etc. If a horse showed minor claudication, it is difficult to be settled in causal locus by using X-ray examination and echography. In addition, examinations of CT and MRI are difficult because of the physique of a horse. In general, bone scintigraphy is extremely useful procedure for a horse, because the examination can be carried out simply without anesthetization. However, equine bone scintigraphy is not carried out because the legal specification of radiopharmaceutical use for animals is not enough in Japan now. Therefore we require the data relating to exposure dose of the persons concerned with equine bone scintigraphy. Consequently human external exposure dosage concerned with equine bone scintigraphy was evaluated by using EGS4 for the purpose of getting a database of the safe use of radiopharmaceutical in veterinary nuclear medicine.

2. Materials and Methods

Equine mathematical phantom was made by using CGview. (Figure 1) Mean of 16 head of 4 years old thoroughbred horses was used for determination of the size of the phantom [3]. The position and the weight of organs were quoted from a book of anatomy [2]. Elemental composition and density of each internal organ were based on the documents about human data [1]. The seven kinds of organs and tissues – heart, liver, kidney, bladder, lungs, muscle (water equivalent), and bone – were considered for this simulation calculation. The detectors were installed in the position of 0 m, 1m and 2 m from the body surface of the horse. (Figure 2) The area of detectors assumed it air. An effective dose was calculated using a conversion factor by the energy and the fluence of the photon which passed a detector. ^{99m}Tc was generally used for this examination as radio-nuclide. Main gamma ray energy is 141 keV, half-life are 6.01 hours. Only energy of 141 keV (discharged ratio: 89.1%) was thought about, and the other energy was ignored. External radiation exposure was evaluated by using EGS4. The dosage of ^{99m}Tc assumed it 5.55 GBq. This is a little much quantity than it is used at veterinary teaching hospital of University of Tennessee.

The technetium injection circulates through the blood of the whole body after it was administered in a jugular vein, and accumulates to bones one or two hour later. After it accumulates to bones, it decays by physical half-life. It was considered that there were three patterns of biodistribution of radio-medicine as follows.

【i】Cardiopulmonary distribution phase (0~15 min)

Decided the distribution ratio of the heart is 3%. It was set from heart-blood volume. The distribution ratio of the lungs is 22%. It was reported that 20% of the blood of the whole body are pulmonary circulation, [4] and it was assumed that many medicines were included in heart and the lungs, because it was the time just after the administration from jugular vein.

【ii】Organs distribution phase (15 min~2 h)

During the fixed time, we assumed that the biodistribution of radio-medicine is proportional to the volume of the organs of the whole body.

【iii】Bones distribution phase (2 h~)

This biodistribution data was converted value which based on the data of the biodistribution of rats about ^{99m}Tc-MDP. After technetium accumulated to bones, it was assumed that the radio-medicine of bones attenuate by only physical half-life. And the influence of urination was examined. Two kinds of radiopharmaceutical (^{99m}Tc-MDP and ^{99m}Tc-HMDP) were used in this actual measured study. Dose rates were measured at the inspection of the cases at the teaching hospital of University of Tennessee. (Table 1 Table 2) The detector (ALOKA: ICS-313) used in this study is ionization chamber survey meter. The detector was proofread at Chiyoda Technol Corporation in Japan, and it was employed at University of Tennessee.

Before comparing actual measured value with a simulation calculation value in EGS, we examined whether there was influence of the scattered radiation from a measurer body. A human mathematical phantom was installed at 30cm from left chest of the equine mathematical phantom (Figure 3). The phantom was made of a water equivalent material, 60kg in weight, height 170 cm. The detectors were installed in the right side and the left side of the chest surface of the horse, and dose rate were compared.

As for the general public, the radiation exposure from a horse after the release is expected, so dose rate in 0 m by a horse was calculated. Furthermore, cumulative radiation exposure dose until radioactivity became extinct when a public stayed at the position of 0m and 1m from a horse surface was calculated.

3. Results and Discussion

3.1 Assessment of the scattered radiation of the measurer

As a result of simulation, influence of the scattered radiation was confirmed. However the influence of the dose rate of a standing person was 0.44 μSv/h, and was 0.16%. (Table 3) It was thought that the difference is negligible.

3.2 Comparison between the actual survey value and the simulation calculation value

The result of the dose rate in the chest surface of the horse is shown in Figure 4. At two hours from administration on the chest, there is no difference in a simulation calculation value in urination and non-urination. Just after the administration of radiopharmaceutical, the actual measured value of the chest was higher than the head and the abdomen. As a result that a concept of the RI Cardiopulmonary distribution was taken in, the calculation value and the measurement value were very close.

The result of the dose rate in the abdomen surface of the horse is shown in Figure 5. At two hours from administration, there was difference in a calculation value in urination or non-urination at the abdomen. The dose rates decreased to half when horse urinated, and 92% of actual measured value is close to an urination simulation value.

The result of the dose rate on the head surface of the horse is shown in Figure 6. At two hours from injection, there was no difference in a simulation calculation value on the head between urination and non-urination. At head position, a maximum difference was about 90% between actual measured value and a calculation value immediately after administering. However 24 hours later, the difference between actual measured value and the simulation calculation value was about 3.5%. Afterwards, in the head position, simulation calculation values in EGS became the underestimate than actual values. Immediately after administering, there is still some problem to the quantity of biodistribution in the head position. The brain including a radioactive medicine might have to be added to equine mathematical phantom.

3.3 Cumulative radiation exposure dose for the public

Calculated cumulative radiation exposure dose of the human assumed to have stayed on by equine body surface for a long time are shown in Table4 and Figure7. The cumulative radiation exposure dose from 24 hours post-administration was 42 μSv. It is about 4% of 1 mSv (The radiation dose limit for the public in the ICRP Publication). Calculated cumulative radiation exposure dose at 1m from horse was 5.3 μSv (about 0.5% of 1 mSv). The cumulative radiation dose at infinite time following 24 hours post-administration of the public exposed from a horse is considerably less than the dose limit of ICRP, so it is safe.

4. Conclusions

The cardiopulmonary distribution was considered by the simulation calculation on the surface of equine chest, therefore the simulation value became near to actual measured value. Therefore the cardiopulmonary distribution of the chest was thought to be appropriate. In addition, the dose rate of the chest is very high just after administration of radioactive medicine. It is necessary for the staff not to approach in the vicinity to the equine chest carelessly immediately after administering. On the surface of the abdomen at two hours post-administration, 92% of actual survey value was close to an urination simulation value. It is thought that it became almost same to urinary value, because many horses urinated. There is individual difference in the actual measurement value on equine head until four hours after administration. It is thought that it depends on a difference of metabolic speed of each horse. Moreover, the EGS simulation calculation result of the head was undervalued overall. However, there is no problem because it should evaluate the exposed dose of the public after the next day. The cumulative radiation exposure dose of the public is considerably less than the international recommendation value. We conclude that the setting condition of EGS was suitable, and realistic simulation was possible.

Acknowledgments

This work was supported by High Energy Accelerator Research Organization. And we acknowledge the valuable advices sincerely.

References

1) ICRU Report 46, Photon, Electron, Proton and Neutron Interaction Data for Body tissues.
2) JRA Equine Research Institute, 1996, "The book of medical science of horses", pp.90-92, JRA, Tokyo
3) Y. Nagata, "Development and nutrition of racing horses", pp.166-174, Japan Racing Association PR center, Tokyo (1999).
4) Holmes, J. R. 1982. A superb transport system-The circulation. Equine Vet. J. 14: 267-276

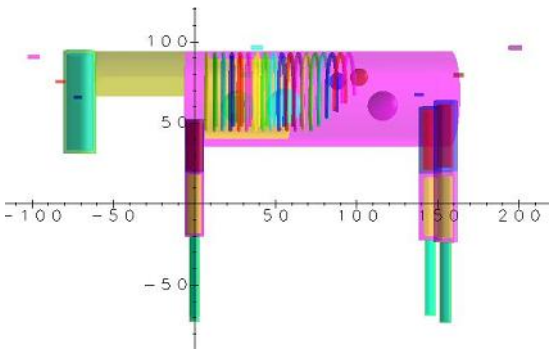

Figure 1 Equine mathematical phantom

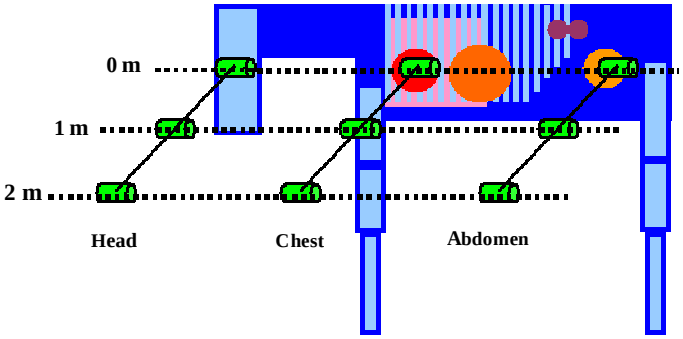

Figure 2 Locations of the detectors around the phantom surface

Table 1 The weight and the medicine dose of the horse used for an experiment

equine	weight (kg)	dose (GBq)	type of ^{99m}Tc
A	445	5.08	MDP
B	522	5.33	MDP
C	481	5.14	MDP
D	481	4.91	MDP
E	499	4.81	HMDP
F	522	5.7	HMDP
G	553	5.03	HMDP

Table 2 Average of the actual measured value (μSv)

time after the administration (h)	head	chest	abdomen
0〜0.25	90〜140	250〜300	180〜240
1	100	120	130
2	100	90	110
6	50	50	50
24	5	4	3

Table 3 Influence of the scattered radiation by measurer on measurements value calculated in EGS

(μSv/h)

	dose rate
The left surface	284.06
The right surface	283.62

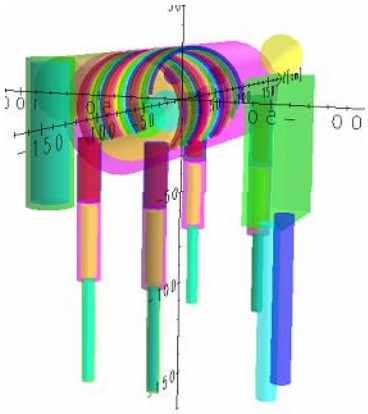

Figure 3 The positions of measurer and horse in mathematical phantom

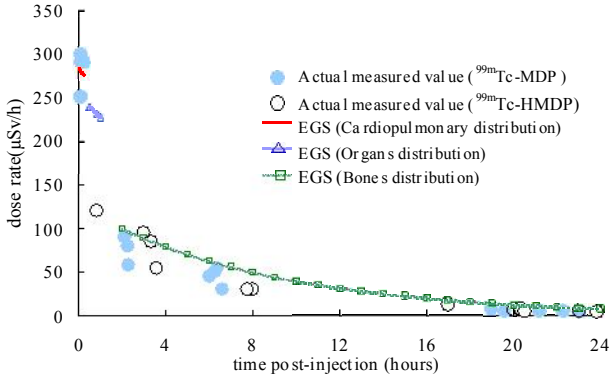

Figure 4 Comparison between simulation calculation value and the actual value of the dose rate at the surface of the equine chest.

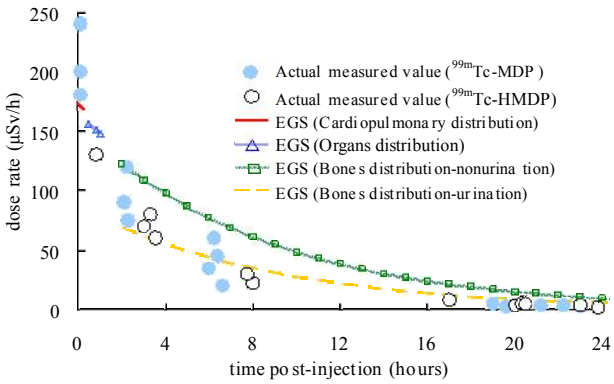

Figure 5 Comparison between simulation calculation value and the actual value of the dose rate at the surface of the equine abdomen.

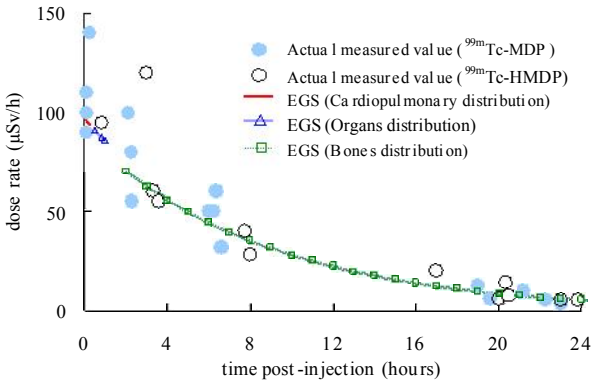

Figure 6 Comparison between simulation calculation value and the actual value of the dose rate at the surface of the equine head.

Table 4 Cumulative radiation exposure dose of the human assumed to have stayed on by equine body surface. (μSv)

time post-injection (h)	0m	1m
4	420	54
8	270	34
12	170	21
16	110	13
20	66	8.5
24	42	5.3
28	26	3.4
32	17	2.1
36	11	1.3
40	6.6	0.8
44	4.2	0.5
48	2.6	0.3

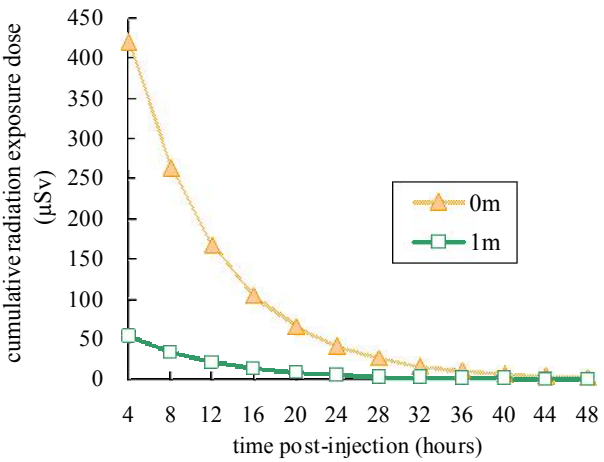

Figure 7 Cumulative radiation exposure dose of the human assumed to have stayed on by equine body surface.

EXTERNAL DOSE DISTRIBUTION OF THE CANINE BODY IN VETERINARY NUCLEAR MEDICINE ESTIMATED BY USING EGS4

M. Nishioka[1], K. Oono[1], E. Kobayashi[1], A. Shibata[1]
T. Kakizaki[1], S. Wada[1], T. Sano[1], Y. Namito[2], H. Hirayama[2], and N. Ito[1]

[1]School of Veterinary Medicine, Kitasato University, Higashi, 23-35-1, Towada, Aomori, 034-8628, Japan
[2]High Energy Accelerator Research Organization, Tsukuba, Ibaraki, 305-0801, Japan

Abstract

Human external exposure dose from the dog which administered radiopharmaceutical in veterinary nuclear medicine was evaluated. The mathematical phantom that modeled a real dog was made anatomical faithfully to examine canine internal exposure in the future. External dose rate of the canine body in veterinary nuclear medicine was estimated by using EGS4.

It was guessed that the existence of urine influenced the dose rate. Therefore the simple urinary mathematical phantom was made, to evaluate the exposure to the human from the canine excreted urine.

Using CGview, the canine and urinary mathematical phantoms were made. ^{99m}Tc was used as a radioisotope (RI) in this study. The RI distribution of canine body was assumed the two cases. One is the distribution in proportion to the weight of the internal organs, and another is considering the kinetic distribution of the pharmacy. Furthermore, the differences of dose rate by the occurrence of urination were evaluated.

The detectors were installed in the position of 0 cm, 30 cm and 100 cm from the body surface of the dog in the vicinity of head, heart, liver, bladder, and trunk center.

The dose rate was greatly different because of two kinds of inside of the body distribution at two hrs after administration. Moreover, there was a great difference at the dose rate from the dog at nearer position when urine existed in the bladder.

In the stage of the early period of RI dosage, the exposure dose from urine was the problem as human external dose.

1. Introduction

Nuclear medicine for dogs, cats and horses are already performed in U.S.A. and Europe. Nuclear medicine is utilized for the evaluation of organ functions, which is difficult to be evaluated by other methods, invariable patients without surgical invasion. The necessity of the veterinary nuclear medicine will increase in future. Nuclear medicine is now preparing to perform in the Japanese veterinary medicine and it is necessary to evaluate human external exposure dose around the dog which is administered radiopharmaceuticals. However, the data of external dose rate of the dogs, which are administered the RI, have been limited. We therefore tried to simulate the external dose distribution of the dog administered the RI. Monte Carlo method has been widely used to calculate the dose distribution in the field of nuclear medicine in human beings and we considered EGS4 code was suitable to Monte Carlo dose calculation in this study. RI administered to the body was attenuated dependent on the physical and biological manner, especially of urinary excretion. In this study, we simulate the external exposure dose of human around the dog administered the RI, and evaluate the differences between the existence or not of urine in the bladder.

2. Materials and Methods

The averages of weight and girth of the abdomen, trunk, head, cervix, tail and extremities were measured in 5 adult female dogs. The morphological data included the size, weight and volume of internal organs (lungs, heart, liver, kidney and bladder) and the skeleton (extremities, spine and skull) were obtained by referring the text book [1] and analysis of X-ray and CT examination.

The canine mathematical phantom was created by the CGview software. (Fig. 1-3) The mathematical phantoms of a columns, spheres and torus were assumed as internal organs, respectively. Phantoms were placed on reference of the data of real dogs. The region of internal organs such as skeleton, soft tissue, fat tissue and muscle tissue were defined as shown in figures 2 and 3. Elemental composition and density of each organ was based on the human data. [2] RI dose was set to 30 MBq/head referred to the text book of veterinary nuclear medicine in USA. [3] The RI was hypothesized to distribute depended on the organ weight.

We simulated the differences of two cases between to consider the pharmacokinetic of RI and not to consider. Pharmacokinetic distribution data were referred to the report of rats (Table. 1)

The regions of detectors were defined as air in CGview. The detectors were placed on expected area, which was necessary to consider the behavior of human and dog during the nuclear medicine examination. The detectors were, therefore, installed in the position of 0, 30 and 100 cm from the body surface, which placed in horizontally from the head, heart, trunk center, liver and bladder phantoms.

In this study, ^{99m}Tc (the energy of gamma-rays is 141 keV and a physical half life is 6.01 h)was used as RI and assumed to be administered in mathematical phantom. The energy and fluencies of the photon which passed a detector area were calculated by EGS4. Furthermore, dose rate was calculated from an effective dose (Sv) per one photon.

The influences of urination were evaluated as follows. The dog was hypothesized to urinate every 4 hour. The urine volume at the once urination was assumed 50 ml in the 11.6 kg beagle because normal urine volume of a dog is 20-40 ml/kg/day. [4]

3. Results and Discussion

The created dog phantom was suggested as 11.6 kg, which was similar to a real dog described in the references. [1] Moreover, we defined and produced the resemble dog phantom after due consideration of animal tissue construction (Fig. 1-3). This phantom will have the potential to assess the internal exposure of the dog administered an RI and to be able to the correction of absorbance of gamma-rays in nuclear medicine.

The external dose rates were then compared at a different distance between the dog phantom and each detector. In all condition, except for the 0 cm at the bladder region, effective dose rate around the dog was tend to lower in considering the kinetic distribution condition than simple distribution accompanied with the organ weight (Fig. 4). At once, if the dog had urination, the dose rate of bladder region was apparently decreased for one-fifth of non-urination condition. The urination contributed to the heterogeneous effective dose rate on the surface of the dog. The assembly of the simulation systems included the kinetic parameters were suggested that took also important role in the realistic calculation of exposed dose by simulations.

On the other hand, dose rates were more homogenously distributed according to leaving from the surface of the dog. There were little differences of dose rates in each region corresponding to the organ from 100 cm away from the dog phantom. This is the reason why the phantom was assumable as a point radiation source when detectors were leaving far from the phantom.

We also estimated the radiation exposure from urine as a pilot study with considering to early period after RI administration by above systems. It was thought that the dose rate was enough decreasing lower than recommended value in BSS, which is 1×10^7 Bq of ^{99m}Tc, leaving 30 cm away from excreted urine [4] and the dose rate at the same place (30 cm) was 3.8×10^5 Bq within 24 hours after injection.

4. Conclusion

Our results showed the great influence on external exposed dose of the urine existence in and out of the body. During the hospitalization of the dog administered radiopharmaceuticals, our study suggested the recommendation to remove the urine as rapidly as possible and it make possible to suppress human external radiation exposure as minimum.

In future, it will be able to compare between our simulation results and actual survey by revision of the low. Because radiation absorbance by the tissue can be calculated with our dog phantom system, more quantitative veterinary nuclear medicine will be expected to be done. The EGS code and our dog phantom play an important role in the progression of Japanese veterinary nuclear medicine.

References

[1] Evans, H. E., Christensen, G. C. (1978) In Miller's ANATOMY OF THE DOG, p. 389-495.

[2] ICRU Report 46, (1992) Photon,Electron,Proton and Neutron Interaction Data for Body tissues.

[3] Gregory, B. D., Anne, B. and Federica, M. (2003) Canine Bone Scintigraphy, in Nuclear Medicine Short Course. University of Tennessee, Knoxville.

[4] Iwasaki, T. et al., (2005) In Textbook of VETERINARY INTERNAL MEDICINE, Japan Veterinary Internal Medicine Academy, p. 259.

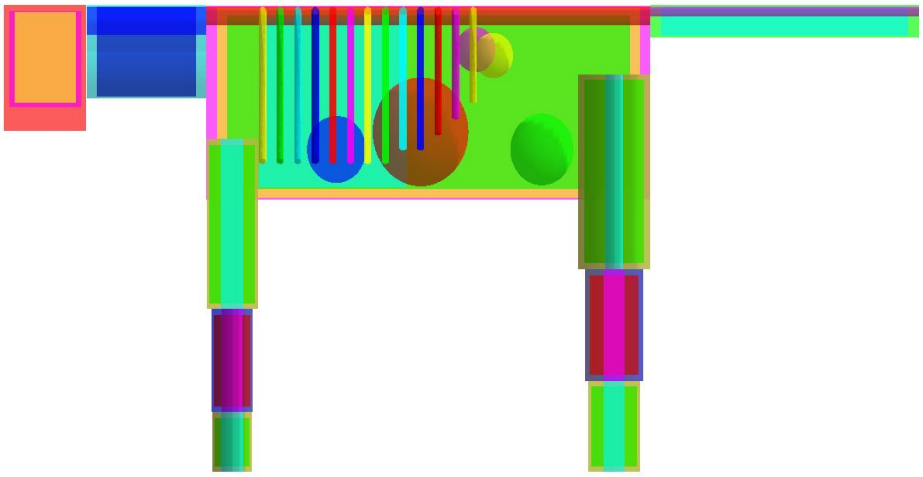

Fig. 1 Over view of the mathematical phantom of a dog.

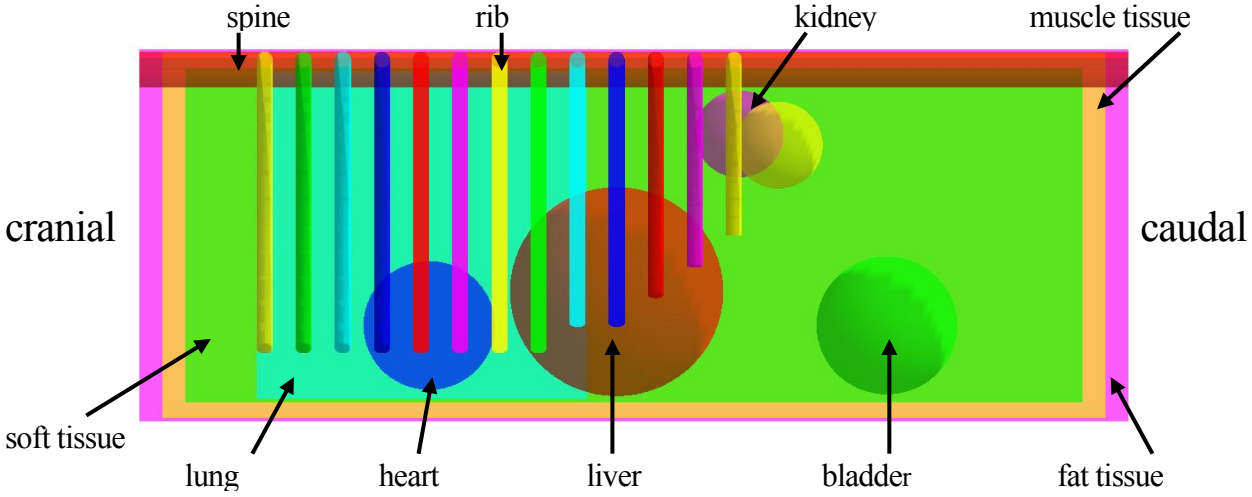

Fig. 2 The canine phantom of thoracic and abdominal organs.

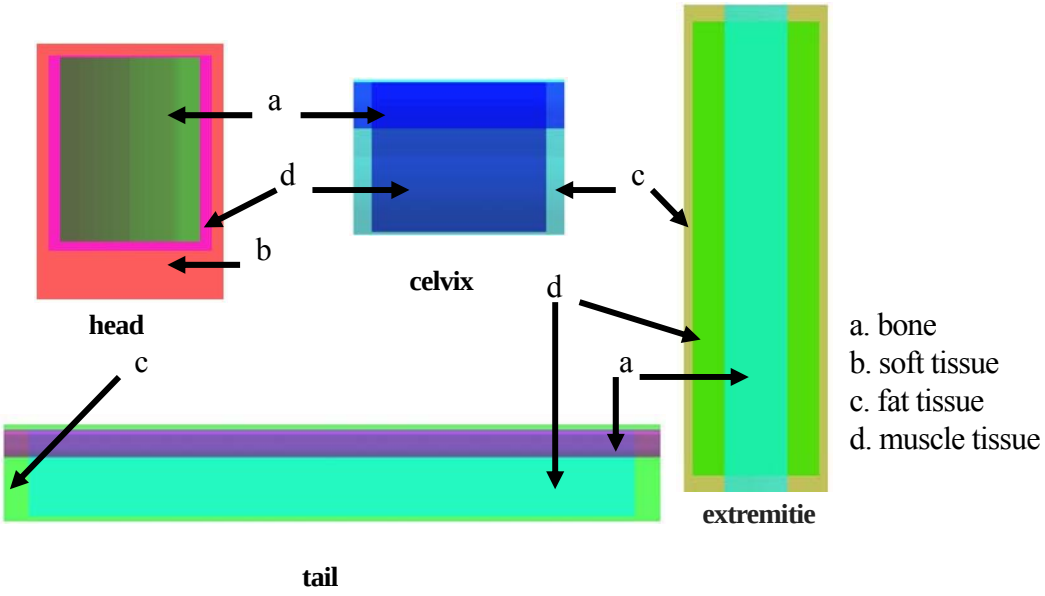

Fig. 3 Phantoms of the head and appedicular organs.

Table. 1 The dose distribution of ^{99m}Tc 2 hours after injection. (%)

Liver	0.29	L. humerus	1.39	R. armend	0.49	R. cruris	0.75
R. kidney	0.5	L. forearm	0.69	L. femoris	1.06	R. footend	0.62
L. kidney	0.5	L. armend	0.49	L. cruris	0.75	Skull	3.06
Bladder	38.8	R. humerus	1.39	L. footend	0.62	Others	43.04
Spine	3.82	R. forearm	0.69	R. femoris	1.06		

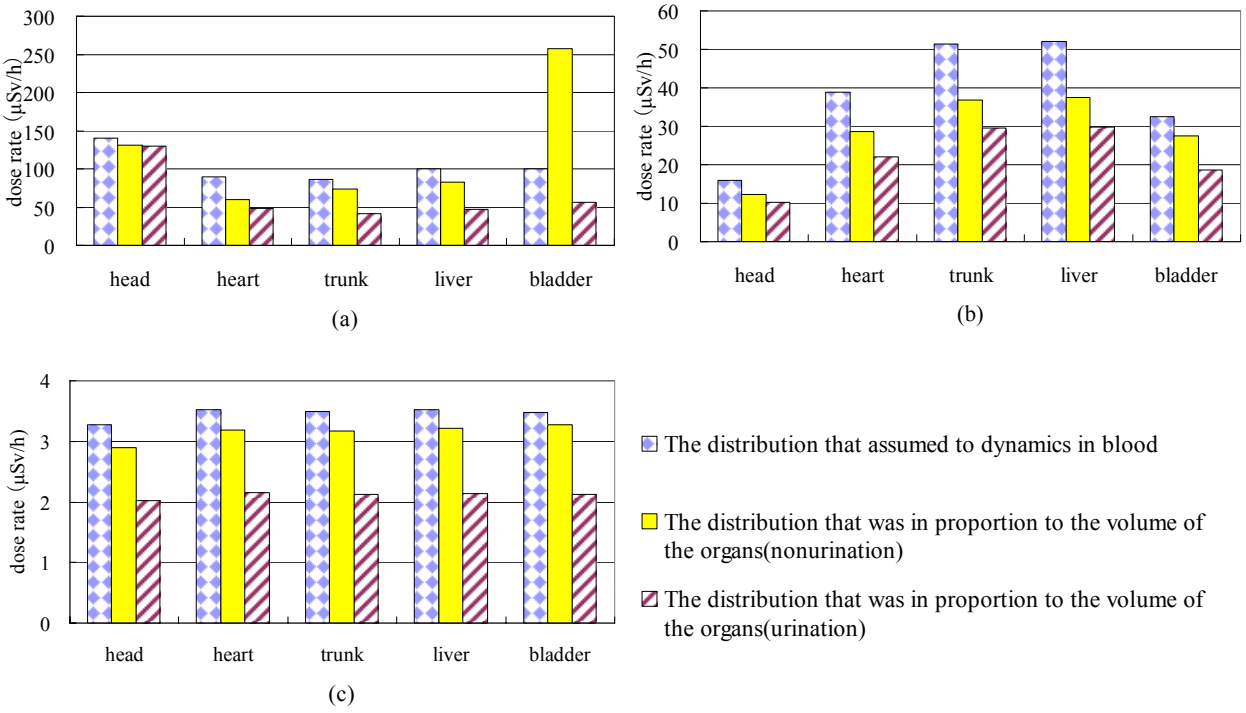

Fig. 4 External exposure dose rate of the detector regions corresponded to each organ at (a) 0cm (b) 30cm (c) 100cm leaving from the surface of the dog phantom.